UNIMORE
UNIVERSITÀ DEGLI STUDI DI
MODENA E REGGIO EMILIA

UNIVERSITÀ DEGLI STUDI
DI MODENA E REGGIO EMILIA

Dottorato di ricerca in Ingegneria industriale e del territorio

Cycle XXXVIII

Lumped-parameter model of an external spur-gear pump: development and experimental validation

Candidato: Giuseppe Totaro

Relatore: Prof. Barbara Zardin

Correlatore: Dott. Federica Franzoni

Secondo Correlatore: Prof. Massimo Borghi

Coordinatore del Corso di Dottorato: Prof. Alberto Muscio

Contents

Abstract

External spur gear pumps are fixed-displacement positive-displacement machines widely employed in fluid power systems for both mobile and stationary applications, owing to their compactness, robustness, and manufacturing simplicity. The progressive electrification of hydraulic actuation has increased the need for pumps that are more efficient and quieter, particularly in mobile machinery. In this context, numerical tools that can predict performance, losses, and key internal phenomena are valuable for supporting design choices, reducing development time, and guiding optimisation.

This thesis presents the PhD work carried out at the Fluid Power Laboratory of the "Enzo Ferrari" Department of Engineering (University of Modena and Reggio Emilia), in collaboration with Dana Motion Systems Italia S.r.l., specifically its subsidiary DPC Hydraulics S.r.l. in Reggio Emilia, which specialises in the development and manufacture of hydraulic components.

The main objective is the development of a lumped-parameter (0-D) model of an external spur gear pump to serve as a digital design-support tool. The model is implemented in Simcenter Amesim by creating a dedicated custom library of components, and it is complemented by MATLAB-based procedures where required. The modelling framework is formulated under the assumptions of incompressible and isothermal fluid, steady-state operating conditions, and a fixed lateral clearance. Despite these simplifying hypotheses, the model is designed to capture the main mechanisms governing the dynamic behaviour, pressure transients, the evolution of running-in wear and finally an estimation of volumetric behaviour and hydro-mechanical losses.

The proposed tool predicts volumetric performance through the evaluation of pressure evolution in the tooth-space chambers and at the suction and delivery ports, the delivered flow rate, and the internal leakage contributions through the main lubricating interfaces. These include leakage paths associated with tooth-tip clearances, the lateral gap, and tooth-flank gaps. The hydro-mechanical sub-model estimates the forces and torque acting on the gears due to fluid pressure and gear contact and quantifies torque losses associated with viscous shear in the clearances (including the lateral gaps, tooth-tip gaps, and journal bearings), as well as mechanical losses related to gear meshing. A journal-bearing modelling approach is employed to estimate the average gear-centre positions by enforcing force equilibrium, accounting for the contributions of pressure forces, gear-contact forces, and hydrodynamic lift. Gear eccentricities are therefore obtained and used to improve the estimation of tip- and flank-gap leakages and to support the running-in analysis. In addition, the framework provides a prediction of the outlet pressure ripple on a delivery line, which is strongly related to fluid-borne noise.

Model validation is performed through an experimental campaign conducted at the DPC Hydraulics S.r.l. laboratories. Two pump displacements are investigated (8.2 cc

and 16 cc), and three samples are tested for each displacement. Prior to assembly, geometric dimensions relevant to model definition are measured; detailed measurements are also carried out on the internal profiles of the pump housings. The pumps are then assembled, run in, and disassembled to repeat the housing measurements and quantify wear induced by the running-in process. Performance tests are conducted at different operating points to assess volumetric and hydro-mechanical efficiency at two oil temperatures (30 °C and 60 °C). The experimental campaign is completed with pressure-ripple measurements, in which a rigid line is mounted at the pump outlet and pressure oscillations are recorded across the same operating points and temperatures.

The results demonstrate that the model can predict volumetric performance with good accuracy over the tested ranges and provides a resonable estimation of housing wear due to running-in using purely geometric considerations. The model underestimates the average maximum gear penetration, while providing a good estimation of the angular extension of the wear zone.

Regarding hydro-mechanical performance, the model tends to underestimate torque under all operating conditions, plausibly due to neglected phenomena such as floating bearing blocks, tilting and mixed-lubrication effects, although the overall trends are captured. Conversely, the pressure-ripple predictions show discrepancies, with the model generally overpredicting the amplitude of oscillations measured on the delivery line.

Overall, this work delivers a validated lumped-parameter modelling tool that supports the analysis and design optimisation of external spur gear pumps, with specific emphasis on efficiency, losses, running-in wear, and pressure ripple.

1. Introduction

External spur gear pumps are fixed-displacement machines that are widely used in fluid power applications, both stationary and mobile.
This type of pump is compact, robust, and of simple construction.
Figure 1 shows an exploded view of an external spur gear pump, in which it is possible to observe the main components of the pump:

- A pair of spur gears. One of these gears is the driving gear, connected to the prime mover, and the other is the driven gear. During gear rotation, the oil moves from the suction port into the spaces between the gear teeth and is trapped between the gears and the housing. As the gears rotate, the oil is transported from the suction side to the delivery side. The contact points between the gears create a separation between the low-pressure and high-pressure zones. In general, the gears used in this type of machine are identical.
- A pair of floating bearing blocks that support the gear shafts. These elements are referred to as 'floating' because they can undergo micromovements in the axial direction to compensate for variations in the lateral clearance between the gear faces and the journal bearings under different operating conditions.
- Gaskets. These components are important for compensating the lateral clearance, which is achieved through the application of suction and delivery pressures on dedicated areas of the floating bearing blocks, while the gasket separates these areas.
- All the previous components are enclosed within the pump housing and closed with end plates.

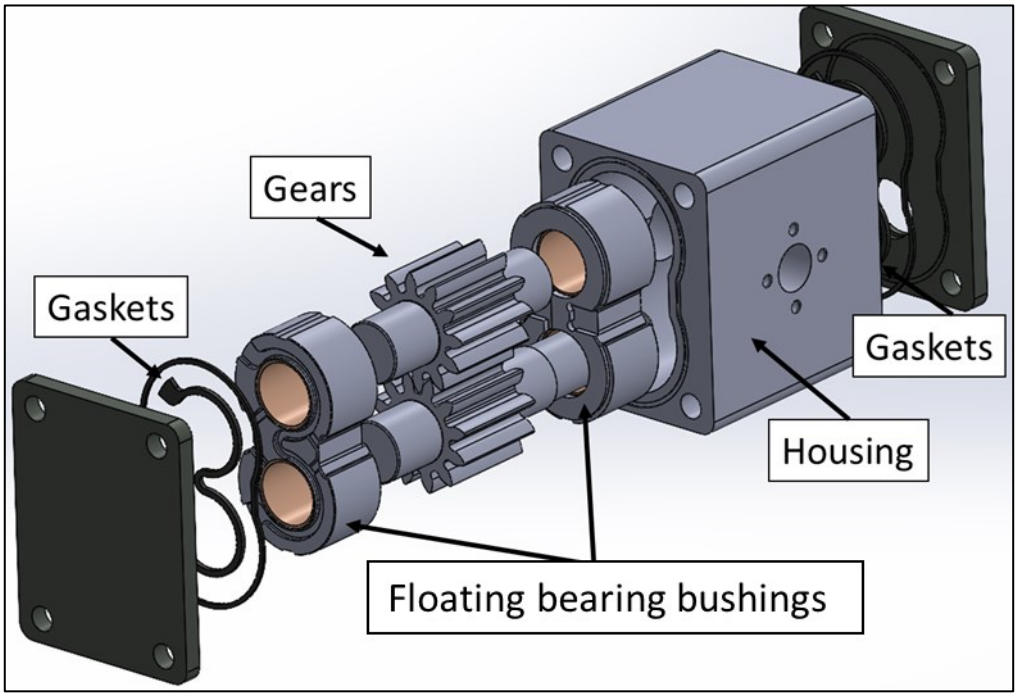

Figure 1 - Exploded view of an external spur gear pump

Although this type of machine is relatively simple, several aspects must be considered in its design. Some of these are:

- The definition of the gear profile, which in the general case is involute. The gears are manufactured using cutting tools whose dimensions differ from those of standard tools used for transmission gears.
- The geometry of the anti-noise recesses on the bearings blocks. These recesses are introduced to reduce pressure peaks during the gear meshing (engagement) phase and to reduce cavitation phenomena in the disengagement phase. An appropriate design of these recesses can reduce pressure peaks, cavitation, and the resulting pump noise; however, it may also reduce the volumetric efficiency of the pump.
- The geometry of the balancing areas on the floating bearing blocks. The correct definition of these areas is important to avoid an excessively large lateral gap, which would lead to low volumetric efficiency, or, conversely, contact between the gears and the floating bearing blocks, which would result in high volumetric efficiency but low hydro-mechanical efficiency.

The reduction of energy consumption is an important topic nowadays, particularly in the context of the electrification of fluid power applications, which requires pumps that are more efficient and quieter.
The use of virtual models to simulate the behaviour and the various aspects of interest of spur gear pumps is a valuable tool for the design of new pumps or the improvement of existing models, reducing both development time and cost.

The choice of a simulation tool is based on the aspects to be analysed, the required accuracy of the results, and the available computation time. The phenomena represented within a model vary according to the objectives of the simulation; for example, thermal effects, cavitation, leakages, or micromovements of the machine components may or may not be included. A possible classification of simulation models can be made based on the discretisation of the fluid domain [1]. In particular, there are:

- 0-D models or lumped-parameter models: each volume into which the fluid domain is divided is characterised by homogeneous pressure and temperature at every point. Therefore, pressure and temperature are functions only of time and not of space.
- 1-D models or distributed-parameter models: a single volume is subdivided into several interconnected sub-volumes. In each of these sub-volumes, pressure and temperature are considered homogeneous. As a result, the pressure and temperature in the overall volume are functions not only of time but also of space.
- 2-D and 3-D models, based on CFD simulations: these models allow the fluid behaviour inside the machine to be represented by numerically solving the Navier–Stokes, energy, continuity, and state equations, which admit analytical solutions only in simple cases. This type of model can be the most accurate

(depending on the mesh definition, turbulence model adopted, ability to include small gaps in the fluid domain, etc), but it requires the longest computation time, which also depends on the simplifications introduced and on whether a 2-D or a 3-D model is adopted.

- Mixed models, in which the model is obtained by combining the previous approaches.

In general, models with a higher level of discretisation increase the accuracy of the simulation but require longer execution times.
0-D/1-D models provide good results with relatively modest computation times and model set-up effort, whereas 3-D modelling makes it possible to determine the pressure and temperature distribution at a finite, but large, number of points in the domain. This highlights behaviours that are not evident in lumped-parameter models, where pressure and temperature are assumed to be homogeneous in each chamber/control volume, but it entails significantly higher computation times.

S. Manco and N. Nervegna [2] proposed a 0-D model of an external gear pump to estimate the volumetric performance of the pump, assuming a constant lateral gap and fixed gear centres. The model was validated experimentally, showing good agreement with the measured delivery pressure and volumetric efficiency. Although it does not account for the dynamics of the micromovements of the gears, the model makes it possible to calculate the forces acting on the gears and to predict the wear profile of the casing.

A. Vacca and M. Guidetti [3] developed a 0-D model to simulate the volumetric performance of the pump while also considering gear micromotions. The 0-D model is combined with CFD simulations to model leakage through the lateral gap, which is assumed to be fixed. Accounting for gear micromotions allows a better approximation of pump-housing wear.

Previous works mainly study the volumetric performance of the pump. B. Zardin et al. [4] present a 0-D model for evaluating the hydro-mechanical efficiency of external gear machines by accounting for the main friction losses: viscous losses at the tooth-tip gaps, at the gaps between bearing blocks and gears, at the journal bearings, and meshing losses. The contribution of meshing losses is evaluated in terms of an average value using the formulation proposed by ISO/TR 14179-1. The model predictions are compared with experimental data from commercial pumps.

R. Rituraj et al. [5] developed a lumped-parameter model for the evaluation of hydro-mechanical losses, considering the main friction losses due to the tooth-tip gaps, lateral gaps, and journal bearings. For meshing losses, they employ an elastohydrodynamic lubrication formulation to define friction in the contact. This method allows the determination of the local meshing force along the contact line.

The study of the axial balancing of the floating bearing blocks is an important aspect in the design of external gear pumps.
M. Borghi et al. [6] investigated the axial balance of hydraulically balanced external

gear pumps, focusing on the design of bearing-block balancing surfaces. A 2-D numerical procedure based on the Reynolds equation was developed to compute the pressure distribution within the lateral clearance, and to derive both the widening thrust and its application point. The balancing thrust generated by external active areas was also evaluated. Two industrial pumps were analysed over a wide operating range and different meshing positions, considering both constant and variable clearance heights and the effect of bearing-block tilt. The approach was validated against experimental data from the literature and used to propose practical design guidelines. The same authors [7] also accounted for the elastic deformation of the internal bushing surfaces and the variation in the dynamic viscosity of the fluid - phenomena that affect the determination of bushing behaviour and the pressure distribution in the lubricating gap.

Torrent et al. [8] proposed a fast, experimentally validated model to predict the motion of floating bearing blocks in external gear pumps. Instead of CFD, the approach uses Bond Graph modelling and dimensional analysis to represent lubrication at the gear–bushing interface as the combination of a fixed-incline sliding bearing (hydrodynamic wedge) and a parallel-surface thrust/squeeze-film mechanism. The rigid-body dynamics include axial translation and tilting, driven by hydrostatic forces from delivery pressure, seal compression, casing–bushing viscous damping, hydrodynamic lift/torque, and journal-bearing stiffness. Validation was performed on a laboratory pump using laser micrometers to measure bushing displacement and tilt. The model reproduces key behaviours such as hysteresis in film thickness and shows that pressure pulsations are strongly damped, enabling the interpretation of volumetric and mechanical efficiency trends across operating conditions.

S. Dhar and A. Vacca [9] developed a coupled CFD model to compute the gap pressure field and leakages, while a 0-D model provides time-varying tooth-space and port pressures as boundary conditions and receives leakage flow rates for the lumped-parameter continuity equations. An axial-motion algorithm updates film thickness and bushing orientation by enforcing quasi-static force and moment equilibrium. The method was applied to an industrial pump over different speeds and pressure levels to predict gap heights and quantify competing losses due to drain leakage and viscous shear.

The running-in process is an important phase for this type of pump because it ensures correct coupling between pump components, reduces surface micro-asperities, and ensures the required pump performance.
Mucchi et al. [10] modelled the running-in process of an external gear pump, aiming to reduce manufacturing time. Mean pressure forces/torques, meshing forces, motor torque, and hydrodynamic bearing reactions - defined using a lumped-parameter model - are used to determine the static equilibrium position of the gears at the end of each running-in step. The model predicts the evolving internal wear profile of the casing, as well as the radial thickness and volume of removed material per step. Results were validated against profilometer measurements on an industrial steering

pump, showing good agreement and highlighting a strong sensitivity to clearance tolerances. The analysis reveals that most material is removed in early steps and supports a revised running-in schedule achieving a reduction in total running-in time.

Most of the previous models are based on the assumption of an isothermal fluid and rigid bodies.
A. Pawar et al. [11] compared how different modelling assumptions affect the predicted performance of an external gear pump. Using a multi-domain model, they simulated a commercial unit through five cases of increasing complexity, from an isothermal lumped-parameter model with simplified film equations to a coupled framework including Reynolds-based lubrication (mixed lubrication, cavitation/aeration), rigid-body micromotions, and pressure/thermal deformation of gears, bushings, and housing with solid heat transfer. Predictions of pressure ripple, chamber pressurisation, wear, leakages, and torque-loss breakdown were compared with experiments. Results indicate that simplified models can capture pressure ripple, whereas accurate predictions of losses, leakage, and wear require deformation effects and are improved further by including thermal behaviour. As model complexity increases, simulation time also increases.

In the following, some examples of 3-D models used to study external gear pump behaviour are presented.
A. Corvaglia et al. [12] developed a 3-D CFD model of an external gear pump coupled with the delivery line in SimericsMP+ and validated it against measured pressure ripple. The CFD-predicted and measured flow oscillations showed very good agreement over several operating points, supporting both the model fidelity and the flowmeter reliability.

P. Szwemin et al. [13] built CFD models to quantify leakage through radial and axial gaps in an external gear pump and assessed the impact of gap size/shape and gear eccentricity on volumetric efficiency. Simulations indicated that increasing radial clearance reduces flow rate, while eccentricity can mitigate radial leakage and alter circumferential pressure build-up. A 3-D model including axial flow showed axial-gap losses to be dominant at higher pressures; experimental efficiency data agreed well with CFD trends.

E. Frosina et al. [14] presented a 3-D CFD model using PumpLinx of a high-pressure external gear pump including detailed internal leakages and groove effects, and validated it on a dedicated test bench. The model predicted volumetric efficiency and delivery pressure ripple with good accuracy, while torque discrepancies highlighted unmodelled mechanical friction. Chamber-pressure histories were used to identify low-pressure regions and, with a cavitation sub-model, to locate cavitating zones.

F. Orlandi et al. [15] compared two STAR-CCM+ meshing strategies for external gear pump CFD under realistic operating conditions: overset meshes enabling zero-contact modelling and dynamic/adaptive remeshing requiring a finite tooth gap. The overset approach better reproduced pressure evolution within tooth spaces and confined low-pressure regions, while the dynamic approach yielded mean flow rates

closer to theoretical values but resulted in larger pressure ripple and more extended low-pressure (aeration/cavitation-prone) zones due to continuous inter-tooth leakage. The study highlights how the tooth-contact treatment strongly affects predicted pressure fields and cavitation/aeration localisation.

This thesis presents the PhD work carried out at the Fluid Power Laboratory of the "Enzo Ferrari" Department of Engineering, University of Modena and Reggio Emilia, in collaboration with Dana Motion Systems Italia S.r.l., specifically its subsidiary DPC Hydraulics S.r.l. in Reggio Emilia, which specialises in the development and manufacture of hydraulic components.

The aim of this research is to develop a lumped-parameter model of an external spur gear pump, to provide a design-support tool for this class of machines. In fact, although many research works have been carried out during the last decades, the simulation tools developed rarely are commercialized and available for industry and design applications. In Simcenter Amesim, a more detailed model for external gear pumps has been recently introduced, but it is still lacking the micromotion of the gears, which is considered crucial in determining the pump behaviour [17].

It was chosen to develop the model in Simcenter Amesim, since the company is familiar with this simulation tool, by developing a custom component library, enabling the investigation of volumetric and hydro-mechanical performance as well as the running-in process.

Simcenter Amesim is a simulation environment for modelling and analysing multi-domain physical systems. Through ready-to-use libraries, it supports the design and optimisation of complex systems that include mechanical, hydraulic, pneumatic, thermal, and electrical domains.
In addition, it provides an environment (Simcenter Submodel Editor) where coding is possible, to create personalized components and dedicated libraries, that then can interact with all the other elements available in the software.

The first part of the thesis introduces the model and its formulation:

- **Section 2** describes the fluid-dynamic modelling. It presents the fundamental equations used to define the gear geometry and chamber volumes, and the formulations adopted to represent volumetric leakages. The fluid-dynamic model predicts the pressure evolution in the pump chambers and at the suction and delivery ports, the flow rate, and the leakage flows through the lubricating interfaces.
- **Section 3** presents the hydro-mechanical modelling used to estimate the forces and torque acting on the gears due to fluid pressure and gear contact, as well as torque losses associated with viscous friction and gear meshing friction.
- **Section 4** describes the journal-bearing modelling adopted to estimate the gear-centre positions by enforcing force equilibrium on the gears. The force balance includes contributions from fluid pressure, gear contact, and the

hydrodynamic lift generated by the journal bearings. Gear eccentricities are crucial for modelling the running-in process and for accurately predicting pump performance.

- **Section 5** details the modelling of the running-in process.

The second part of the thesis presents the experimental activities and the validation results. The experimental campaign was conducted at the DPC Hydraulics S.r.l. laboratories. Two pump displacements were considered (8.2 cc and 16 cm^3); for each displacement, three samples were tested. Before assembly, geometric dimensions relevant to model definition were measured, with more detailed measurements performed on the internal profiles of the pump housings. The pumps were then assembled, run in, and disassembled to repeat housing measurements and quantify running-in wear.

Performance tests were carried out to evaluate volumetric and hydro-mechanical efficiency at different operating points and at two oil temperatures (30 °C and 60 °C). The campaign concluded with pressure-ripple tests: a rigid line was mounted at the pump outlet and pressure oscillations were recorded over the same operating points and temperatures.
The experimental activities and the model validation results are presented in the following sections:

- **Section 6** describes the experimental set-up and test procedures.
- **Section 7** compares the model predictions of housing wear due to running-in with experimental measurements.
- **Section 8** analyses volumetric performance and compares experimental data with model results.
- **Section 9** discusses the pressure-ripple results, comparing simulations and experiments.

Section 10 presents the final conclusions.

2. Fluid dynamic modelling

According to the lumped-parameter modelling approach, each pump chamber is represented as a control volume (capacity) connected to the others through orifices, which may exhibit either turbulent or laminar flow behaviour. The volume of each chamber and the flow areas of the orifices depend on the angular position of the gears.

In the modelled gear pump, the driving and driven gears are identical. In this case, the number of modelled chambers is $2 * z$, where z is the number of teeth per gear, corresponding to the number of chambers generated by one gear (V_1, i and $V_{2,i}$) . Two additional control volumes are considered in the model: one for the delivery (V_D) and one for the suction (V_S) , resulting in a total of $2 * z + 2$ control volumes.

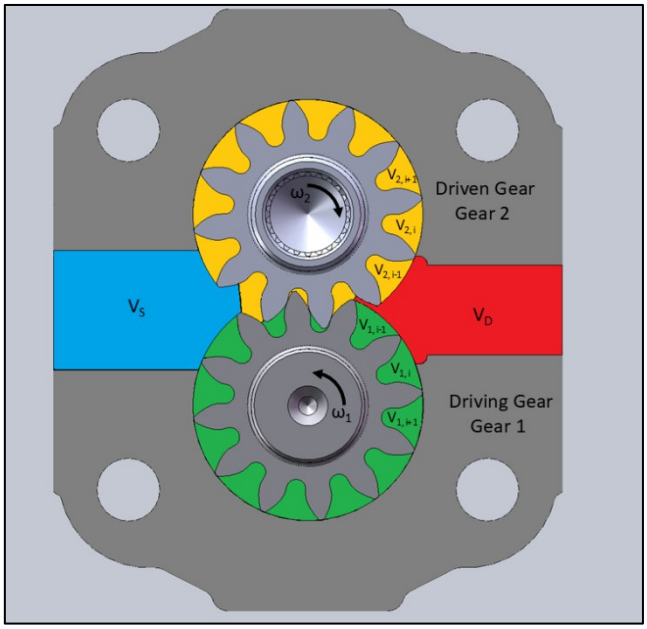

Figure 2 – Control volumes defined in the lumped-parameter model of the external gear pump

In the model, the following connections between the control volumes are considered (see Figure 3):

- **Pump Chambers – Delivery (CD)**: the pump chambers and the delivery volume are connected through two different areas. The first is the opening that becomes active when the chambers are exposed to the delivery volume, generating a radial flow. The second is the communication area created by the anti-noise recesses located on the face of the floating bearing blocks. These types of connections are modelled using the laminar-turbulent orifice equation, presented later.
- **Pump Chambers – Suction (CS)** : the pump chambers and the suction volume are connected through two different areas. The first is the opening that becomes active when the chambers are exposed to the suction volume, generating a radial flow. The second is the communication area created by the anti-noise recesses located on the face of the floating bearing blocks. These

types of connections are modelled using the laminar-turbulent orifice equation.

- **Adjacent Pump Chambers (CA)** : adjacent chambers on the same gear are in communication with each other through the clearances between the gear side faces and the floating bearing blocks, as well as through the clearances between the gear tooth tips and the pump casing. These connections introduce volumetric leakages into the pump and are modelled by assuming laminar flow conditions.
- **Chambers – Drain (CDr) :** the pump chambers are connected to the drain through the clearance between the gear side faces and the floating bearing blocks. These connections also introduce volumetric leakages into the pump and are modelled by assuming laminar flow conditions. In the model, the drain is represented as part of the suction volume, making this an additional connection between the chambers and the suction port.
- **Suction – Delivery (SD):** in the model, the suction and delivery volumes are connected through the clearance between the gear side faces and the floating bearing blocks in the meshing zone. This connection introduces volumetric leakages into the pump and is modelled by assuming laminar flow conditions.
- **Driving Gear Chambers – Driven Gear Chambers (CC):** the chambers of the driving gear and those of the driven gear are in communication with each other in the meshing zone, through the clearance between the gear flanks.

The **suction and delivery volumes** are connected to the **external of pump** through the suction (**SP**) and delivery ports (**DP**) , respectively.

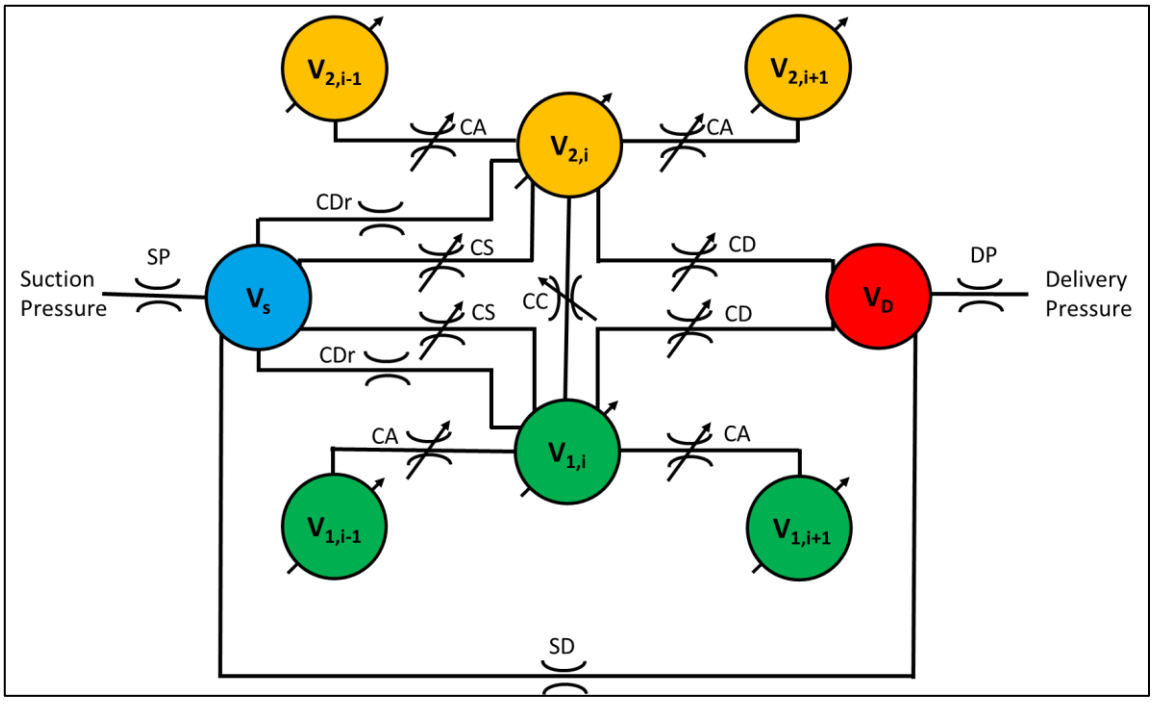

Figure 3 – Lumped-parameter model layout and control volume connections

2.1. Pressure Calculation in the Control Volumes

In the lumped-parameter model, it is assumed that the pressure within each control volume depends only on time, and that the pressure is uniform at every point within the fluid domain bounded by the control volume. The pressure in the i-th control volume is calculated by integrating the following equation [16]:

$$\frac{dp_i}{dt} = \frac{\beta(p_i)}{V_i}\left(Q_{\Sigma\,\mathrm{i}} * \frac{\rho(0)}{\rho(p_i)} - \frac{dV_i}{dt}\right) \qquad \textit{Eq. 1}$$

Where:

- $p_i = p_i(t)$: pressure in the i-th control volume.
- $\beta(p_i)$: isentropic bulk modulus of the oil at pressure p_i
- $V_i = V_i(t)$: volume of the i-th control volume.
- $Q_{\Sigma\,\mathrm{i}}$: total flow rate exchanged between the i-th control volume and the other control volumes. Inflows are considered positive, while outflows are negative.
- $\frac{\rho(0)}{\rho(p_i)}$: ratio between the oil density at 0 bar gauge pressure and the oil density at pressure p_i.This ratio is used as a conversion factor to adjust a flow rate defined at 0 bar gauge pressure (such as $Q_{\Sigma\,i}$) to the corresponding flow rate at pressure p_i.

In the standard hydraulic submodels of Simcenter Amesim [17], volumetric flow rates are computed at a reference pressure of 0 bar gauge. Therefore, the flow rate exchanged at the ports of the hydraulic submodels is defined at 0 bar gauge pressure. For any pressure p_i, the following relation holds:

$$Q_{\Sigma\,\mathrm{i}}(p_i).\rho(p_i) = Q_{\Sigma\,\mathrm{i}}(0).\rho(0) \qquad \textit{Eq. 2}$$

Hence, the relation between a flow rate computed at pressure p_i and the corresponding flow rate at 0 bar gauge pressure is:

$$Q_{\Sigma\,\mathrm{i}}(p_i) = Q_{\Sigma\,\mathrm{i}}(0).\frac{\rho(0)}{\rho(p_i)} \qquad \textit{Eq. 3}$$

For the calculation of pressure, it is necessary to define the control volumes, as well as other geometric quantities such as communication areas and the shape of leakage clearances, which are required to determine the flow rates exchanged between the control volumes.
A dedicated element within the model is responsible for computing the geometric quantities of interest.

2.2. Gear geometry definition

2.2.1. Gear parameters

For the definition of the control volumes, it is necessary to introduce the geometry of the gears that compose the pump.
The pump under study consists of a pair of identical spur gears with an involute profile.
The definition of the gear parameters is based on the gear cutting process, which can be traced back to the meshing between the gear and a rack. Therefore, the gear geometry is defined with reference to the parameters of the gear generating tool and the cutting conditions [18] [19].

The parameters used to define the cutting tool are (Figure 4):

- $\boldsymbol{m}$**: modulus**.
- $\boldsymbol{ad_c}$**: addendum**, the distance from the tip of the cutting tool tooth to the reference line L_0.
- $\boldsymbol{dd_c}$**: dedendum**, the distance from the root of the cutting tool tooth to the reference line L_0.
- $\boldsymbol{\alpha_c}$**: pressure angle,** the inclination of the cutting tool flank
- $\boldsymbol{r_u}$**: tooth tip radius** of the cutting tool.

The following relation exists between the pitch of the cutting tool, p_c, and the modulus:

$$m = \frac{p_c}{\pi} \qquad \textit{Eq. 4}$$

On the reference line L_0, the width of the tooth and the space between adjacent teeth of the cutting tool are both equal to $\frac{p_c}{2}$.

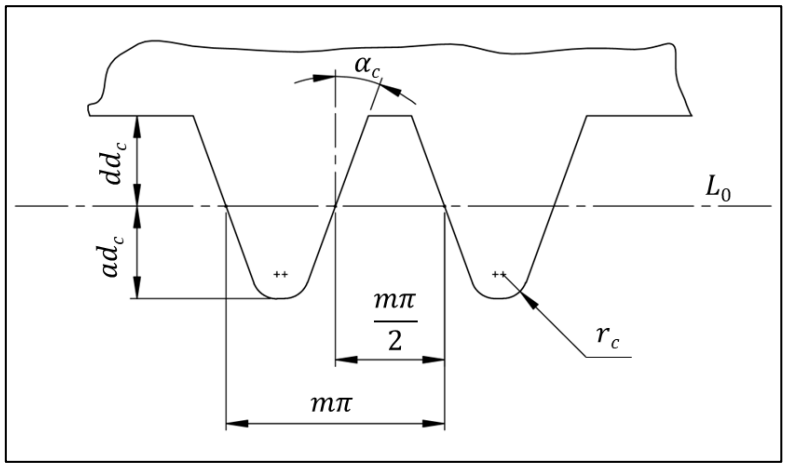

Figure 4 – Cutting tool parameters

During the cutting process, the tool performs a translational movement orthogonal to the plane of the gear, which removes material, and a translational movement within the plane, with a velocity that ensures rolling without slipping between the cutting primitives, represented by the circumference of radius R_{p0} and the line L_0. The involute profile of the gear teeth is obtained as the envelope of the cutting tool flank.

The cutting pitch radius of the gear is defined as :

$$R_{p0} = \frac{m\,z}{2} \qquad \textit{Eq. 5}$$

where z is the number of gear teeth.

The relation between the cutting pitch radius and the base radius is :

$$r_b = R_{p0}\cos(\alpha_c) \qquad \textit{Eq. 6}$$

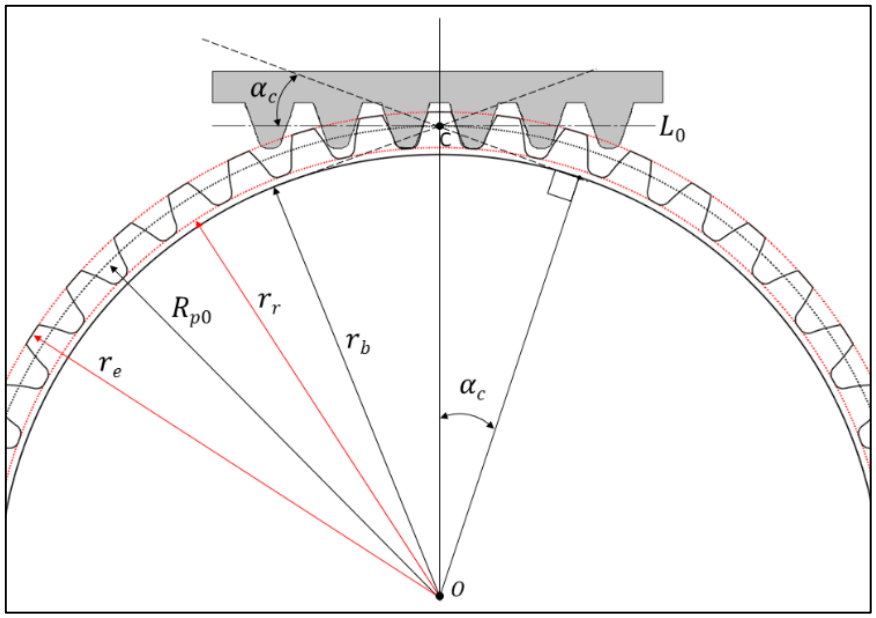

Figure 5 – External spur gear cutting process

A gear generated with a pitch circle of radius R_{p0} , which is tangent to the reference line L_0, has the following geometric properties:

- Tooth width : $s_T = \frac{m\pi}{2}$.
- Tooth space : $v_T = \frac{m\pi}{2}$
- External radius: $r_e = R_{p0} + dd_c$.
- Root radius: $r_r = R_{p0} - ad_c$.
- Tooth height : $h = ad_c + dd_c$.
- Addendum of the gear tooth: $ad_g = dd_c$.
- Dedendum of the gear tooth: $dd_g = ad_c$.

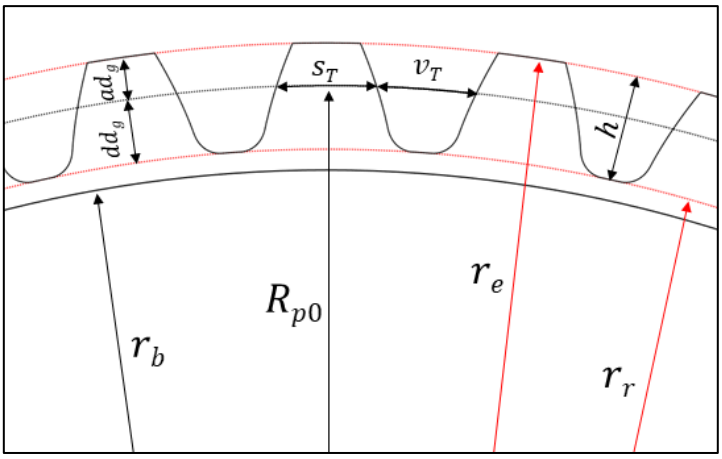

Figure 6 – Dimensional characteristics of spur gear teeth

Considering the cutting primitive of radius $R_{p0} = \frac{m\,Z}{2}$, which remains constant and fixed to the gear, and the same cutting tool as before, with the reference line L_0 fixed to it, moving the cutting tool closer to or farther from the gear alters the geometry of the gear teeth. This technique is known as **profile shift**.

With a profile shift, the cutting primitive becomes tangent to a new reference line L, which is located at a distance c from the original line L_0.

This **correction** c is positive when the cutting tool is moved away from the gear, and negative when it is moved closer.

Profile shifting is used to avoid assembly or manufacturing issues and to improve the mechanical strength of the gear teeth.

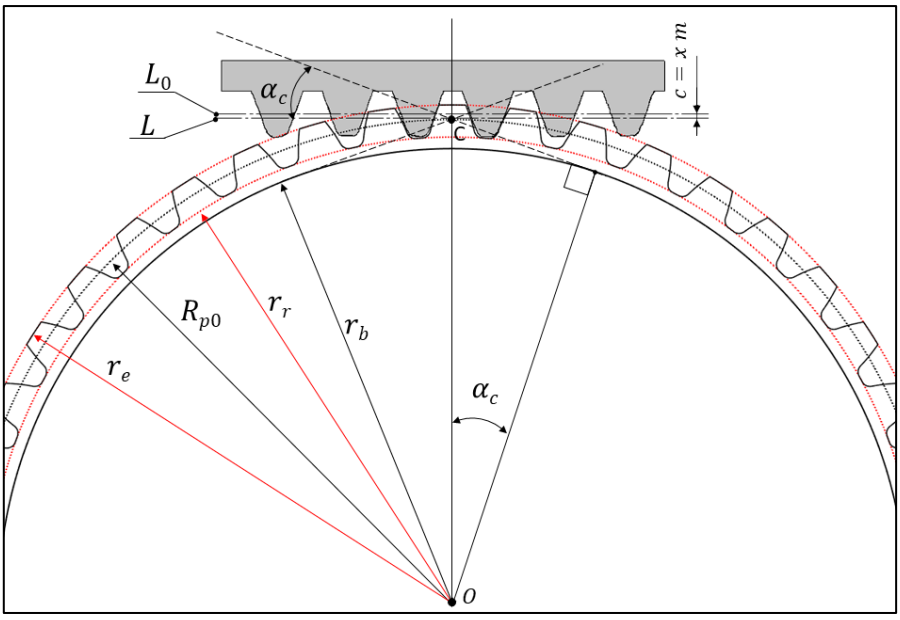

Figure 7 – External spur gear cutting process with profile shift modification

A gear generated with a profile correction c, has the following geometric properties:

- Tooth width : $s_T = \frac{m\pi}{2} + 2\,c\tan(\alpha_c)$.
- Tooth space : $v_T = \frac{m\pi}{2} - 2\,c\tan(\alpha_c)$.
- External radius: $r_e = R_{p0} + dd_c + c$.
- Root radius: $r_r = R_{p0} - ad_c + c$.
- Tooth height : $h = ad_c + dd_c$.
- Addendum of the gear tooth: $ad_g = dd_c + c$.
- Dedendum of the gear tooth: $dd_g = a_{dc} - c$.

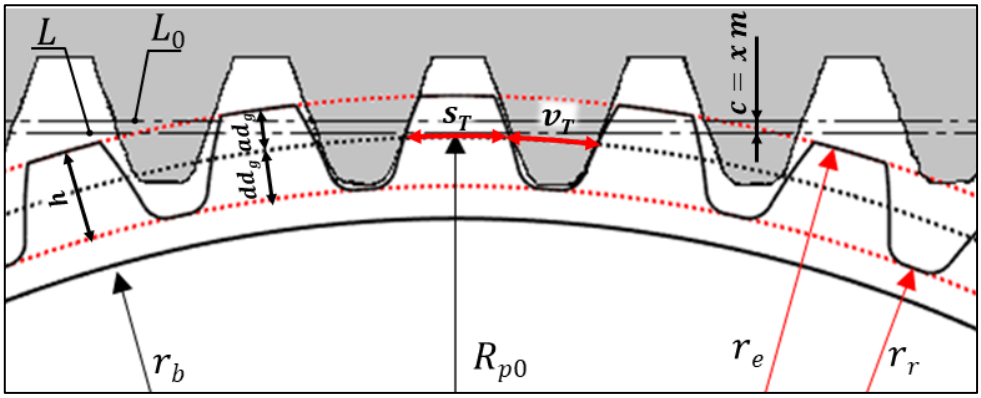

Figure 8 – Dimensional characteristics of spur gear teeth with profile shift modification

The profile shift can also be expressed using the **correction coefficient** $x = \frac{c}{m}$, which is the correction value made dimensionless by normalizing with the modulus of the cutting tool.

2.2.2. Tooth Width, Tooth Space and Gap Calculation

To ensure proper gear meshing at a fixed centre distance, it is necessary to verify whether the circumferential gap is positive, null or negative.

The tooth width of a gear, s_r, at a generic radius r, is given by:

$$s_r = r\left(\frac{s_T}{R_{p0}} + 2\,inv(\alpha_c) - 2\,inv(\alpha_r)\right) \qquad \textit{Eq. 7}$$

Where:

- s_T:tooth width at the cutting pitch radius $R_{p0} = \frac{mz}{2}$.
- α_c= pressure angle of the cutting tool.
- $inv\,(\alpha) = \tan(\alpha) - \alpha$: involute function.
- α_r: pressure angle at radius r.

The pressure angle at radius r, α_r, can be calculated from the following relation:

$$\cos(\alpha_r) = \frac{r_b}{r} \quad \textit{Eq. 8}$$

The tooth space, v_r, is calculated as:

$$v_r = p_r - s_r = \frac{2\pi r}{z} - s_r \quad \textit{Eq. 9}$$

where p_r is the circular pitch at radius r.

When two gears mesh with a fixed centre distance, denoted as the working centre distance I_w, the following relation holds:

$$I_w = R_{w1} + R_{w2} = \frac{r_{b1} + r_{b2}}{\cos(\alpha_w)} \quad \textit{Eq. 10}$$

Where:

- R_{w1} and R_{w2} are the working pitch radii of gear 1 and gear 2, which depend on the centre distance.
- r_{b1} and r_{b2} are the base radii of gear 1 and gear 2, which are independent of the centre distance.
- α_w is the working pressure angle, which depends on the centre distance.

In the case where the two gears mesh using the cutting primitive, the centre distance is referred to as the cutting centre distance I_c:

$$I_c = R_{p0,1} + R_{p0,2} = \frac{r_{b1} + r_{b2}}{\cos(\alpha_c)} \quad \textit{Eq. 11}$$

From Eq. 10 and Eq. 11, it is possible to derive the following relation, which is useful for determining the working pressure angle α_w:

$$\cos(\alpha_w) = \frac{I_c}{I_w}\cos(\alpha_c) \quad \textit{Eq. 12}$$

The circumferential gap on the working pitch circle, g_w, is given by:

$$g_w = v_{w2} - s_{w1} \quad \textit{Eq. 13}$$

Where :

- v_{w2} : tooth space on the working pitch radius of the gear 2.
- s_{w1} : tooth witch on the working pitch radius of the gear 1.

The normal gap on the line of action, $g_{n,w}$, can be defined as:

$$g_{n,w} = g_w \cos(\alpha_w) \qquad \textit{Eq. 14}$$

The line of action is the straight line along which the force is transmitted between meshing gear teeth. It is tangent to both base circles and inclined at the pressure angle. In involute gears, the contact between teeth always occurs along this line, ensuring a constant velocity ratio during engagement.

To ensure proper gear meshing, it is required that $\boldsymbol{g_w \geq 0}$.

If the cutting tool parameters, the number of gear teeth, and the correction coefficients are fixed, Eq. 14 can be used to define the working centre distance required to obtain the desired gap. Conversely, if the cutting tool parameters, the number of gear teeth, and the centre distance are fixed, Eq. 14 can be used to define the correction coefficients needed to achieve the desired gap.

In the case of zero gap, $g_w = 0$, the Eq. 13 becomes:

$$s_{w1} = v_{w2} \qquad \textit{Eq. 15}$$

By substituting into Eq. 15 the expressions for tooth width and tooth space at the working pitch radius of gear 1 and gear 2 (from Eq. 7 and Eq. 9), the following relation is obtained :

$$inv(\alpha_w) - inv(\alpha_c) = 2\ \tan(\alpha_c)\frac{x_1 + x_2}{z_1 + z_2} \qquad \textit{Eq. 16}$$

Using the Eq. 16, if the cutting tool parameters, the number of gear teeth, and the centre distance are fixed, it is possible to define the sum of the correction coefficients in order to achieve zero-gap meshing.
In general, the values of x_1 and x_2 are chosen to be equal or similar in magnitude.

In the case of the external spur gear pump analysed, the pair of gears is identical, and Eq. 16 can be rewritten as:

$$inv(\alpha_w) - inv(\alpha_c) = 2\ \tan(\alpha_c)\frac{x}{z} \qquad \textit{Eq. 17}$$

2.2.3. Tooth profile equations

The profile of a gear tooth, generated by the cutting tool, is composed of four curves[16]:

1. **Tooth tip curve**: this is also an arc of a circle.
2. **Involute profile**: this curve represents the tooth flank, along which contact between mating gears occurs.

3. **Root fillet**: he transition curve between the root and the flank. The root fillet of a gear tooth is an **trochoid**, resulting from the envelope of the tool tip's fillet radius path during the gear cutting process.
4. **Tooth root curve**: an arc of a circle.

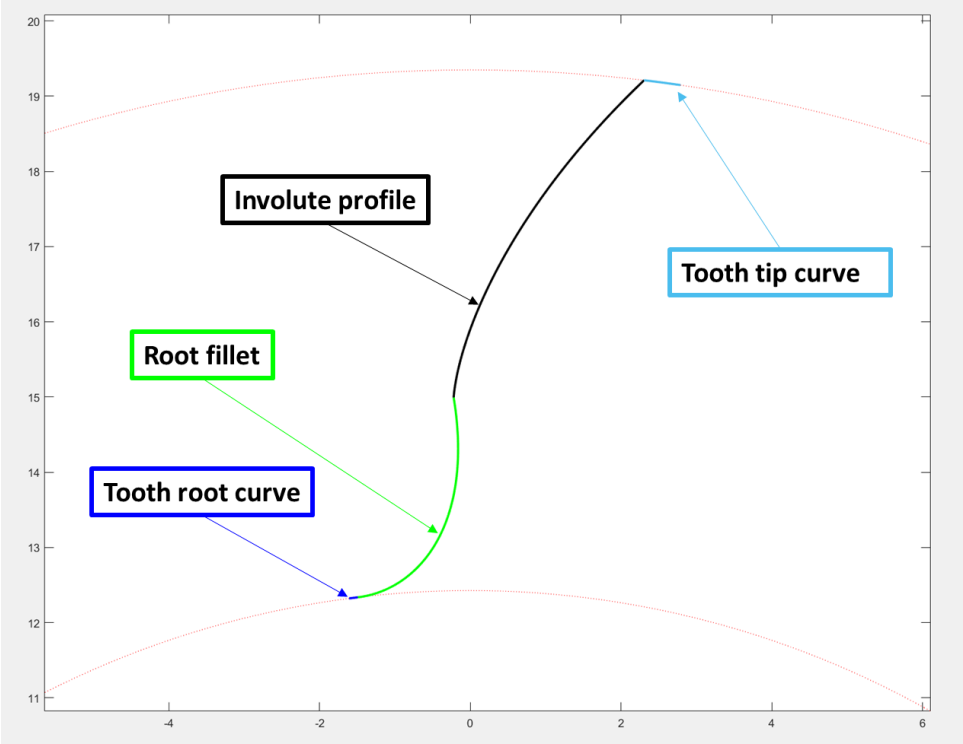

Figure 9 – Curves that define the flank of a gear tooth

To define the equations of the tooth profile, some preliminary definitions are introduced.
In the Figure 10, the following reference systems are shown:

- A fixed reference system, with origin at the gear centre, denoted by the subscript **f**.
- A reference system attached to the gear, also with origin at the gear centre, denoted by the subscript **g**.
- A reference system attached to the cutting tool, with origin on the reference line L, denoted by the subscript **c**.

When the gear rotates by an angle φ, the gear reference system rotates by φ relative to the fixed reference system, while the cutting tool reference system translates by a distance $R_{p0} \cdot \varphi$.

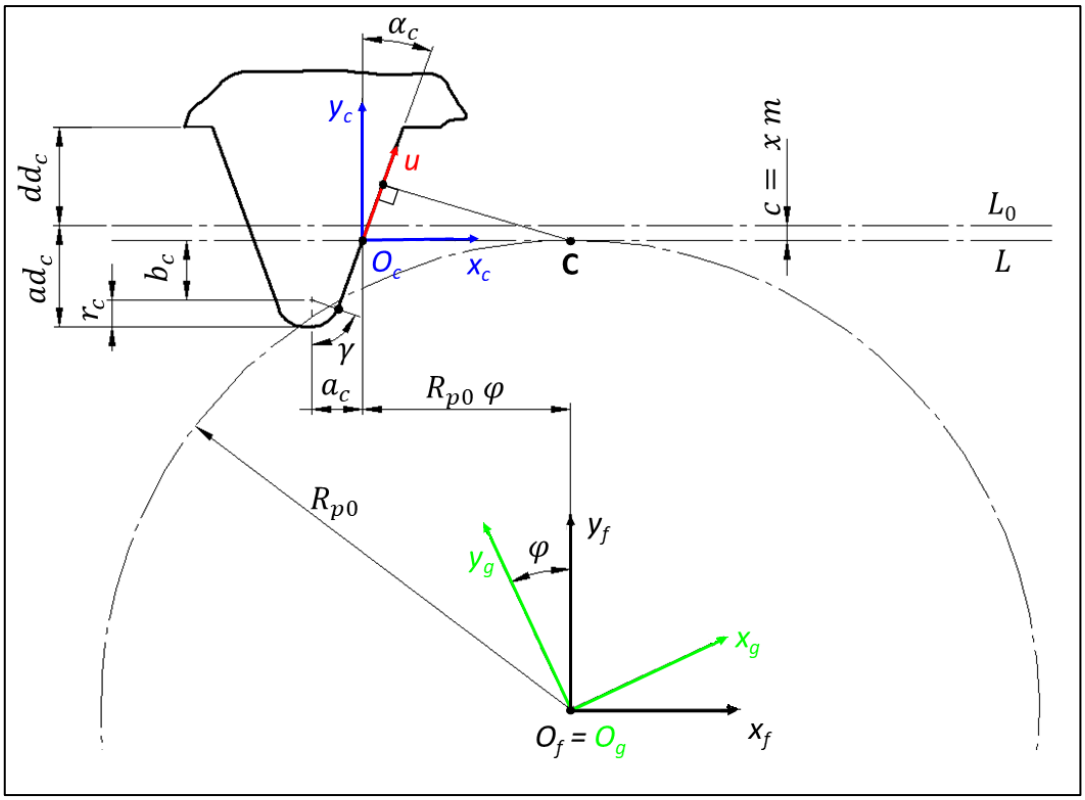

Figure 10 – Reference systems used in the definition of the gear tooth profile

2.2.3.1. Involute profile curve

The involute profile curve of the gear tooth is obtained as the envelope of the cutting tool flank. During meshing, the cutting tool flank and the gear's involute profile are tangent, and their normal vectors intersect at the centre of instantaneous rotation, the pitch point $\boldsymbol{C}$.

The meshing condition can be written as:

$$\frac{X_C - x_c}{N_x} = \frac{Y_C - y_c}{N_y} \qquad \textit{Eq. 18}$$

Where:

- $[X_C, Y_C]$ are the coordinates of pitch point in the reference system of cutting tool:

$$\begin{cases} X_C = R_{p0}\,\varphi \\ Y_C = 0 \end{cases} \qquad \textit{Eq. 19}$$

- $[N_x, N_y]$ are the components of the unit normal vector to the cutting tool flank, expressed in the cutting tool reference system:

$$\begin{cases} N_x = \cos(\alpha_c) \\ N_y = -\sin(\alpha_c) \end{cases} \qquad \textit{Eq. 20}$$

- $[x_c, y_c]$ are the coordinates of the contact point in the cutting tool reference system. During meshing, the contact point moves along the flank of the cutting tool.
  Introducing an auxiliary parameter u, the contact point can be expressed as:

$$\begin{cases} x_c = u \sin(\alpha_c) \\ y_c = u \cos(\alpha_c) \end{cases} \quad \textit{Eq. 21}$$

By substituting the expressions from Eq. 19, Eq. 20, Eq. 21, into Eq. 18, the meshing equation becomes :

$$f(u, \varphi) = u - R_{p0}\, \varphi \sin(\alpha_c) = 0 \quad \textit{Eq. 22}$$

Using Eq. 21 and Eq. 22, the coordinates of the contact point in the cutting tool reference system, as a function of the rotation angle φ, can be written as :

$$\begin{cases} x_c = R_{p0}\, \varphi \sin(\alpha_c) \sin(\alpha_c) \\ y_c = R_{p0}\, \varphi \sin(\alpha_c) \cos(\alpha_c) \end{cases} \quad \textit{Eq. 23}$$

To define the equation of the involute profile, it is necessary to express the position of the contact point, currently given in the cutting tool reference system (Eq. 23), in the gear reference system.
This transformation is performed using the roto-translation matrix $\boldsymbol{M_{cg}}$, which allows a vector defined in the gear reference system to be expressed in the cutting tool reference system:

$$\boldsymbol{M_{cg}} = \begin{bmatrix} \cos(\varphi) & -\sin(\varphi) & R_{p0} \cdot \varphi \\ \sin(\varphi) & \cos(\varphi) & -R_{p0} \cdot \varphi \\ 0 & 0 & 1 \end{bmatrix} \quad \textit{Eq. 24}$$

The roto-translation matrix $\boldsymbol{M_{cg}} = \boldsymbol{M_{gc}^{-1}}$, which allows a vector defined in the cutting tool reference system to be expressed in the gear reference system:

$$\boldsymbol{M_{gc}} = \begin{bmatrix} \cos(\varphi) & \sin(\varphi) & R_{p0}\,(\sin(\varphi) - \varphi\cos(\varphi)) \\ -\sin(\varphi) & \cos(\varphi) & R_{p0}\,(\cos(\varphi) + \varphi\sin(\varphi)) \\ 0 & 0 & 1 \end{bmatrix} \quad \textit{Eq. 25}$$

Using the roto-translation matrix $\boldsymbol{M_{gc}}$, the vector $\boldsymbol{r_g} = [x_g, y_c, 1]^T$, which represents the contact point in the gear reference system, can be obtained as::

$$\boldsymbol{r_g} = \boldsymbol{M_{gc}}\, \boldsymbol{r_c} \quad \textit{Eq. 26}$$

Where $\boldsymbol{r_c} = [x_c\,, y_c\,, 1]^{\boldsymbol{T}}$.

Substituting Eq. 23, Eq. 25 in Eq. 26, the equation of the involute profile in the gear reference system is obtained as:

$$\begin{cases} x_g = R_{p0}\sin(\varphi) - R_{p0}\,\varphi\cos(\alpha_c)\cos(\varphi+\alpha_c) \\ y_g = R_{p0}\cos(\varphi) + R_{p0}\,\varphi\cos(\alpha_c)\sin(\varphi+\alpha_c) \end{cases} \quad \textit{Eq. 27}$$

2.2.3.2.Root fillet – Trochoid profile curve

The root fillet of the gear tooth is generated by the fillet radius at the tip of the cutting tool. The definition of the trochoid profile curve follows the same logic as that of the involute profile.
However, in this case, the contact point moves along the circular arc defined by the tool tip's fillet radius, rather than along the linear flank of the cutting tool.
The auxiliary parameter u is now replaced by a new parameter γ, which traces the position along the arc.
The coordinates of the contact point in the cutting tool reference system are now expressed as:

$$\begin{cases} x_c = a_c + r_c\sin(\gamma) \\ y_c = -b_c - r_c\cos(\gamma) \end{cases} \quad \textit{Eq. 28}$$

Where a_c and b_c are geometric constants related to the cutting tool:

$$b_c = ad_c - r_c - xm \quad \textit{Eq. 29}$$

$$a_c = -\frac{r_u}{\cos(\alpha_c)} - b_c\tan(\alpha_c) \quad \textit{Eq. 30}$$

Using the meshing condition Eq. 18, with the same coordinates of the pitch point $\boldsymbol{C}$ (Eq. 19), but with the components of the unit normal vector to the tool tip's fillet radius expressed in the cutting tool reference system,

$$\begin{cases} N_x = \mathrm{r_u}\sin(\gamma) \\ N_y = -\mathrm{r_u}\ cos(\gamma) \end{cases} \quad \textit{Eq. 31}$$

the meshing condition can be rewritten as :

$$R_{p0}\varphi - a_c + b_u\tan(\gamma) = 0 \quad \textit{Eq. 32}$$

By applying the same reference system transformation used for the involute profile (through Eq. 25, Eq. 26, Eq. 28 and Eq. 32), the coordinates of the trochoid curve in the gear reference system are obtained as:

$$\begin{cases} x_g = r_u\sin(\gamma-\varphi) + a_c\cos(\varphi) - b_c\sin(\varphi) + R_{p0}\,(\sin(\varphi) - \varphi\cos(\varphi)) \\ y_g = -r_c\cos(\gamma-\varphi) - a_c\ \sin(\varphi) - b_c\cos(\varphi) + R_{p0}(\cos(\varphi) + \varphi\sin(\varphi)) \end{cases} \quad \textit{Eq. 33}$$

Where:

$$\gamma = \arctan\left(\frac{a_c - R_{p0}\varphi}{b_c}\right) \qquad \textit{Eq. 34}$$

The case of a cutting tool with a sharp edge at the tip, rather than a fillet radius, can be modelled by setting $r_u = 0$.

2.2.4. Definition of tooth profile in the model

The gear profile in the model is treated as a discrete curve, i.e., as an array of *x* and y coordinates.
Each curve segment that composes the tooth profile is defined by a specific number of points.
As shown in the Figure 11, the profile of a gear tooth, moving in the clockwise direction, is composed of:

- An arc of a circle with $\boldsymbol{n_r}$ points, corresponding to the tooth root radius.
- A trochoid arc with $\boldsymbol{n_{tr}}$ points.
- An involute profile with $\boldsymbol{n_{inv}}$ points.
- An arc of a circle with $\boldsymbol{n_h}$ points, corresponding to the tooth head radius.
- Another involute profile with $\boldsymbol{n_{inv}}$ points.
- Another trochoid arc with $\boldsymbol{n_{tr}}$ points.
- A final arc of a circle with $\boldsymbol{n_r}$ points, again corresponding to the tooth root radius.

In the following treatment, the equations that define the involute profile are given as:

$$\begin{cases} x_{inv}(\varphi_{inv}) = R_{p0}\sin(\varphi_{inv}) - R_{p0}\,\varphi\cos(\alpha_c)\cos(\varphi_{inv} + \alpha_c) \\ y_{inv}(\varphi_{inv}) = R_{p0}\cos(\varphi_{inv}) + R_{p0}\,\varphi\cos(\alpha_c)\sin(\varphi_{inv} + \alpha_c) \end{cases} \qquad \textit{Eq. 35}$$

And the equations that define the trochoid curve are:

$$\begin{cases} x_{tr}(\varphi_{tr}) = r_u\sin(\gamma - \varphi_{tr}) + a_c\cos(\varphi_{tr}) - b_c\sin(\varphi_{tr}) + R_{p0}\,(\sin(\varphi_{tr}) - \varphi_{\mathrm{tr}}\cos(\varphi_{tr})) \\ y_{tr}(\varphi_{tr}) = -r_c\cos(\gamma - \varphi_{tr}) - a_c\ \sin(\varphi_{tr}) - b_c\cos(\varphi_{tr}) + R_{p0}(\cos(\varphi_{tr}) + \varphi\sin(\varphi_{tr})) \end{cases} \qquad \textit{Eq. 36}$$

To define each curve segment of the tooth profile, it is necessary to identify the start and end points of every arc.

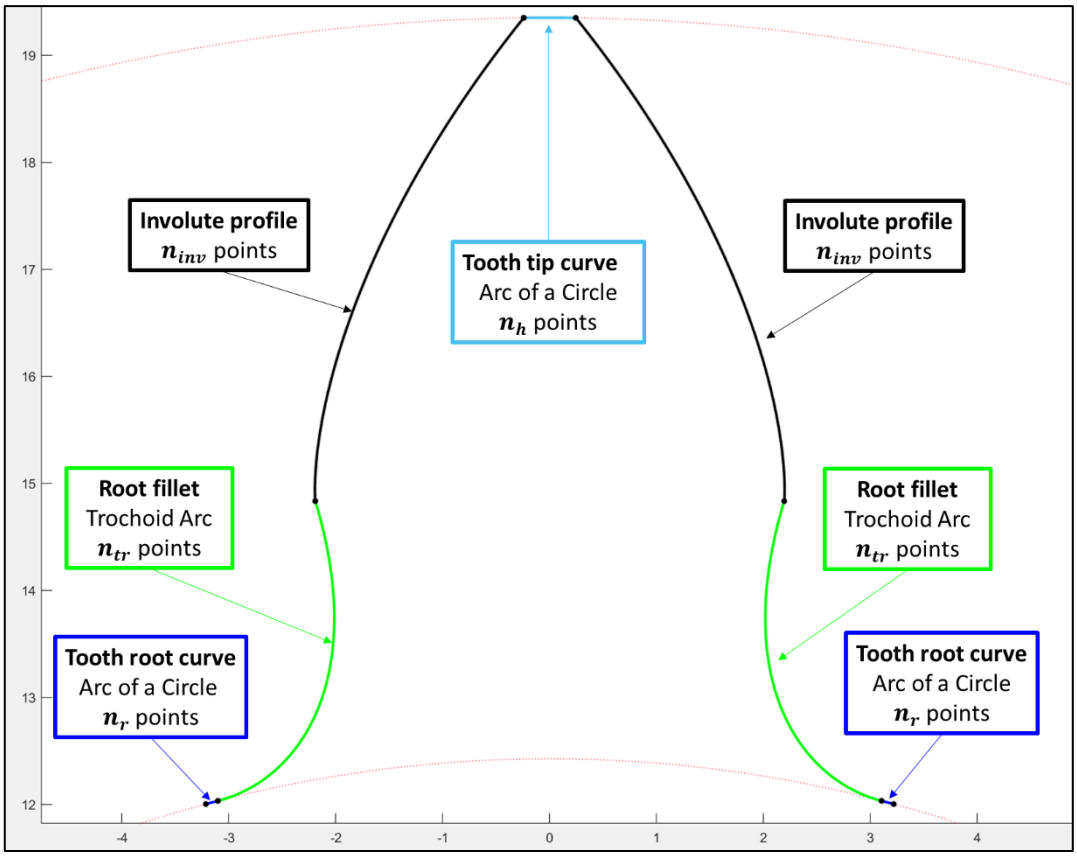

Figure 11 - Curves that define a gear tooth

2.2.4.1. Intersection between the Trochoid and Involute curves

The intersection point between the trochoid and involute curves defines the end of the trochoid segment and the beginning of the involute profile, Figure 12.
This point is found by solving the following nonlinear system of two equations in two unknowns, φ_{inv} and φ_{tr}:

$$\begin{cases} x_{inv}(\varphi_{inv}) = x_{tr}(\varphi_{tr}) \\ y_{inv}(\varphi_{inv}) = y_{tr}(\varphi_{tr}) \end{cases} \qquad \textit{Eq. 37}$$

The solutions of the system are denoted as $\overline{\varphi_{inv,start}}$ and $\overline{\varphi_{tr,end}}$.
The system is solved numerically using the Newton–Raphson method.

2.2.4.2. Intersection between the Involute Curve and Tooth Head Circle

The intersection point between the involute curve and the circle arc of tooth head defines the end of the involute profile and the beginning of circle arc , Figure 12.

This point is found by solving the following nonlinear equation in one unknowns, φ_{inv}:

$$x_{inv}(\varphi_{inv})^2 + y_{inv}(\varphi_{inv})^2 = r_e^2 \qquad \textit{Eq. 38}$$

The solution of the equation is denoted as $\overline{\varphi_{inv,end}}$.
The equation is solved numerically using the Newton–Raphson method.

2.2.4.3. Intersection between the Trochoid Curve and Tooth Root Circle

The intersection point between the trochoid curve and the circle arc of tooth root defines the beginning of the trochoid segment and the beginning of root circle arc, Figure 12.

This point is found by solving the following nonlinear equation in one unknowns, φ_{tr}:

$$x_{tr}(\varphi_{tr})^2 + y_{tr}(\varphi_{tr})^2 = r_r^2 \qquad \textit{Eq. 39}$$

The solution of the equation is denoted as $\overline{\varphi_{tr,start}}$.
The equation is solved numerically using the Newton–Raphson method.

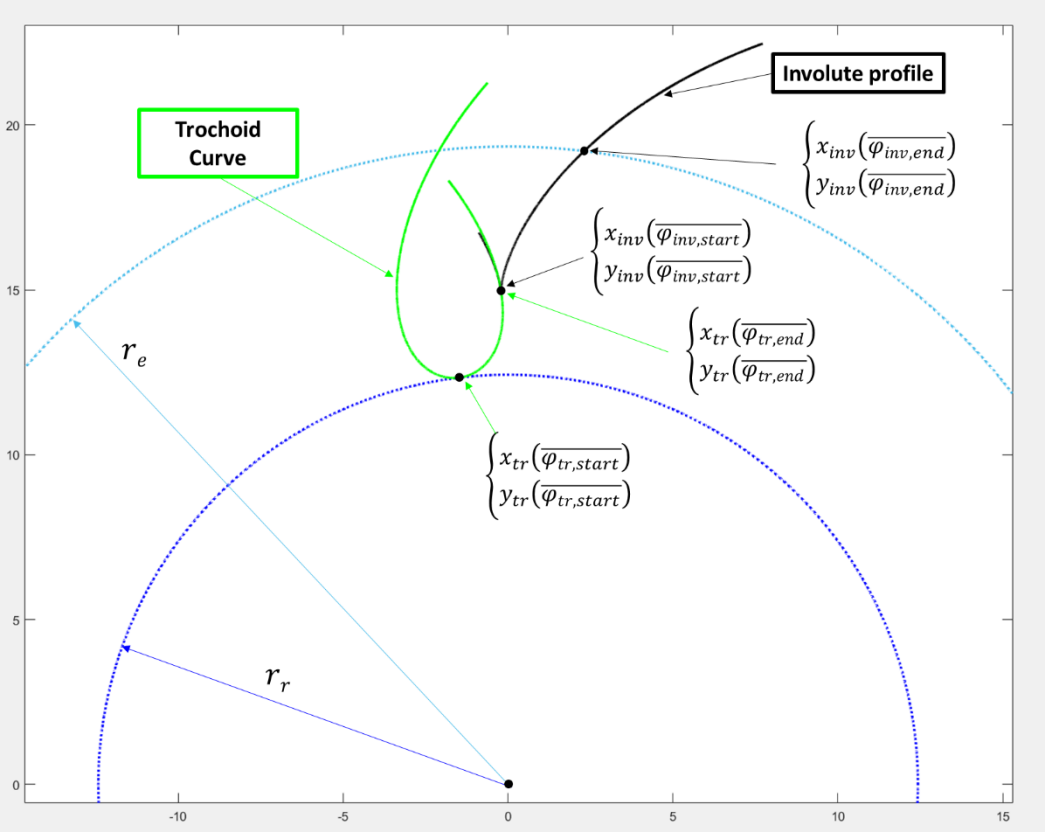

Figure 12 – Intersections between the segments composing the gear tooth profile

2.2.4.4. Beginning Point of Root Circle Arc

The angular extension of a gear tooth, also called the angular pitch, is defined as $\alpha_{pitch} = \frac{2\pi}{z}$.

With a reference system whose origin is at the gear centre, the angular position of the tooth's symmetry axis is obtained by subtracting from the angular position of the involute end point ($\arctan\left(\frac{y_{inv}(\overline{\varphi_{inv,end}})}{x_{inv}(\overline{\varphi_{inv,end}})}\right)$) one-half of the angular extension of the tooth tip ($\frac{s_{tip}}{2\,r_e}$).

By then adding one-half of the angular pitch ($\frac{\alpha_{pitch}}{2}$) to the symmetry-axis position, the angular position of the starting point of the root circle arc ($\overline{\varphi_{root,start}}$) is found, as shown in the following expression:

$$\overline{\varphi_{root,start}} = \arctan\left(\frac{y_{inv}(\overline{\varphi_{inv,end}})}{x_{inv}(\overline{\varphi_{inv,end}})}\right) - \frac{s_{tip}}{2\,r_e} + \frac{\alpha_{pitch}}{2} \qquad \textit{Eq. 40}$$

where the tip width s_{tip} is defined according to Eq. 7 and Eq. 8 .

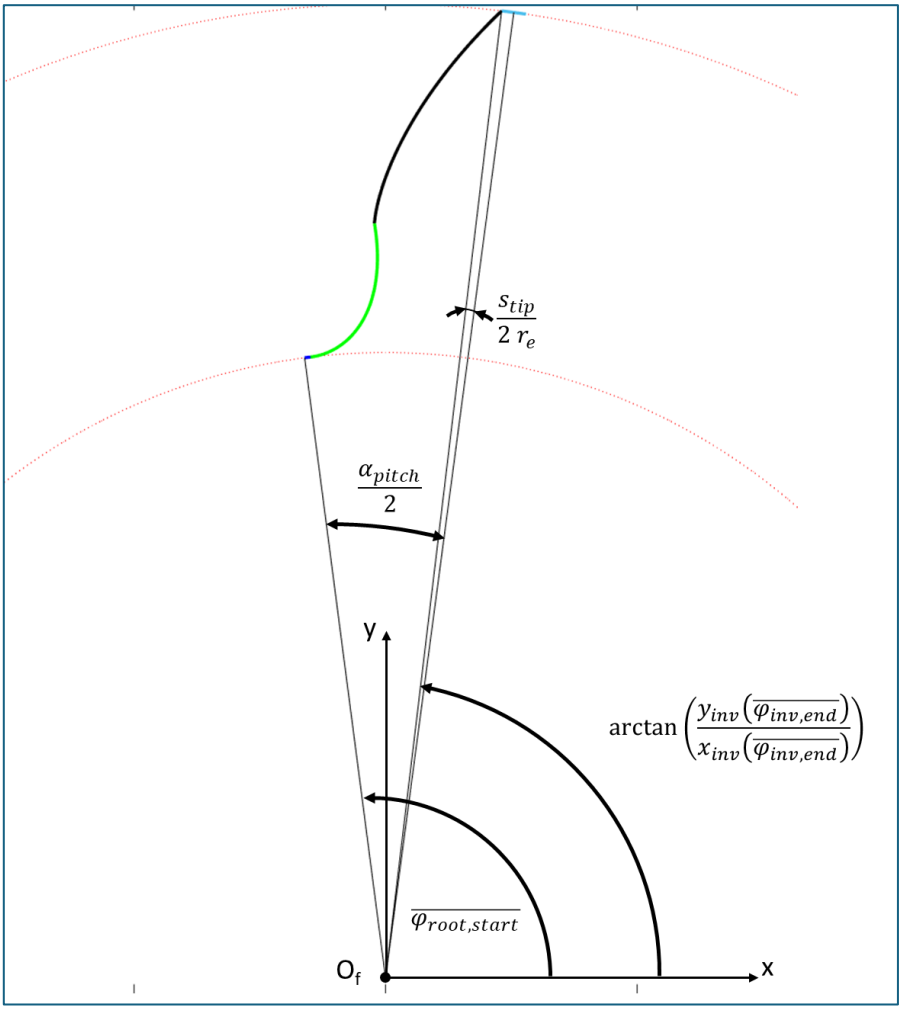

Figure 13 – Beginning Point of Root Circle Arc

2.2.4.5. Vector of Points Defining the Tooth Profile

The first curve of the tooth profile is the **root circle arc**.

In the reference system whose origin is at the gear centre, the angular position of the starting point of the root circle arc is denoted by $\overline{\varphi_{root,start}}$, and the angular position of the end point is defined as:

$$\overline{\varphi_{root,end}} = \arctan\left(\frac{y_{tr}(\overline{\varphi_{tr.start}})}{x_{tr}(\overline{\varphi_{tr,start}})}\right) \qquad \textit{Eq. 41}$$

The angular step between two adjacent points on the arc is given by:

$$\Delta\varphi_{root} = \frac{\overline{\varphi_{root,start}} - \overline{\varphi_{root,end}}}{n_r - 1} \qquad \textit{Eq. 42}$$

The vectors defining the discrete points of the root circle arc are:

$$\boldsymbol{x_r} = \begin{bmatrix} r_r \cos(\overline{\varphi_{root,start}}) \\ r_r \cos(\overline{\varphi_{root,start}} - \Delta\varphi_{root}) \\ \vdots \\ r_r \cos(\overline{\varphi_{root,start}} - i * \Delta\varphi_{root}) \\ \vdots \\ r_r \cos(\overline{\varphi_{root,start}} - (n_r - 2) * \Delta\varphi_{root}) \\ r_r \cos(\overline{\varphi_{root,end}}) \end{bmatrix} \qquad \textit{Eq. 43}$$

$$\boldsymbol{y_r} = \begin{bmatrix} r_r \sin(\overline{\varphi_{root,start}}) \\ r_r \sin(\overline{\varphi_{root,start}} - \Delta\varphi_{root}) \\ \vdots \\ r_r \sin(\overline{\varphi_{root,start}} - i * \Delta\varphi_{root}) \\ \vdots \\ r_r \sin(\overline{\varphi_{root,start}} - (n_r - 2) * \Delta\varphi_{root}) \\ r_r \sin(\overline{\varphi_{root,end}}) \end{bmatrix}$$

The second curve of the tooth profile is the **trochoid segment**.

It is defined as a function of the parameter φ_{tr}, ranging from the start value $\overline{\varphi_{tr,start}}$, o the end value $\overline{\varphi_{tr,end}}$.

The angular step between adjacent points is given by:

$$\Delta\varphi_{tr} = \frac{\overline{\varphi_{tr,start}} - \overline{\varphi_{tr,end}}}{n_{tr} - 1} \qquad \textit{Eq. 44}$$

The vectors defining the trochoid segment are:

$$\boldsymbol{x_{tr}} = \begin{bmatrix} x_{tr}\left(\overline{\varphi_{tr,start}} - \Delta\varphi_{tr}\right) \\ x_{tr}\left(\overline{\varphi_{tr,start}} - 2 * \Delta\varphi_{tr}\right) \\ \vdots \\ x_{tr}\left(\overline{\varphi_{tr,start}} - i * \Delta\varphi_{tr}\right) \\ \vdots \\ x_{tr}\left(\overline{\varphi_{tr,start}} - (n_{tr} - 2) * \Delta\varphi_{tr}\right) \\ x_{tr}\left(\overline{\varphi_{tr,end}}\right) \end{bmatrix} \qquad \textit{Eq. 45}$$

$$\boldsymbol{y_{tr}} = \begin{bmatrix} y_{tr}\left(\overline{\varphi_{tr,start}} - \Delta\varphi_{tr}\right) \\ y_{tr}\left(\overline{\varphi_{tr,start}} - 2 * \Delta\varphi_{tr}\right) \\ \vdots \\ y_{tr}\left(\overline{\varphi_{tr,start}} - i * \Delta\varphi_{tr}\right) \\ \vdots \\ y_{tr}\left(\overline{\varphi_{tr,start}} - (n_{tr} - 2) * \Delta\varphi_{tr}\right) \\ y_{tr}\left(\overline{\varphi_{tr,end}}\right) \end{bmatrix}$$

The first point of the vectors $\boldsymbol{x_{tr}}$ and $\boldsymbol{y_{tr}}$ are defined to avoid overlap between the end point of the root arc and the starting point of the trochoid segment. Therefore, the vectors $\boldsymbol{x_{tr}}$ and $\boldsymbol{y_{tr}}$ contain $n_{tr} - 1$ points.

The third curve of the tooth profile is the **involute profile**.
It is defined as a function of the parameter φ_{inv}, ranging from the start value $\overline{\varphi_{inv,start}}$, o the end value $\overline{\varphi_{inv,end}}$.
The angular step between adjacent points is given by:

$$\Delta\varphi_{inv} = \frac{\overline{\varphi_{inv,start}} - \overline{\varphi_{inv,end}}}{n_{inv} - 1} \qquad \textit{Eq. 46}$$

The vectors defining the involute profile are:

$$\boldsymbol{x_{inv}} = \begin{bmatrix} x_{inv}\left(\overline{\varphi_{inv,start}} - \Delta\varphi_{inv}\right) \\ x_{inv}\left(\overline{\varphi_{inv,start}} - 2 * \Delta\varphi_{inv}\right) \\ \vdots \\ x_{inv}\left(\overline{\varphi_{inv,start}} - i * \Delta\varphi_{inv}\right) \\ \vdots \\ x_{inv}\left(\overline{\varphi_{inv,start}} - (n_{inv} - 2) * \Delta\varphi_{inv}\right) \\ x_{inv}\left(\overline{\varphi_{inv,end}}\right) \end{bmatrix} \qquad \textit{Eq. 47}$$

$$\boldsymbol{y_{inv}} = \begin{bmatrix} y_{inv}\left(\overline{\varphi_{inv,start}} - \Delta\varphi_{inv}\right) \\ y_{inv}\left(\overline{\varphi_{inv,start}} - 2 * \Delta\varphi_{inv}\right) \\ \vdots \\ y_{inv}\left(\overline{\varphi_{inv,start}} - i * \Delta\varphi_{inv}\right) \\ \vdots \\ y_{inv}\left(\overline{\varphi_{inv,start}} - (n_{inv} - 2) * \Delta\varphi_{inv}\right) \\ y_{inv}\left(\overline{\varphi_{inv,end}}\right) \end{bmatrix}$$

The first point of the vectors $\boldsymbol{x_{inv}}$ and $\boldsymbol{y_{inv}}$ are defined to avoid overlap between the end point of the trochoid segment and the starting point of the involute profile. Therefore, the vectors $\boldsymbol{x_{inv}}$ and $\boldsymbol{y_{inv}}$ contain $n_{inv} - 1$ points.

By combining the previously defined vectors, the left profile of the tooth is obtained and denoted by the vectors $\boldsymbol{x'_{tooth,left}}$ and $\boldsymbol{y'_{tooth,left}}$.

$$\boldsymbol{x'_{tooth,left}} = \begin{bmatrix} \boldsymbol{x_r} \\ \boldsymbol{x_{tr}} \\ \boldsymbol{x_{inv}} \end{bmatrix} \qquad \textit{Eq. 48}$$

$$\boldsymbol{y'_{tooth,left}} = \begin{bmatrix} \boldsymbol{y_r} \\ \boldsymbol{y_{tr}} \\ \boldsymbol{y_{inv}} \end{bmatrix}$$

The vectors $\boldsymbol{x'_{tooth,left}}$ and $\boldsymbol{y'_{tooth,left}}$ contain $n_r + n_{tr} + n_{inv} - 2$ points.

Based on the previous equations, the tooth profile has an orientation as shown in Figure 13. In order to align the tooth's axis of symmetry with the **y-axis**, a rotation by an angle $\bar{\theta}$ is applied to the vectors $\boldsymbol{x'_{tooth,left}}$ and $\boldsymbol{y'_{tooth,left}}$.

The rotation angle is defined as :

$$\bar{\theta} = \frac{\pi}{2} - \left(\arctan\left(\frac{y_{inv}\left(\overline{\varphi_{inv,end}}\right)}{x_{inv}\left(\overline{\varphi_{inv,end}}\right)}\right) - \frac{s_{tip}}{2\,r_e}\right) \qquad \textit{Eq. 49}$$

The rotated left tooth profile is denoted by the vectors $\boldsymbol{x_{tooth,left}}$ and $\boldsymbol{y_{tooth,left}}$, whose components are defined as :

$$x^i_{tooth,left} = {x'_{tooth,left}}^{\,i}\, cos(\bar{\theta}) - {y'_{tooth,left}}^{\,i}\, sin(\bar{\theta})$$

$$y^i_{tooth,left} = {x'_{tooth,left}}^{\,i}\, sin(\bar{\theta}) + {y'_{tooth,left}}^{\,i}\, cos(\bar{\theta}) \qquad \textit{Eq. 50}$$

$$\text{for } i = 1, \dots, n_r + n_{tr} + n_{inv} - 2$$

Where ${x'_{tooth,left}}^{\,i}$ and ${y'_{tooth,left}}^{\,i}$ indicate the i-th components of the vectors $\boldsymbol{x'_{tooth,left}}$ and $\boldsymbol{y'_{tooth,left}}$, respectively.

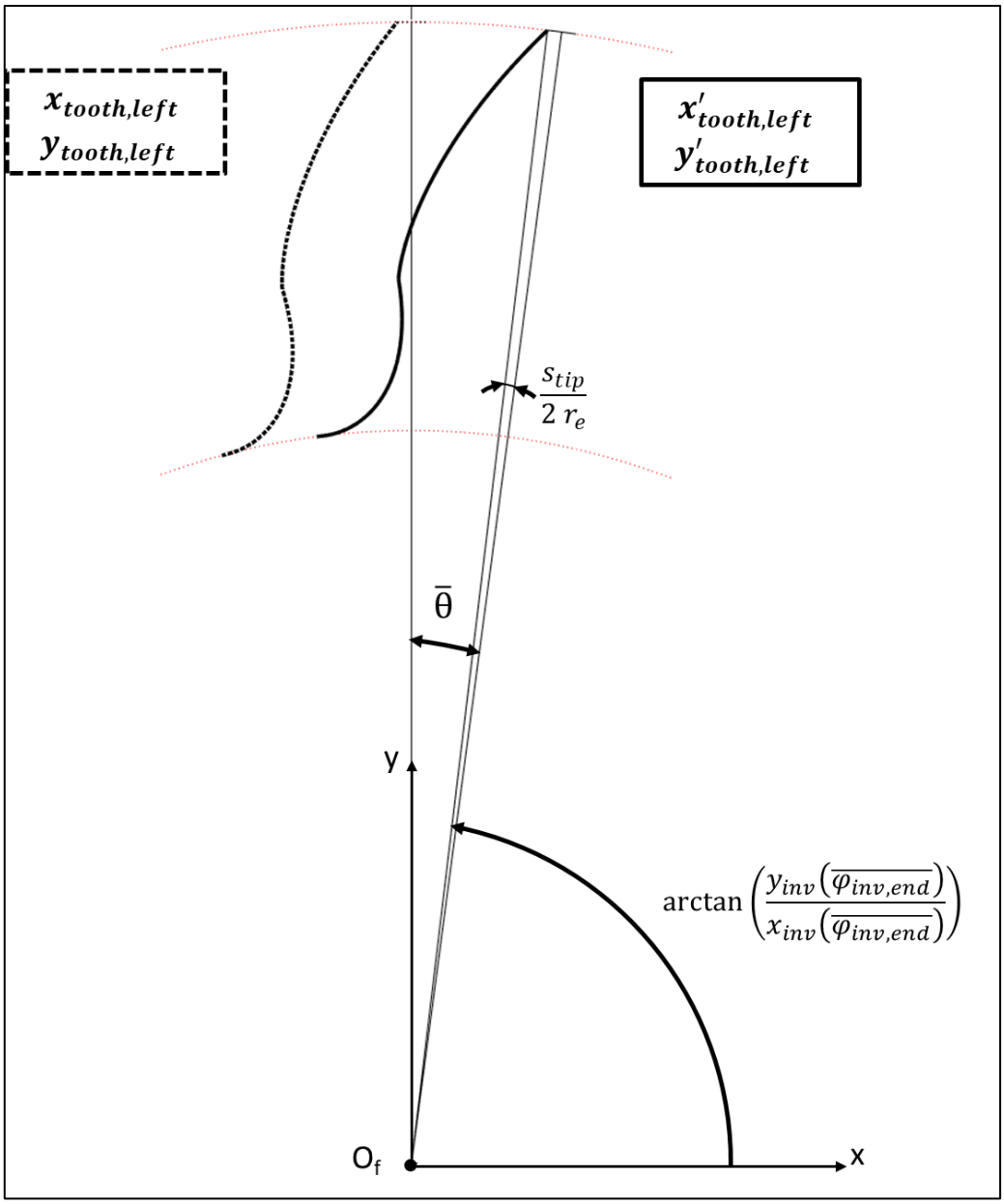

Figure 14 – Left flank of the gear tooth

To complete the definition of the tooth profile, it is necessary to define both the head arc and the right-side profile of the tooth.

The angular position of the starting point of the head arc is computed as:

$$\overline{\varphi_{h,start}} = -\arctan\left(\frac{y_{tooth,left}(n_r + n_{tr} + n_{inv} - 2)}{x_{tooth,left}(n_r + n_{tr} + n_{inv} - 2)}\right) + \frac{\pi}{2} \qquad \textit{Eq. 51}$$

The end angular position of the head arc is obtained by subtracting the angular extension of the tooth's tip from $\overline{\varphi_{h,start}}$.

$$\overline{\varphi_{h,end}} = \overline{\varphi_{h,start}} - \frac{s_{tip}}{r_e} \qquad \textit{Eq. 52}$$

The angular step between two adjacent points on the head arc is given by:

$$\Delta\varphi_h = \frac{\overline{\varphi_{h,start}} - \overline{\varphi_{h,end}}}{n_h - 1} \qquad \textit{Eq. 53}$$

The vectors defining the discrete points of the head circle arc are:

$$\boldsymbol{x_h} = \begin{bmatrix} r_e \cos\left(\overline{\varphi_{h,start}} - \Delta\varphi_h\right) \\ \vdots \\ r_e \cos\left(\overline{\varphi_{root,start}} - i * \Delta\varphi_h\right) \\ \vdots \\ r_e \cos\left(\overline{\varphi_{h,start}} - (n_h - 2) * \Delta\varphi_{root}\right) \\ r_e \cos\left(\overline{\varphi_{h,end}}\right) \end{bmatrix} \qquad \textit{Eq. 54}$$

$$\boldsymbol{y_h} = \begin{bmatrix} r_e \sin\left(\overline{\varphi_{h,start}} - \Delta\varphi_h\right) \\ \vdots \\ r_e \sin\left(\overline{\varphi_{h,start}} - i * \Delta\varphi_h\right) \\ \vdots \\ r_e \sin\left(\overline{\varphi_{h,start}} - (n_r - 2) * \Delta\varphi_h\right) \\ r_e \sin\left(\overline{\varphi_{h,end}}\right) \end{bmatrix}$$

The first point of the vectors $\boldsymbol{x_h}$ and $\boldsymbol{y_h}$ are defined to avoid overlap between the end point of the involute profile and the starting point of the head arc. Therefore, the vectors $\boldsymbol{x_h}$ and $\boldsymbol{y_h}$ contain $n_h - 1$ points.

The right profile of the tooth, $\boldsymbol{x_{tooth,right}}$ and $\boldsymbol{y_{tooth,right}}$, is obtained by mirroring the left profile with respect to the symmetry y-axis.

$$x^{i}_{tooth,right} = -x^{(n_r+n_{tr}+n_{inv}-2-i)}_{tooth,left}$$

$$y^{i}_{tooth,right} = y^{(n_r+n_{tr}+n_{inv}-2-i)}_{tooth,left} \qquad \textit{Eq. 55}$$

$$\text{for } i = 1, \dots, n_r + n_{tr} + n_{inv} - 3$$

The first point of vectors $\boldsymbol{x_{tooth,right}}$ and $\boldsymbol{y_{tooth,right}}$ are defined to avoid overlap between the end point of the head arc and the starting point of the right tooth profile. As a result, both vectors contain $n_r + n_{tr} + n_{inv} - 3$ points.

The complete profile of the gear tooth is defined as :

$$\boldsymbol{x_{tooth}} = \begin{bmatrix} \boldsymbol{x_{tooth,left}} \\ \boldsymbol{x_h} \\ \boldsymbol{x_{tooth,right}} \end{bmatrix}$$

$$\boldsymbol{y_{tooth}} = \begin{bmatrix} \boldsymbol{y_{tooth,left}} \\ \boldsymbol{y_h} \\ \boldsymbol{y_{tooth,right}} \end{bmatrix} \qquad \textit{Eq. 56}$$

The vectors $\boldsymbol{x_{tooth}}$ and $\boldsymbol{y_{tooth}}$ are composed of a total of $2n_r + 2n_{tr} + 2n_{inv} + n_h - 6$ points.

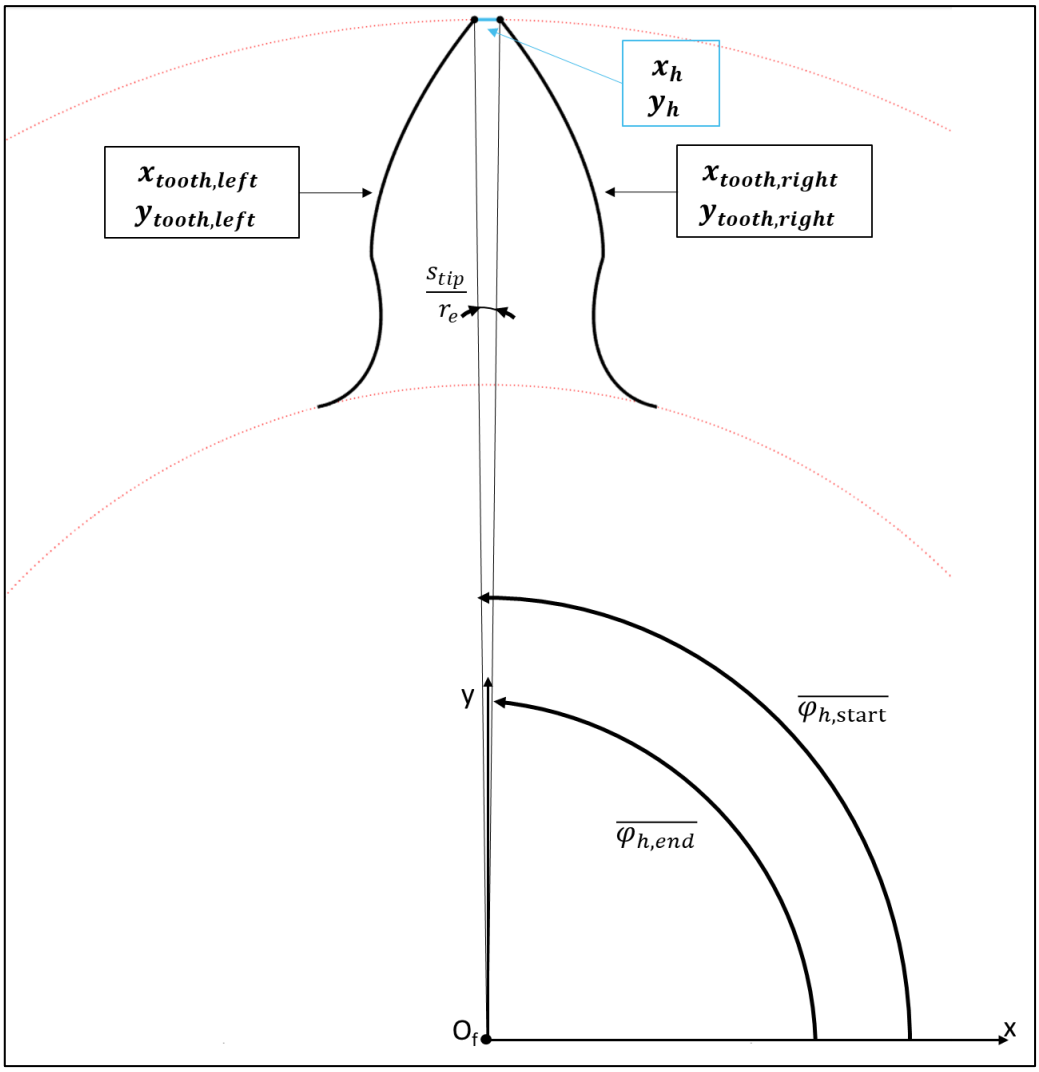

Figure 15 – Complete gear tooth profile

2.2.5. Driving gear and driven gear profile

In the following treatment, the terms gear 1 and gear 2 will be used as synonyms for the driving and driven gear, respectively.
The orientation of the gear pump considered in the model is shown in Figure 2. Gear 1 is located at the bottom of the pump casing, while gear 2 is positioned at the top. The delivery port is on the right side, and the suction port is on the left. The pump shaft enters the plane of the figure. Gear 1 rotates in a counterclockwise direction, and gear 2 rotates in a clockwise direction.

The developed model aims to study the behaviour of the pump under steady-state conditions. In external gear pumps, the geometric quantities of interest for each chamber are identical and shifted by an angular pitch equal to $\alpha_{pitch} = \frac{2\pi}{z}$. Therefore, analysing a single chamber for each gear is sufficient.
In the model, the complete profiles of gear 1 and gear 2 are not included. Instead, only two teeth per gear are modelled, which is sufficient to define one chamber for gear 1 and one chamber for gear 2.

The definition of the profile of the second tooth of gear 1 begins from the previously defined vectors $\boldsymbol{x_{tooth}}$ and $\boldsymbol{y_{tooth}}$. By applying a clockwise rotation of α_{pitch}, it is possible to obtain the profile of the second tooth, indicated as $\boldsymbol{x_{tooth,2nd}}$ and $\boldsymbol{y_{tooth,2nd}}$, with components :

$$x^i_{tooth,2nd} = x^i_{tooth}\, cos(\alpha_{pitch}) + y^i_{tooth} \sin(\alpha_{pitch})$$

$$y^i_{tooth,2nd} = -x^i_{tooth}\, sin(\alpha_{pitch}) + y^i_{tooth}\, cos(\alpha_{pitch}) \qquad \textit{Eq. 57}$$

$$\text{for } i = 2, \dots, 2n_r + 2n_{tr} + 2n_{inv} + n_h - 6$$

The vectors $\boldsymbol{x_{tooth,2nd}}$ and $\boldsymbol{y_{tooth,2nd}}$ are composed of a total of $2n_r + 2n_{tr} + 2n_{inv} + n_h - 7$ points.

The complete profile of gear 1 used in the model is obtained by combining the profiles of the first and second gear tooth.

$$\boldsymbol{x_{gear1}} = \begin{bmatrix} \boldsymbol{x_{tooth}} \\ \boldsymbol{x_{tooth,2nd}} \end{bmatrix}$$

$$\boldsymbol{y_{gear1}} = \begin{bmatrix} \boldsymbol{y_{tooth}} \\ \boldsymbol{y_{tooth,2nd}} \end{bmatrix} \qquad \textit{Eq. 58}$$

The tooth profile of gear 2 is obtained by translating the vectors $\boldsymbol{x_{gear1}}$ and $\boldsymbol{y_{gear1}}$ long the y-axis by I_w, and then applying a clockwise rotation of $\pi - \frac{3}{2}\,\alpha_{pitch}$:

$$x^i_{gear2} = x^i_{gear1}\, cos\left(\pi - \frac{3}{2}\,\alpha_{pitch}\right) + y^i_{gear1} \sin\left(\pi - \frac{3}{2}\,\alpha_{pitch}\right)$$

$$y^i_{gear2} = -x_{gear1}(i)\, sin\left(\pi - \frac{3}{2}\,\alpha_{pitch}\right) + y^i_{gear1}\, cos\left(\pi - \frac{3}{2}\,\alpha_{pitch}\right) + \mathrm{I_w} \qquad \textit{Eq. 59}$$

$$\text{for } i = 1, \dots, 4n_r + 4n_{tr} + 4n_{inv} + 2n_h - 13$$

The vectors $\boldsymbol{x_{gear1}}$,$\boldsymbol{y_{gear1}}$, $\boldsymbol{x_{gear2}}$ and $\boldsymbol{y_{gear2}}$ each contain a total of $4n_r + 4n_{tr} + 4n_{inv} + 2n_h - 13$ points.

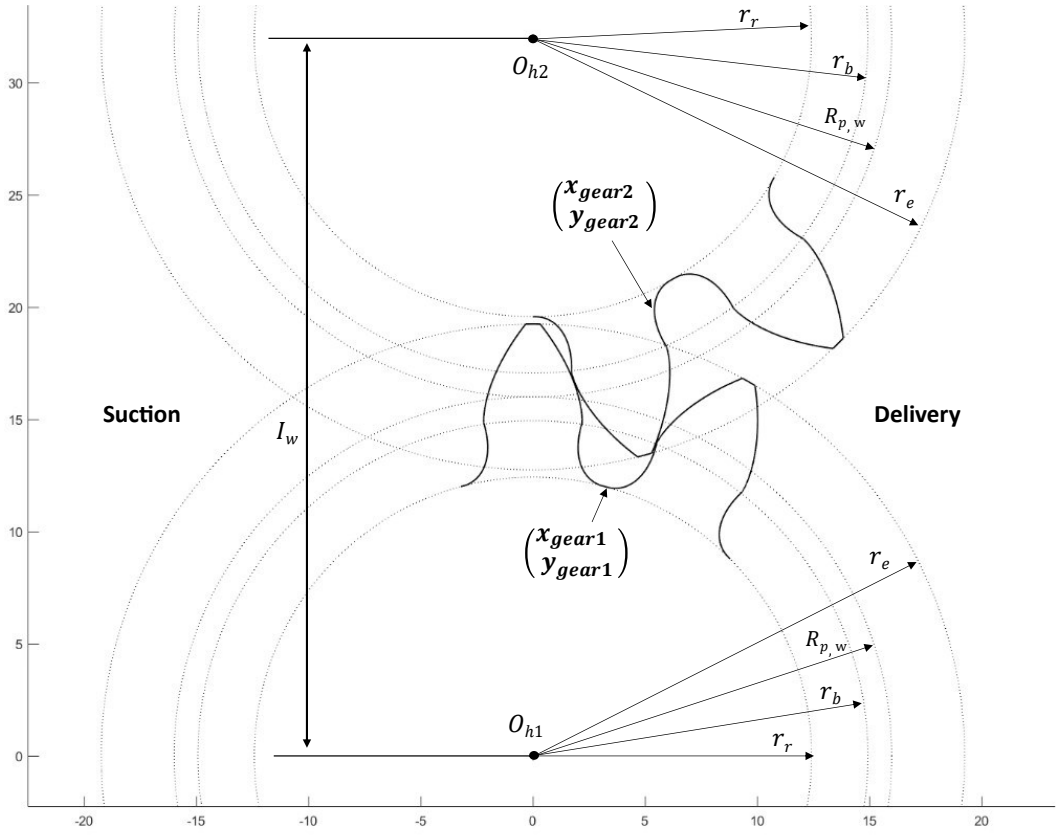

Figure 16 – Gear profiles used in the model

I_w represents the *working centre distance*, corresponding to the mounting distance between gear 1 and gear 2 in the pump. During operation, due to internal clearances between components and the fluid forces, the gears undergo micromotions, which result in slight variations of the actual centre distance. Therefore, I_w is considered **a nominal value**.

These micromotions are primarily induced by fluid pressure forces, which push the gears and floating bearing blocks toward the suction port.

In the model, the following micromotions are considered:

- **Relative micromotion of the gears and floating bearing blocks with respect to the pump housing**: The gears are supported by floating bearing blocks, which are separated from the pump housing by a radial clearance $g_{jb,h}$. It is assumed in the model that fluid pressure causes a horizontal displacement of the gears and bearing blocks relative to the housing, equal to this radial clearance (Figure 17).

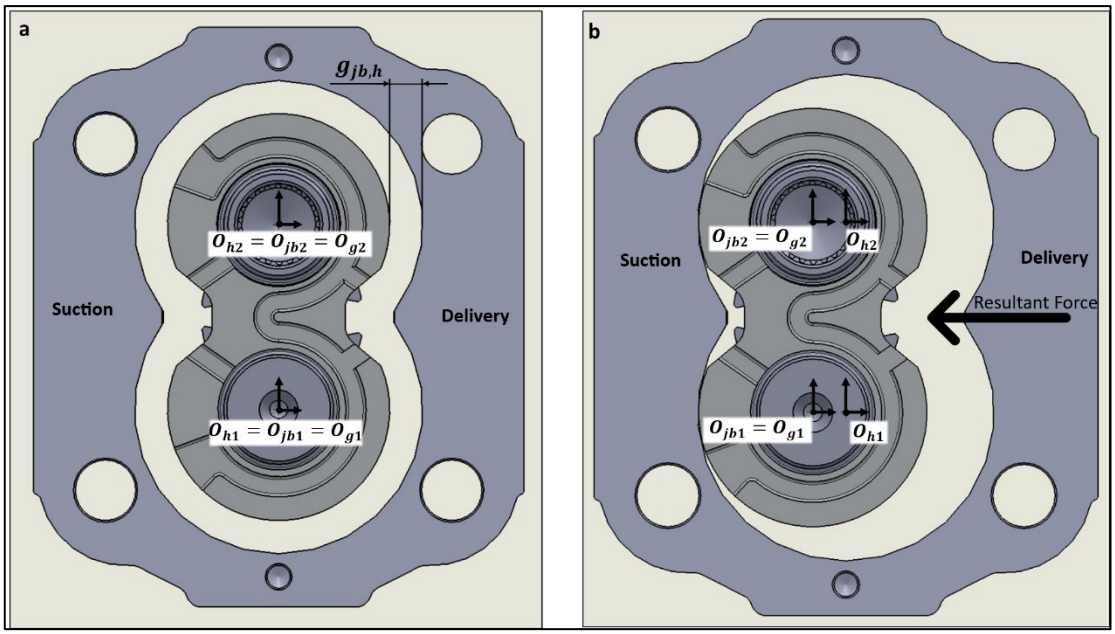

Figure 17 – Relative micromotion of the gears and floating bearing blocks with respect to the pump housing

- **Relative micromotion of the gears with respect to the floating bearing blocks**: The gears exhibit an additional micromotion relative to the bearing blocks, which depends on the operating conditions and the geometry of the bearings. This eccentricity is determined by the balance of pressure and contact forces acting on the gears, and the hydrodynamic lift force generated within the journal bearings (Figure 18).

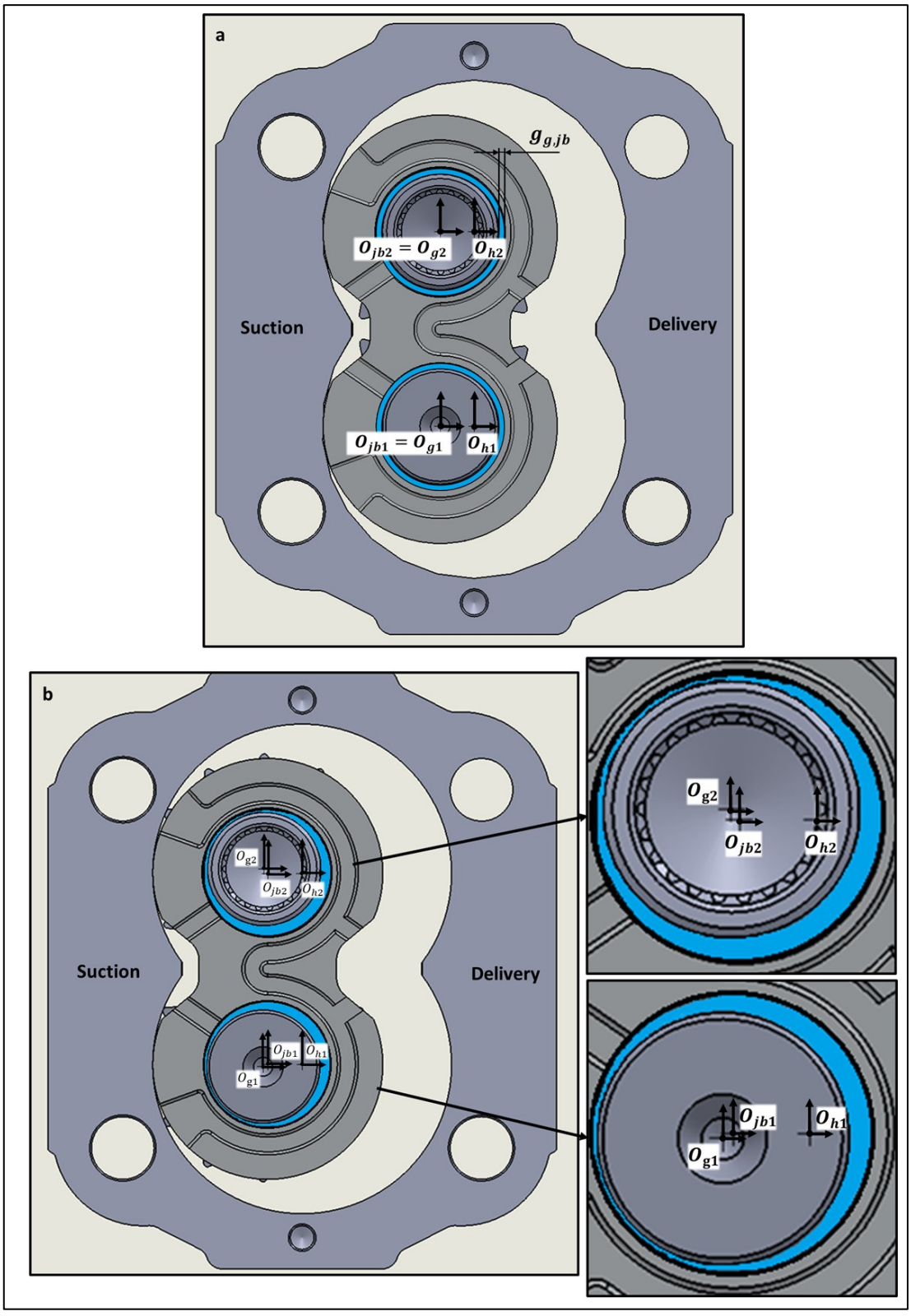

Figure 18 – Relative micromotion of the gears with respect to the floating bearing blocks

In the model, the following reference systems are introduced to account for the effects of micromotion (see Figure 18):

- **Pump Housing Reference Systems** $O_{h1}$and O_{2h}: These coordinate systems are fixed to the pump housing, with their origins located at the centers of the housing bores that accommodate the floating bearing blocks. O_{h1} corresponds to the driving gear side, while O_{h2}corresponds to the driven gear side.
- **Journal Bearing Reference Systems** $O_{jb1}$and O_{jb2}: These systems are fixed to the journal bearings, with their origins at the centers of the bearings. O_{jb1} corresponds to the driving gear side, and O_{jb2} to the driven gear side. Although the origins of these systems move with the bearing blocks during micromotion, the x- and y-axes remain parallel to those of O_{h1} and O_{h2} respectively.
- **Gear Reference Systems** $O_{g1}$and O_{g2}: These systems are fixed to the gears, with origins located at the centers of the gears. O_{g1} refers to the driving gear and $O_{g2}$to the driven gear. As with the bearing blocks, only the origins move with the gears during micromotion; the coordinate axes remain parallel to those of the corresponding housing reference systems ($O_{h1}$and O_{h2}).

The vectors $\boldsymbol{x_{gear1}}$,$\boldsymbol{y_{gear1}}$, $\boldsymbol{x_{gear2}}$ and $\boldsymbol{y_{gear2}}$ define the gear profiles in the pump housing reference system O_{h1}.

To define the geometric entities relevant to the fluid-dynamic model, it is necessary to determine the gear profiles at various angular positions.

Before proceeding, it is important to note that, in this type of pump, the gears are generally installed with a centre distance I_w which ensures **single-flank contact** during operation. This means that meshing occurs exclusively on one side of the tooth flanks, a typical condition in external gear pumps.

In the **reference configuration** shown in Figure 16, the gears are positioned **without considering micromotions**, meaning that the gear centres coincide with those of the pump housing ($O_{g1} = O_{h1}$and $O_{g2} = O_{h2}$) and the centre distance is equal to the nominal working centre distance I_w .
This configuration is the same one used to define the vectors $\boldsymbol{x_{gear1}}$,$\boldsymbol{y_{gear1}}$, $\boldsymbol{x_{gear2}}$ and $\boldsymbol{y_{gear2}}$.
It also represents the **initial angular position** of the gears, denoted by $\boldsymbol{\varphi = 0}$, where $\boldsymbol{\varphi}$ indicates the angular position of the pump shaft.
Under these conditions, no contact occurs between the tooth flanks.

Figure 19 shows the same reference configuration as Figure 16, but with increased gear backlash to facilitate understanding.

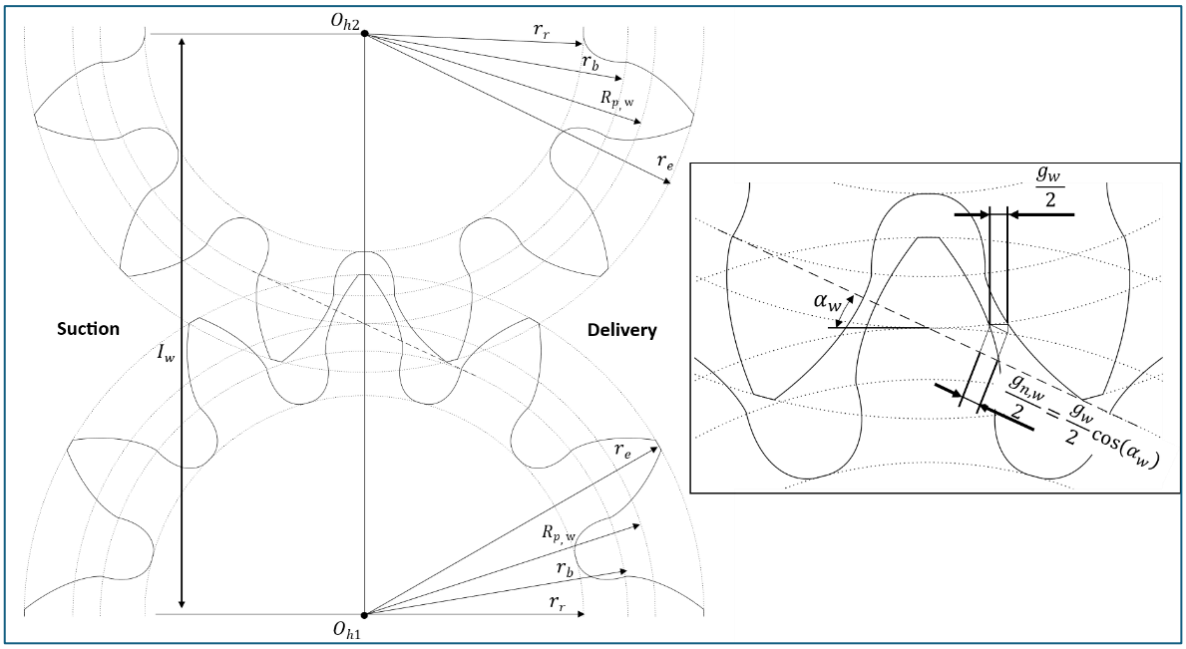

Figure 19 – Gear backlash

To model a realistic gear engagement, a **small angular rotation** is applied to the driving gear to **compensate for the backlash** and establish contact between the flanks (Figure 20).
The required angular displacement $\overline{\varphi_{gap1}}$ is determined based on the **normal gap** along the line of action, $g_{n,w}$ (Eq. 14), evaluated at the **nominal working pitch radius** $R_{p,w} = \frac{I_w}{2}$, and is calculated as:

$$\overline{\varphi_{gap1}} = \frac{g_{n,w}}{2r_b} \qquad \textit{Eq. 60}$$

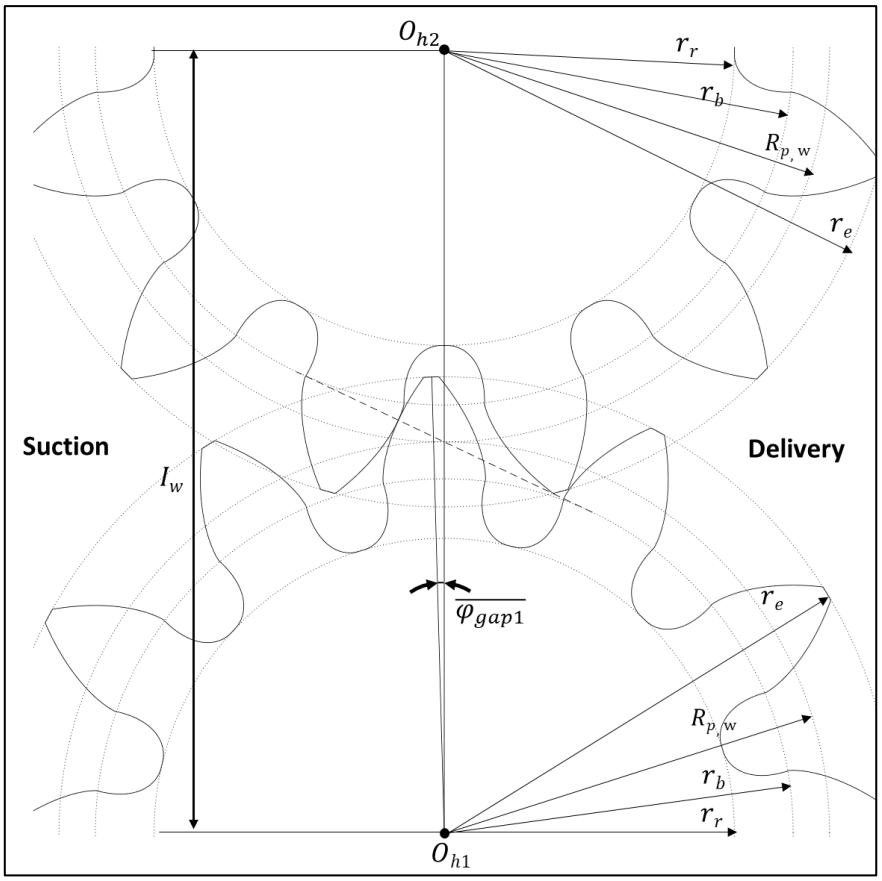

Figure 20 – Gear with rotation to compensate for the backlash

Now consider Figure 21, which shows the gears **with micromotions** and with $\boldsymbol{\varphi = 0}$, but **without** the angular rotation $\overline{\varphi_{gap1}}$ applied to the driving gear.
The positions of the gear centres relative to the pump housing reference system O_{h1} are given by:

$$O_{g1,O_{h1}} = \begin{bmatrix} xO_{g1,O_{h1}} \\ yO_{g1,O_{h1}} \end{bmatrix} = \begin{bmatrix} -g_{jb,h} + ecc_{x1} \\ ecc_{y1} \end{bmatrix}$$

$$O_{g2,O_{h1}} = \begin{bmatrix} xO_{g2,O_{h1}} \\ yO_{g2,O_{h1}} \end{bmatrix} = \begin{bmatrix} -g_{jb,h} + ecc_{x2} \\ I_w + ecc_{y1} \end{bmatrix}$$

Eq. 61

The terms ecc_{x1}, ecc_{y1}, ecc_{x2} and ecc_{y2} denote the coordinates of the centres of gear 1 and gear 2 relative to the centres of their respective journal bearings, defined in the reference frames O_{jb1} and O_{jb2}. The procedures used to determine these values are explained in detail in the following sections.

However, due to micromotions, the actual **working pitch radius** becomes:

$$R_{p,wm} = \frac{I_{wm}}{2}$$

Eq. 62

where I_{wm} is the **effective centre distance** considering micromotions, defined as:

$$I_{wm} = \sqrt{\left(xO_{g1,O_{h1}} - xO_{g2,O_{h1}}\right)^2 + \left(yO_{g1,O_{h1}} - yO_{g2,O_{h1}}\right)^2} \qquad \textit{Eq. 63}$$

If, in this configuration, the driving gear is rotated by $\overline{\varphi_{gap1}}$, contact between the flanks **might still not occur** or may result in **overlap** depending on the relative angular misalignment.

In Figure 19, the **symmetry axis** of the driving gear tooth and that of the driven gear tooth space **coincide** with the line connecting the gear centres, prior to the application of the rotation $\overline{\varphi_{gap1}}$ shown in Figure 20.
To restore this condition while accounting for micromotions, an additional rotation $\overline{\varphi_{gap2}}$ must be applied (Figure 21):

$$\overline{\varphi_{gap2}} = \arctan\left(\frac{xO_{g1,O_{h1}} - xO_{g2,O_{h1}}}{yO_{g2,O_{h1}} - yO_{g1,O_{h1}}}\right) \qquad \textit{Eq. 64}$$

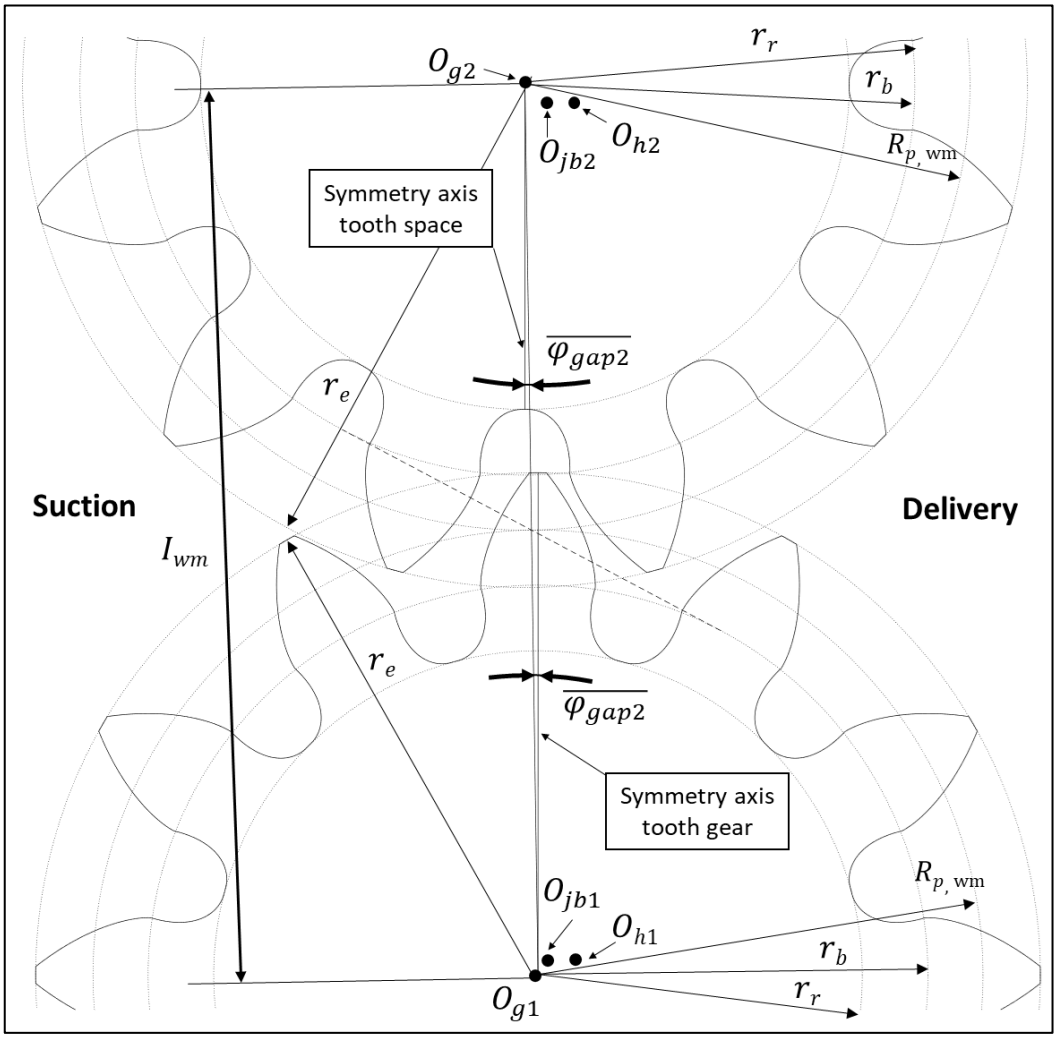

Figure 21 – Gears with micromotions

A rotation of $\overline{\varphi_{gap2}}$ is applied to the driving gear and to the driven gear.
This ensures that the **tooth flank of gear 1** and the **tooth space of gear 2** remain aligned with the connecting axis between their centres (Figure 22).

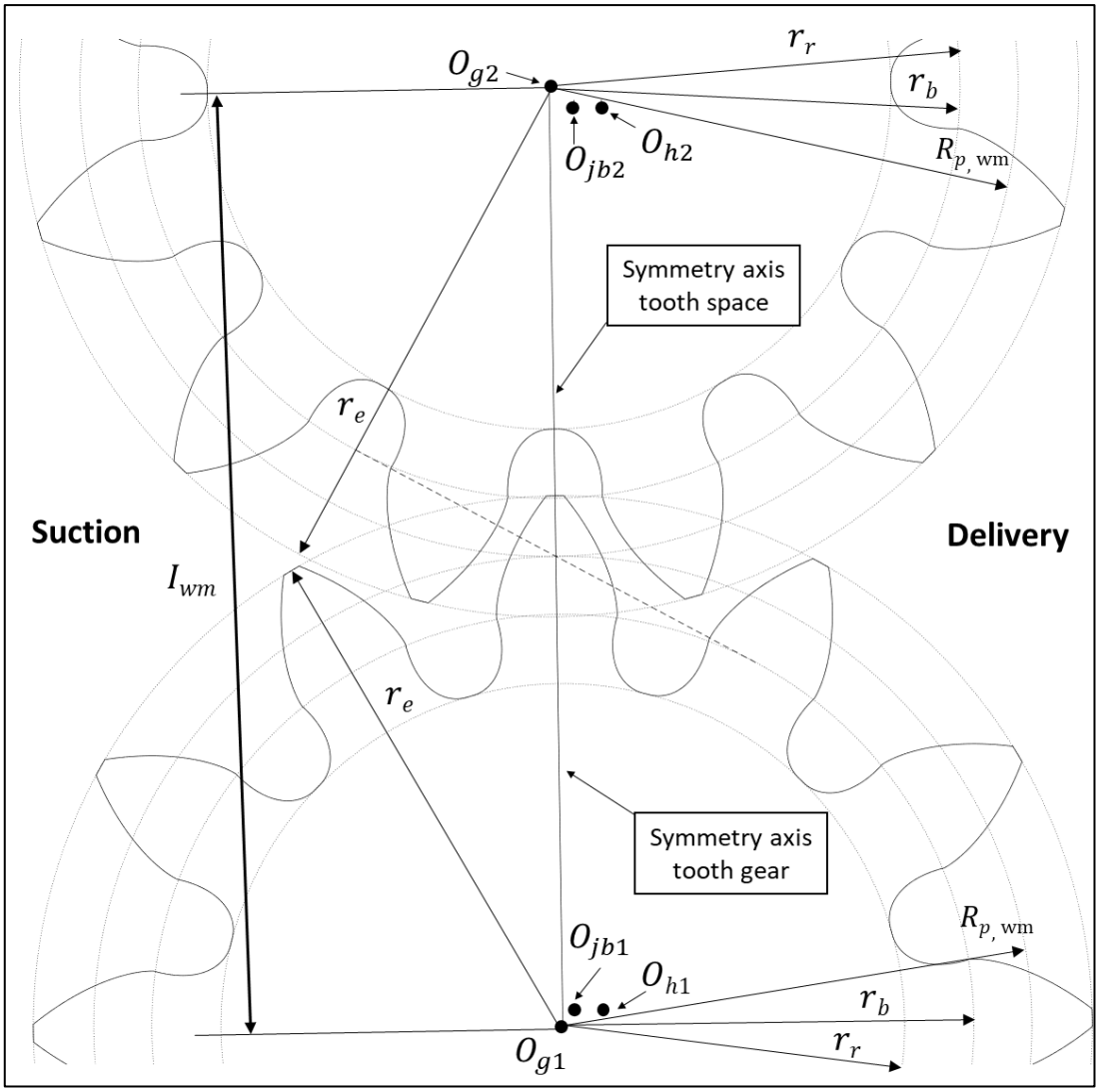

Figure 22 – Gears with micromotions and application of rotation $\overline{\varphi_{gap2}}$

Applying only the angular correction $\overline{\varphi_{gap1}}$ to the driving gear **guarantee contact** between the tooth flanks (Figure 23).

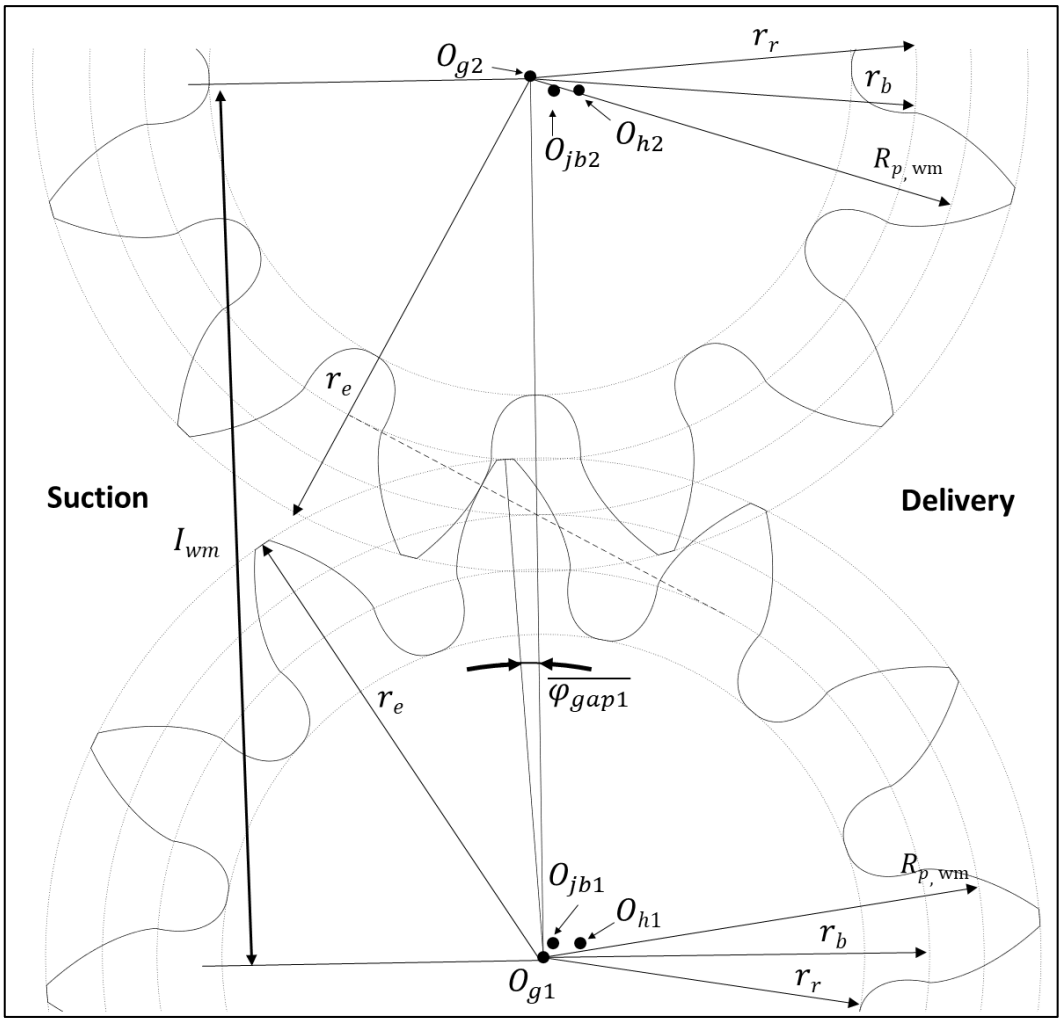

Figure 23 – Gears with micromotions and the application of rotations $\overline{\varphi_{gap1}}$ and $\overline{\varphi_{gap2}}$

In the model, the profile of gear 1 at a generic angular position φ is described by the vectors $\boldsymbol{x_{gear1}}(\varphi)$ and $\boldsymbol{y_{gear1}}(\varphi)$, whose components are computed as:

$$x_{gear1}(\varphi)^i = x^i_{gear1}\cos\left(\overline{\varphi_{gap1}} + \overline{\varphi_{gap2}} - \varphi\right) + y^i_{gear1}\sin\left(\overline{\varphi_{gap1}} + \overline{\varphi_{gap2}} - \varphi\right) + xO_{g1,O_{h1}}$$

Eq. 65

$$y_{gear1}(\varphi)^i = -x^i_{gear1}\sin\left(\overline{\varphi_{gap1}} + \overline{\varphi_{gap2}} - \varphi\right) + y^i_{gear1}\cos\left(\overline{\varphi_{gap1}} + \overline{\varphi_{gap2}} - \varphi\right) + yO_{g1,O_{h1}}$$

$$\text{for } i = 1, \ldots, 4n_r + 4n_{tr} + 4n_{inv} + 2n_h - 13$$

The terms x^i_{gear1} and x^i_{gear1} are the *i*-th components of the vectors defined in Eq. 58. The vectors $\boldsymbol{x_{gear1}}(\varphi)$ and $\boldsymbol{y_{gear1}}(\varphi)$ are obtained by applying a rotation of angle $\left(\overline{\varphi_{gap1}} + \overline{\varphi_{gap2}} - \varphi\right)$ and a translation of $(xO_{g1,O_{h1}}, yO_{g1,O_{h1}})$ to the original vectors $\boldsymbol{x_{gear1}}$ and $\boldsymbol{y_{gear1}}$.

Similarly, the profile of gear 2 at the same angular position φ, represented by the vectors $\boldsymbol{x_{gear2}}(\varphi)$ and $\boldsymbol{y_{gear2}}(\varphi)$, is given by :

$$x_{gear2}(\varphi)^i = x^i_{gear2}\cos\left(\varphi - \overline{\varphi_{gap2}}\right) + \left(y^i_{gear2} - I_w\right)\sin\left(\varphi - \overline{\varphi_{gap2}}\right) + xO_{g2,O_{h1}}$$

Eq. 66

$$y_{gear2}(\varphi)^i = -x^i_{gear2}\sin\left(\varphi - \overline{\varphi_{gap2}}\right) + \left(y^i_{gear2} - I_w\right)\cos\left(\varphi - \overline{\varphi_{gap2}}\right) + yO_{g2,O_{h1}}$$

$$\text{for } i = 1, \dots, 4n_r + 4n_{tr} + 4n_{inv} + 2n_h - 13$$

The terms x^i_{gear2} and x^i_{gear2} are the components of the vectors define in Eq. 59. To obtain the vectors $\boldsymbol{x_{gear2}}(\varphi)$ and $\boldsymbol{y_{gear2}}(\varphi)$, the following operations are performed to the original vectors $\boldsymbol{x_{gear2}}$ and $\boldsymbol{y_{gear2}}$:

1. A translation of $(0, -I_w)$, aligning the centre of gear 2 with the origin O_{h1}.
2. A rotation by an angle $\left(\varphi - \overline{\varphi_{gap2}}\right)$.
3. A final translation by the displacement vector $\left(xO_{g2,O_{h1}}, yO_{g2,O_{h1}}\right)$, accounting for micromotions.

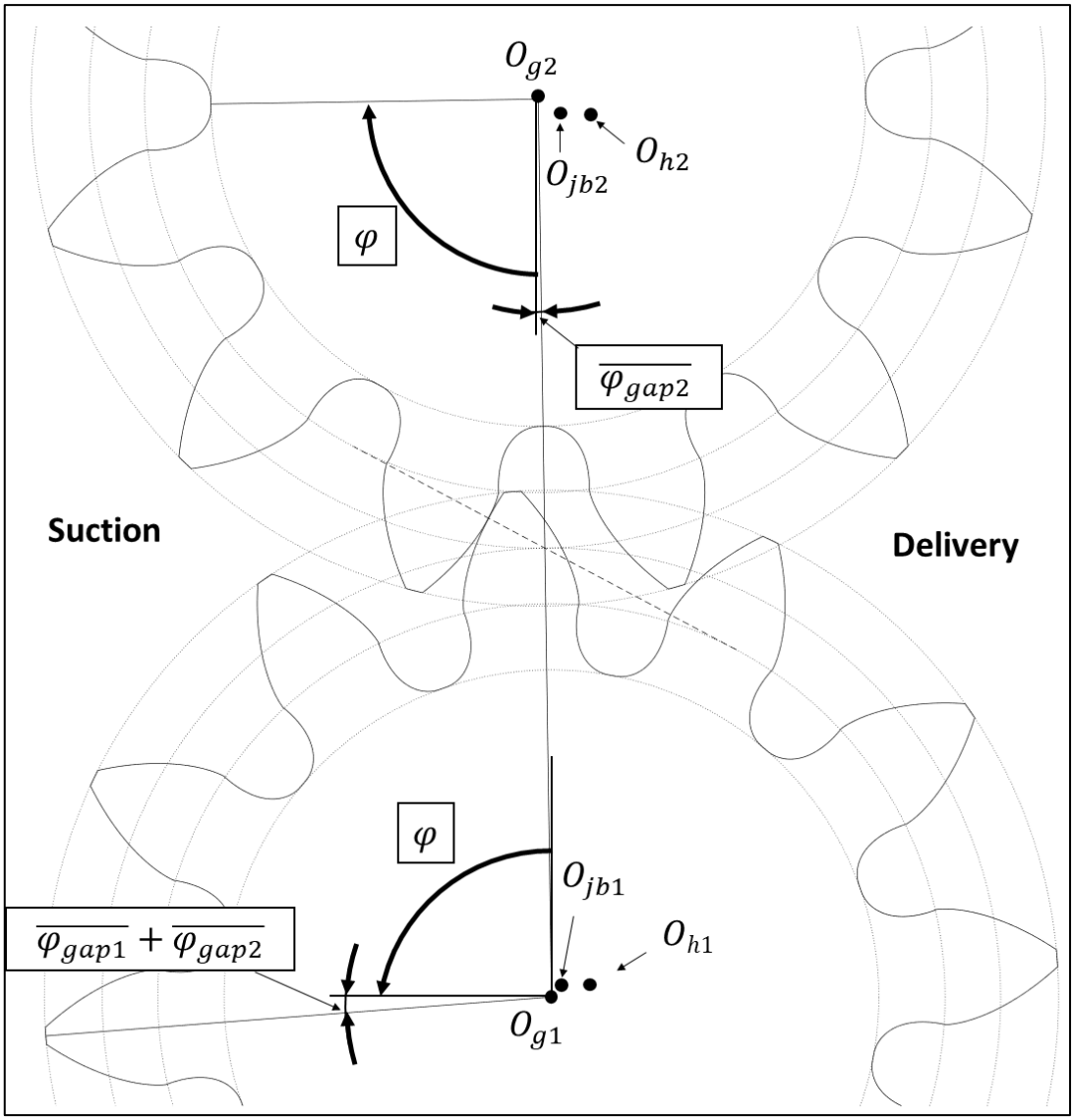

Figure 24 – Gears at a generic angular position φ

2.2.6. Control Volumes Definition

This section describes how the control volumes representing the pump chambers ($V_{1,i}$, $V_{2,i}$) and the delivery and suction volumes (V_D,V_s) are defined [20].
To establish the chamber control volumes, the reference volumes $V_{1,1}$, and $V_{2,1}$, corresponding to the first chamber of gear 1 and gear 2, respectively, are first identified. The remaining chambers are obtained by applying a circumferential shift equal to the pitch angle α_{pitch} :

$$V_1, i(\varphi) = V_{1,1}\left(\varphi - (i-1)\,\alpha_{pitch}\right)$$

$$V_2, i(\varphi) = V_{2,1}\left(\varphi - (i-1)\,\alpha_{pitch}\right) \qquad \textit{Eq. 67}$$

$$for\ i = 2, \dots, z$$

The delivery and suction volumes are divided into three components (see Figure 25):

- V_{d0} and V_{s0} the cylindrical volumes of the delivery and suction ports, calculated from the port diameter and length;
- V_{d1} and V_{s1}: constant volumes that can be extracted directly from the pump's CAD model;
- $V_{d,var}$ and $V_{s,var}$ variable volumes that change with the angular position of the gears. Their formulation is provided in the following sections.

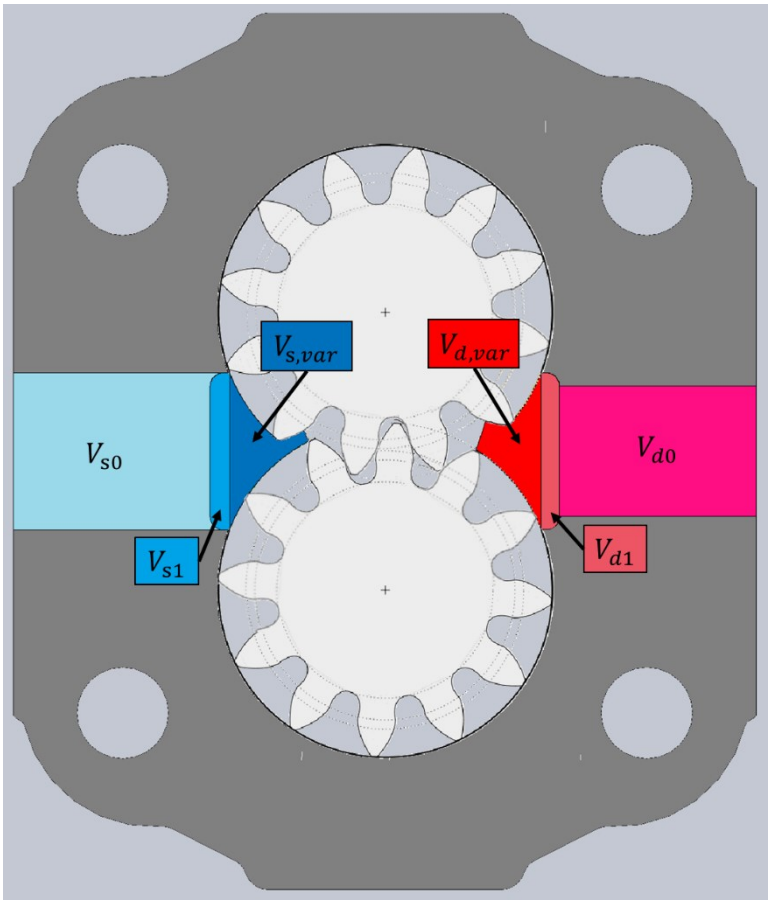

Figure 25 – Components of the delivery and suction volumes

With reference to the Figure 26, the following definitions are introduced:

- **Point $A1$:** the point that identifies the beginning of the head arc of the first tooth of gear 1.
- **Point $A1s$:** the point that identifies the end of the head arc of the first tooth of gear 1.
- **Point A2:** the point that identifies the beginning of the head arc of the second tooth of gear 1.
- **Point A2s:** the point that identifies the end of the head arc of the second tooth of gear 1.
- **Point A3:** the point that identifies the beginning of the head arc of the first tooth of gear 2.
- **Point A3s:** the point that identifies the end of the head arc of the first tooth of gear 2.
- **Point A4**: the point that identifies the beginning of the head arc of the second tooth of gear 2.
- **Point A4s:** the point that identifies the end of the head arc of the second tooth of gear 2.
- **Length** $d1$**:** the distance between point **A1** and the centre of gear 2 $(\mathrm{xO}_{\mathrm{g2,O_{h1}}}, \mathrm{yO}_{\mathrm{g2,O_{h1}}})$.
- **Length** $d2$**:** the distance between point **A2** and the centre of gear 2 $(\mathrm{xO}_{\mathrm{g2,O_{h1}}}, \mathrm{yO}_{\mathrm{g2,O_{h1}}})$.
- **Length** $d3$**:** the distance between point **A3** and the centre of gear 1 $(\mathrm{xO}_{\mathrm{g1,O_{h1}}}, \mathrm{yO}_{\mathrm{g1,O_{h1}}})$.
- **Length** $d4$**:** the distance between point **A4** and the centre of gear 1 $(\mathrm{xO}_{\mathrm{g1,O_{h1}}}, \mathrm{yO}_{\mathrm{g1,O_{h1}}})$.
- **Point P_{D1}:** the point that identifies the boundary of the pump housing on the delivery side of gear 1.
- **Point P_{D2} :** the point that identifies the boundary of the pump housing on the delivery side of gear 2.
- **Point P_{S1}:** the point that identifies the boundary of the pump housing on the suction side of gear 1.
- **Point P_{S2}:** the point that identifies the boundary of the pump housing on the suction side of gear 2.

To define the control volumes, five cases are identified based on the position of the pump chambers. The position of the chambers is determined using the distance values $d1, d2, d3$ and $d4$. For example, if $d1 < r_e$ this indicates that the tip of the first tooth of gear 1 is inside the meshing zone; conversely, if $d1 > r_e$, it is outside the meshing zone. The same considerations apply to the other distances.

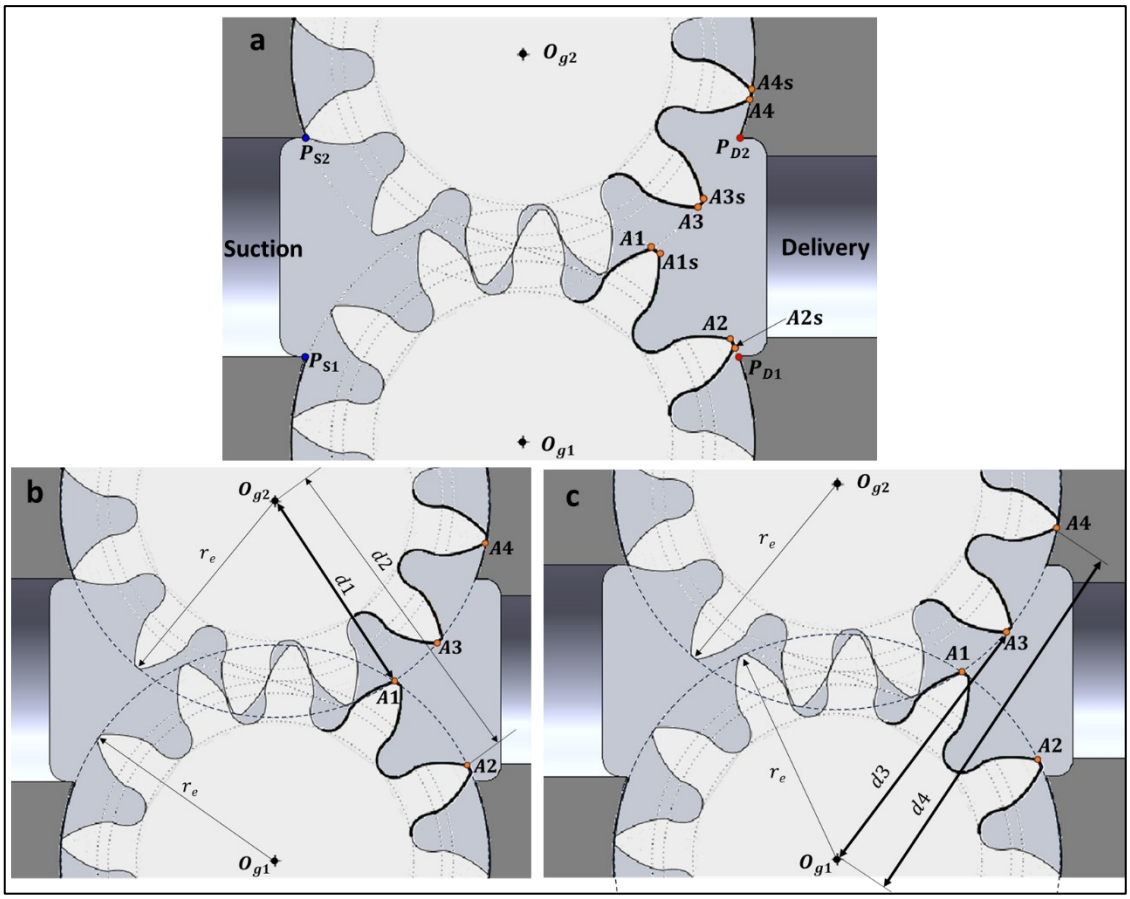

Figure 26 – Points and lengths used in the definition of control volumes

The five identified cases are:

- **CASE 1** – $d1 > r_e \; AND \; d2 > r_e \; AND \; d3 > r_e \; AND \; d4 > r_e$: n this case, both chambers $V_{1,1}$, and $V_{2,1}$ are outside the meshing zone.
- **CASE 2** – $d1 \leq r_e \; AND \; d2 > r_e$: chamber $V_{1,1}$ is about to enter the meshing zone, while chamber $V_{2,1}$ is outside the meshing zone.
- **CASE 3** – $d1 \leq r_e \; AND \; d2 \leq r_e$: chambers $V_{1,1}$ and $V_{2,1}$ are inside the meshing zone.
- **CASE 4** – $d1 > r_e \; AND \; d2 \leq r_e$: chamber $V_{1,1}$ is about to exit the meshing zone, while chamber $V_{2,1}$ is inside the meshing zone.
- **CASE 5** – $d1 > r_e \; AND \; d2 > r_e \; AND \; d4 < r_e$: chamber $V_{1,1}$ is outside the meshing zone, while chamber $V_{2,1}$ is about to exit the meshing zone.

2.2.6.1. Control Volumes Definition: CASE 1

CASE 1

$d1 > r_e \; AND \; d2 > r_e \; AND \; d3 > r_e \; AND \; d4 > r_e$

$$V_{1,1}(\varphi) = V_{max}$$
$$V_{2,1}(\varphi) = V_{max}$$
$$V'_{d,var}(\varphi) = 0$$
$$V'_{s,var}(\varphi) = 0$$

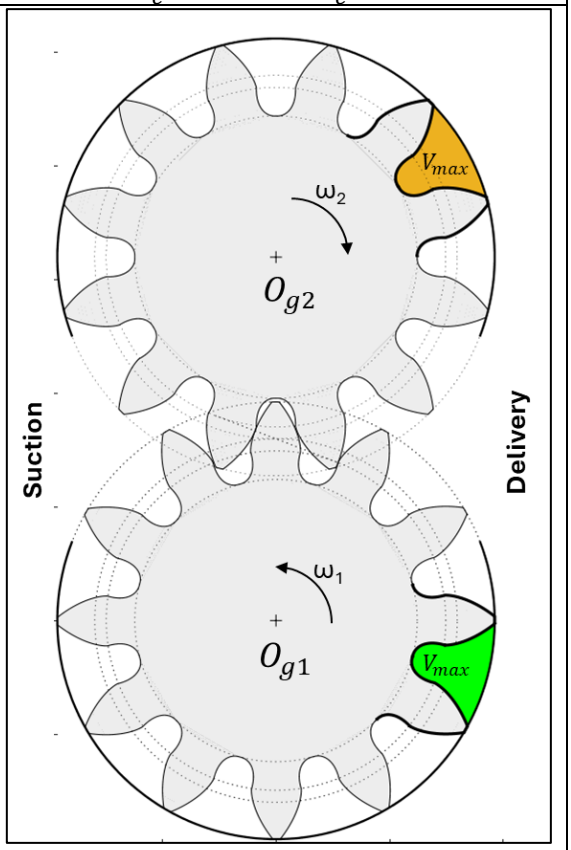

Figure 27 - CASE 1

In Figure 27, the control volumes representing the first chamber of the driving gear ($V_{1,1}(\varphi)$) and the first chamber of the driven gear ($V_{2,1}(\varphi)$) are highlighted in green and orange, respectively. The gear teeth used to define the chambers in the model are shown with thicker black lines, while the circular arc in black represents the pump housing.

In **CASE 1**, the chambers of the driving and driven gears assume their maximum volume. For most of the time in this case, the chambers are delimited by the gear teeth and the pump housing.

2.2.6.2. Control Volumes Definition: CASE 2

In **CASE 2**, the first tooth of the driving gear is located within the meshing zone ($d1 \leq r_e$), while the second tooth lies outside the meshing zone ($d2 > r_e$).
To define the control volumes, which are highlighted in the following figure, the lengths $l1$, $l2$ and $l3$ are introduced.

- $l1$ is calculated as the minimum Euclidean distance between the points of the head arc and the second involute profile of the first tooth of the driving gear, and the first involute profile of the first tooth of the driven gear.
- $l2$ is calculated as the minimum Euclidean distance between the points of the first involute profile of the second tooth of the driving gear and the head arc of the first tooth of the driven gear.
- $l3$ is calculated as the minimum Euclidean distance between the points of the head arc of the second tooth of the driving gear and the first involute profile of the second tooth of the driven gear.

The minimum length l_{min}, used to define the various subcases, is set to 0.9 mm.

<table>
<tr><th colspan="2">CASE 2
$d1 \leq r_e \; AND \; d2 > r_e$</th></tr>
<tr><td>Calculate of the length $l1$</td><td></td></tr>
<tr><td>

- **IF** $l1 > l_{min}$

$$V_{1,1}(\varphi) = V_{max}$$
$$V_{2,1}(\varphi) = V_{max}$$
$$V'_{d,var}(\varphi) = \overline{V_d}$$
$$V'_{s,var}(\varphi) = 0$$

</td><td>
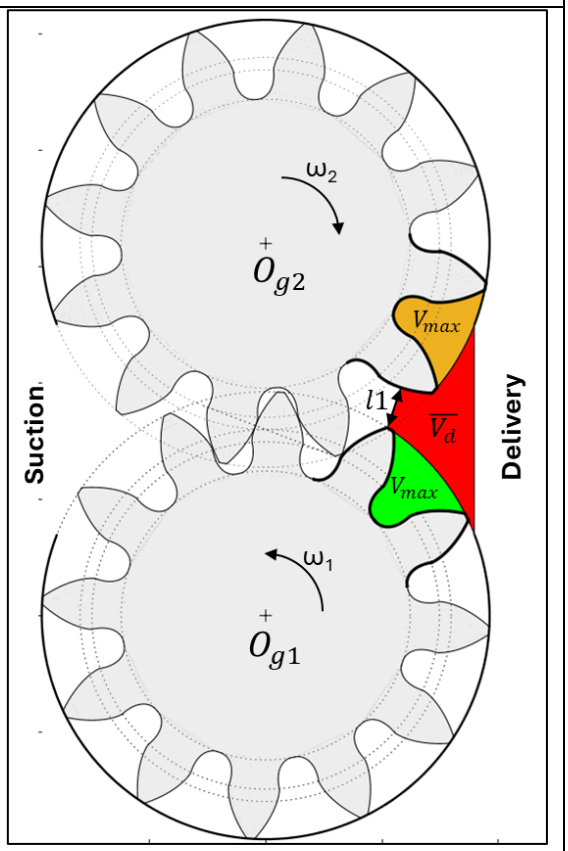

Figure 28 - CASE 2 : $l1 > l_{min}$
</td></tr>
</table>

- **IF** $l1 \leq l_{min}$

Calculate of the length $l2$

- **IF** $l2 > l_{min}$

$$V_{1,1}(\varphi) = \overline{V_1}$$
$$V_{2,1}(\varphi) = V_{max}$$
$$V'_{d,var}(\varphi) = \overline{V_d}$$
$$V'_{s,var}(\varphi) = 0$$

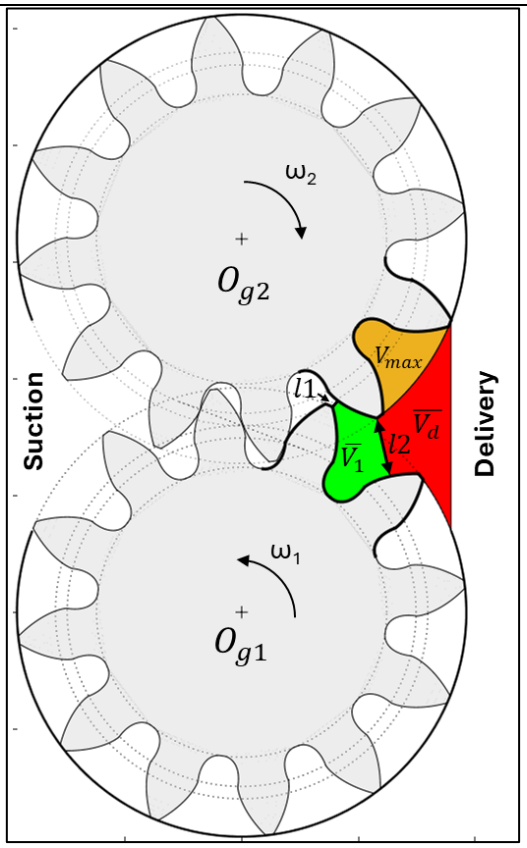

Figure 29 - CASE 2 : $l1 \leq l_{min}$ and $l2 > l_{min}$

- **IF** $l2 \leq l_{min}$

Calculate of the length $l3$

$$V_{1,1}(\varphi) = \overline{V_1}$$
$$V_{2,1}(\varphi) = \overline{V_2}$$
$$V'_{d,var}(\varphi) = \overline{V_d}$$
$$V'_{s,var}(\varphi) = 0$$

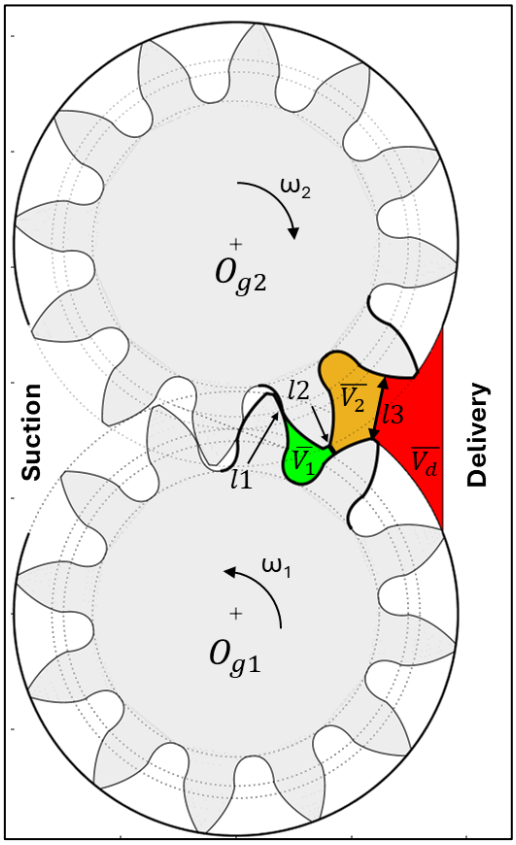

Figure 30 - CASE 2 : $l1 \leq l_{min}$ and $l2 \leq l_{min}$

2.2.6.3. Control Volumes Definition: CASE 3

CASE 3 $d1 \leq r_e \; AND \; d2 \leq r_e$	
Calculate of the lengths $l1$, $l2$, $l3$ $V_{1,1}(\varphi) = \overline{V_1}$ $V_{2,1}(\varphi) = \overline{V_2}$ $V'_{d,var}(\varphi) = 0$ $V'_{s,var}(\varphi) = 0$	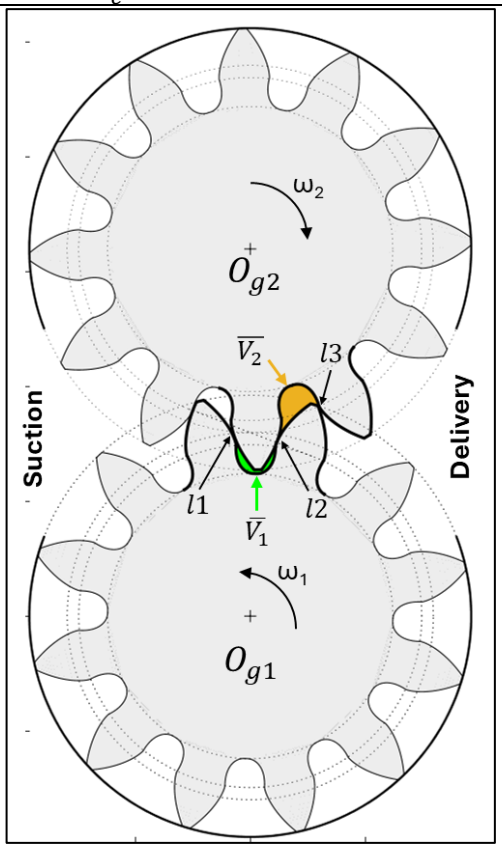 *Figure 31 - CASE 3*

In **CASE 3**, the first and second teeth of the driving gear are located within the meshing zone ($d1 \leq r_e$ and $d2 \leq r_e$).

- $l1$ is calculated as the minimum Euclidean distance between the points of the second involute profile of the first tooth of the driving gear and the first involute profile of the first tooth of the driven gear.
- $l2$ is calculated as the minimum Euclidean distance between the points of the first involute profile of the second tooth of the driving gear and the second involute profile of the first tooth of the driven gear.
- $l3$ is calculated as the minimum Euclidean distance between the points of the second involute profile of the second tooth of the driving gear and the first involute profile of the second tooth of the driven gear.

2.2.6.4. Control Volumes Definition: CASE 4

In **CASE 4**, the first tooth of the driving gear is outside the meshing zone ($d1 > r_e$), while the second tooth is within the meshing zone ($d2 \leq r_e$).

- $l1$ is calculated as the minimum Euclidean distance between the points of the second involute profile of the first tooth of the driving gear and the head arc of the first tooth of the driven gear.
- $l2$ is calculated as the minimum Euclidean distance between the points of the head arc and the first involute profile of the second tooth of the driving gear, and the second involute profile of the first tooth of the driven gear.
- $l3$ is calculated as the minimum Euclidean distance between the points of the second involute profile of the second tooth of the driving gear, and the first involute profile of the second tooth of the driven gear.

<table>
<tr><th colspan="2">CASE 4
$d1 > r_e \; AND \; d2 \leq r_e$</th></tr>
<tr><td>Calculate of the length $l1, l2$</td><td></td></tr>
<tr><td>

- **IF** $l2 > l_{min}$

$$V_{1,1}(\varphi) = V_{max}$$
$$V_{2,1}(\varphi) = \bar{V}_2$$
$$V'_{d,var}(\varphi) = 0$$
$$V'_{s,var}(\varphi) = \bar{V}_s$$

</td><td>

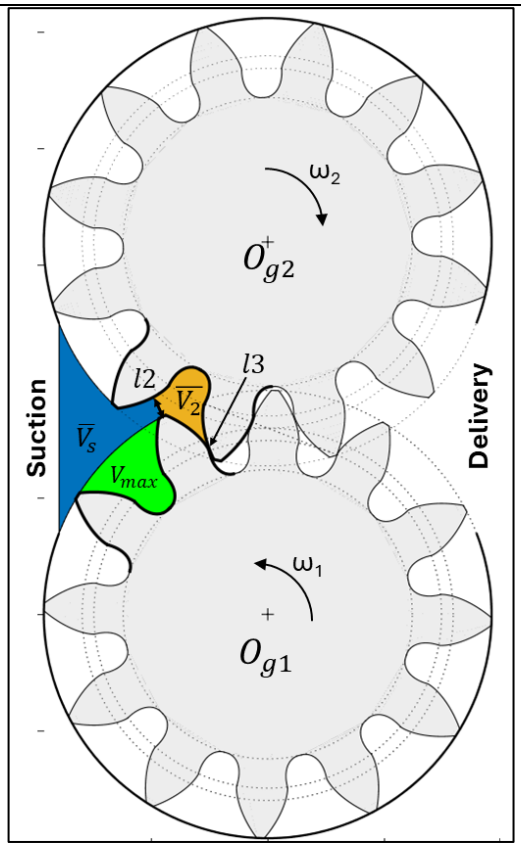

Figure 32 - CASE 4: $l2 > l_{min}$

</td></tr>
</table>

- **IF** $l2 \leq l_{min}$

Calculate of the length $l1$

  - **IF** $l1 > l_{min}$

$$V_{1,1}(\varphi) = \bar{V}_1$$
$$V_{2,1}(\varphi) = \bar{V}_2$$
$$V'_{d,var}(\varphi) = 0$$
$$V'_{s,var}(\varphi) = \bar{V}_s$$

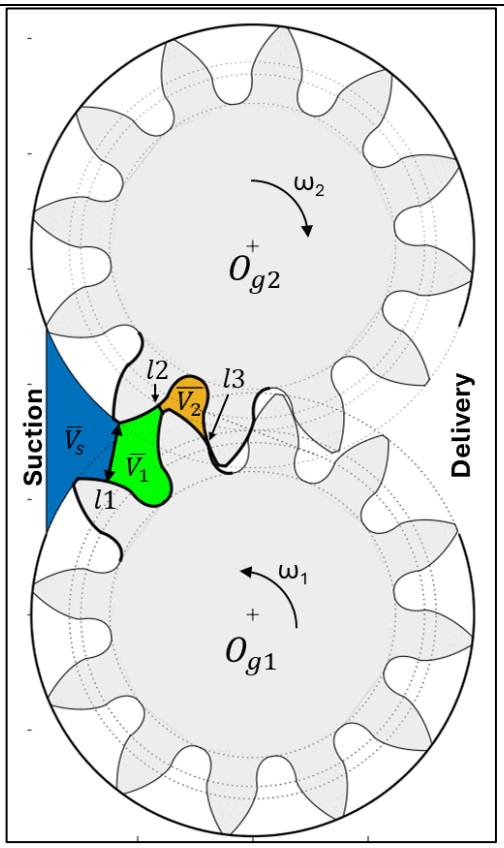

Figure 33 - CASE 4 : $l2 \leq l_{min}$ and $l1 > l_{min}$

  - **IF** $l1 \leq l_{min}$

$$V_{1,1}(\varphi) = \bar{V}_1$$
$$V_{2,1}(\varphi) = \bar{V}_2$$
$$V'_{d,var}(\varphi) = 0$$
$$V'_{s,var}(\varphi) = 0$$

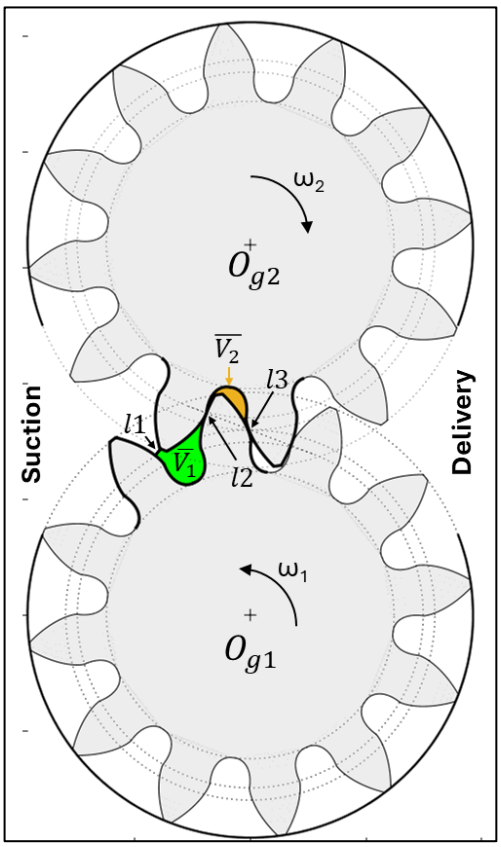

Figure 34 - CASE 4 : $l2 \leq l_{min}$ and $l1 \leq l_{min}$

2.2.6.5. Control Volumes Definition: CASE 5

In **CASE 5**, the first and second tooth of the driving gear are located outside the meshing zone ($d1 > r_e$ and $d2 > r_e$), while the second tooth of the driven gear is within the meshing zone ($d4 < r_e$).

- $l2$ is calculated as the minimum Euclidean distance between the points of the head arc of the second tooth of the driving gear and the second involute profile of the first tooth of the driven gear.
- $l3$ is calculated as the minimum Euclidean distance between the points of the second involute profile of the second tooth of the driving gear and the head arc and the first involute profile of the second tooth of the driven gear.

<table>
<tr><th colspan="2">CASE 5
$d1 > r_e \; AND \; d2 > r_e \; AND \; d4 < r_e$</th></tr>
<tr><td>Calculate of the length l3</td><td></td></tr>
<tr><td>

- **IF** $l3 > l_{min}$

$$V_{1,1}(\varphi) = V_{max}$$
$$V_{2,1}(\varphi) = V_{max}$$
$$V'_{d,var}(\varphi) = 0$$
$$V'_{s,var}(\varphi) = 0$$

</td><td> 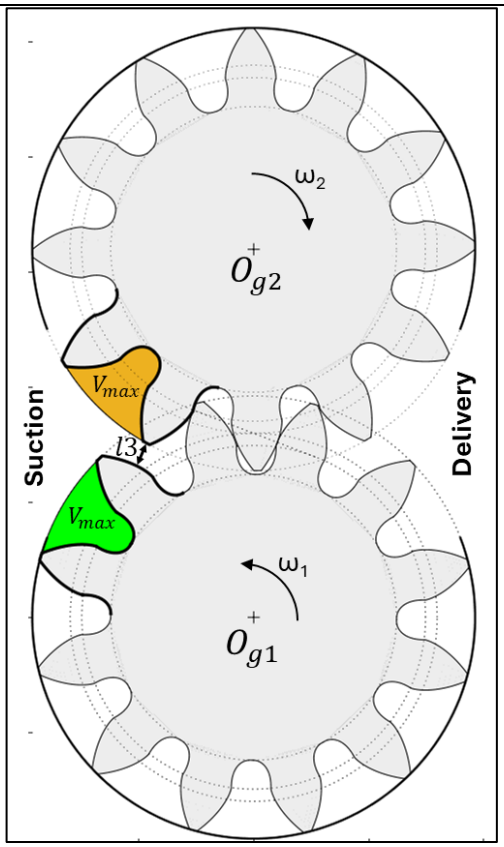

Figure 35 - CASE 5 : $l3 > l_{min}$</td></tr>
</table>

- **IF** $l3 \leq l_{min}$

Calculate of the length $l2$

$$V_{1,1}(\varphi) = V_{max}$$
$$V_{2,1}(\varphi) = \overline{V_2}$$
$$V'_{d,var}(\varphi) = 0$$
$$V'_{s,var}(\varphi) = \overline{V_s}$$

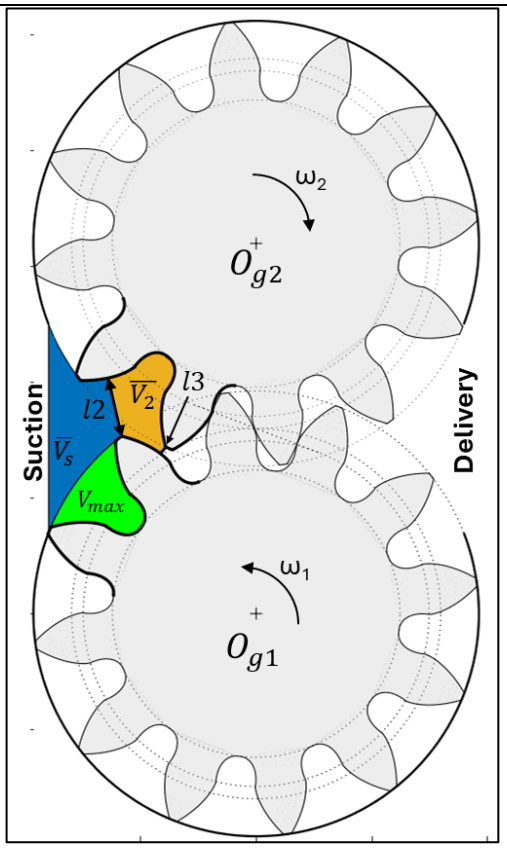

Figure 36 - CASE 5 : $l3 \leq l_{min}$

2.2.6.6. Control Volumes: Pump chambers

Figure 37 shows the trend of the control volumes of the first chamber of the driving gear ($V_{1,1}(\varphi)$) and the first chamber of the driven gear ($V_{2,1}(\varphi)$) over a complete rotation.

The control volume $V_{1,1}(\varphi)$ and $V_{2,1}(\varphi)$ exhibit the same trend, but shifted by an angular distance of $\frac{\alpha_{pitch}}{2}$. In Figure 37, the angular shift is of 15°, since the gears have 12 teeth ($\alpha_{pitch} = 360°/z = 360°/12 = 30°$).

At the angular position 0°, both $V_{1,1}$ and $V_{2,1}$ are within the meshing zone. From 0° to approximately 15°, $V_{1,1}$ undergoes a decreasing phase, reaching its minimum value at 15°. After this point, the volume begins to increase until it reaches its maximum value. For most of the rotation, the volume remains at this maximum. Around 335°, $V_{1,1}$ re-enters the meshing zone and begins to decrease again.
The control volume $V_{2,1}$ follows the same behaviour, but with a 15° phase shift.
This behaviour repeats with every full rotation.

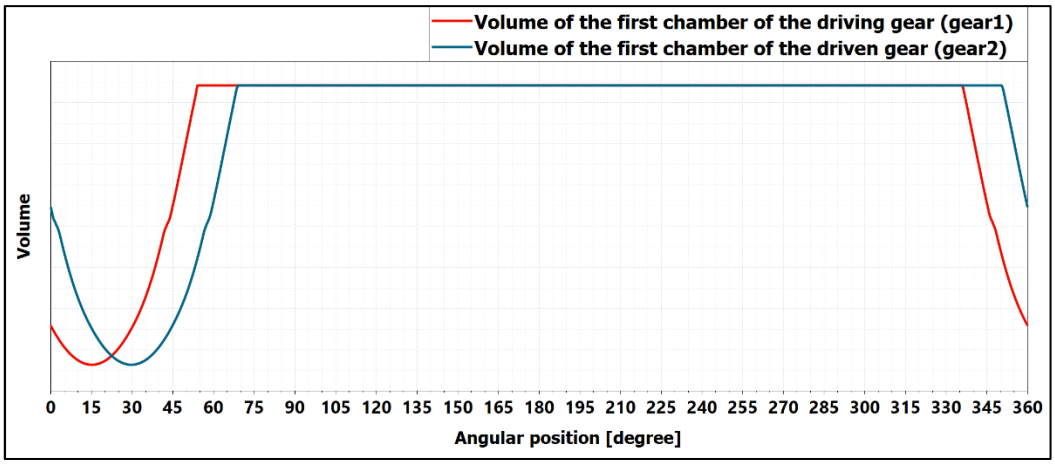

Figure 37 – Chamber volume variations of driving and driven gears during rotation

The other control volumes for the driving and driven gears are obtained using Eq. 67. Figure 38 shows the case of a gear pump with 12 teeth. The red curve represents $V_{1,1}$, while the blue curve corresponds to $V_{1,i=6}$. In this case, the angular shift is equal to $(6-1) * 30° = 150°$.

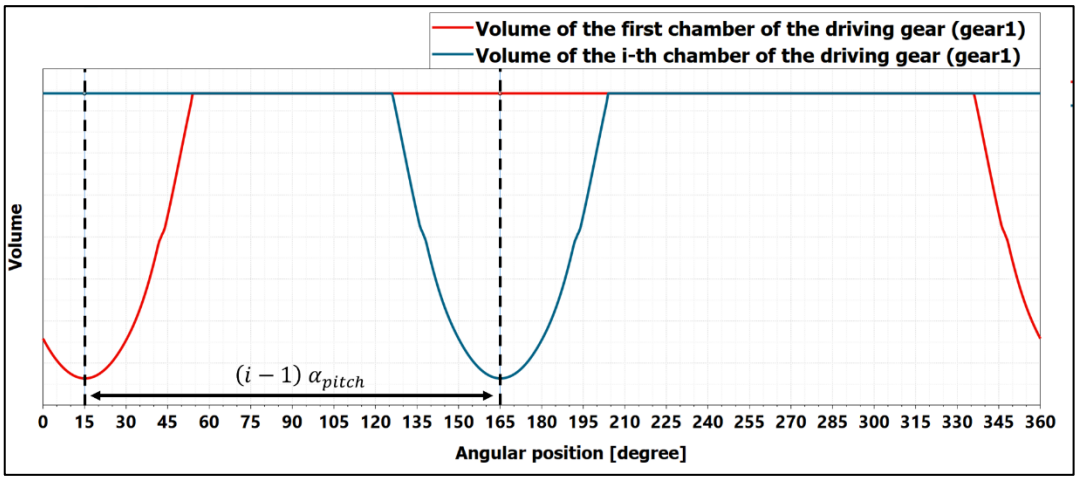

Figure 38 – Control volume of the i-th chamber of the driving gear

2.2.6.7. Control Volumes: Delivery and Suction

As previously introduced, the control volumes for the delivery and suction phases are divided into different parts.

V_{d0}, V_{d1}, V_{s0} and V_{s1} are the portions of volume that remain constant during gear rotation, while $V_{d,var}$ and $V_{s,var}$ are the variable volumes that change with the angular position of the gears.

The volumes $V'_{d,var}$ and $V'_{s,var}$ represent the variable portions of the delivery and suction volumes exclusively when the control volumes $V_{1,1}$ and $V_{2,1}$ are exposed to the delivery and suction phases, respectively. An example of the trend of these curves is shown in Figure 39.

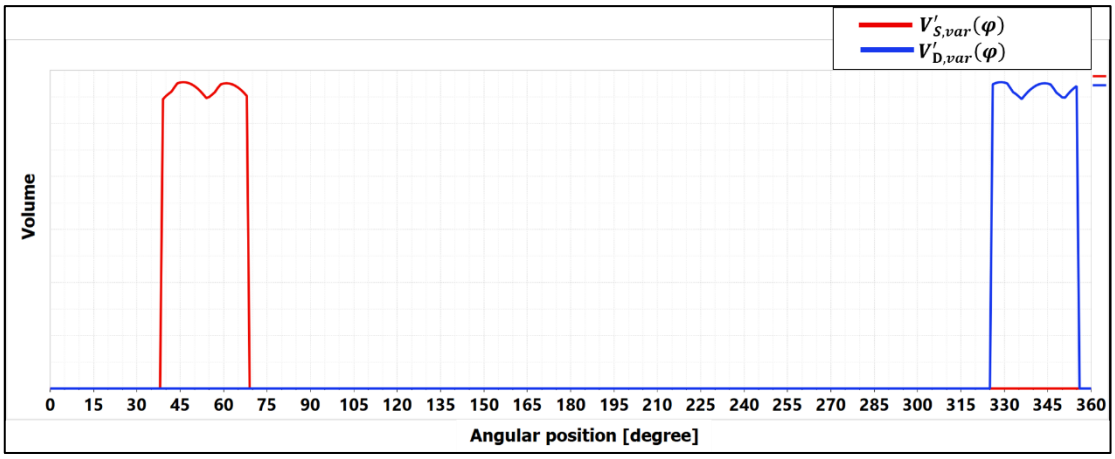

Figure 39 – Curves of the $V'_{d,var}$ and $V'_{s,var}$ volumes

The suction and delivery variable volumes observed by the other control volumes when they are exposed to suction or delivery can be obtained by applying an angular shift of α_{pitch}, in a similar manner to the method used to define the pump chambers from $V_{1,1}(\varphi)$ and $V_{2,1}(\varphi)$.
The delivery and suction volumes at a generic angular position φ are defined as:

$$V_D(\varphi) = \sum_{i=1}^{z} V'_{d,var}\left(\varphi - (i-1)\,\alpha_{pitch}\right) + V_{d0} + V_{d1}$$

$$V_S(\varphi) = \sum_{i=1}^{z} V'_{s,var}\left(\varphi - (i-1)\,\alpha_{pitch}\right) + V_{s0} + V_{s1}$$

Eq. 68

Figure 40 shows the trend of the suction and delivery control volumes as obtained from Eq. 68. It can be observed that the curves exhibit a number of peaks equal to $2z$; in the case shown, the peaks are 24 since the gears have 12 teeth.

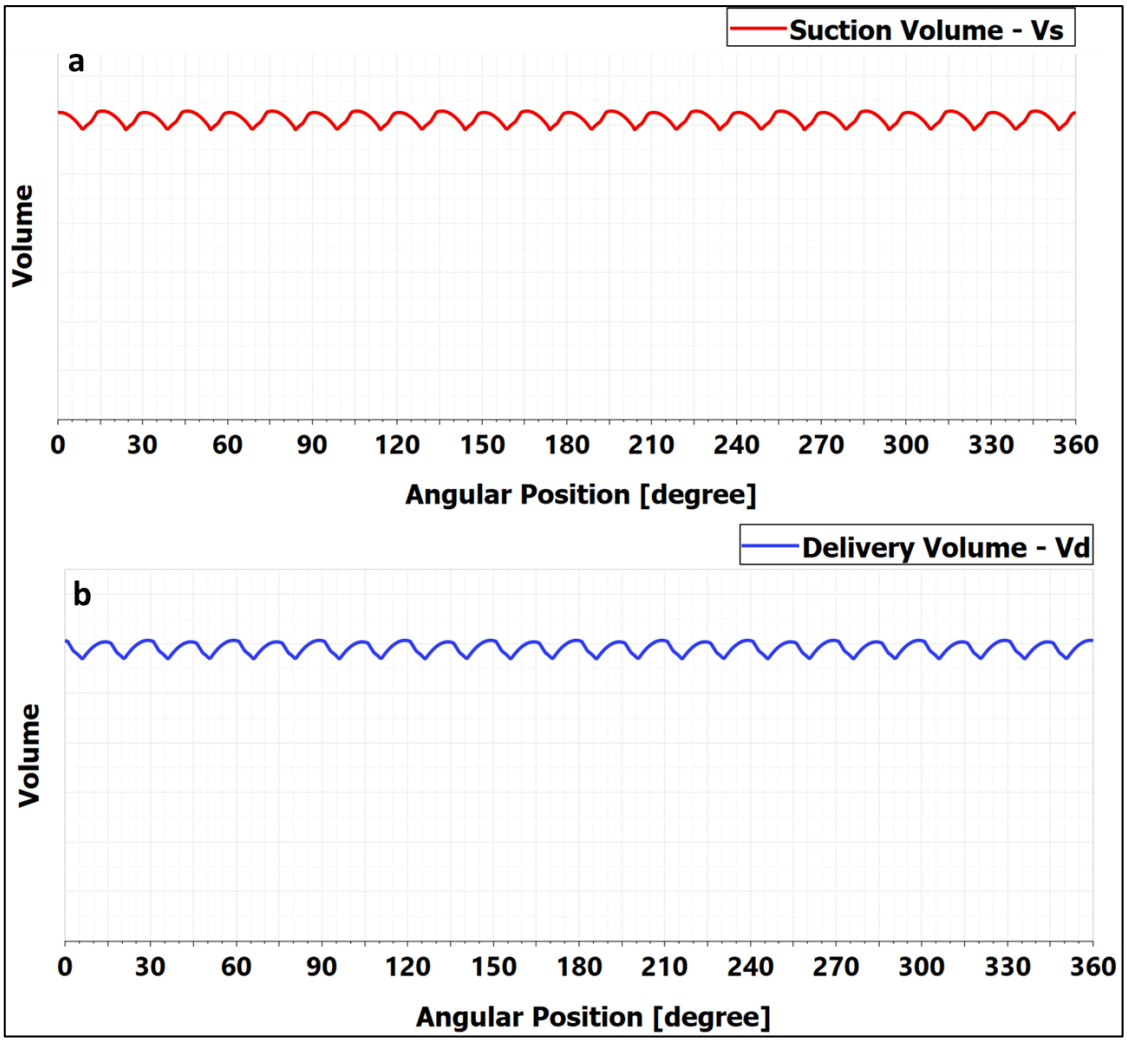

Figure 40 – Trend of Suction (a) and Delivery (b) Volumes

2.3. Radial Connection between Pump Chambers and Delivery/Suction Control Volumes

The pump chambers communicate with the delivery and suction control volumes through connection areas, which open when the chambers are exposed to the corresponding control volumes. This communication generates a flow in the radial direction.

Figure 41 shows the radial connection areas between the first chambers of the driving and driven gears and the delivery control volume, for a gear pump with 12 teeth. While Figure 42 illustrates the corresponding connection areas with the suction control volume.

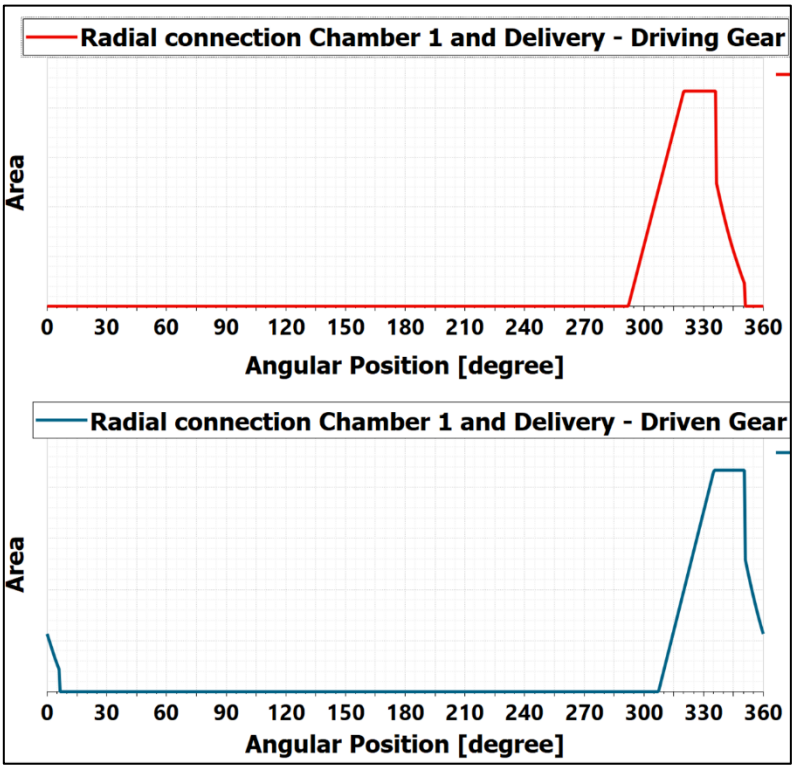

Figure 41 – Area of the radial connection between the chambers and the delivery

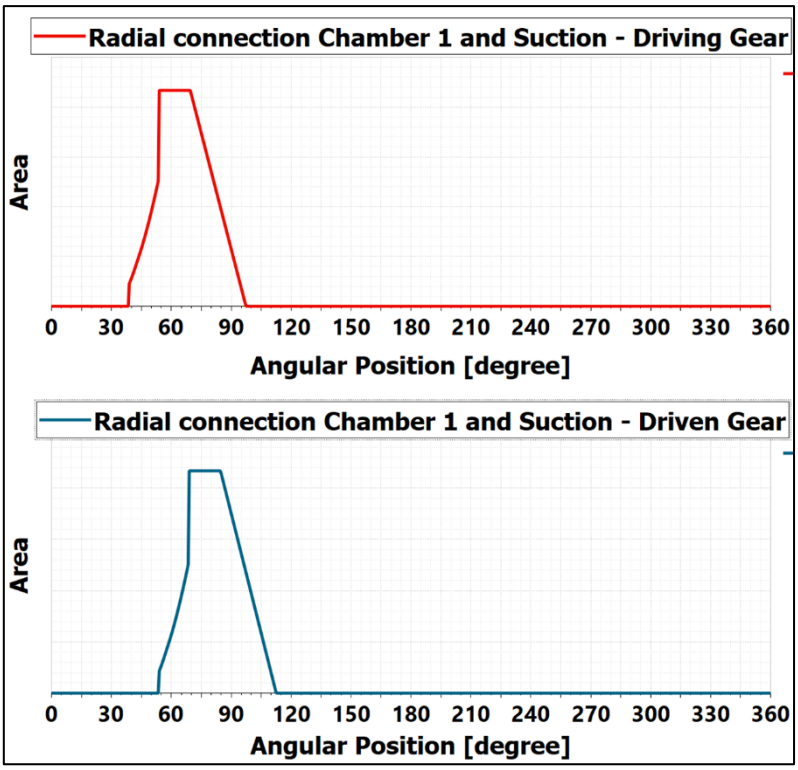

Figure 42 - Area of the radial connection between the chambers and the suction

To explain the behaviour of the radial communication areas, Figure 43 is provided. This figure shows the evolution of the communication area between the first chamber of the driving gear and the delivery control volume. However, the following considerations also apply to the driven gear and to the communication area with the suction control volume.

Referring to the driving gear, which is located at the bottom of Figure 43 and rotates in a counter-clockwise direction, with the delivery port on the right-hand side of the pump and the suction port on the left-hand side:

- **Position 1:** the chamber is fully exposed to the pump housing, and no communication occurs between the chamber and the delivery control volume.
- **Position 2:** the chamber starts to communicate with the delivery control volume through an area defined by a circular arc, extending from the tooth tip to the beginning of the housing wall.
- **Position 3:** as the rotation continues, the chamber becomes fully connected to the delivery volume, and the communication area reaches its maximum.
- **Position 4:** the communication area begins to decrease due to the meshing of the gears.
- **Position 5:** the chamber of the driving gear comes into contact with the chamber of the driven gear, and the radial communication area with the delivery control volume becomes zero.

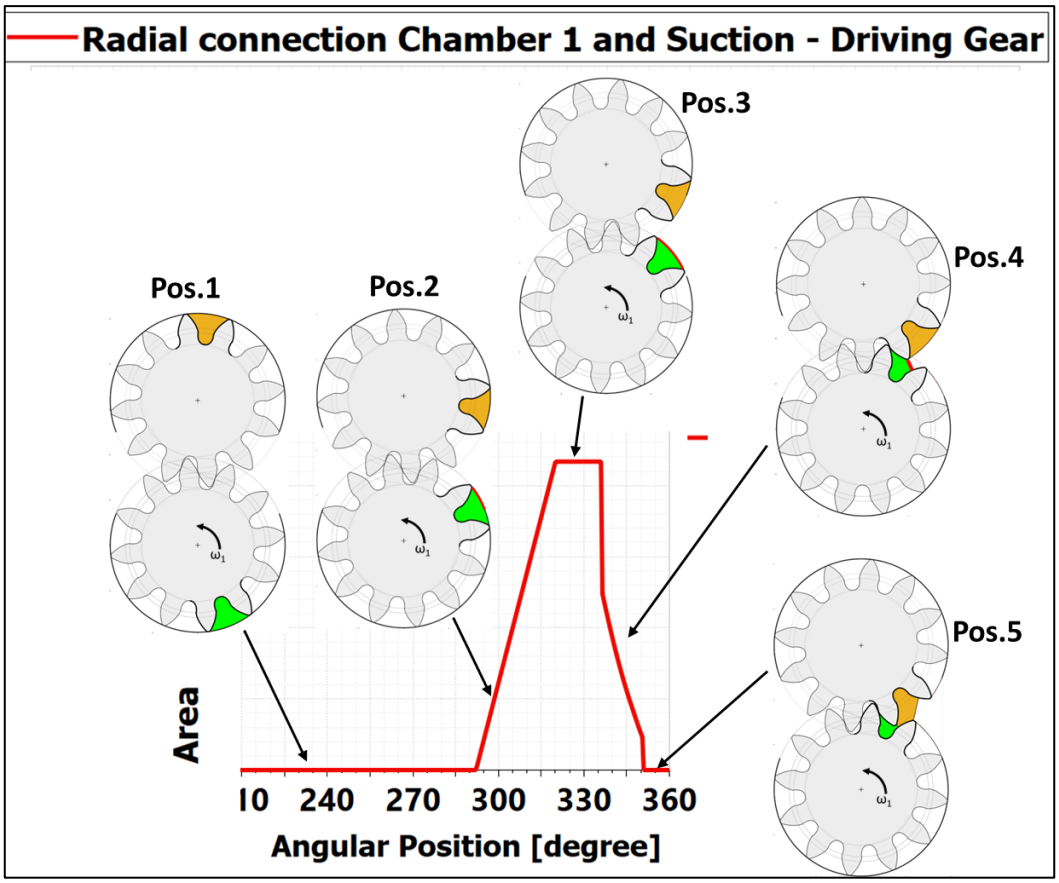

Figure 43 - Development of the communication area between the pump chamber and the delivery control volume during rotation

The flow rate exchanged between the pump chamber and the delivery or suction control volume is evaluated using the following equation [16]:

$$Q_{j,i,k} = c_q \, A_{j,i,k} \sqrt{2 \frac{|\Delta p|}{\rho} \frac{\rho}{\rho(0)}} \, sign(\Delta p) \qquad \text{Eq. 69}$$

Where:

- $Q_{j,i,k}$ is the flow rate exchanged between the driving pump chamber ($V_{j=1,i}$) or the driven pump chamber ($V_{j=2,i}$), and the delivery (V_D, k=D) or suction (V_S, k=S) control volume.
- c_q is the flow coefficient.
- $A_{j,i,k}$ is the communication area between the control volumes (see Figure 41 and Figure 42).
- $\Delta p = p_k - p_{j,i}$ is the pressure difference between the pump chamber (j=1 for the driving chamber, j=2 for the driven chamber) and the delivery (k=D) or suction (k=S) control volume.
- $\rho = \rho\left(\frac{p_{j,i}+p_k}{2}\right)$ is the oil density at the mean pressure.
- $\rho(0)$ is the oil density at 0 bar gauge pressure.

- $sign(\Delta p)$ accounts for the direction of the flow: $Q > 0$ when the flow is from the pump chamber to the delivery or suction control volume, $Q < 0$ when it flows in the opposite direction.

The flow coefficient is defined as :

$$c_q = c_{q\,max} \tanh\left(\frac{2\lambda}{\lambda_{crit}}\right) \qquad \textit{Eq. 70}$$

$c_{q\,max}$ is the maximum value of the flow coefficient, which can vary in the range [0,1], and is set to 0.7 in the model.

The flow number λ is defined as:

$$\lambda = \frac{hd_{j,i,k}}{\nu}\sqrt{2\frac{|\Delta p|}{\rho}} \qquad \textit{Eq. 71}$$

Where:

- $hd_{j,i,k} = \frac{4A_{j,i,k}}{perimeter_{j,i,k}}$ is the hydraulic diameter, with $A_{j,i,k}$ being the communication area and $perimeter_{j,i,k}$ the perimeter of that area.
- ν is the kinematic viscosity of the oil at the mean pressure.

The flow number λ is analogous to the Reynolds number and characterises the transition between laminar and turbulent flow, based on the value of the critical flow number λ_{crit}.

When $\lambda > \lambda_{crit}$ the flow is turbulent and the flow coefficient remains constant at $c_{q\,max}$.
When $\lambda < \lambda_{crit}$ the flow is laminar and the flow coefficient varies approximately linearly with Δp.
In the model, the critical flow number is set to 100 to represent this transition.

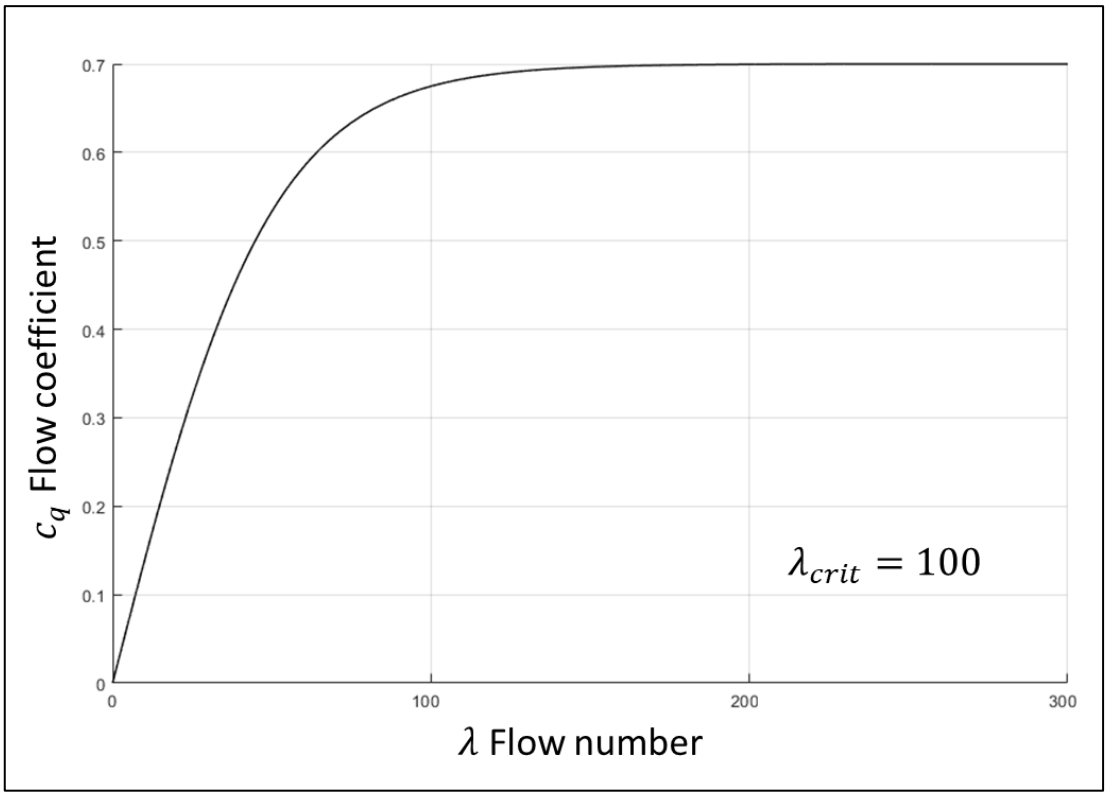

Figure 44 – Flow coefficient trend

In the model, the reference communication areas $A_{1,1,k}$, and $A_{2,1,k}$, corresponding to the first chambers of gear 1 and gear 2, respectively, are first identified. The remaining communication area are obtained by applying a circumferential shift equal to the pitch angle α_{pitch} :

$$A_{1,i,k}(\varphi) = A_{1,1,k}\left(\varphi - (i-1)\,\alpha_{pitch}\right)$$

$$A_{2,i,k}(\varphi) = A_{2,1,k}\left(\varphi - (i-1)\,\alpha_{pitch}\right) \qquad \textit{Eq. 72}$$

$$for\ i = 2, \dots, z$$
$$k = D, S$$

2.4. Connection Between the Driving and Driven Pump Chambers

During gear meshing, the chambers of the driving gear come into communication with the chambers of the driven gear.

As shown in Figure 43, in Position 4 the chamber *i*-th of the driving gear is still connected to the delivery port. However, in Position 5, the distance between the teeth of the driving and driven gears decreases, and - according to the control volume definition algorithm used in the model (see Sections 0, 0 and 0) - the driving gear chamber ends its communication with the delivery control volume and establishes a connection with the *i*-th chamber of the driven gear. A similar behaviour occurs on the suction side.

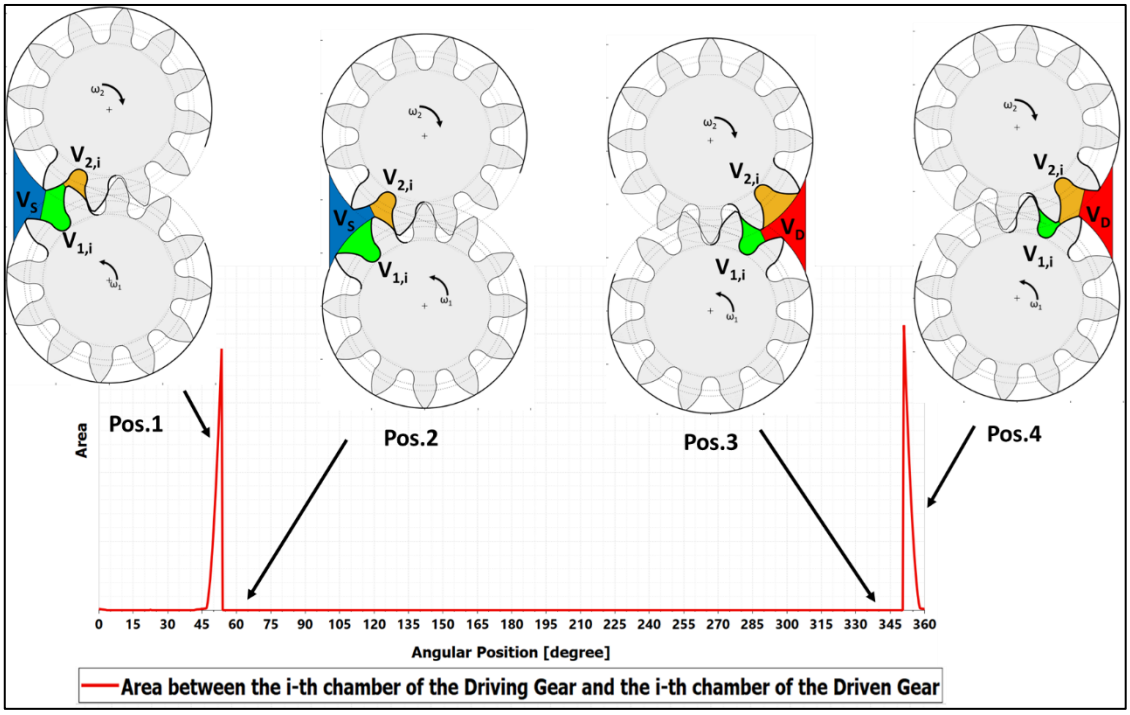

Figure 45 - The trend of the communication area between the i-th chambers of the driving and driven gears

The trend of the communication area between the *i*-th chambers of the driving and driven gears is shown in Figure 45:

- **Before Position 1**, the teeth of the driving and driven gears are in contact, and there is no communication between chambers $V_{1,i}$ and $V_{2,i}$.
- **At Position 1**, the tooth contact ends, and chambers $V_{1,i}$ and $V_{2,i}$ come into communication. As the gears continue to rotate, the communication area increases until it reaches a maximum.
- **At Position 2**, chamber $V_{1,i}$ reaches its maximum volume and ends its communication with $V_{2,i}$ while chamber $V_{2,i}$ establishes a connection with the suction control volume V_S .
- **At Position 3**, chamber $V_{1,i}$ is in communication with the delivery control volume V_D, while chamber $V_{2,i}$is at its maximum volume.

- **At Position 4,** chamber $V_{1,i}$ re-establishes communication with $V_{2,i}$ and ends its communication with the delivery control volume V_D. As the gears rotate, the communication area gradually decreases until it becomes zero when the teeth come back into contact.

The flow between the chamber *i*-th of the driving gear and the chamber *i*-th of the driven gear is defined using the same formulation of the Eq. 69 :

$$Q_{c\,i} = c_q\, A_{c\,i} \sqrt{2\frac{|\Delta p|}{\rho}\frac{\rho}{\rho(0)}}\; sign(\Delta p) \qquad \textit{Eq. 73}$$

Where:

- $Q_{c\,i}$ is the flow rate exchanged between the driving pump chamber ($V_{1,i}$) and the driven pump chamber ($V_{2,i}$) .
- c_q is the flow coefficient.
- $A_{c\,i}$ is the communication area between the chambers $V_{1,i}$ and $V_{2,i}$.
- $\Delta p = p_{2,i} - p_{1,i}$ is the pressure difference between the pump chambers
- $\rho = \rho\left(\frac{p_{1,i}+p_{2,i}}{2}\right)$ is the oil density at the mean pressure.
- $\rho(0)$ is the oil density at 0 bar gauge pressure.
- $sign(\Delta p)$ accounts for the direction of the flow: $Q > 0$ when the flow is from $V_{2,i}$ and $V_{1,i}$, $Q < 0$ when it flows in the opposite direction.

In the model, the reference communication area $A_{c\,1}$, corresponding to the first chamber of gear 1 and gear 2, is first identified. The remaining communication area are obtained by applying a circumferential shift equal to the pitch angle α_{pitch} :

$$A_{c\,i}(\varphi) = A_{c\,1}\left(\varphi - (i-1)\,\alpha_{pitch}\right) \qquad \textit{Eq. 74}$$
$$for\ i = 2, \dots, z$$

2.5. Connection between Pump Chambers and Delivery/Suction Control Volumes through Recesses in the Floating bearing blocks

On floating bearing blocks, recesses are present that introduce additional communication paths between the pump chambers and the delivery and suction control volumes. These recesses are important because they affect pump performance.

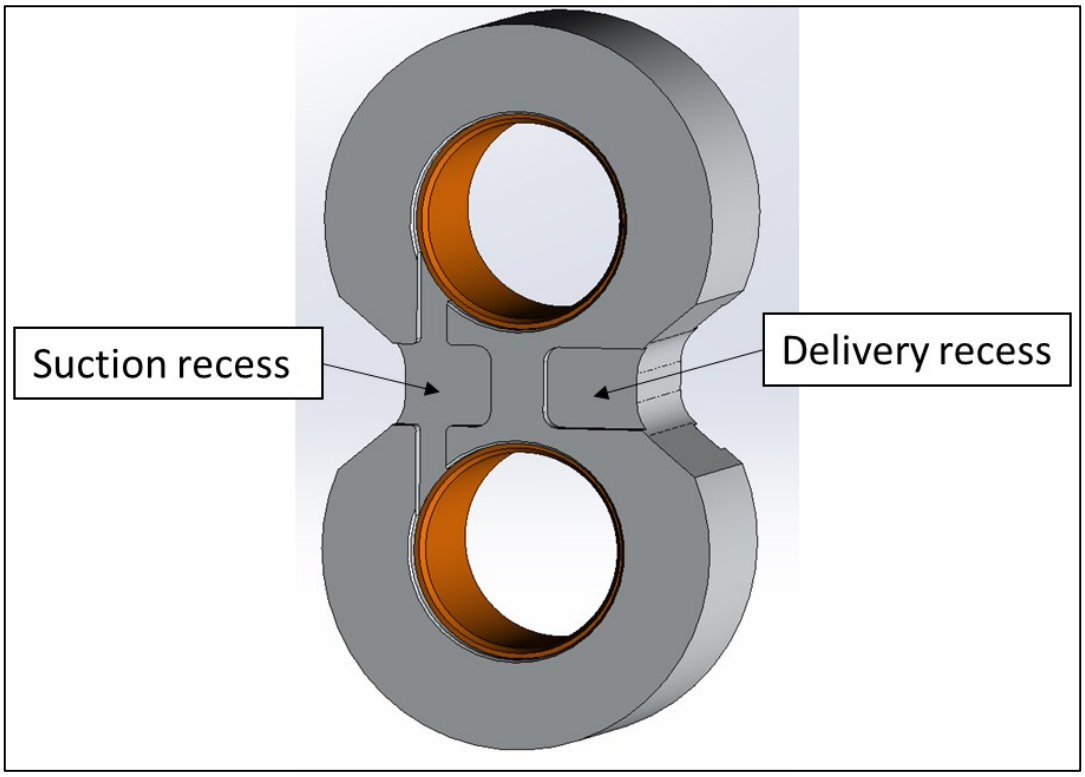

Figure 46 – Recess on the floating bearing bushing

As seen in Section 0, the chamber volumes undergo a decreasing phase and an increasing phase. During the decreasing phase, the pressure inside the chamber rises, while during the increasing phase, the pressure drops. Recesses on the floating bearing blocks are introduced to avoid or reduce pressure peaks or cavitation inside the chambers.

The recess on the delivery side creates a communication area between the pump chamber and the delivery port during the decreasing volume phase, helping to reduce pressure spikes. Conversely, the recess on the suction side allows communication between the pump chamber and the suction port during the increasing volume phase, mitigating aeration and cavitation phenomena. These recesses are also referred to as anti-noise recesses, as pressure peaks and cavitation contribute significantly to pump noise.

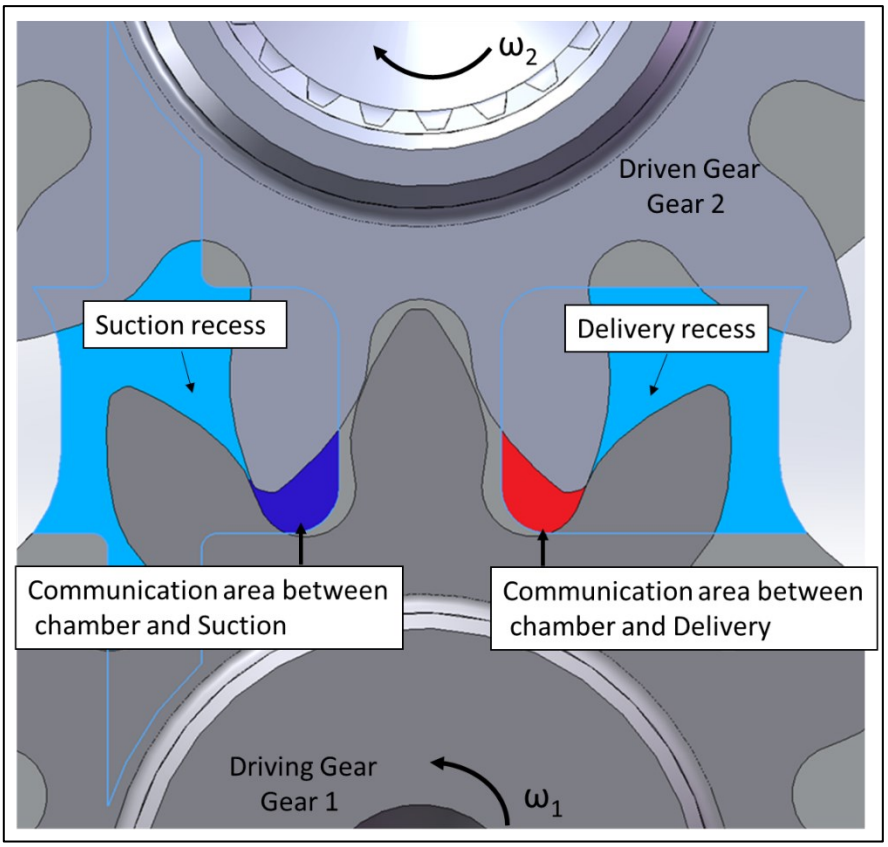

Figure 47 – Communication area through recesses in the floating bearing blocks

Different shapes of these recesses exist. In general, reducing the distance between the delivery and suction recesses increases the communication time between the chamber and the control volumes, thereby reducing pressure peaks, cavitation, and consequently pump noise. However, this can also introduce a bypass between the delivery and suction control volumes, reducing the volumetric efficiency of the pump.

Therefore, the design of these recesses is based on a compromise between noise reduction and volumetric efficiency.

These types of communication are included in the model, and the flow rate between the pump chambers and the suction/delivery control volumes is evaluated using the orifice equation previously introduced (Eq. 69), with $c_{q\,max} = 0.7$ and $\lambda_{crit} = 1000$.

The terms $Q_{1,i,jbD}$ and $Q_{1,i,jbS}$ are used to indicate the flow rates exchanged between the i-th chamber of the driving gear and the delivery and suction control volume, respectively, through the anti-noise recesses. Similarly, the terms $Q_{2,i,jbD}$ and $Q_{2,i,jbS}$ refer to the corresponding flow rates for the driven gear.

In the model, it is assumed that gear micromotions do not influence the communication area generated by the recesses in the floating bearing blocks. These areas are defined by considering the gears in their nominal working position (I_w).

A MATLAB app has been developed to calculate these areas and to generate a lookup table, which is then imported into the Simcenter Amesim model.

Figure 48 shows the communication area between the first chamber of the driving gear and the delivery (red curve) and suction (blue curve) control volumes, through the recesses in the floating bearing blocks. The shapes of these recesses are shown in Figure 46. A similar trend is observed for the chambers of the driven gear.

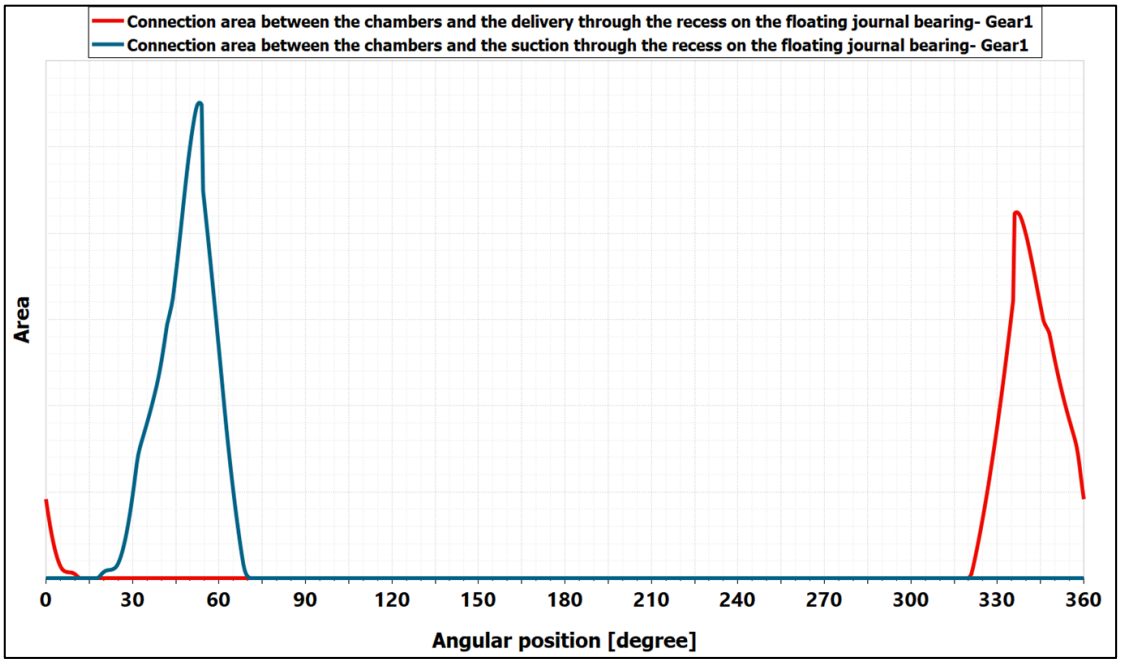

Figure 48 - Angular evolution of the communication area through recesses in the floating bearing blocks

In the model, the reference communication areas corresponding to the first chamber of the driving and driven gears are first identified.
The remaining communication areas are then obtained by applying a circumferential shift equal to the pitch angle α_{pitch}.

2.6. Volumetric leakages

In this section, the volumetric leakages considered in the model are analysed.

Volumetric leakages consist of flow rates exchanged between control volumes, which reduce the volumetric efficiency of the pump. These leakages are caused by clearances in the lubricated interfaces between the moving and fixed parts of the pump.

The main clearances considered in the model are:

- **Clearance between the gear tooth tips and the pump housing**
  This gap introduces a volumetric leakage between adjacent chambers of the same gear. The clearance height is not constant along the circumferential direction; due to gear micromotions, the distance between the tooth tip and the housing increases from the suction side to the delivery side.
  The height of this gap is influenced by the pump's operating conditions.
- **Lateral clearance between the gear faces and the floating bearing blocks**
  In the model, the volumetric leakages caused by this gap are represented as:
  - flow rate exchange between adjacent chambers of the same gear,
  - flow rate exchange between the chambers and the drain,
  - flow rate exchange between the delivery and suction control volumes.

  The model assumes a constant lateral gap height, which is defined by the user and does not vary with pump operating conditions.
- **Clearance between the tooth flanks in the meshing zone**
  Gear pumps assembled with a single contact point between gears exhibit backlash between the flanks of the teeth in the meshing zone. In the model, this volumetric leakage is represented as a flow rate exchanged between the i -th chamber of the driving gear and the $(i-1)$th chamber of the driven gear.

2.6.1. Volumetric Leakages Through Clearance Between Gear Tooth Tips and Pump Housing

In the model, the distance between the tooth tip and the housing is not constant along the circumferential direction; instead, it increases from the suction side to the delivery side. This is a consequence of gear micromotions caused by pressure and contact forces that push the gear towards the suction port, as well as wear on the pump housing resulting from the run-in process, which is accounted for in the model (this aspect will be analysed in a dedicated section).

The leakage flow between adjacent chambers of the same gear is modelled assuming laminar flow, due to the small size of the clearance.

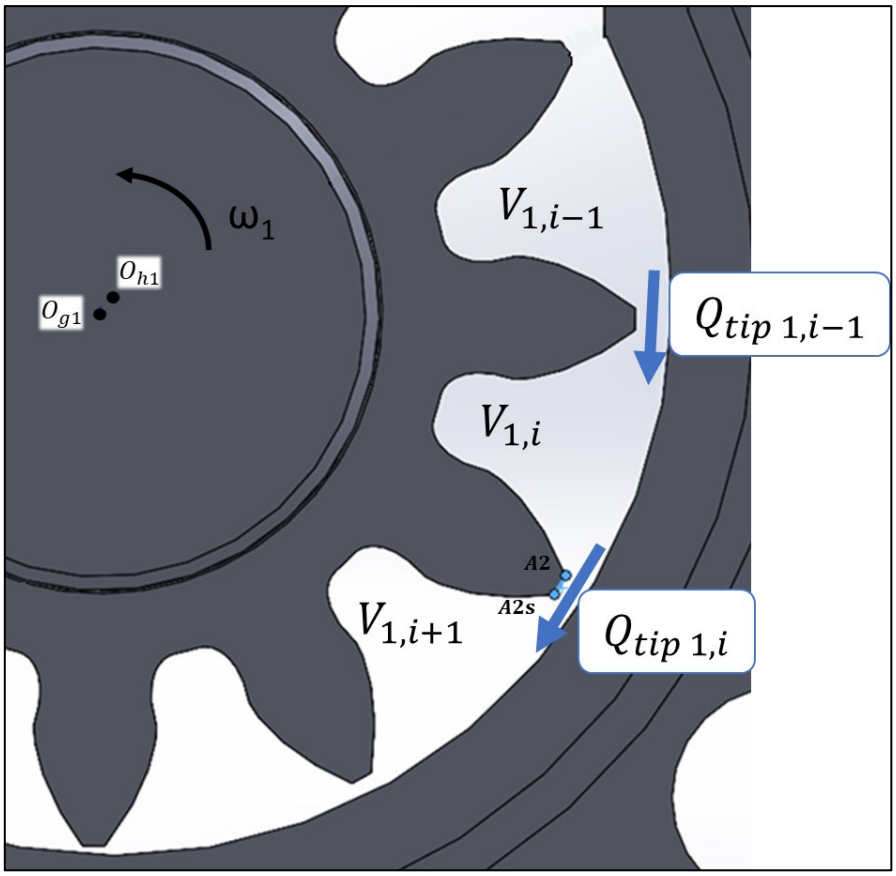

Figure 49 - Leakage Through Gear Tooth Tip Clearance

The flow rate between the i -th and $(i+1)$ -th chambers of the driving (j=1) or driven (j=2) gear through the tooth tip gap is defined as [21]:

$$Q_{tip\ j,i} = \frac{L_{axis}\ h_i^3 \Delta p}{12\ l_{tip}\ \mu}\frac{\rho}{\rho(0)} - \frac{r_e\ \omega_j\ h\ L_{axis}}{2}\frac{\rho}{\rho(0)} \qquad \textit{Eq. 75}$$

Where:

- $Q_{tip\ j,i}$ is the flow rate, with $Q_{tip\ j,i} > 0$ if the flow is from $V_{j,i+1}$ to $V_{j,i}$, and $Q_{tip\ j,i} < 0$ otherwise.
- L_{axis} is the axial length of the gear.
- h_i is the height of the gap. Since the gap height varies along the tooth tip, h is defined as the average between the gap height at the beginning of the tooth tip (h_{start}) and at the end (h_{end}). The tip gap is approximated as a rectangular gap of constant height, where $h_i = \frac{h_{start}+h_{end}}{2}$. The height values are defined in the reference systems O_{1g} for the driving gear and O_{2g} for driven gear (see Figure 50 and Figure 51).
  With reference to the points defined in Figure 26:
  - When the tooth tip is exposed to the pump housing, h_{start} is defined at point $A2$ for the driving gear and point $A4$ for the driven gear (see Figure 50).

- Correspondingly, h_{end} is defined at point $A2s$ for the driving gear and point $A4s$ for the driven gear.

When the tooth tip is near the delivery zone, h_{start} is defined at point $P1_D$ for the driving gear and $P2_D$ for the driven gear (see Figure 51).
Conversely, when the tooth tip is near the suction zone, h_{end} i is defined at point $P1_S$ for the driving gear and $P2_S$, for the driven gear.

- $\Delta p = p_{j,i+1} - p_{j,i}$ is the pressure difference between adjacent chambers.
- l_{tip} is the length of the gap. For most angular positions, this length corresponds to the tooth tip thickness (see Figure 50). However, near the suction and delivery zones, the gap length varies (see Figure 26 and Figure 51):
  - Near the suction side, the gap length is the distance between the point P_1S and A2 for the driving gear, and P_2S and A4 for the driven gear.
  - Near the delivery side, the gap length is the distance between the point P_1D and A2s for the driving gear, and P_2D and A4s for the driven gear.
- μ is the dynamic viscosity of the oil at the mean pressure.
- r_e is the gear external radius.
- ω_j is the gear angular velocity of the gear, where j=1 for the driving gear and j=2 for the driven gear.
- $\rho = \rho\left(\frac{p_{j,i}+p_{j,i+1}}{2}\right)$ is the oil density at the mean pressure.
- $\rho(0)$ is the oil density at 0 bar gauge pressure.

The first term of Eq. 75 represents the Poiseuille flow, the laminar flow caused by the pressure gradient between the chambers, while the second term represents the Couette flow, the laminar flow generated by the relative motion between the gear tooth tips and the pump housing.

With reference to Figure 49, the total volumetric leakage through the tooth tips gaps of the chamber $V_{1,i}$ (driving gear) is expressed as $Q_{tip\ 1,i} - Q_{tip\ 1,i-1}$. At the same time, the chamber $V_{1,i}$ exchanges oil with the chamber $V_{1,i+1}$ and $V_{1,i-1}$. The same considerations apply to the chambers of the driven gear.

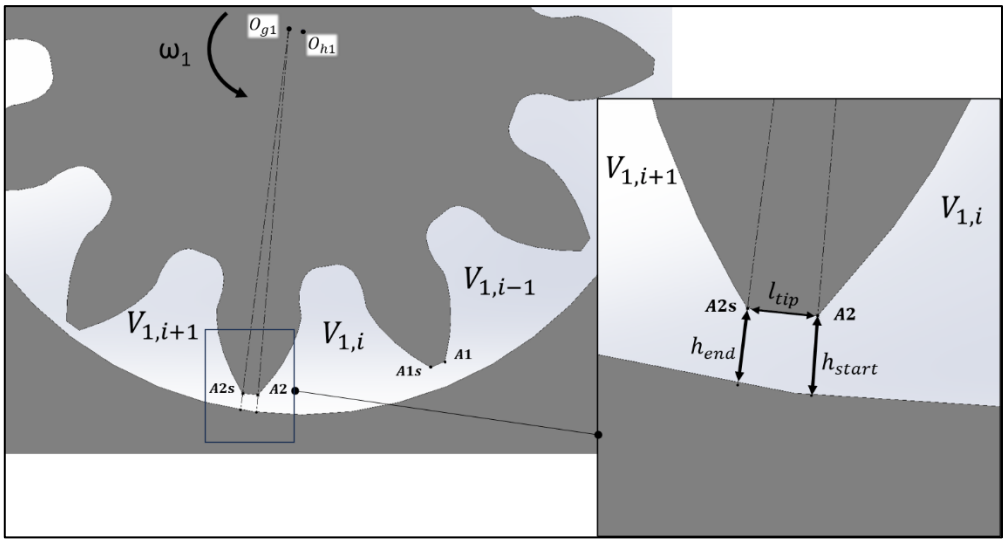

Figure 50 – Length and height of the tooth tip gap when the tip is exposed to the pump housing

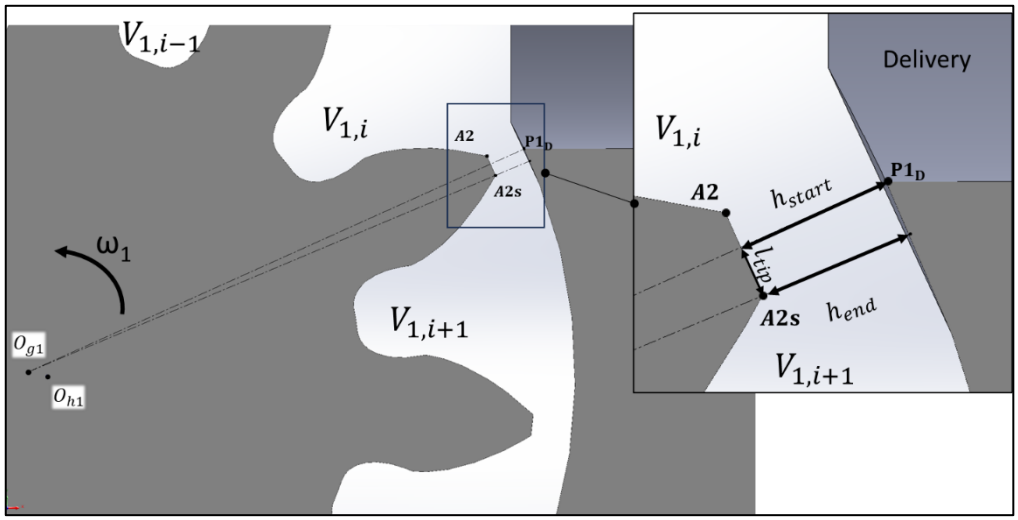

Figure 51 – Length and height of the tooth tip gap near the delivery port

In the model, a minimum threshold is imposed on the gap height: if the height is smaller than 1e-6 m, it is considered to be zero.
Considering the first term of Eq. 75, the denominator includes the gap length l_{tip}. As shown in Figure 51 near the delivery and suction zones this length decreases, which consequently increases the Poiseuille flow. In the case of very small gap lengths, the Poiseuille flow would theoretically tend towards infinity
To avoid this issue, when $l_{tip} \leq 0.2\ l_{tip\ max}$, the gap length is set to $0.2\ l_{tip\ max}$, where $l_{tip\ max}$ is the maximum value of the tooth tip gap length, which occurs when the tip is fully exposed to the pump housing.

Eq. 75 can be rewritten by grouping the terms that depend only on the pump geometry and not on the operating conditions:

$$Q_{tip\ j,i} = \frac{\rho}{\rho(0)} \frac{\Delta p}{\mu} fhtip_{p\ j,i} - \frac{\rho}{\rho(0)} \omega_j\, fhtip_{v\ j,i} \qquad \textit{Eq. 76}$$

The term $fhtip_{p\ j,i}$ contains the geometric contributions that influence the volumetric leakage caused by the pressure gradient, while $fhtip_{v\ j,i}$ contains the geometric contributions that affect the leakage caused by the relative motion between the gear tooth and the pump housing.

$$fhtip_{p\ j,i} = \frac{L_{axis}\, h^3}{12\, l_{tip}} \qquad \textit{Eq. 77}$$

$$fhtip_{v\ j,i} = \frac{r_e\, h\, L_{axis}}{2}$$

In the model, the reference geometric functions $fhtip_{p\ 1,1}$, $fhtip_{p\ 2,1}$, $fhtip_{v\ 1,1}$ and $fhtip_{v\ 2,1}$ corresponding to the first chambers of gear 1 and gear 2, respectively, are first identified. The remaining geometric function are obtained by applying a circumferential shift equal to the pitch angle α_{pitch} :

$$fhtip_{p\ 1,i}\ (\varphi) = fhtip_{p\ 1,1}\ \left(\varphi - (i-1)\ \alpha_{pitch}\right)$$

$$fhtip_{p\ 2,i}\ (\varphi) = fhtip_{p\ 2,1}\ \left(\varphi - (i-1)\ \alpha_{pitch}\right)$$

$$fhtip_{v\ 1,i}\ (\varphi) = fhtip_{v\ 1,1}\ \left(\varphi - (i-1)\ \alpha_{pitch}\right) \qquad \textit{Eq. 78}$$

$$fhtip_{v\ 2,i}\ (\varphi) = fhtip_{v\ 2,1}\ \left(\varphi - (i-1)\ \alpha_{pitch}\right)$$

$$for\ i = 2, \dots, z$$

2.6.2. Volumetric Leakages Through the Lateral Clearances Between Adjacent Chambers

The clearance between the gear faces and the floating bearing blocks is referred to in this work as lateral clearances or lateral gaps.
These gaps are illustrated in Figure 52 where their dimensions have been exaggerated for clarity.

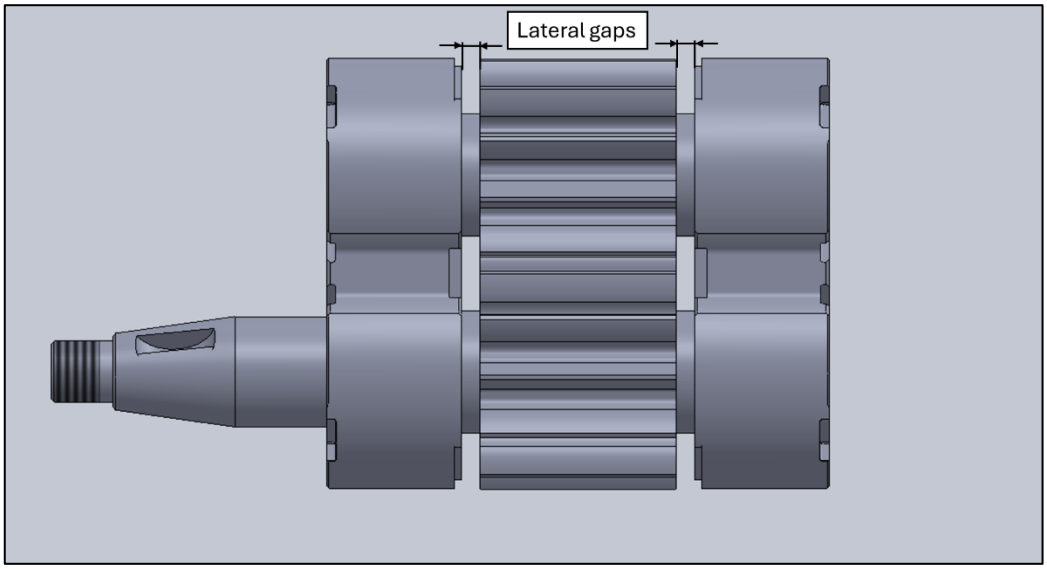

Figure 52 – Lateral gaps

The floating bearing blocks are allowed to move in the axial direction due to the pressure forces acting on them. On the gear-side face of each bearing blocks, pressure forces are applied that tend to push the bearing away from the gears. These forces are generated by the pressurised fluid inside the chambers (Figure 53.(b)), the pressure distribution within the lateral clearance (Figure 53.(c)), and the delivery and suction pressures acting on the anti-noise recesses of the bearing bushings (Figure 53.(a)).

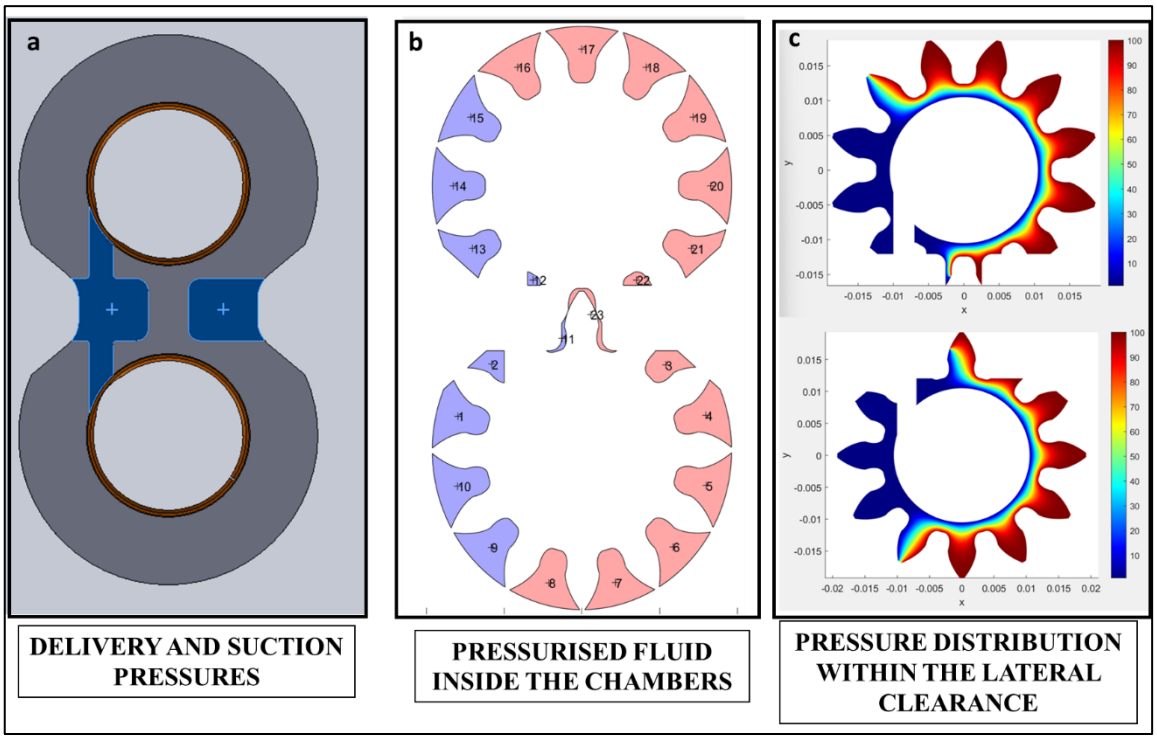

Figure 53 – Forces contributing to push the floating bearing bushing away from the gears

On the opposite side of the floating bearing blocks, balancing forces are applied. These are generated by applying the delivery and suction pressures to predefined balancing surfaces (see Figure 54). These surfaces are designed so that the resulting balancing force is greater than the force pushing the bearing away, ensuring that the bearing bushings is pressed towards the gears. This allows the formation of small clearances, which improve the pump's volumetric efficiency.

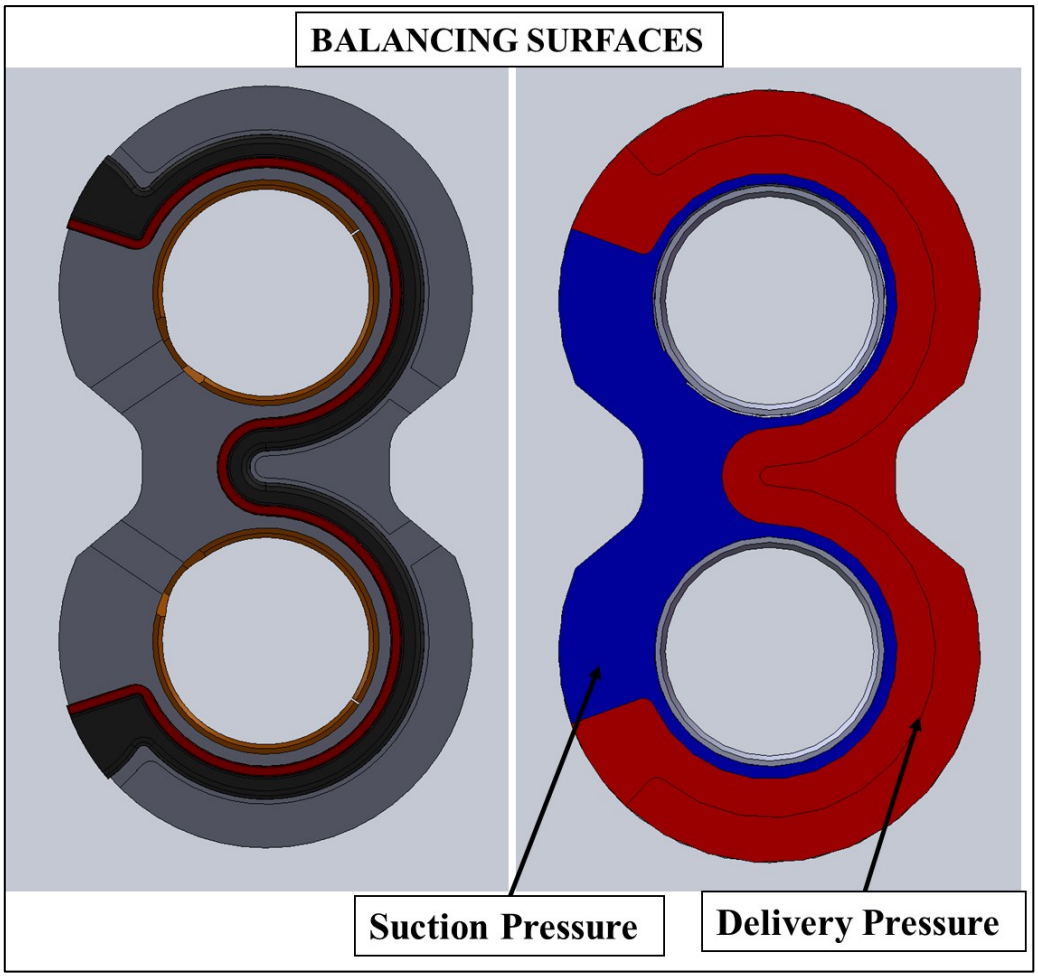

Figure 54 – Balancing surfaces

A lubrication interface is maintained between the gears faces and the bearing blocks. Direct contact between the gears and bearing blocks must be avoided: although it would reduce volumetric leakage, it would also decrease the hydro-mechanical efficiency of the pump.

During pump operation, the floating bearing blocks exhibit a slight inclination due to the different application points of the balancing and pushing forces. As a result, the height of the lateral clearances is not constant.

Assuming steady-state operating conditions and constant delivery and suction pressures, the balancing forces remain constant both in magnitude and in their point of application. In contrast, the pushing forces vary with the angular position of the gear - both in magnitude and in point of application - with a periodicity of $\frac{1}{\omega z}$. Consequently, the axial position and inclination of the bearing blocks change as the gears rotate.

In the present model, however, the lateral clearance height is assumed to be constant. This value is defined by the user and does not change with operating conditions.

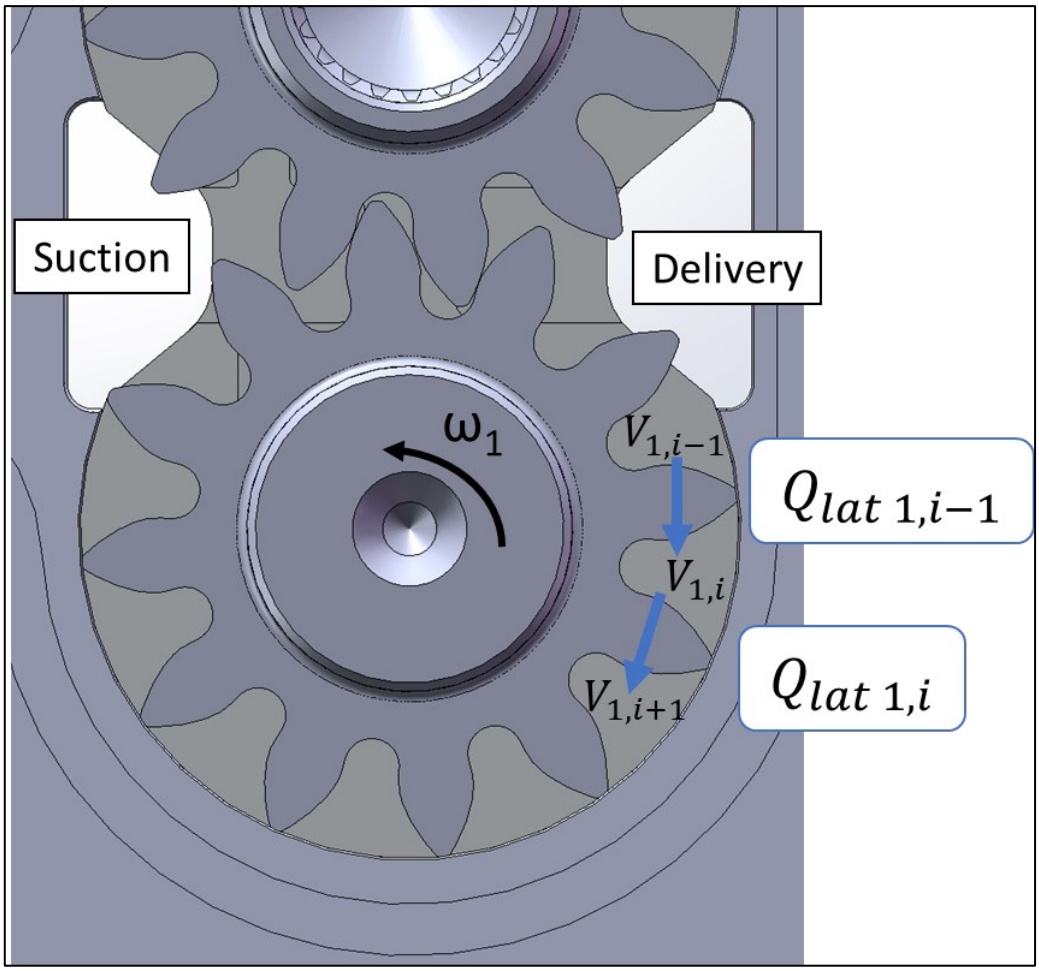

Figure 55 – Lateral volumetric leakages between adjacent chambers

This section analyses the modelling of volumetric leakage between adjacent chambers of the same gear.
Before addressing this, the laminar flow through a clearance between two parallel planes connecting two control volumes, V1 and V2, is introduced [22]:

$$Q = \frac{b\ h^3 \Delta p}{12\ \mu\ l} - \frac{V}{2} bh \qquad \textit{Eq. 79}$$

Where:

- Q is the flow rate, with Q>0 if the flow is from $V2$ to $V1$, and Q<0 otherwise.
- b is the width of the clearance.
- h is the hight of the clearance.
- $\Delta p = p2 - p1$, pressure difference between the control volume V2 and V1.
- μ is the dynamic viscosity of the oil.
- l is the length of the clearance.
- V is the relative velocity between the two planes.

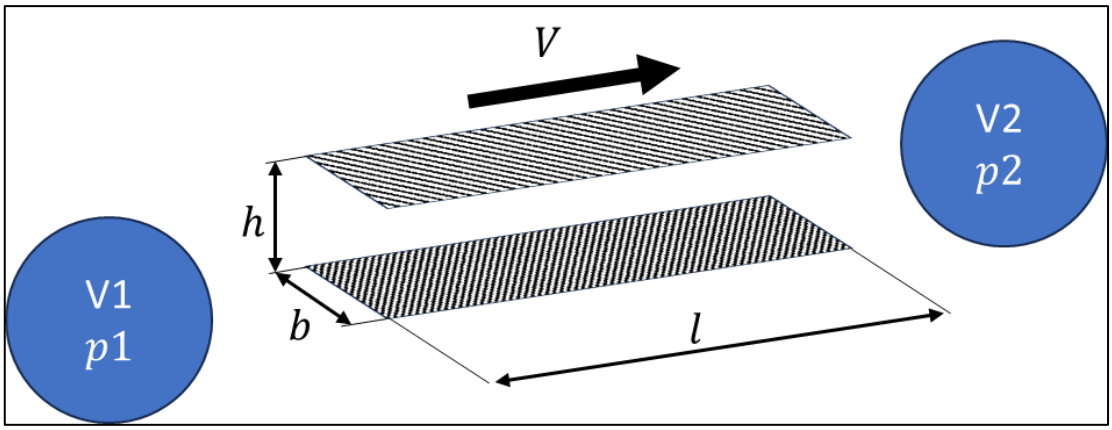

Figure 56 – Laminar flow rate between two parallel plates

As shown in Figure 55, the shape of the lateral clearance connecting adjacent chambers is defined by the gear tooth geometry.
In the model, this geometry is approximated as a set of rectangular clearances through which laminar flow occurs.
The flow rate between the i -th and $(i+1)$ -th chambers of the driving (j=1) or driven (j=2) gear through the lateral gap is calculated by summing the individual contributions given by Eq. 79 for each rectangular segment (see Figure 57):

$$Q_{lat\ j,i} = 2\left(\frac{\rho}{\rho(0)}\frac{{h_{lat}}^3 \Delta p}{12\,\mu}\sum_{k=1}^{n_{tr}+n_{ev}-2}\frac{b_k}{l_k} - \frac{\rho}{\rho(0)}\frac{\omega_j\, h_{lat}}{2}\sum_{k=1}^{n_{tr}+n_{ev}-2} r_k\, b_k\right) \qquad \textit{Eq. 80}$$

Where:

- $Q_{lat\ j,i}$ is the flow rate, with $Q_{lat\ j,i} > 0$ if the flow is from $V_{j,i+1}$ to $V_{j,i}$, and $Q_{lat\ j,i} < 0$ otherwise.
- h_{lat} is the height of lateral clearances.
- $\Delta p = p_{j,i+1} - p_{j,i}$ is the pressure difference between adjacent chambers.
- μ is the dynamic viscosity of the oil at the mean pressure.
- ω_j is the gear angular velocity of the gear, where j=1 for the diving gear and j=2 driven gear.
- b_k is the width of the k-th rectangular section approximating the lateral gap.
- l_k is the length of the k-th rectangular section.
- r_k is the radial distance from the gear centre (O_{1g} or O_{2g}) to the central plane (parallel to l_k) of the k-th rectangular section.
- $\rho = \rho\left(\frac{p_{j,i}+p_{j,i+1}}{2}\right)$ is the oil density at the mean pressure.
- $\rho(0)$ is the oil density at 0 bar gauge pressure.
- The multiplication factor 2 is used to account for the volumetric leakage on both faces of the gears.

In the model, the shape of the lateral clearance extends from the beginning of the trochoidal curve to the tooth tip and is assumed to be identical for all chambers. (see Figure 57).

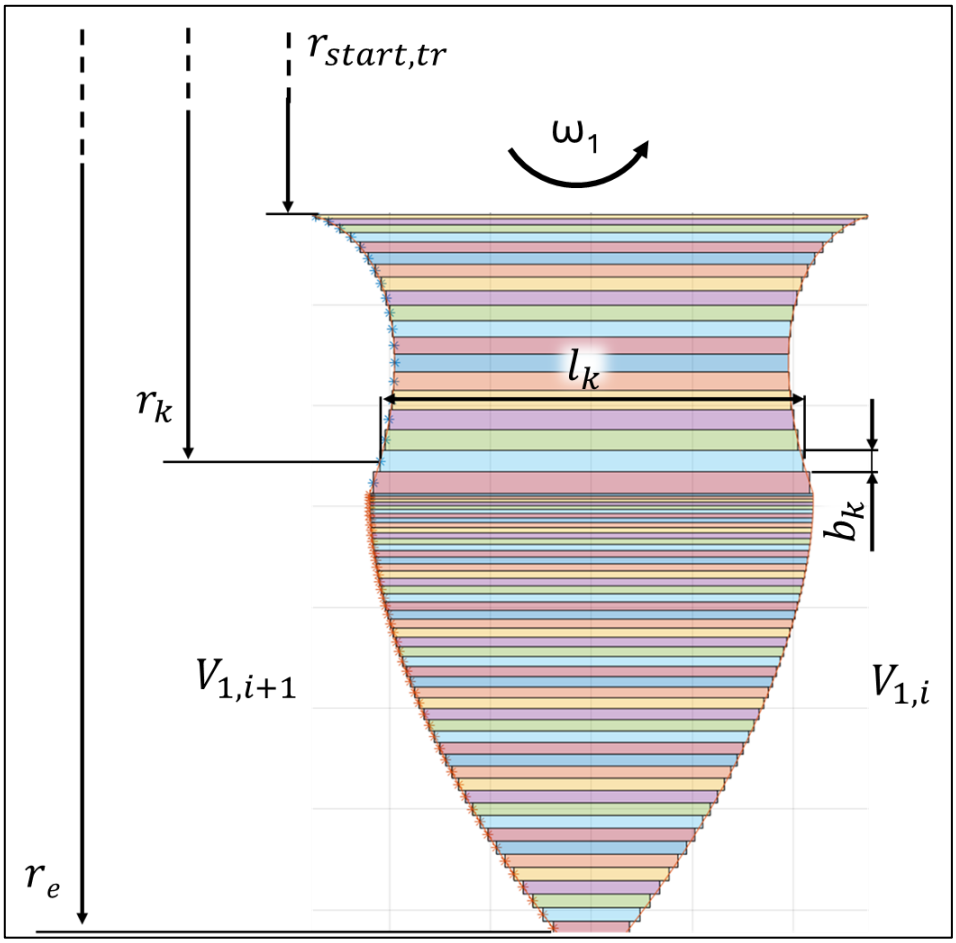

Figure 57 – Subdivision of the lateral clearance in rectangular segments

To define the dimensions of the rectangular segments, we refer to the vectors $\boldsymbol{x_{tooth,left}}$ and $\boldsymbol{y_{tooth,left}}$, introduced in Eq. 50, which define the left profile of the gear tooth

The dimensions of the k-th rectangular segment are defined as:

$$b_k = y_{tooth,left}^{n_r+k} - y_{tooth,left}^{n_r-1+k}$$

$$r_k = \frac{y_{tooth,left}^{n_r+k} + y_{tooth,left}^{n_r-1+k}}{2}$$

$$l_k = 2\, r_k \tan\left(-\frac{x_{tooth,left}^{n_r+k} + x_{tooth,left}^{n_r-1+k}}{y_{tooth,left}^{n_r+k} + y_{tooth,left}^{n_r-1+k}}\right) \qquad \textit{Eq. 81}$$

$$for\ k = 1, \dots, n_{tr} + n_{ev} - 2$$

The radius defining the start of the lateral gap is:

$$r_{start,tr} = \sqrt{\left(x_{tooth,left}^{n_r}\right)^2 + \left(y_{tooth,left}^{n_r}\right)^2} \qquad \textit{Eq. 82}$$

The number of rectangular segments used to approximate the lateral gap is $n_{tr} + n_{ev} - 2$.

Eq. 80 can be rewritten by grouping the terms that depend only on the pump geometry and not on the operating conditions:

$$Q_{lat\ j,i} = 2\left(\frac{\rho}{\rho(0)}\frac{\Delta p}{\mu} fhl_{p\ j,i} - \frac{\rho}{\rho(0)}\omega_j\, fhl_{v\ j,i}\right) \qquad \textit{Eq. 83}$$

The term $fhl_{p\ j,i}$ contains the geometric contributions that influence the volumetric leakage caused by the pressure gradient, while $fhl_{v\ j,i}$ contains the geometric contributions that affect the leakage caused by the relative motion between the gear tooth and the pump housing.

$$fhl_{p\ j,i} = \frac{{h_{lat}}^3}{12} \sum_{k=1}^{n_{tr}+n_{ev}-2} \frac{b_k}{l_k}$$
$$fhl_{v\ j,i} = \frac{h_{lat}}{2} \sum_{k=1}^{n_{tr}+n_{ev}-2} r_k\, b_k \qquad \textit{Eq. 84}$$

In the model, volumetric leakage through the lateral gap between adjacent chambers is considered only when both chambers are at their maximum volume.
Therefore, in the meshing zone—where the chamber volume is reduced—this type of leakage is not considered.
This condition is implemented by setting $fhl_{p\ j,i}$ and $fhl_{v\ j,i}$ o zero whenever the involved chambers are not at their maximum volume (see Figure 58).

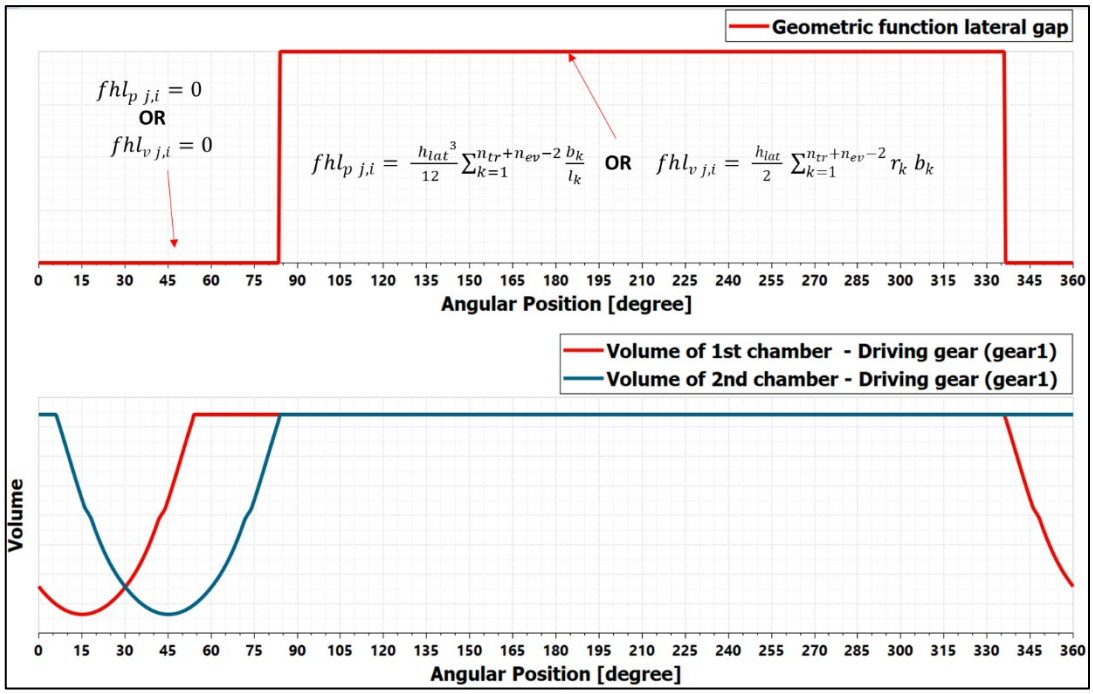

Figure 58 - $fhl_{p\ j,i}$ and $fhl_{v\ j,i}$

In the model, the reference geometric functions $fhl_{p\ 1,1}$, $fhl_{p\ 2,1}$, $fhl_{v\ 1,1}$ and $fhl_{v\ 2,1}$ corresponding to the first chambers of gear 1 and gear 2, respectively, are first identified. The remaining geometric function are obtained by applying a circumferential shift equal to the pitch angle α_{pitch} :

$$fhl_{p\ 1,i}\ (\varphi) = fhl_{p\ 1,1}\ \left(\varphi - (i-1)\ \alpha_{pitch}\right)$$

$$fhl_{p\ 2,i}\ (\varphi) = fhl_{p\ 2,1}\ \left(\varphi - (i-1)\ \alpha_{pitch}\right)$$

$$fhl_{v\ 1,i}\ (\varphi) = fhl_{v\ 1,1}\ \left(\varphi - (i-1)\ \alpha_{pitch}\right) \qquad \textit{Eq. 85}$$

$$fhl_{v\ 2,i}\ (\varphi) = fhl_{v\ 2,1}\ \left(\varphi - (i-1)\ \alpha_{pitch}\right)$$

$$for\ i = 2, \dots, z$$

2.6.3. Volumetric Leakages Through the Lateral Clearances Between Chambers and Drain

The lateral gap introduces a connection between the pump chambers and the drain. Suction pressure is applied to the faces of the bushes via dedicated channels that directly connect to the anti-noise recesses on the gear faces and to the balancing surfaces, in order to ensure a proper oil supply for the lubrication of the journal bearings.
In the model of the unidirectional gear pump under study, the drain zone corresponds to the suction control volume.

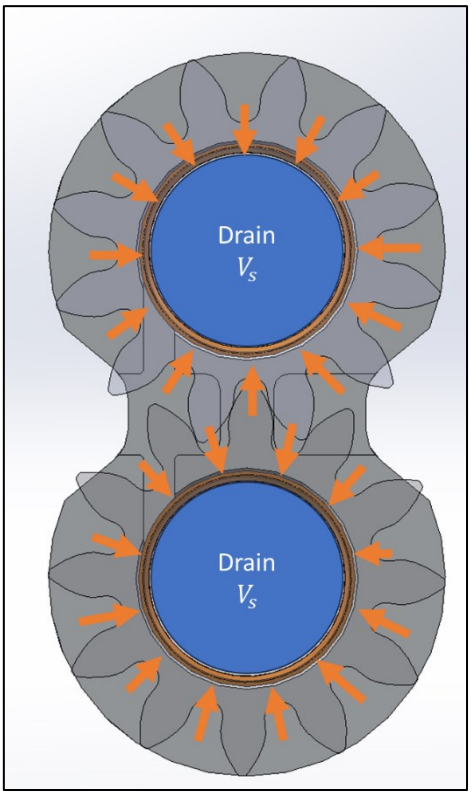

Figure 59 – Volumetric Leakage Through the Lateral Gap to the Drain

These volumetric leakages are modelled by considering a connection between the pump chambers and the suction control volume through a rectangular gap, defined by:

- Height:h_{lat}.
- Length: $r_r - r_{hole\ jb}$.
- Width: $\frac{2\,\pi\,r_r}{z}\ 0.4$.

The flow rate, assuming a laminar flow, is given by:

$$Q_{drain\ j,i} = 2\left(\frac{h_l^3}{12\,\mu}\,\frac{1}{(r_r - r_{hole\ jb})}\,\frac{2\,\pi\,r_r}{z}\,0.4\,\Delta p\,\frac{\rho}{\rho(0)}\right) \qquad \textit{Eq. 86}$$

Where:

- $Q_{drain\ j,i}$ is the flow rate, with $Q_{drain\ j,i} > 0$ if the flow is from V_S to $V_{j,i}$, and $Q_{drain\ j,i} < 0$ otherwise.
- h_{lat} is the height of lateral clearances.
- $\Delta p = p_S - p_{j,i}$ is the pressure difference between the suction control volume and the pump chamber.
- $\rho = \rho\left(\frac{p_{j,i}+p_S}{2}\right)$ is the oil density at the mean pressure.
- $\rho(0)$ is the oil density at 0 bar gauge pressure.
- μ is the dynamic viscosity of the oil at the mean pressure.

- r_r is the root radius of the gears.
- $r_{hole\ jb}$ is the radius that defines the beginning of the drain lateral gap.
- z is the number of gear teeth.

The multiplication factor 2 accounts for leakage from both faces of the gear.
The factor 0.4 is introduced to reduce the width of one tooth at the root radius ($\frac{2\,\pi\,r_r}{z}$) to better approximate the actual chamber width at that radius (see Figure 60).
The value of 0.4 is proposed by the Simcenter Amesim documentation for their proprietary gear pump model (model name: HCDEGP0**)**

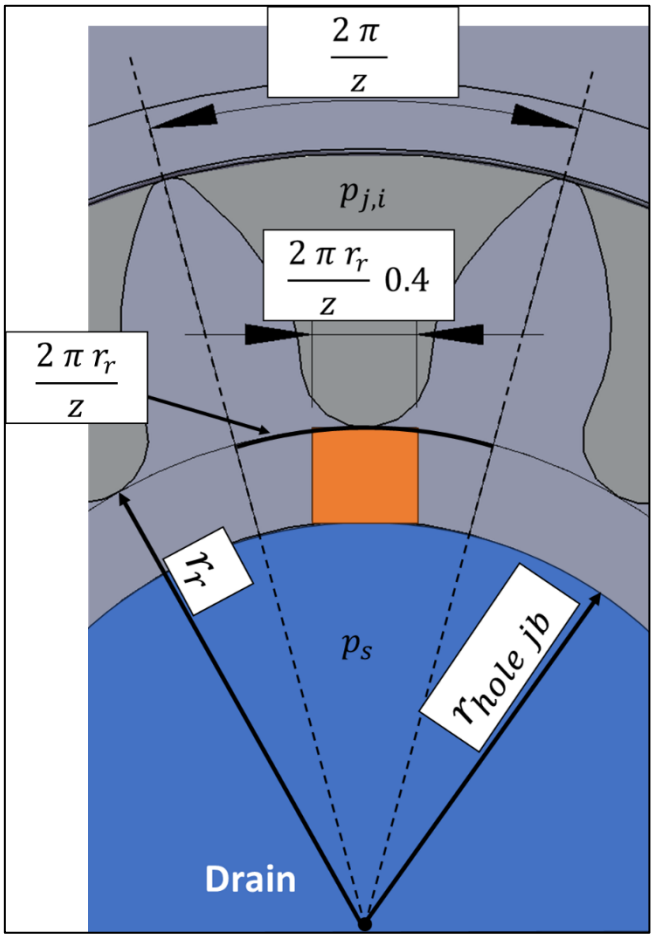

Figure 60 – Geometry of the Lateral Gap Connecting the Chamber to the Drain

The chambers are always considered to be in communication with the drain through the lateral clearance described above, including the area near the channel that connects the bushing to the suction anti-noise recesses

2.6.4. Volumetric Leakages Through the Lateral Clearances Between Suction and Delivery Control Volumes

In the meshing zone, volumetric leakage between adjacent chambers through the lateral gaps is not considered, as it would affect the estimation of the pressure inside the pump chambers.
However, a direct connection between the suction and delivery control volumes is included in the model for this zone, in order to improve the accuracy of the volumetric efficiency prediction.
This connection is modelled as a rectangular clearance, where laminar flow is assumed.
The flow rate is given by:

$$Q_{lat\ SD} = 2\left(\frac{b_{lat\ SD}\ h_{lat}^3\ \Delta p}{12\ l_{lat\ SD}\ \mu}\frac{\rho}{\rho(0)}\right) \qquad \textit{Eq. 87}$$

Where:

- $Q_{lat\ SD}$ is the flow rate, with $Q_{lat\ SD} > 0$ if the flow is from the suction control volume V_S to the delivery control volume V_D, and $Q_{lat\ SD} < 0$ otherwise.
- h_{lat} is the height of lateral clearances.
- $\Delta p = p_S - p_D$ is the pressure difference between suction and delivery.
- $\rho = \rho\left(\frac{p_D + p_S}{2}\right)$ is the oil density at the mean pressure.
- $\rho(0)$ is the oil density at 0 bar gauge pressure.
- μ is the dynamic viscosity of the oil at the mean pressure.
- $b_{lat\ SD}$ is the gap width.
- $l_{lat\ SD}$ is the gap length.

The multiplication factor 2 accounts for leakage from both faces of the gear.

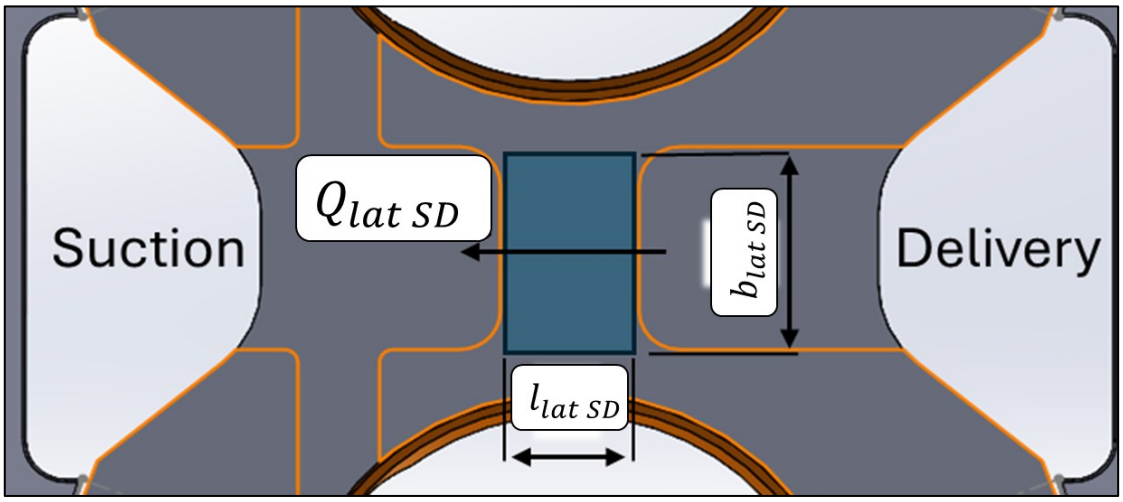

Figure 61 – Volumetric leakage between suction and delivery through the lateral gap in meshing zone

In the model, the geometry of the clearance is assumed to be constant and independent of the angular position of the gears.
In reality, however, the geometry of the lateral gaps changes with gear rotation. This assumption allows for a good estimation of the average volumetric leakages over one full revolution.

2.6.5. Volumetric Leakage Through Tooth Flank Clearances in the Meshing Zone Between Driving and Driven Gear Chambers

The connection between the *i*-th chamber of the driving gear and the (*i*-1)-th chamber of the driven gear is a direct consequence of the single-contact gear assembly, achieved by selecting an appropriate centre distance between the gears. This connection occurs through the flank clearances in the meshing zone, as shown in Figure 62.

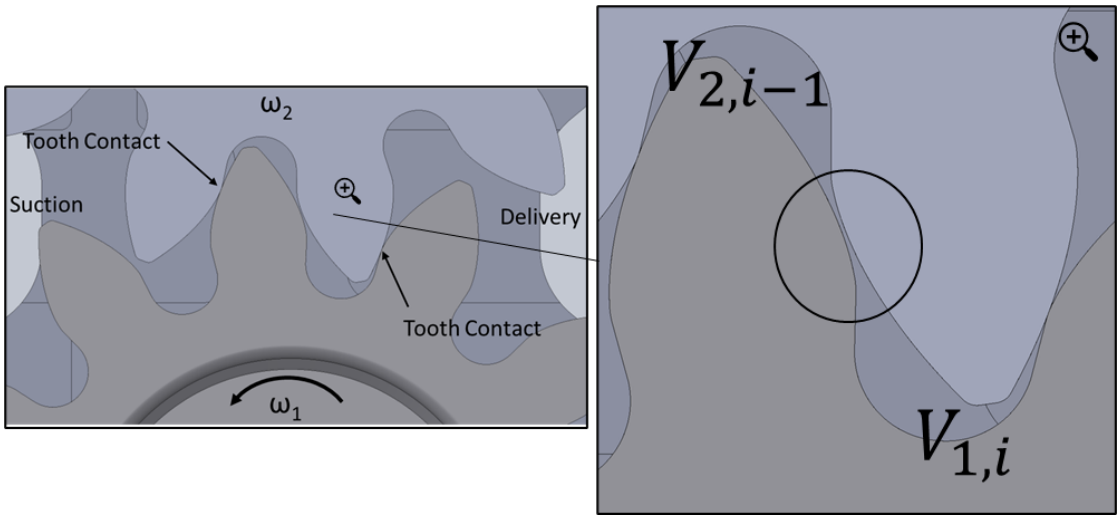

Figure 62 - Clearance between the tooth flanks in the meshing zone

The trend of the flank clearance height between the *i*-th chamber of the driving gear and the (*i*-1)-th chamber of the driven gear is shown in Figure 63:

- **Position 1:** Chambers $V_{1,i}$ and $V_{2,i-1}$ are connected through the flank clearance. For most of the meshing interval, the height of the gap remains constant.
- **Position 2:** The chambers are approaching the end of the meshing zone, and the gap height increases until it reaches a maximum value.
- **Position 3:** Chamber $V_{1,i}$ terminates its connection with $V_{2,i-1}$ and establishes a connection with the suction control volume V_S.
- **Position 4:** The chambers are near the entrance of the meshing zone. $V_{1,i}$ and $V_{2,i-1}$ are not connected to each other, but are both connected to the delivery control volume V_D.

- **Position 5:** Chamber $V_{2,i-1}$ ends its communication with the delivery control volume V_D. and begins to interact with chamber $V_{1,i}$. The flank clearance height starts from a maximum value and decreases with gear rotation until reaching a constant value, returning to a condition similar to Position 1.

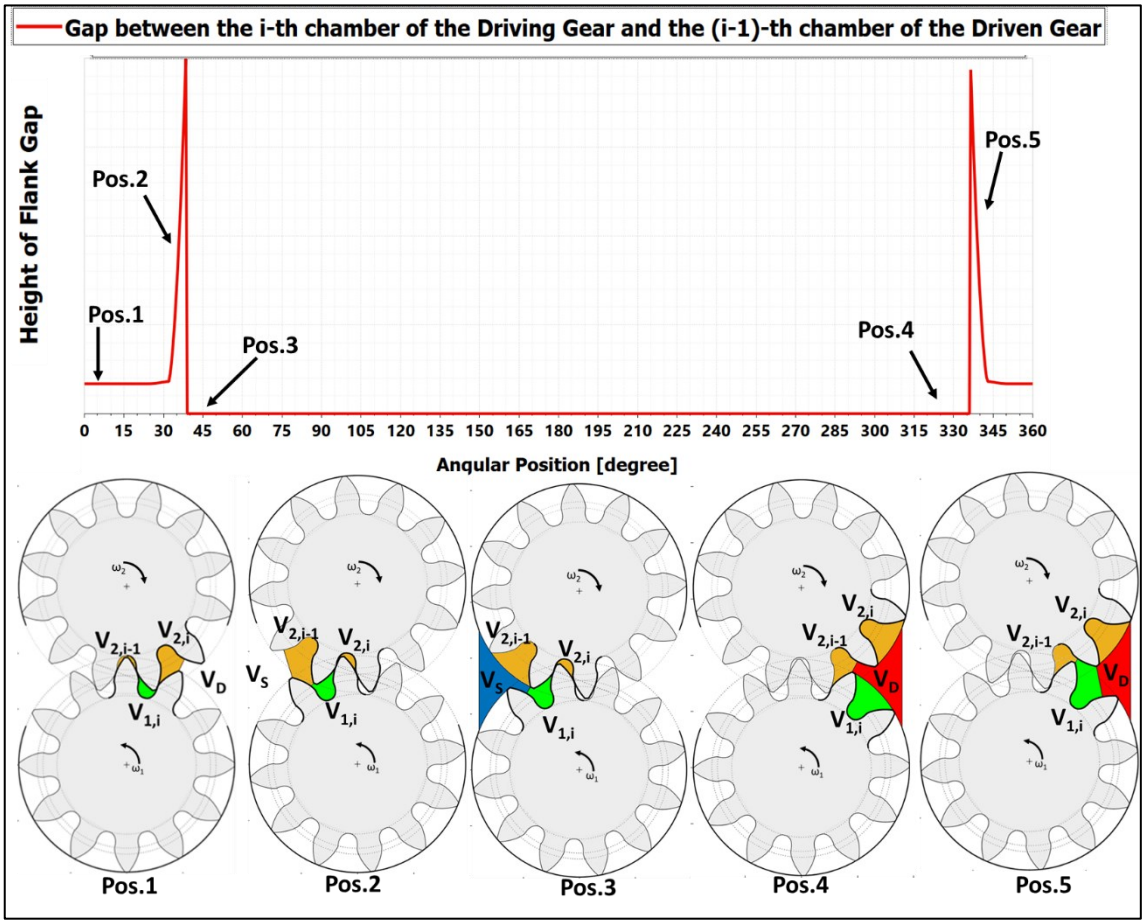

Figure 63 – The Trend of the Tooth Flank Clearance Height

The flow rate through the flank clearance is modelled in two ways:

1. **Formulation 1** – The flow rate is computed using the formulation proposed by R. Rituraj and A. Vacca, which describes laminar flow between two curved surfaces.
2. **Formulation 2** – The flow rate is calculated using the laminar–turbulent orifice equation previously introduced (see Eq. 69).

These two approaches are analysed in the following sections.

2.6.5.1. Tooth Flank Clearance Flow Rate - Formulation 1

In Formulation 1, the flow rate is calculated using the equation proposed by R. Rituraj and A. Vacca [23], which describes laminar flow between two curved surfaces - in this case, the tooth flanks.

The flow rate between the chambers $V_{1,i}$ and $V_{2,i-1}$,through the flank gap, is defined as :

$$Q_{flank\ i} = \frac{0.05\ L_{axis}\ h_{flank\ i}^{2.5}}{\mu\ R_{eq}^{0.5}}\ \Delta p\ \frac{\rho}{\rho(0)} \qquad \textit{Eq. 88}$$

Where:

- $Q_{flank\ i}$ is the flow rate exchanged between the driving pump chamber ($V_{1,i}$) and the driven pump chamber ($V_{2,i-1}$) .
- L_{axis} is the gear axial length.
- $h_{flank\ i}$ is the height of the flank gap.
- $\Delta p = p_{2,i-1} - p_{1,i}$ is the pressure difference between the pump chambers
- $\rho = \rho\left(\frac{p_{1,i}+p_{2,i-1}}{2}\right)$ is the oil density at the mean pressure.
- $\rho(0)$ is the oil density at 0 bar gauge pressure.
- $\mu = \mu\left(\frac{p_{1,i}+p_{2,i-1}}{2}\right)$ is the dynamic oil viscosity at the mean pressure.
- R_{eq} is the equivalent curvature radius of the gap, defined as :

$$\frac{1}{R_{eq}} = \frac{1}{R_1} + \frac{1}{R_2} \qquad \textit{Eq. 89}$$

  R_1 is radius of curvature of the driving gear tooth flank at the gap point corresponding to height $h_{flank\ i}$, while R_2 is radius of curvature of the driven gear tooth flank at the same point.

Eq. 88 is applicable under laminar flow conditions. However, the flank gap height must remain sufficiently small for the flow to remain laminar.

To account for this, a threshold value of the flank gap height, denoted $h_{flank\ min}$, is introduced to determine the appropriate flow formulation.

- If $h_{flank\ i} \leq h_{flank\ min}$ the laminar flow equation between two curved surfaces (Eq. 88) is used.
- If $h_{flank\ i} > h_{flank\ min}$, the laminar-turbulent orifice equation (Eq. 90) , as used in Formulation 2, is applied instead.

In the model, the threshold for the flank gap height, $h_{flank\ min}$, is defined based on the geometry of the gear pump. This threshold ensures that the laminar flow equation

between two curved surfaces (Eq. 88) is applied only within the angular range where the flank gap height remains approximately constant (see Figure 64).

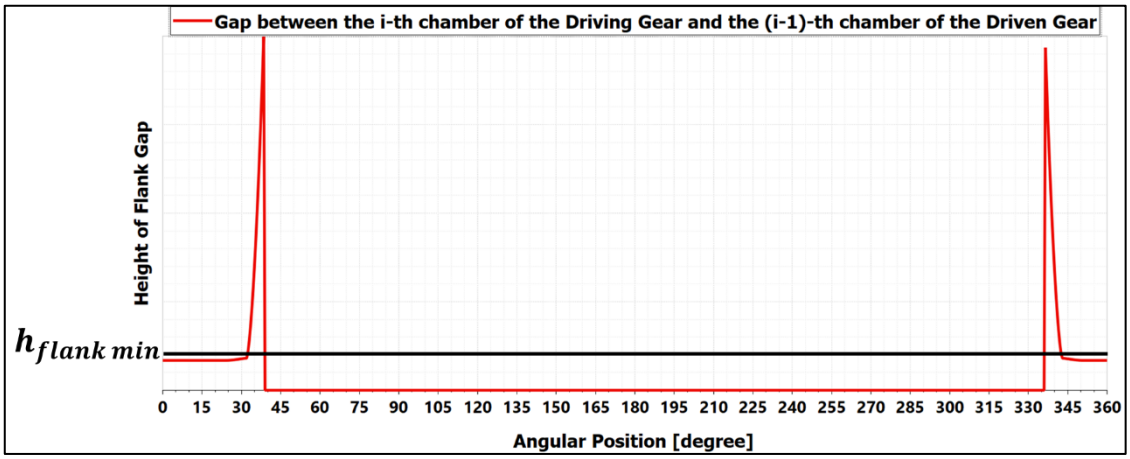

Figure 64 – Definition of the threshold for the flank gap height

2.6.5.2. Tooth Flank Clearance Flow Rate - Formulation 2

In Formulation 2, the flow rate through the flank gap is calculated using the laminar–turbulent orifice equation. By analysing Figure 63, it emerges that for most of the gear rotation within the meshing zone, the height of the flank gap remains constant and small, which satisfies the conditions for laminar flow. When the height deviates from this constant value and increases, the assumption of laminar flow no longer holds. The orifice equation remains applicable for both laminar and turbulent regimes, as the flow coefficient is defined according to the flow conditions (see Figure 44).

The flow rate between the chambers $V_{1,i}$ and $V_{2,i-1}$ is defined as :

$$Q_{flank\ i} = c_q\, A_{flank\ i} \sqrt{2 \frac{|\Delta p|}{\rho} \frac{\rho}{\rho(0)}}\ sign(\Delta p) \qquad \textit{Eq. 90}$$

Where:

- $Q_{flank\ i}$ is the flow rate exchanged between the driving pump chamber ($V_{1,i}$) and the driven pump chamber ($V_{2,i-1}$) .
- c_q is the flow coefficient that depends on the flow number.
- $A_{flank\ i}$ is the communication area between the chambers $V_{1,i}$ and $V_{2,i-1}$.
- $\Delta p = p_{2,i-1} - p_{1,i}$ is the pressure difference between the pump chambers
- $\rho = \rho\left(\frac{p_{1,i}+p_{2,i-1}}{2}\right)$ is the oil density at the mean pressure.
- $\rho(0)$ is the oil density at 0 bar gauge pressure.

- $sign(\Delta p)$ accounts for the direction of the flow: $Q > 0$ when the flow is from $V_{2,i-1}$ to $V_{1,i}$, $Q < 0$ when it flows in the opposite direction.

In the model, the reference communication area $A_{flank\,1}$, corresponding to the connection between the first chamber of gear 1 and the last chamber of gear 2, is first identified. The remaining communication areas are then obtained by applying a circumferential shift equal to the pitch angle α_{pitch} :

$$A_{flank\,i}(\varphi) = A_{flank\,1}\left(\varphi - (i-1)\,\alpha_{pitch}\right) \qquad \text{Eq. 91}$$
$$for\ i = 2, \dots, z$$

The area $A_{flank\,i}$ is obtained by multiplying the height of the flank gap, denoted as $h_{flank\,i}$ (curve in Figure 63) by the axial gear length L_{axis} :

$$A_{flank\,i} = h_{flank\,i}\,L_{axis} \qquad \text{Eq. 92}$$

The main advantage of **Formulation 1** is that it does not require the definition of empirical parameters such as $c_{q\,max}$ and λ_{crit} , which are necessary in the orifice equation used in **Formulation 2**.
Although it is true that, for flank gap heights greater than $h_{flank\,min}$, the laminar–turbulent orifice equation is also applied in Formulation 1, this occurs over a narrow angular range. In these angular positions, the chambers are already in large communication with the suction or delivery volumes through the anti-noise recesses, which predominantly influence the chamber pressure compared to the flow through the flank gap.
Therefore, in Formulation 1, the selection of $c_{q\,max}$ and λ_{crit} is less critical than in Formulation 2. In the present model for the **Formulation 1**, the values used are $c_{q\,max} = 0.7$ and $\lambda_{crit} = 1000$.
The selection of the parameters $c_{q\,max}$ and λ_{crit} in **Formulation 2** may require comparison with CFD simulations or experimental data, in order to ensure an accurate representation of the flow behaviour.

Properly modelling the flow through the flank gap is crucial to improve the accuracy of the model in predicting peak pressures within the meshing zone.

2.7. Ordinary Differential Equation System for the Fluid-Dynamic Submodel

The objective of the fluid dynamic submodule is to determine the flow rates within the pump, the pressure inside the pump chambers, and the volumetric leakages, in order to provide an overview of the volumetric performance of the gear pump.
To achieve this, a system of ordinary differential equations (ODEs) is solved. This system, based on Eq. 1 , is composed of $2\,z + 2$ equations:

- z equations for the chambers of the driving gear,
- z equations for the chambers of the driven gear,
- one equation for the suction control volume and
- one equation for the delivery control volume.

The system of ordinary differential equations (ODEs) is defined as follows:

$$\begin{cases} \dfrac{dp_{1,i}}{dt} = \dfrac{\beta(p_{1,i})}{V_{1,i}}\left(Q_{\Sigma\,1,\mathrm{i}} - \dfrac{dV_{1,i}}{dt}\right) \\ \dfrac{dp_{2,i}}{dt} = \dfrac{\beta(p_{2,i})}{V_{2,i}}\left(Q_{\Sigma\,2,\mathrm{i}} - \dfrac{dV_{2,i}}{dt}\right) \\ \dfrac{dp_S}{dt} = \dfrac{\beta(p_S)}{V_S}\left(Q_{\Sigma\,\mathrm{S}} - \dfrac{dV_S}{dt}\right) \\ \dfrac{dp_D}{dt} = \dfrac{\beta(p_D)}{V_D}\left(Q_{\Sigma\,\mathrm{D}} - \dfrac{dV_D}{dt}\right) \end{cases} \qquad \textit{Eq. 93}$$

$$for\ i = 1, \dots, z$$

Where:

- $Q_{\Sigma\,1,\mathrm{i}}$ is the total flow rate exchanged by the *i*-th control volume of the driving gear with the other control volumes.
- $Q_{\Sigma\,2,\mathrm{i}}$ is the total flow rate exchanged by the *i*-th control volume of the driven gear with the other control volumes.
- $Q_{\Sigma\,\mathrm{S}}$ is the total flow rate exchanged by the suction control volume with the other control volumes and the external environment.
- $Q_{\Sigma\,\mathrm{D}}$ is the total flow rate exchanged by the delivery control volume with the other control volumes and the external environment.

The z terms $Q_{\Sigma\,1,\mathrm{i}}$, corresponding to the driving gear, are defined as follows:

$$\begin{aligned} Q_{\Sigma\,1,1} = {} & Q_{1,1,D} + Q_{1,1,jbD} + Q_{1,1,S} + Q_{1,1,jbS} + Q_{drain\,1,1} + \\ & + Q_{lat\,1,1} - Q_{lat\,1,z} + Q_{tip\,1,1} - Q_{tip\,1,z} + \\ & + Q_{c\,1} + Q_{flank\,1} \end{aligned} \qquad \textit{Eq. 94}$$

$$\begin{aligned} Q_{\Sigma\,1,\mathrm{i}} = {} & Q_{1,i,D} + Q_{1,i,jbD} + Q_{1,i,S} + Q_{1,i,jbS} + Q_{drain\,1,i} + \\ & + Q_{lat\,1,i} - Q_{lat\,1,i-1} + Q_{tip\,1,i} - Q_{tip\,1,i-1} + \end{aligned}$$

$$+Q_{c\,i} + Q_{flank\,i}$$

$$Q_{\Sigma\,1,z} = Q_{1,z,D} + Q_{1,z,jbD} + Q_{1,z,S} + Q_{1,z,jbS} + Q_{drain\,1,z} + \\ +Q_{lat\,1,z} - Q_{lat\,1,z-1} + Q_{tip\,1,z} - Q_{tip\,1,z-1} + \\ +Q_{c\,z} + Q_{flank\,z}$$

$$for\ i = 2, \dots, z-1$$

Similarly, the z terms $Q_{\Sigma\,2,i}$, corresponding to the driven gear, are defined as follows:

$$Q_{\Sigma\,2,1} = Q_{2,1,D} + Q_{2,1,jbD} + Q_{2,1,S} + Q_{2,1,jbS} + Q_{drain\,2,1} + \\ +Q_{lat\,2,1} - Q_{lat\,2,z} + Q_{tip\,2,1} - Q_{tip\,2,z} + \\ -Q_{c\,1} - Q_{flank\,2}$$

$$Q_{\Sigma\,2,i} = Q_{2,i,D} + Q_{2,i,jbD} + Q_{2,i,S} + Q_{2,i,jbS} + Q_{drain\,2,i} + \\ +Q_{lat\,2,i} - Q_{lat\,2,i-1} + Q_{tip\,2,i} - Q_{tip\,2,i-1} + \\ -Q_{c\,i} - Q_{flank\,i+1} \qquad \textit{Eq. 95}$$

$$Q_{\Sigma\,2,z} = Q_{2,z,D} + Q_{2,z,jbD} + Q_{2,z,S} + Q_{2,z,jbS} + Q_{drain\,2,z} + \\ +Q_{lat\,2,z} - Q_{lat\,2,z-1} + Q_{tip\,2,z} - Q_{tip\,2,z-1} + \\ -Q_{c\,z} - Q_{flank\,1}$$

$$for\ i = 2, \dots, z-1$$

The total flow rate exchanged by the suction control volume is defined as:

$$Q_{\Sigma\,S} = \sum_{i=1}^{z} Q_{1,i,S} + Q_{1,i,jbS} + Q_{drain\,1,i} + \\ + \sum_{i=1}^{z} Q_{2,i,S} + Q_{2,i,jbS} + Q_{drain\,2,i} + \\ -Q_{lat\,SD} + Q_{SP} \qquad \textit{Eq. 96}$$

The term Q_{SP} represents the flow rate exchanged between the suction control volume and the external environment through the suction port, and it is defined as:

$$Q_{SP} = c_q\, A_{SP} \sqrt{2 \frac{|\Delta p|}{\rho} \frac{\rho}{\rho(0)}}\ sign(\Delta p) \qquad \textit{Eq. 97}$$

Where:

- c_q is the flow coefficient.
- A_{SP} is the area of the suction port.
- $\Delta p = p_{SP} - p_S$ is the pressure difference between the external pressure at the suction port and the suction control volume.

- $\rho = \rho\left(\frac{p_{SP}+p_S}{2}\right)$ is the oil density at the mean pressure.
- $\rho(0)$ is the oil density at 0 bar gauge pressure.
- $sign(\Delta p)$ accounts for the direction of the flow: $Q > 0$ when the flow enters the pump from the external environment, $Q < 0$ when the flow exits the pump. Since the pump under study is unidirectional, the flow always enters through the suction port, and therefore $Q_{SP} > 0$ at all times.

The total flow rate exchanged by the delivery control volume is defined as:

$$Q_{\Sigma\,\mathrm{D}} = \sum_{i=1}^{z} Q_{1,i,D} + Q_{1,i,jbD} + \sum_{i=1}^{z} Q_{2,i,S} + Q_{2,i,jbS} + Q_{lat\,SD} + Q_{SD} \qquad \textit{Eq. 98}$$

The term Q_{DP} represents the flow rate exchanged between the delivery control volume and the external environment through the delivery port, and it is defined as:

$$Q_{DP} = c_q\, A_{DP} \sqrt{2\frac{|\Delta p|}{\rho}\frac{\rho}{\rho(0)}}\; sign(\Delta p) \qquad \textit{Eq. 99}$$

Where:

- c_q is the flow coefficient.
- A_{DP} is the area of the delivery port.
- $\Delta p = p_{DP} - p_D$ is the pressure difference between the external pressure at the delivery port and the delivery control volume.
- $\rho = \rho\left(\frac{p_{DP}+p_D}{2}\right)$ is the oil density at the mean pressure.
- $\rho(0)$ is the oil density at 0 bar gauge pressure.
- $sign(\Delta p)$ accounts for the direction of the flow: $Q > 0$ when the flow enters the pump from the external environment, $Q < 0$ when the flow exits the pump. Since the pump under study is unidirectional, the flow always exits through the delivery port, and therefore $Q_{DP} < 0$ at all times.

The values of $c_{q\,max}$ and λ_{crit} used in the definitions of Q_{SP} and Q_{DP} are set to $c_{q\,max} = 0.7$ and $\lambda_{crit} = 1000$.

2.8. Volumetric efficiency

The volumetric efficiency of an external gear pump, as well as for other types of displacement pumps, is defined as:

$$\eta_{vol} = \frac{Q_{real}}{Q_{th}} \qquad \textit{Eq. 100}$$

Where:

- Q_{real} is the actual pump flow rate at the delivery port.
  In this case, $Q_{real} = |Q_{DP}|$.
- Q_{th} is the theoretical flow rate of an ideal pump without losses.

Thee theoretical flow rate can be express as:

$$Q_{th} = V_d\, n \qquad \textit{Eq. 101}$$

Where

- V_d is the pump displacement
- n is the pump rotation speed.

The pump displacement can be express as:

$$V_d = \left(\max(V_{1,1}) - \min(V_{1,1})\right) z + \left(\max(V_{2,1}) - \min(V_{2,1})\right) z \qquad \textit{Eq. 102}$$

The terms $\max(V_{1,1})$ and $\max(V_{2,1})$ represent the maximum volume of the first chamber of the driving and driven gears, respectively, during rotation. Similarly, $\min(V_{1,1})$ and $\min(V_{2,1})$ represent the minimum volume.

3. Hydro-Mechanical modelling

To define the hydro-mechanical performance of the gear pump, the various contributions of forces and torques acting on the gears are evaluated.
In the model, the following force components are considered:

- **Pressure forces**: forces exerted by the pressurised fluid on the driving and driven gears.
- **Contact forces**: forces resulting from the contact between the two gears.

The torque contributions taken into account are:

- **Pressure torques**: torque generated by the fluid pressure acting on the gears.
- **Viscous loss torques**: torque contributions due to viscous losses in the lateral clearances, tooth tip clearances, and journal bearings.
- **Meshing losses**: torque contributions resulting from the meshing of the gears.

The external torque required to operate the pump is obtained by summing the above torque components.

In the following sections, each force and torque component is defined and analysed in detail.

3.1. Forces and Torques Generated by Fluid Pressure

The pressure exerted by the fluid generates a force that pushes the gears towards the suction port, while simultaneously producing a torque that opposes their rotation.

In the proposed model, the pressure forces are evaluated by considering the tooth profiles that define the first chambers of both the driving and driven gears. These are the same profiles used in the calculation of the chamber volumes (see Figure 16).

Each profile is subdivided into multiple surface segments, with a distinct pressure value applied to each one.
By knowing the pressure distribution and the geometry of the individual surfaces, the resulting force contributions can be accurately determined [3], [24].

Figure 65 shows the first chamber of the driving gear under pressure p. The pressure acts on surface S (highlighted in green). The projection of surface S onto the planes parallel to x_{1g} and y_{1g} yields the projected surfaces Sx and Sy:

$$Sx = -(A2_x - A1s_x)\, L_{axis}$$
$$Sy = \left(A2_y - A1s_y\right) L_{axis} \qquad \textit{Eq. 103}$$

where A1s and A2 are the endpoints of surface S.
The product of pressure and the projected surfaces gives the components of the pressure force along the x_{1g} and y_{1g}:

$$Fx = p\ Sy$$
$$Fy = p\ Sx$$ *Eq. 104*

The projections Sx and Sy are defined so that the resulting force components are positive when aligned with the x_{1g} and y_{1g} directions, respectively.

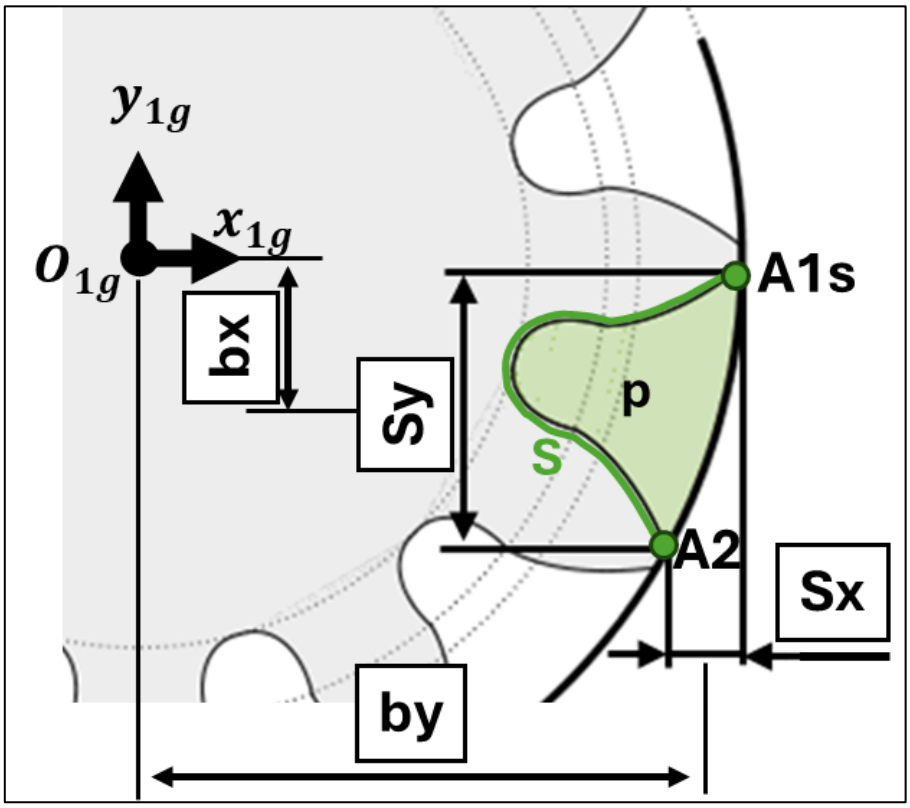

Figure 65 – Example of calculation of force and torque fluid pressure

By considering the force components Fx and Fy applied in the mid-plane of the surface Sy and Sx, respectively, it is possible to define the torque contributions due to the fluid pressure, Mx and My.

$$Mx = Fx\ bx$$
$$My = Fy\ by$$ *Eq. 105*

where bx is the distance between the point of application of Fx and the gear reference point O_{1g}, and by is the distance between the application point of F_y and O_{1g} (see Figure 65). These distances are defined as:

$$bx = -\frac{A1s_y + A2_y}{2}$$
$$by = \frac{A1s_x + A2_x}{2}$$ *Eq. 106*

The moment arms bx and by are defined such that the resulting torque components are positive when they produce a counterclockwise moment.

During gear rotation, the tooth profiles associated with the *i*-th chambers of the driving or driven gears are subdivided into the following surfaces, based on the pressure applied to each of them (see Figure 66 - Figure 71):

- $S1_i$: portion of the tooth profiles associated with the *i*-th chamber of the driving gear, where the pressure $p_{1,i}$ is applied.
- $S1ht_i$: surface of the tooth tip located between the *i*-th and *(i+1)*-th chambers of the driving gear, where the average pressure $\frac{p_{1,i}+p_{1,i+1}}{2}$ is applied.
- $S1dht_i$: portion of the tooth tip surface associated with the *i*-th chamber of the driving gear, where the delivery pressure p_D is applied.
- $S1dcht_i$: portion of the tooth tip surface located between the *i*-th and *(i+1)*-th chambers of the driving gear, where the average pressure between the delivery and pressure of *(i+1)*-th chamber is applied $\left(\frac{p_D+p_{1,i+1}}{2}\right)$.
- $S1d_i$: portion of the teeth profile associated with the *i*-th chamber of the driving gear, where the delivery pressure p_D is applied.
- $S1sht_i$: portion of the tooth tip surface associated with the *i*-th chamber of the driving gear, where the suction pressure p_S is applied..
- $S1scht_i$: portion of the tooth tip surface located between the *i*-th and *(i+1)*-th chambers of the driving gear, where the average pressure between the suction and pressure of *i*-th chamber is applied, $\frac{p_S+p_{1,i}}{2}$, is applied.
- $S1s_i$: portion of the tooth profiles associated with the *i*-th chamber of the driving gear, where the suction pressure p_S is applied.
- $S1c_i$: portion of the tooth profiles associated with the *i*-th chamber of the driving gear, where the pressure of the *i*-th driven gear chamber, $p_{2,i}$, is applied.

All the previously defined surfaces are also considered for the driven gear.

The surfaces are projected onto planes parallel to x_{1g} and y_{1g} for the driving gear, and to x_{2g} and y_{2g} for the driven gear, as shown in Figure 65.

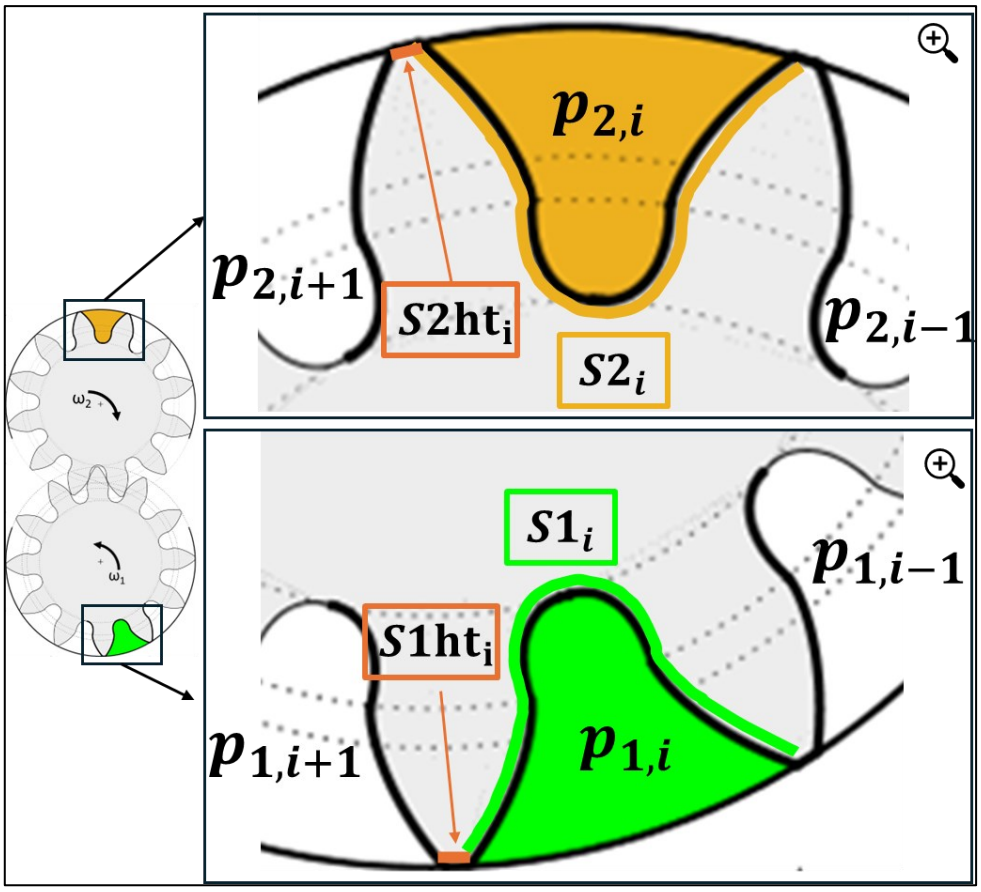

Figure 66 – Surface subdivision when the chambers are exposed to the pump housing

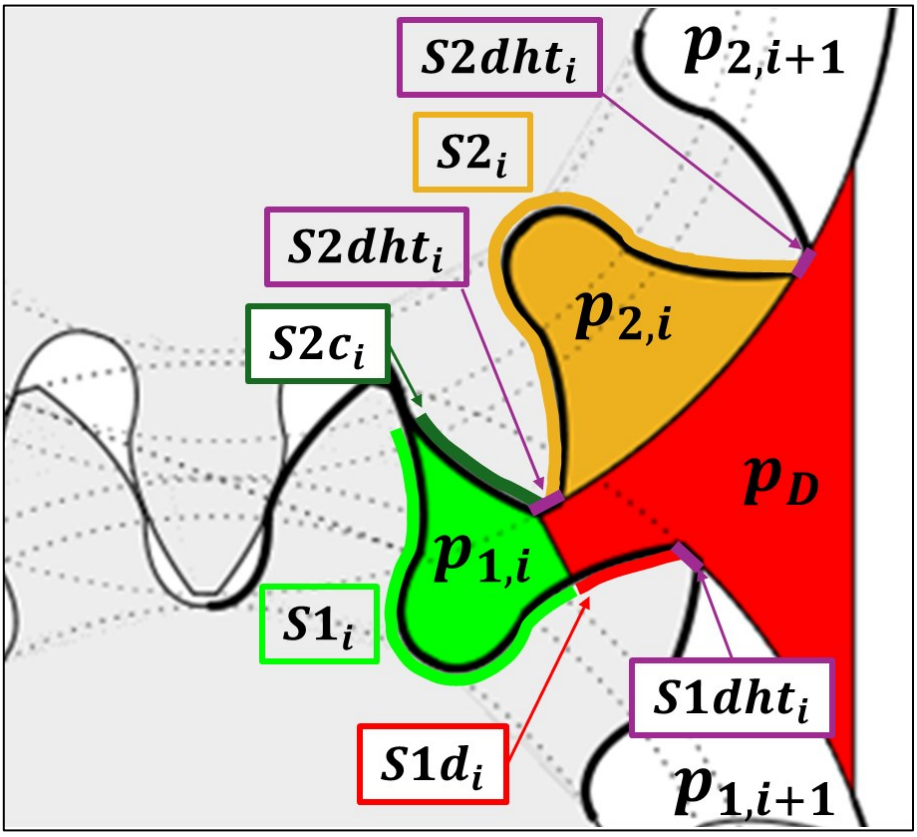

Figure 67 - Subdivision of the chamber surfaces in the meshing zone (delivery side)

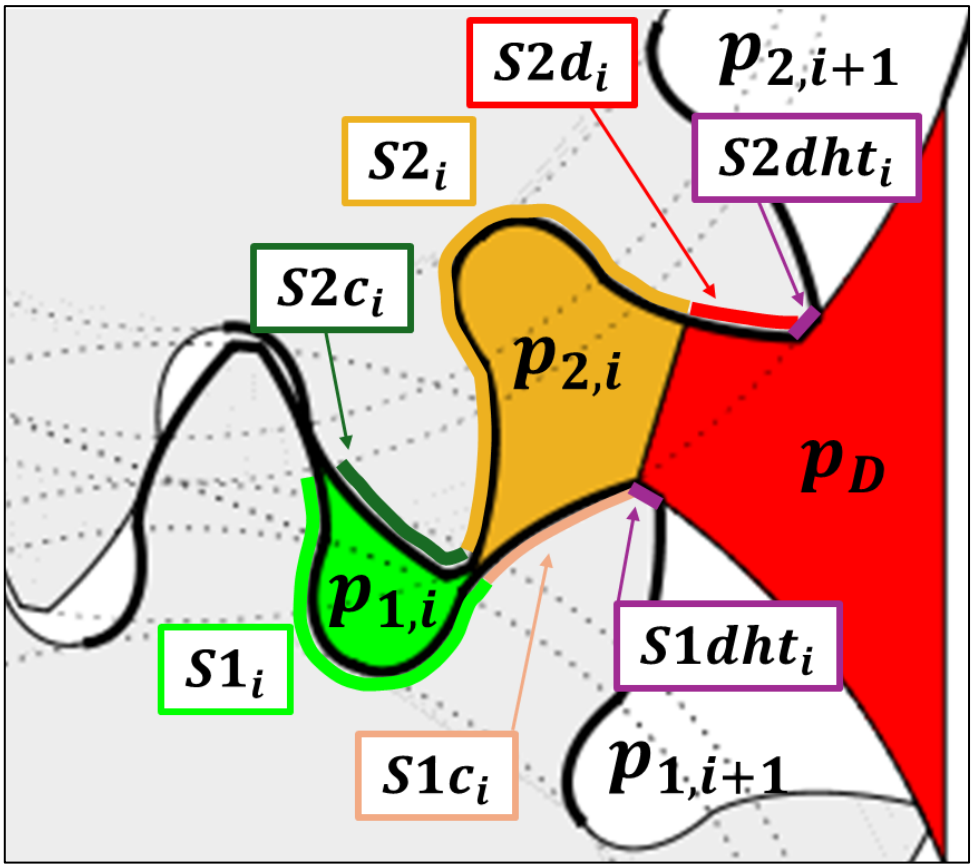

Figure 68 - Subdivision of the chamber surfaces in the meshing zone (delivery side)

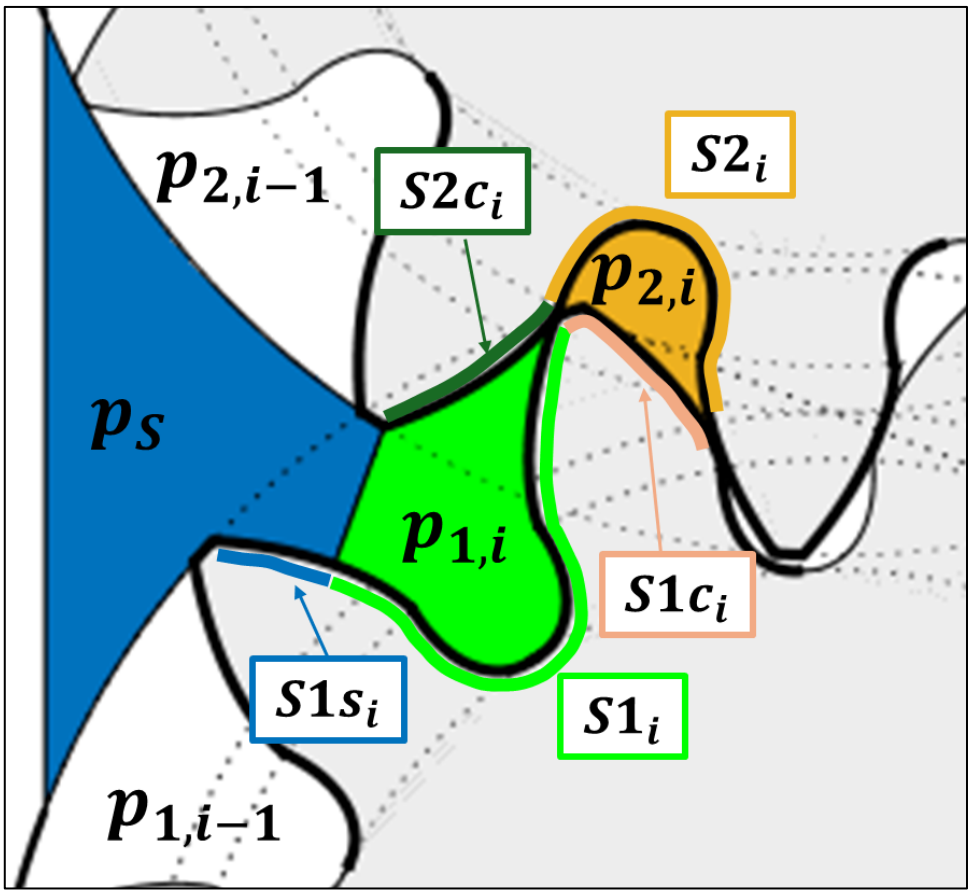

Figure 69 - Subdivision of the chamber surfaces in the meshing zone (suction side)

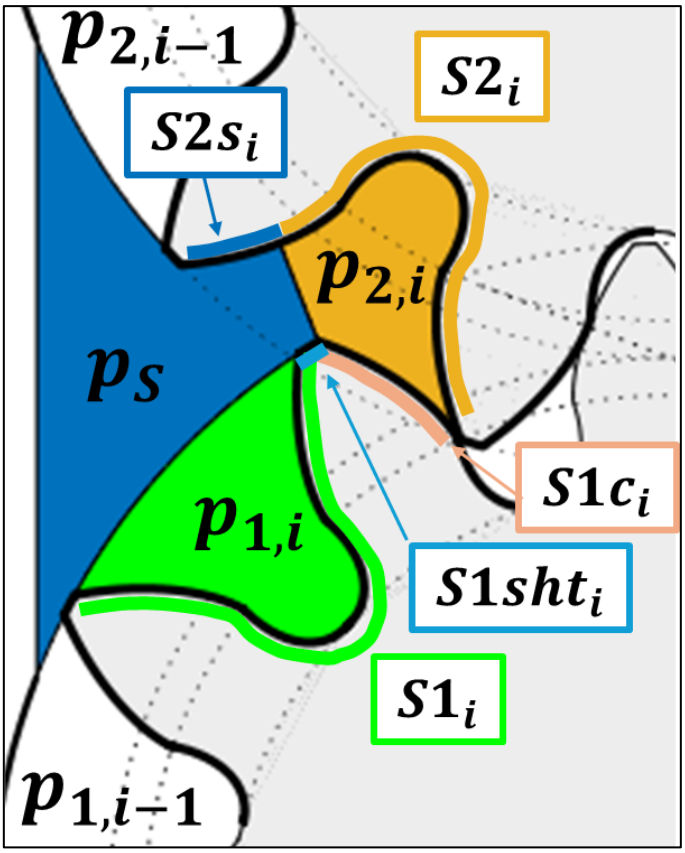

Figure 70- Subdivision of the chamber surfaces in the meshing zone (suction side)

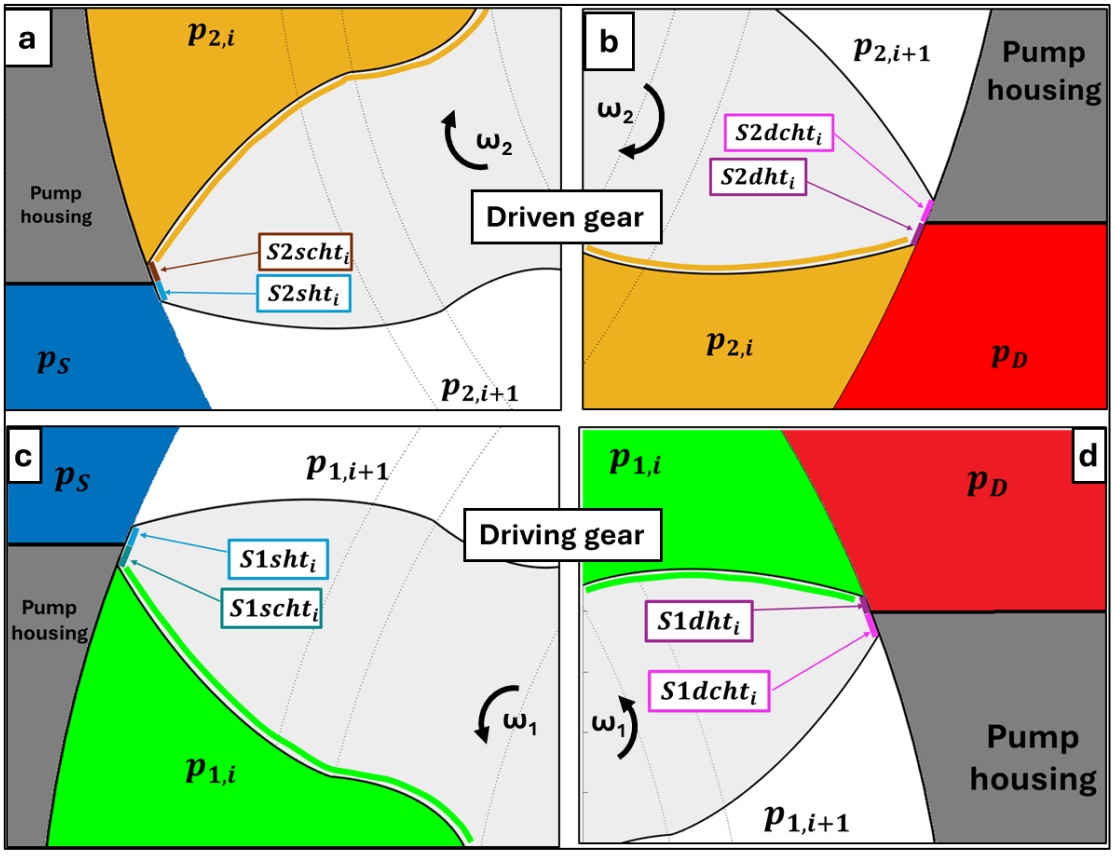

Figure 71 - Tooth tip surface subdivision during chamber transition to/from delivery and suction zones

To evaluate the pressure torques, the following moment arms, associated with the *i*-th chambers of the driving gear, are defined:

- $b1_{x,i}$: perpendicular distance from the mid-plane of the projected surface $S1_{y,i}$ to the reference point O_{1g}.
- $b1_{y,i}$: perpendicular distance from the mid-plane of the projected surface $S1_{x,i}$ to the reference point O_{1g}.
- $b1d_{x,i}$: perpendicular distance from the mid-plane of the projected surface $S1d_{y,i}$ to the reference point O_{1g}.
- $b1d_{y,i}$: perpendicular distance from the mid-plane of the projected surface $S1d_{x,i}$ to the reference point O_{1g}.
- $b1s_{x,i}$: perpendicular distance from the mid-plane of the projected surface $S1s_{y,i}$ to the reference point O_{1g}.
- $b1s_{y,i}$: perpendicular distance from the mid-plane of the projected surface $S1s_{x,i}$ to the reference point O_{1g}.
- $b1c_{x,i}$: perpendicular distance from the mid-plane of the projected surface $S1c_{y,i}$ to the reference point O_{1g}.
- $b1c_{y,i}$: perpendicular distance from the mid-plane of the projected surface $S1c_{x,i}$ to the reference point O_{1g}.

All the above moment arms are also defined for the driven gear, with respect to the reference point O_{2g}.
Examples of moment arms and projected surfaces are shown in Figure 72 and Figure 73

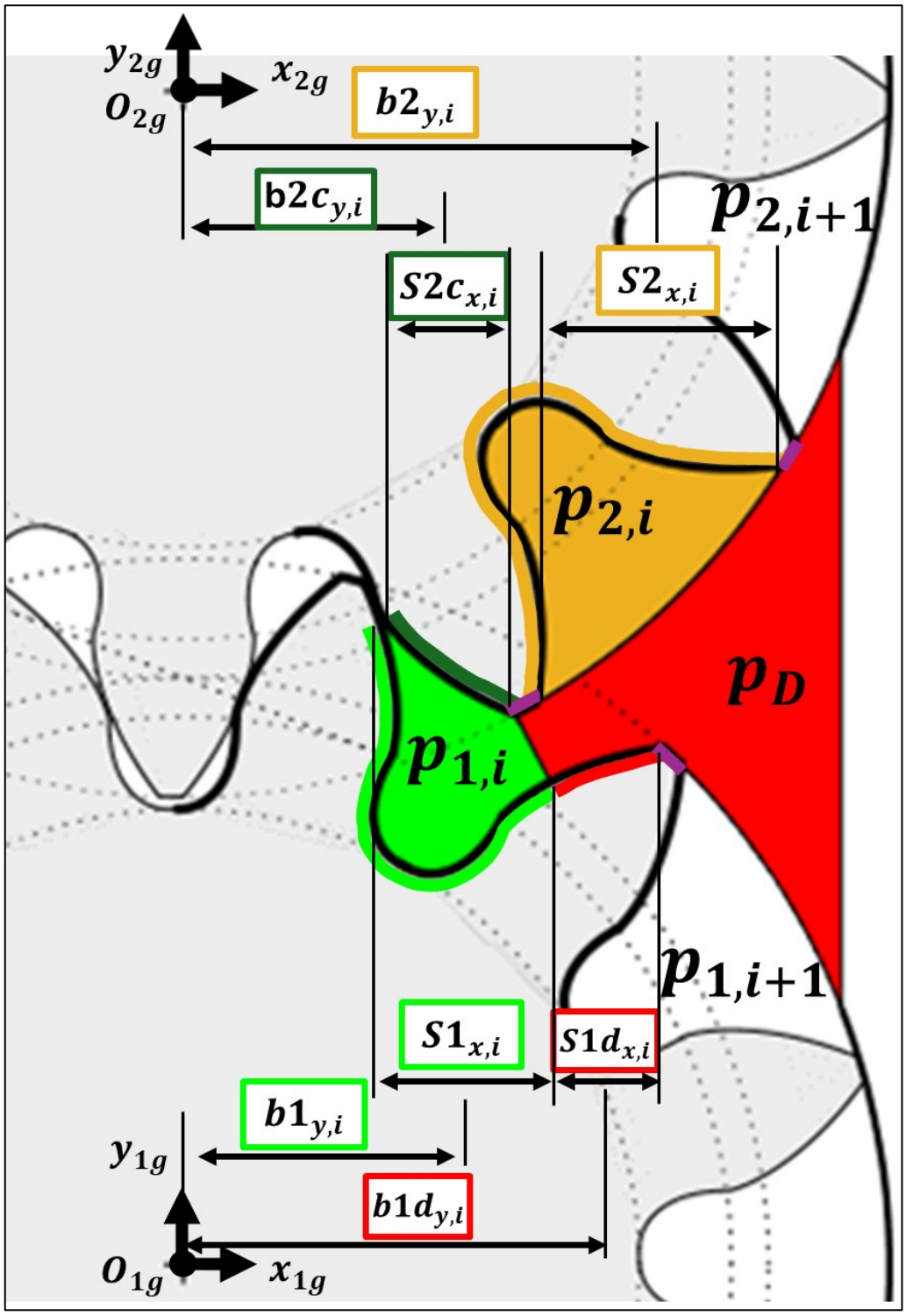

Figure 72 – Moment arm definition for pressure forces aligned with the y-axis

It should be noted that moment arms are not defined for the surfaces $S1ht_i$, $S1dht_i$, $S1dcht_i$, $S1sht_i$, $S1scht_i$, and the corresponding surfaces of the driven gear.
In these cases, the pressure is applied to the tooth tip, which is geometrically defined as an arc of a circle.
A pressure distribution applied to a circular arc does not generate any net torque contribution, and therefore the moment is considered zero.

However, the force contributions are not-zero and are still taken into account in the model.

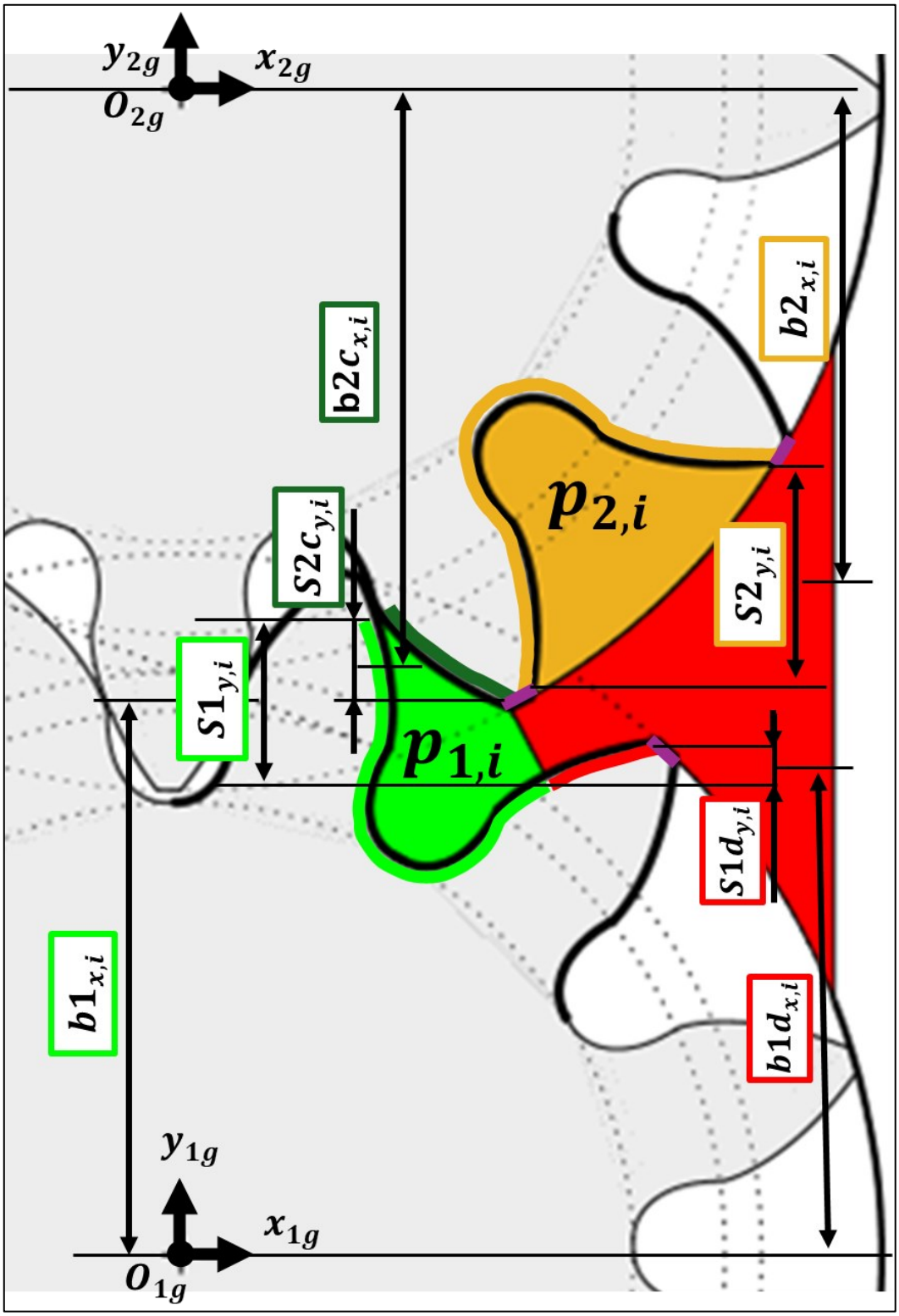

Figure 73 - Moment arm definition for pressure forces aligned with the x-axis

The components of the pressure forces, aligned with the *x*-axis and associated with the previously defined surfaces of the driving gear, are defined as follows:

$$F_{S1,x} = \sum_{i=1}^{z} S1_{y,i}\, p_{1,i}$$

$$F_{S1ht,x} = \sum_{i=1}^{z-1} S1ht_{y,i}\, \frac{p_{1,i} + p_{1,i+1}}{2} + S1ht_{y,z}\, \frac{p_{1,z} + p_{1,1}}{2}$$

$$F_{S1dht,x} = \sum_{i=1}^{z} S1dht_{y,i}\, p_D$$

$$F_{S1dcht,x} = \sum_{i=1}^{z-1} S1dcht_{y,i}\, \frac{p_D + p_{1,i+1}}{2} + S1dcht_{y,z}\, \frac{p_D + p_{1,1}}{2}$$

$$F_{S1d,x} = \sum_{i=1}^{z} S1d_{y,i}\, p_D \qquad \textit{Eq. 107}$$

$$F_{S1sht,x} = \sum_{i=1}^{z} S1sht_{y,i}\, p_S$$

$$F_{S1scht,x} = \sum_{i=1}^{z} S1dcht_{y,i}\, \frac{p_S + p_{1,i}}{2}$$

$$F_{S1s,x} = \sum_{i=1}^{z} S1s_{y,i}\, p_S$$

$$F_{S1c,x} = \sum_{i=1}^{z} S1c_{y,i}\, p_{2,i}$$

The pressure force components of the driving gear aligned with the *y*-axis are defined analogously:

$$F_{S1,y} = \sum_{i=1}^{z} S1_{x,i}\, p_{1,i}$$

$$F_{S1ht,y} = \sum_{i=1}^{z-1} S1ht_{x,i}\, \frac{p_{1,i} + p_{1,i+1}}{2} + S1ht_{x,z}\, \frac{p_{1,z} + p_{1,1}}{2} \qquad \textit{Eq. 108}$$

$$F_{S1dht,x} = \sum_{i=1}^{z} S1dht_{x,i}\, p_D$$

$$F_{S1dcht,y} = \sum_{i=1}^{z-1} S1dcht_{x,i} \frac{p_D + p_{1,i+1}}{2} + S1dcht_{x,z} \frac{p_D + p_{1,1}}{2}$$

$$F_{S1d,y} = \sum_{i=1}^{z} S1d_{x,i}\, p_D$$

$$F_{S1sht,y} = \sum_{i=1}^{z} S1sht_{x,i}\, p_S$$

$$F_{S1scht,y} = \sum_{i=1}^{z} S1dcht_{x,i} \frac{p_S + p_{1,i}}{2}$$

$$F_{S1s,y} = \sum_{i=1}^{z} S1s_{x,i}\, p_S$$

$$F_{S1c,y} = \sum_{i=1}^{z} S1c_{x,i}\, p_{2,i}$$

In the same way, the pressure force components along the *x*- and *y*-axes are defined for the driven gear, using the corresponding surfaces and pressure values.

By summing the individual pressure force components defined in Eq. 107 and Eq. 108, the total pressure force acting on the driving gear can be obtained:

$$F1p_x = F_{S1,x} + F_{S1ht,x} + F_{S1dht,x} + F_{S1dcht,x} + F_{S1d,x} + F_{S1sht,x} + \\ + F_{S1scht,x} + F_{S1s,x} + F_{S1c,x} \qquad \textit{Eq. 109}$$

$$F1p_y = F_{S1,y} + F_{S1ht,y} + F_{S1dht,y} + F_{S1dcht,y} + F_{S1d,y} + F_{S1sht,y} + \\ + F_{S1scht,y} + F_{S1s,y} + F_{S1c,y}$$

$F1p_x$ and $F1p_y$ represent the total pressure force components acting on the driving gear along the x- and y-axes, respectively.
For the driven gear, the total pressure force components are defined analogously as::

$$F2p_x = F_{S2,x} + F_{S2ht,x} + F_{S2dht,x} + F_{S2dcht,x} + F_{S2d,x} + F_{S2sht,x} + \\ + F_{S2scht,x} + F_{S2s,x} + F_{S2c,x} \qquad \textit{Eq. 110}$$

$$F2p_y = F_{S2,y} + F_{S2ht,y} + F_{S2dht,y} + F_{S2dcht,y} + F_{S2d,y} + F_{S2sht,y} + \\ + F_{S2scht,y} + F_{S2s,y} + F_{S2c,y}$$

In the same way as the components of the pressure forces associated with the previously defined surfaces have been introduced, the corresponding pressure torque components are now defined.
For the driving gear:

$$M_{S1} = \sum_{i=1}^{z} S1_{y,i}\, p_{1,i}\, b1_{x,i} + \sum_{i=1}^{z} S1_{x,i}\, p_{1,i}\, b1_{y,i}$$

$$M_{S1d} = \sum_{i=1}^{z} S1d_{y,i}\, p_D\, b1d_{x,i} + \sum_{i=1}^{z} S1d_{x,i}\, p_D\, b1d_{y,i}$$

$$M_{S1s} = \sum_{i=1}^{z} S1s_{y,i}\, p_S\, b1s_{x,i} + \sum_{i=1}^{z} S1s_{x,i}\, p_S\, b1s_{y,i}$$

$$M_{S1c} = \sum_{i=1}^{z} S1c_{y,i}\, p_{2,i}\, b1c_{x,i} + \sum_{i=1}^{z} S1c_{x,i}\, p_{2,i}\, b1c_{y,i}$$

Eq. 111

For the driven gear:

$$M_{S2} = \sum_{i=1}^{z} S2_{y,i}\, p_{2,i}\, b2_{x,i} + \sum_{i=1}^{z} S2_{x,i}\, p_{2,i}\, b2_{y,i}$$

$$M_{S2d} = \sum_{i=1}^{z} S2d_{y,i}\, p_D\, b2d_{x,i} + \sum_{i=1}^{z} S2d_{x,i}\, p_D\, b2d_{y,i}$$

$$M_{S2s} = \sum_{i=1}^{z} S2s_{y,i}\, p_S\, b2s_{x,i} + \sum_{i=1}^{z} S2s_{x,i}\, p_S\, b2s_{y,i}$$

$$M_{S2c} = \sum_{i=1}^{z} S2c_{y,i}\, p_{1,i}\, b2c_{x,i} + \sum_{i=1}^{z} S1c_{x,i}\, p_{1,i}\, b2c_{y,i}$$

Eq. 112

By summing the individual pressure torque components, the total pressure torque acting on the driving and driven gears can be obtained:

$$M1_p = M_{S1} + M_{S1d} + M_{S1s} + M_{S1c}$$

$$M2_p = M_{S2} + M_{S2d} + M_{S2s} + M_{S2c}$$

Eq. 113

It should be noted that all the previously introduced quantities - such as surfaces, moment arms, forces, and torques - vary as a function of the gear's angular position, φ. However, the explicit dependence on φ is omitted from the equations in order to simplify both their writing and reading.

3.2. Viscous Torque Losses Due to Tooth Tip Clearances

A part of the torque that it is opposes to the gears rotation is attributed to the viscous losses due to the lubricated clearance between the gear tooth tips and the pump housing.
The clearance is modelled as a rectangular gap through which laminar flow of a Newtonian fluid occurs. A representation of the clearance is shown in Figure 74.

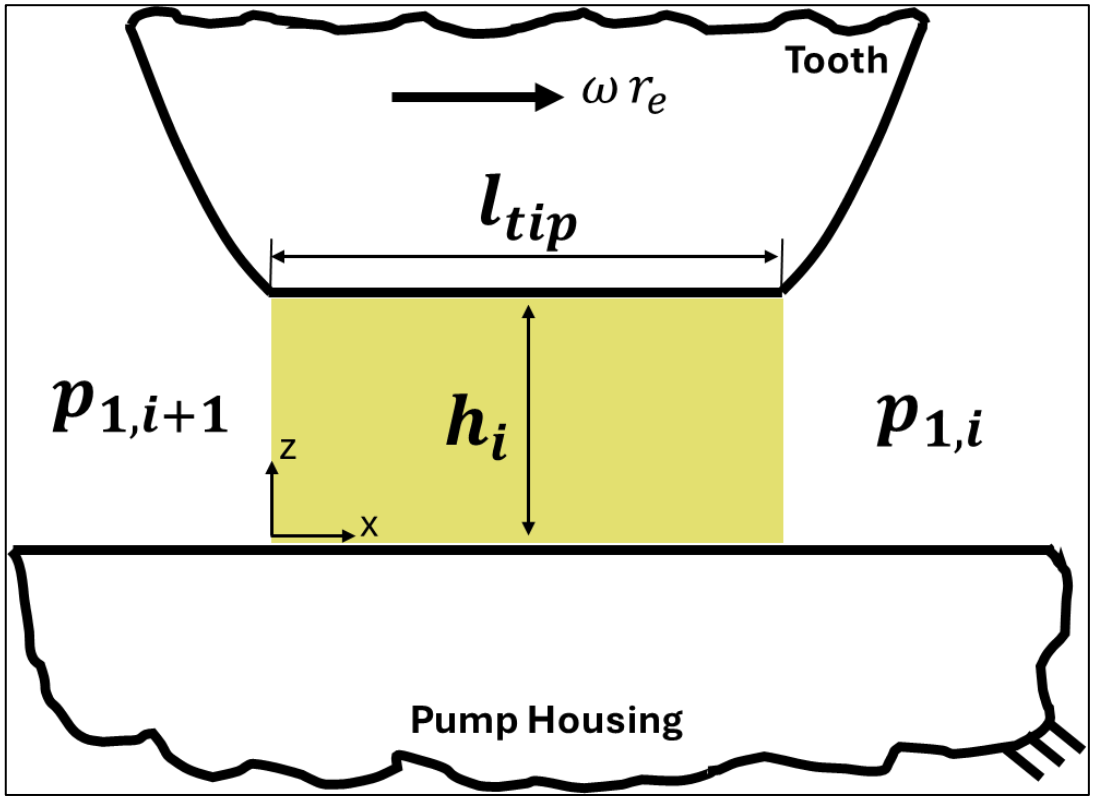

Figure 74 – Tooth Tip Clearances -Torque Evaluation

The clearance is defined between two parallel planes: the stationary pump housing and the tooth tip, which moves at a tangential velocity $\omega\, r_e$, where $\omega = |\omega_1| = |\omega_2|$. Although both the housing and the tooth tip are curved, due to the small dimensions of the clearance, these surfaces are approximated as planar surfaces.
The gap is characterised by a length l_{tip}, height h_i, and width L_{axis}, which corresponds to the gear axial length.

The parameters l_{tip} and $h_i$are defined according to the same criteria used for the evaluation of volumetric leakage through the tip gaps, as described in Section 0.

The shear force acting on the tooth tip, within the clearance between the *i*-th and *(i+1)*-th chambers of the driving gear, is defined as [4], [25]:

$$F_{tip\ 1,i} = -\mu \left.\frac{dv}{dz}\right|_{z=h_i} l_{tip}\, L_{axis} \qquad \textit{Eq. 114}$$

Where:

- μ is the dynamic viscosity of the oil, evaluated at the mean pressure $\frac{p_{1,i}+p_{1,i+1}}{2}$.
- $\left.\frac{dv}{dz}\right|_{z=h_i}$ is the velocity gradient evaluated at the surface of the tooth tip, $z = h_i$.

The velocity profile of the fluid inside the clearance is given by [22]:

$$v(z) = -\frac{z}{h_i}(h_i - z)\,\frac{dp}{dx} + \omega r_e \frac{z}{h_i} \qquad \textit{Eq. 115}$$

Where:

- $v(z)$ is the fluid velocity at position z (see Figure 74)
- $\frac{dp}{dx}$ is the pressure gradient, which, assuming constant gap height, is expressed as $\frac{p_{1,i}-p_{1,i+1}}{l_{tip}}$.

From the velocity definition, the velocity gradient at the tooth tip surface is obtained as:

$$\left.\frac{dv}{dz}\right|_{z=h_i} = \frac{h_i}{2\mu}\frac{p_{1,i} - p_{1,i+1}}{l_{tip}} + \frac{\omega r_e}{h_i} \qquad \textit{Eq. 116}$$

The viscous torque loss due to the shear force acting on the tooth tip is defined as:

$$M_{tip\ 1,i} = -F_{tip\ 1,i}\ r_e \qquad \textit{Eq. 117}$$

Using the definition of shear force (Eq. 114), the torque expression becomes:

$$M_{tip\ 1,i} = \frac{h_i}{2}\ L_{axis}\ r_e\ \Delta p - \omega\ \mu \frac{L_{axis} l_{tip}}{h_i}\ r_e^2 \qquad \textit{Eq. 118}$$

Where the pressure difference between the chambers is $\Delta p = p_{1,i+i} - p_{1,i}$.

In the above expression, the terms that depend only on the geometry of the pump and not on the operating conditions can be grouped as follows:

$$M_{tip\ 1,i} = fMtip_{p\ 1,i}\ \Delta p - \omega\ \mu\ fMtip_{v\ 1,i} \qquad \textit{Eq. 119}$$

The term $fMtip_{p\ 1,i}$ contains the geometric contributions that influence the torque caused by the pressure gradient, while $fMtip_{v\ 1,i}$ contains the geometric contributions that affect the torque caused by the relative motion between the gear tooth and the pump housing.

$$fMtip_{p\,1,i} = \frac{h_i}{2} L_{axis}\, r_e$$

Eq. 120

$$fMtip_{v\,1,i} = \frac{L_{axis} l_{tip}}{h_i} r_e^2$$

$M_{tip\,1,i}$ is considered positive when the torque direction is counterclockwise, and negative otherwise.
Since the driving gear rotates counterclockwise, a negative viscous torque is required to oppose its rotation.
Considering the terms in Eq. 119 :

- The first term, $fMtip_{p\,1,i}\ \Delta p$ has a sign that depends only on the pressure gradient.
  In most cases, $p_{1,i+i} \leq p_{1,i}$, so the pressure difference Δp is negative. Given that $fMtip_{p\,1,i} \geq 0$ this torque contribution is therefore negative, opposing the gear rotation.
- The second term $-\omega\, \mu\, fMtip_{v\,1,i}$ is always negative, as $\omega > 0$, $\mu > 0$ and $fMtip_{v\,1,i} \geq 0$. It also opposes the rotation of the driving gear.

The viscous torque acting on the tooth tip clearance between the *i*-th and *(i+1)*- th chambers of the driven gear is defined as:

$$M_{tip\,2,i} = -\, fMtip_{p\,2,i}\ \Delta p + \omega\, \mu fMtip_{v\,2,i}$$

Eq. 121

Since the driven gear rotates clockwise, a positive torque is required to oppose its rotation.

By summing all the viscous torque contributions from the individual tooth tip clearances, the total viscous torque losses on the driving and driven gears are obtained:

$$M1_{tip} = \sum_{i=1}^{z} M_{tip\,1,i}$$

$$M2_{tip} = \sum_{i=1}^{z} M_{tip\,2,i}$$

Eq. 122

3.3. Viscous Torque Losses Due to Lateral Clearances Between Adjacent Chambers

The shear forces generated by the fluid in the lateral clearances introduce an additional viscous torque contribution that opposes the rotation of the gears.

The lateral gap between the *i*-th and (*i*+1)-th chambers of the driving gear follows the shape of the gear profile.
For the purpose of defining viscous torque losses, this gap is approximated as a set of rectangular clearances, using the same approach adopted for the evaluation of volumetric leakage through lateral gaps described in Section 0.

Each rectangular segment is treated as a gap of rectangular cross-section, across which steady-state laminar flow of a Newtonian fluid occurs.
The *k*-th segment is characterised by a length l_k, height h_{lat} and width b_k; for more information, see Section 0.

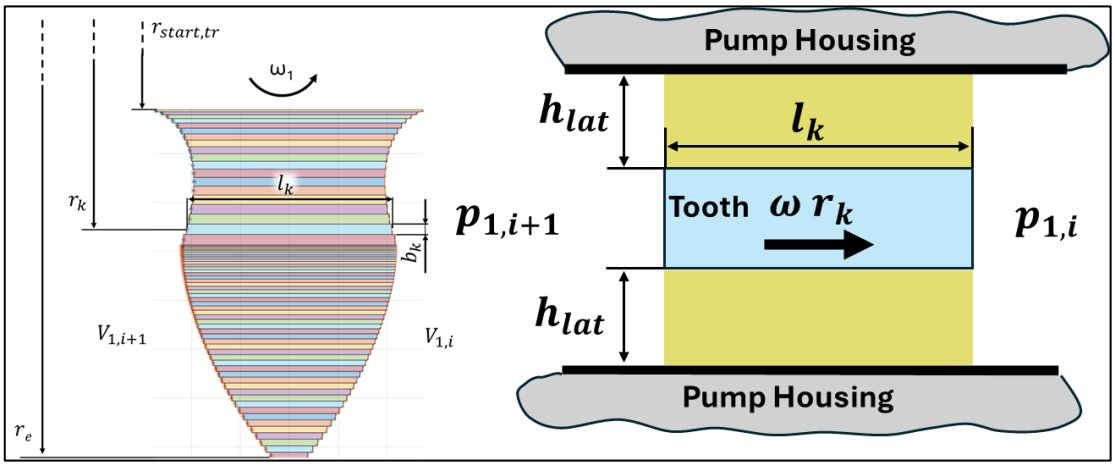

Figure 75 – Lateral gap of the k-th rectangular segment

Using the same formulation as in Eq. 114, the shear force associated with the *k*-th segment can be calculated.
By multiplying this shear force by the radial distance of the *k*-th segment from the gear centre (r_k) the viscous torque contribution of that segment is obtained.
Summing the contributions of all the rectangular segments yields the total viscous torque loss associated with the lateral clearance between the *i*-th and (*i*+*1*)-th chambers of the driving gear [4], [25].

$$M_{lat\ 1,i} = \frac{h_{lat}}{2}\,\Delta p \sum_{k=1}^{n_{tr}+n_{ev}-2} b_k\, r_k - \mu \frac{\omega}{h_{lat}} \sum_{k=1}^{n_{tr}+n_{ev}-2} l_k\, b_k\, r_k^2 \qquad \text{Eq. 123}$$

Where the pressure difference between the chambers is $\Delta p = p_{1,i+i} - p_{1,i}$ and μ is the dynamic viscosity of the oil, evaluated at the mean pressure $\frac{p_{1,i}+p_{1,i+1}}{2}$

By grouping the terms that depend only on the pump geometry and not on the operating conditions, Eq. 123 can be rewritten as:

$$M_{lat\ 1,i} = \ fMlat_{p\ 1,i}\Delta p - \ \mu\omega\ fMlat_{v\ 1,i} \qquad \textit{Eq. 124}$$

The term $fMlat_{p\ 1,i}$ contains the geometric contributions that influence the torque caused by the pressure gradient, while $fMlat_{v\ 1,i}$ contains the geometric contributions that affect the torque caused by the relative motion between the gear tooth and the pump housing.

The two geometric terms are defined as:

$$fMlat_{p\ 1,i} = \frac{h_{lat}}{2} \sum_{k=1}^{n_{tr}+n_{ev}-2} b_k\ r_k$$

$$fMlat_{v\ 1,i} = \frac{1}{h_{lat}} \sum_{k=1}^{n_{tr}+n_{ev}-2} l_k\ b_k\ r_k^2 \qquad \textit{Eq. 125}$$

The viscous torque associated with lateral clearance between the *i*-th and $(i+1)$-th chambers of the driven gear is given by :

$$M_{lat\ 2,i} = \ -fMlat_{p\ 2,i}\Delta p + \ \mu\ \omega\ fMlat_{v\ 2,i} \qquad \textit{Eq. 126}$$

By summing all the viscous torque contributions from the individual lateral clearances, the total viscous torque losses on the driving and driven gears are obtained:

$$M1_{lat} = 2 \sum_{i=1}^{z} M_{lat\ 1,i}$$

$$M2_{lat} = 2 \sum_{i=1}^{z} M_{lat\ 2,i} \qquad \textit{Eq. 127}$$

The multiplication factor 2 accounts for leakage from both faces of the gear.

In the model, volumetric leakage through the lateral gap between adjacent chambers is considered only when both chambers are at their maximum volume.
The same assumption is applied to the viscous torque losses.
Therefore, in the meshing zone - where the chamber volume is reduced - this type of

torque loss is not considered.
This condition is implemented by setting $fMlat_{p\ j,i}$ and $fMlat_{v\ j,i}$ to zero whenever the involved chambers are not at their maximum volume, similarly to what is shown in Figure 58.

3.4. Viscous Torque Losses Due to Drain Lateral Clearances

To define the viscous torque losses associated with the drain lateral clearance, the clearance is approximated as a circular crown, as illustrated in Figure 76.
The circular crown extends from $r_{hole\ jb}$, which represents the radius of the journal bearing housing (i.e., the bore in which the bushing is mounted), to r_r, the root radius of the gear.
The clearance is modelled as a perfect annular region, neglecting the interruption caused by the connection channel between the anti-noise recess and the journal bearing, which would otherwise break the continuity of the clearance geometry.

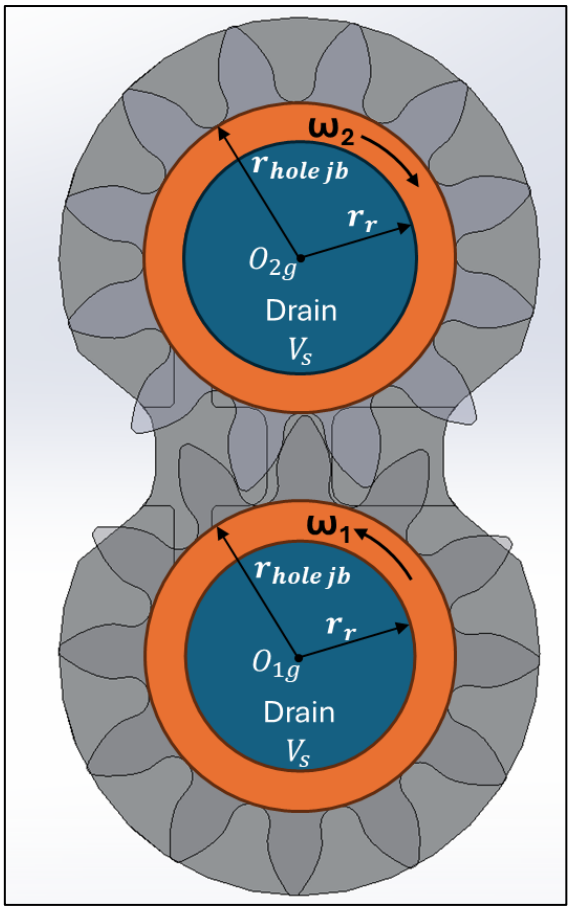

Figure 76 – Drain lateral clearance used for viscous torque evaluation

The viscous torque loss on the driving gear is defined as:

$$M1_{drain} = -2\left(\mu\,\frac{\omega}{h_{lat}}\,\pi\frac{r_r^4 - r_{hole\ jb}^4}{4}\right) \qquad \textit{Eq. 128}$$

The multiplication factor 2 accounts for the torque losses on both lateral faces of the gear.
The torque $M1_{drain}$ is negative because it acts opposite to the counterclockwise rotation of the driving gear.
The corresponding viscous torque loss on the driven gear is:

$$M2_{drain} = 2\left(\mu\,\frac{\omega}{h_{lat}}\,\pi\frac{r_r^4 - r_{hole\ jb}^4}{4}\right) \qquad \textit{Eq. 129}$$

This torque is positive, as it acts opposite to the clockwise rotation of the driven gear.

These torque expressions are derived under the following assumptions:

- The fluid is Newtonian, with dynamic viscosity $\mu = \mu(p_S)$, evaluated at the pressure of the suction control volume.
- The flow within the drain lateral clearance is laminar.
- The clearance height h_{lat} is constant.

The shear force applied by the fluid on an infinitesimal gear surface dF is obtained by multiplying the shear stress $\mu\frac{\omega\, r}{h_{lat}}$ by the infinitesimal area $dA = r\, d\gamma\, dr$, as shown in Figure 77 . Taking the gear centre as the moment reference point, the moment arm associated with the infinitesimal force is r. The total torque is then obtained by integrating the infinitesimal torque over the entire area of the circular crown.

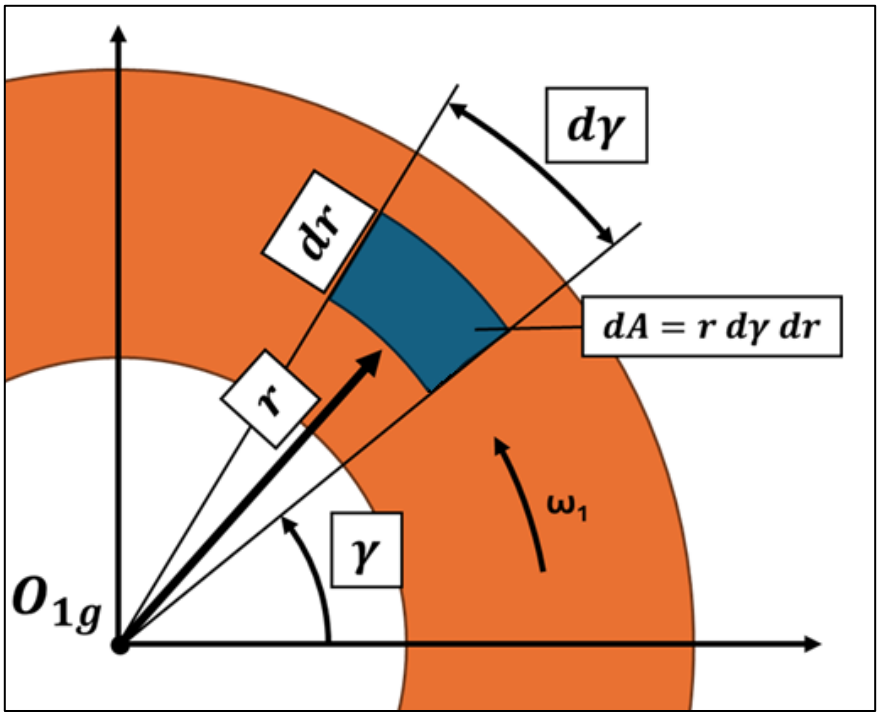

Figure 77 - Infinitesimal element for viscous shear torque calculation

The torque acting on a single face of the driving gear due to drain clearance shear is given by:

$$\frac{M1_{drain}}{2} = -\int_{r_{hole\ jb}}^{r_r}\int_{0}^{2\pi} r\ \mu\frac{\omega\, r}{h_{lat}}\, r\, d\gamma\, dr \qquad \textit{Eq. 130}$$

The same formulation is used for the driven gear, but with a change in sign, since it rotates in the opposite direction to the driving gear.

3.5. Viscous Torque Losses Due to Journal Bearings

The hydrodynamic journal bearings represent another source of viscous losses in the gear pump.
A total of four journal bearings are present in the pump: two support the driving gear, and the other two support the driven gear.
The main geometrical parameters of the journal bearings are illustrated in Figure 78 and listed as follows:

- d_{shaft}diameter of the journal, which corresponds to the gear shaft. The associated radius is denoted by r_{shaft}.
- $d_{bearing}$: diameter of the bearing, which represents the inner diameter of the bushing. The associated radius is denoted by $r_{bearing}$.
- l_{jb}: axial length of the journal–bearing pair.
- $c_{jb} = r_{bearing} - r_{shaft}$: radial clearance between the bearing and the journal.

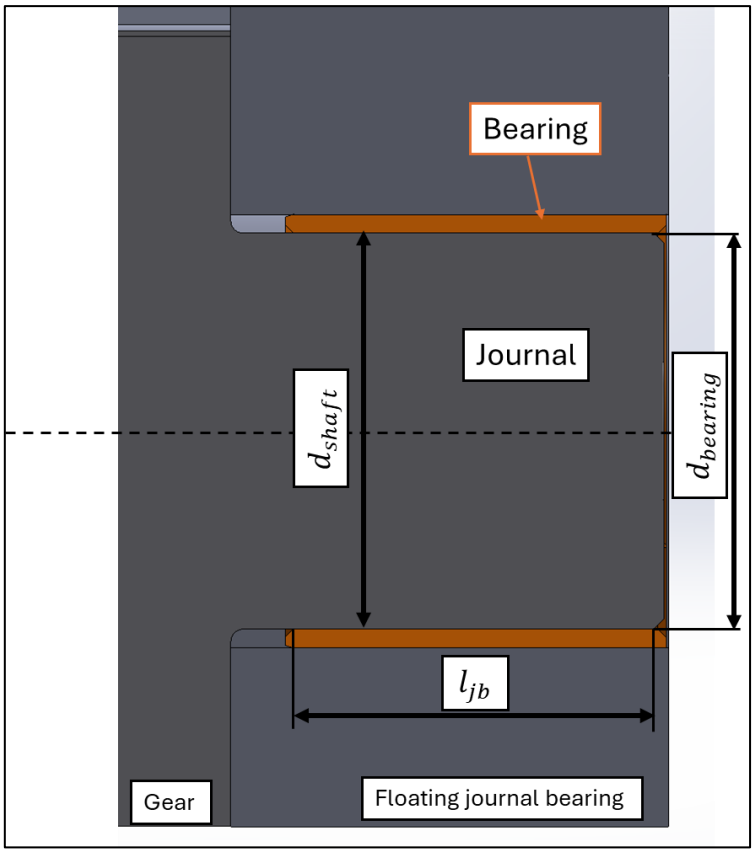

Figure 78 – Geometrical dimensions of the journal bearing

The viscous losses associated with the journal bearings are influenced not only by the geometrical parameters of the bearings, but also by the operating conditions of the pump, the rotational speed of the gears and the fluid pressure.

As discussed in Section 2.2.5, the forces acting on each gear result in an eccentric position relative to the centre of its bearing.
These eccentricities are expressed by the terms ecc_{x1}, ecc_{y1}, ecc_{x2} and ecc_{y2}, which denote the x and y coordinates of the centres of gear 1 and gear 2 relative to the centres of their respective bearings. These positions are defined within the reference frame $O_{jb1}$and O_{jb2}.
The absolute value of eccentricity for the driving and driven gear is express as :

$$ecc_1 = \sqrt{ecc_{x1}^2 + ecc_{y1}^2}$$
$$ecc_1 = \sqrt{ecc_{x2}^2 + ecc_{y2}^2} \qquad \textit{Eq. 131}$$

In this section, the concept of eccentricity is introduced, while a more detailed explanation is provided in Section 4.
During gear rotation, the resultant forces acting on the gears are periodic with a period of $\frac{2\pi}{\omega\, z}$. As a consequence, under steady-state conditions, the gear eccentricities also vary with the same period.

During one complete revolution of the gear, the gear centre traces a closed path repeated z times.
However, a key assumption in the model is that, under steady-state conditions, the gear adopts a fixed eccentricity that generates a hydrodynamic lift force in the journal bearing.
This lift force is assumed to balance the force applied to the gear, which is considered to be constant and equal to the average force acting over one full rotation. This average force is equivalent to the mean force acting over $\frac{1}{z}$ of a rotation.
Where ω is the absolute value of the gear rotation.

One of the most widely used theories for the analysis of journal bearings is the Reynolds equation.
In the case of a journal bearing subjected to a constant force, using a Newtonian lubricant with constant density, the Reynolds equation can be expressed as follows [26]:

$$\frac{1}{R^2}\frac{\partial}{\partial\theta}\left(h^3\frac{\partial p}{\partial\theta}\right)+\frac{\partial}{\partial z}\left(h^3\frac{\partial p}{\partial z}\right)=6\mu\,\omega\frac{dh}{d\theta} \qquad \textit{Eq. 132}$$

Where:

- R : the radius of the bearing.
- θ :the circumferential coordinate of the clearance.
- z: axial position along the journal.
- h : film thickness or clearance height between journal and bearing, expressed as $h = c_{jb} + ecc\cos(\theta)$.
  Where $c_{jb}$is the radial clearance and ecc is the journal eccentricity.
- p : fluid pressure within the clearance, varying with both θ and z.
- μ : dynamic viscosity of the lubricant.
- ω : angular velocity of the journal.

Solving the Reynolds equation allows the determination of the pressure distribution within the clearance, which is essential for calculating both the hydrodynamic lift force of the journal bearing and the viscous torque losses.

In the literature, two simplifying assumptions are commonly proposed for the resolution of the Reynolds equation:

- The **infinite length approximation** which applies when the journal bearing has axial length as the predominant dimension $\left(\frac{l_{jb}}{d_{bearing}} > 1\right)$. Under these conditions, the term $\frac{\partial}{\partial z}\left(h^3\frac{\partial p}{\partial z}\right)$ is neglected, and the equation can be solved analytically.

- The **short bearing approximation** [27] which applies when the journal bearing has diameter as the predominant dimension $\left(\frac{l_{jb}}{d_{bearing}} < 1\right)$. In this case, the term $\frac{\partial}{\partial\theta}\left(h^3\ \frac{\partial p}{\partial\theta}\right)$ is neglected, allowing the equation to be solved analytically.

3.5.1. Infinite Length Journal Bearing Approximation

Under this assumption, the Reynolds equation takes the form:

$$\frac{1}{R^2}\frac{\partial}{\partial\theta}\left(h^3\ \frac{\partial p}{\partial\theta}\right) = 6\mu\,\omega\frac{dh}{d\theta} \qquad \textit{Eq. 133}$$

The solution of this equation yields a pressure distribution with the trend illustrated in Figure 79.
The results show that pressure is positive in the range $0 \leq \theta \leq \pi$,whereas it becomes negative in the range $\pi \leq \theta \leq 2\pi$. Under real operating conditions, negative pressure may lead to oil aeration and cavitation phenomena, which are not captured by the Reynolds equation. These effects influence the estimation of both the lift force and the viscous losses in practical journal bearings.

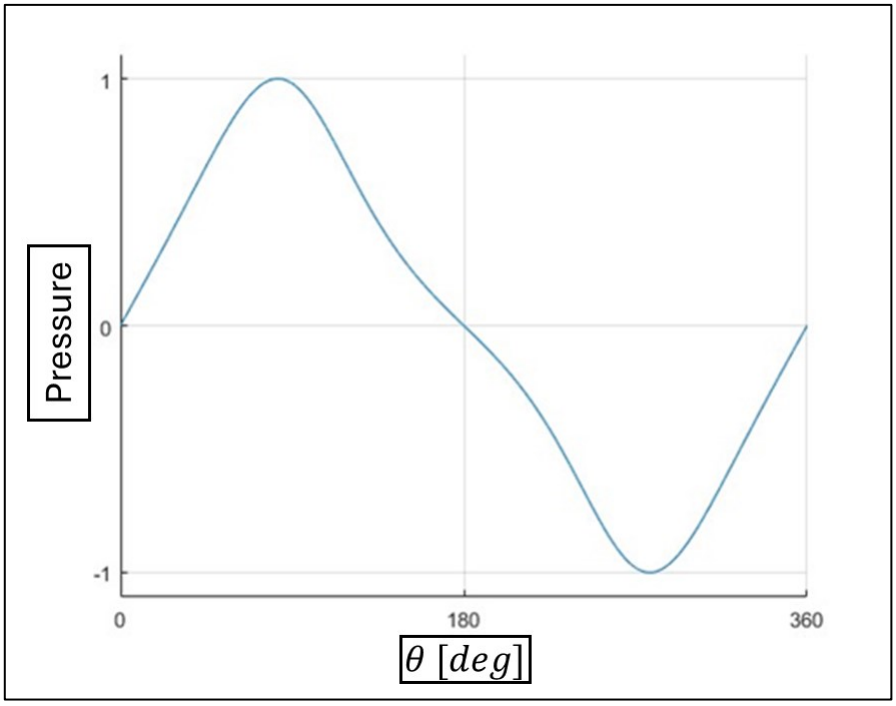

Figure 79 – Pressure distribution journal bearing -Infinite Length Approximation

For the calculation of the lifting force and viscous torque losses, the following oil boundary conditions are adopted in the model:

- **Sommerfeld's boundary condition:** The pressure distribution is evaluated without considering oil film rupture, and both positive and negative pressures are retained as they are. This assumption is valid under conditions of low bearing pressure.
  In this case, the viscous torque losses acting on the driving and driven gears are expressed as:

$$M1_{jb} = -2\left(\frac{2\,\pi\,\mu\,\omega\,r_{bearing}^{2}\,l_{jb}}{c_{jb}}\frac{2(1+2\kappa_1^2)}{(2+\kappa_1^2)(1-\kappa_1^2)^{\frac{1}{2}}}\right)$$

$$M2_{jb} = 2\left(\frac{2\,\pi\,\mu\,\omega\,r_{bearing}^{2}\,l_{jb}}{c_{jb}}\frac{2(1+2\kappa_2^2)}{(2+\kappa_2^2)(1-\kappa_2^2)^{\frac{1}{2}}}\right)$$

Eq. 134

  The multiplication factor of 2 accounts for the torque losses generated by the two journal bearings supporting either the driving or the driven gear.

  The terms κ_1 and κ_2 represent the normalised gear eccentricities for the driving and driven gears, respectively:

$$\kappa_1 = \frac{ecc_1}{c_{jb}}$$

$$\kappa_2 = \frac{ecc_2}{c_{jb}}$$

Eq. 135

  The oil dynamic viscosity $\mu = \mu(p_S)$ is evaluated at the pressure of the suction control volume.

- **Gumbel's boundary condition** : The pressure distribution is calculated without considering oil film rupture as before, but only the positive pressure in the semicircle $0 \leq \theta \leq \pi$ is considered. The negative pressure in the remaining semicircle is set to zero. This assumption is valid under conditions of fairly high pressure. It is also called the half Sommerfeld's condition.

  In this case, the viscous torque losses acting on the driving and driven gears are expressed as:

$$M1_{jb} = -2\left(\frac{2\,\pi\,\mu\,\omega\,r_{bearing}^{2}\,l_{jb}}{c_{jb}}\frac{1}{2(1-\kappa_1^2)^{\frac{1}{2}}}\left(2+\frac{3\kappa_1^2}{2+\kappa_1^2}\right)\right)$$

Eq. 136

$$M2_{jb} = 2\left(\frac{2\,\pi\,\mu\,\omega\,r_{bearing}^{2}\,l_{jb}}{c_{jb}}\frac{1}{2(1-\kappa_2^2)^{\frac{1}{2}}}\left(2+\frac{3\kappa_2^2}{2+\kappa_2^2}\right)\right)$$

The multiplication factor of 2 accounts for the torque losses generated by the two journal bearings supporting either the driving or the driven gear.

For further details regarding the definition of Eq. 134 and Eq. 136, see [26]

3.5.2. Short Length Journal Bearing Approximation

Under this assumption, the Reynolds equation takes the form:

$$\left(h^3\,\frac{\partial p}{\partial z}\right) = 6\mu\,\omega\frac{dh}{d\theta}$$

Eq. 137

For the calculation of the lifting force and viscous torque losses in the case of short journal bearings, only the **Gumbel's boundary condition** is adopted.

In this case, the viscous torque losses acting on the driving and driven gears are expressed as:

$$M1_{jb} = -2\left(\frac{2\,\pi\,\mu\,\omega\,r_{bearing}^{2}\,l_{jb}}{c_{jb}}\frac{1}{(1-\kappa_1^2)^{\frac{1}{2}}}\right)$$

Eq. 138

$$M2_{jb} = 2\left(\frac{2\,\pi\,\mu\,\omega\,r_{bearing}^{2}\,l_{jb}}{c_{jb}}\frac{1}{(1-\kappa_2^2)^{\frac{1}{2}}}\right)$$

For further details regarding the definition of *Eq. 138*, see [26]

3.5.3. Selection of Journal Bearing Approximation in the Model

In the pump model, all the previously described equations for estimating viscous torque losses are implemented, allowing the user to select the most appropriate approximation:

- The **infinite length journal bearing approximation,** suitable when $\left(\frac{l_{jb}}{d_{bearing}} > 1\right)$.
- The **short length journal bearing approximation**, applicable when $\left(\frac{l_{jb}}{d_{bearing}} < 1\right)$.

For the infinite-length approximation, the use of **Gumbel's boundary condition** is recommended, as it provides results that are more representative of real operating conditions.
In the case of an infinitely long journal bearing, and assuming the oil film remains intact (i.e., no rupture), the Reynolds equation predicts a symmetrical pressure distribution: positive pressure over the half of the clearance where it decreases, and negative pressure over the half where it increases, with equal absolute values. This behaviour is valid under low bearing pressure, a condition not typically satisfied in gear pump operation.

Under higher pressure conditions, although the positive pressure can increase without limit, the negative pressure is constrained by physical limitations. Once this limit is reached, **oil film rupture** occurs, and the pressure in the ruptured region no longer continues to decrease.

While **Sommerfeld's boundary condition** is also introduced for the infinite-length approximation, its use is **not recommended** for the simulation of real operating conditions in the present model.

3.6. Gears Contact Force

During the meshing the gears are in contact with them, and this contact force guarantee the rotation of the driven gear. The resolution of the driven gear rotation equilibrium allows the definition of the contact force applied to the driven gear. The opposite of this force is the contact force applied to the driving gear.

The total viscous losses applied to the driving and driven gear are indicated as :

$$M1_{loss} = M1_{tip} + M1_{lat} + M1_{drain} + M1_{jb}$$
$$M2_{loss} = M2_{tip} + M2_{lat} + M2_{drain} + M2_{jb} \quad \textit{Eq. 139}$$

Under the hypothesis of steady-stay conditions, the torque due to the fluid pressure and the viscous losses, applied to the driven gear is balanced by the torque due to the contact force with the driving gear:

$$M2_p + M2_{loss} - |F_{contact}|\, r_{base} = 0 \quad \textit{Eq. 140}$$

From the Eq. 140, the absolute value of the contact force is expressed as :

$$|F_{contact}| = \frac{M2_p + M2_{loss}}{r_{base}} \quad \text{Eq. 141}$$

The contact force between the gears is transmitted along the line of action, which is inclined at the pressure angle α_w.
The components of the contact force aligned with the x-axis push the driving gear towards the delivery port ($F1c_x$) and the driven gear towards the suction port ($F2c_x$).
Along the y-axis, the component of the contact force applied to the driving gear pushes the gear downwards ($F1c_y$), while that applied to the driven gear pushes it upwards ($F2c_y$).
The orientation of the contact force influences the gears eccentricities.
In the case of the driving gear, the pressure force pushes the gear towards the suction port, while the contact force acts in the opposite direction.
In the case of the driven gear, the pressure and contact forces push the gear towards the suction port; the forces therefore have the same direction.
As a consequence, the driven gear is closer to the suction port than the driving gear.
The contact force components applied to the driving and driven gear are defined as:

$$\begin{aligned} F1c_x &= |F_{contact}| \cos(\alpha_w) \\ F1c_y &= -|F_{contact}| \sin(\alpha_w) \\ F2c_x &= -|F_{contact}| \cos(\alpha_w) \\ F2c_y &= |F_{contact}| \sin(\alpha_w) \end{aligned} \quad \text{Eq. 142}$$

3.7. Torque Losses Due to Gear Meshing

The gear meshing losses are mechanical losses due to the relative sliding contact between the gear teeth.
In the model, it was decided to estimate the average meshing losses over one revolution.
The formulation of the meshing torque losses is based on the ISO/TR-14719-1 [28], which proposes an expression for the mesh power losses of gears used mainly for power transmission, rather than for gear pumps.
According to ISO/TR-14719-1, the mesh power loss is expressed as :

$$P_{mesh} = \frac{f_m T_1 n_1 \cos(\beta_w)^2}{9549\ A} \quad \text{Eq. 143}$$

Where:

- P_{mesh} is the mesh power loss [kW].
- f_m is the mesh coefficient of friction.
- T_1 is the pinion torque [N·m]. In the case of the gear pump, this corresponds to the torque applied to the driving gear.
- n_1 is the pump shaft rotation speed [rpm].

- β_w is the working helix angle of the gear; for the gear pump under study this is zero, as the gears are spur.
- A is the mesh mechanical advantage, defined in the following section.

The mesh torque loss is obtained by converting the mesh power loss into [W] and dividing it by the pump shaft angular speed [rad/s] , $\omega_1 = \frac{2\pi n_1}{60}$.

$$M_{mesh} = \frac{f_m T_1}{A} \qquad \textit{Eq. 144}$$

The torque term T_1, used for the mesh torque loss, is defined as :

$$T_1 = \left(M2_p + M2_{loss}\right) - \left(M1_p + M1_{loss}\right) \qquad \textit{Eq. 145}$$

The mesh mechanical advantage is a parameter determined by the gear geometry and is expressed as:

$$A = \frac{2\cos(\alpha_w)\,(H_s + H_t)}{H_s^2 + H_t^2} \qquad \textit{Eq. 146}$$

Where:

- α_w is the working pressure angle.
- H_s is the sliding ratio at start approach.
- H_s is the sliding ratio at the end of recess.

The sliding ratios are defined as:

$$H_s = (\tau + 1)\left[\left(\frac{r_{e,2}^2}{R_{w,2}^2} - \cos(\alpha_w)^2\right)^{0.5} - \sin(\alpha_w)\right]$$

$$H_s = \left(\frac{\tau + 1}{\tau}\right)\left[\left(\frac{r_{e,1}^2}{R_{w,1}^2} - \cos(\alpha_w)^2\right)^{0.5} - \sin(\alpha_w)\right] \qquad \textit{Eq. 147}$$

Where:

- τ is the gear ratio.
- $r_{e,2}$ is the driven gear external radius.
- $R_{w,2}$ is the driven gear working pitch radius.
- $r_{e,1}$ is the driving gear external radius.
- $R_{w,1}$ is the driving gear working pitch radius.

For an external gear pump, the driving and driven gears are identical ($\tau = 1$, $R_w = R_{w,1} = R_{w,2}$, $r_e = r_{e,1} = r_{e,2}$).
Therefore, the sliding ratios simplify to:

$$H_{st} = H_s = H_t = 2\left[\left(\frac{r_e^2}{R_w^2} - \cos(\alpha_w)^2\right)^{0.5} - \sin(\alpha_w)\right] \quad \textit{Eq. 148}$$

Substituting into Eq. 146, the mesh mechanical advantage in the case of an external gear pump can be expressed as:

$$A = \frac{2\cos(\alpha_w)}{H_{st}} \quad \textit{Eq. 149}$$

According to the ISO/TR-14719-1, the friction coefficient is defined as:

$$f_m = \frac{\upsilon^{-0.223} K^{-0.40}}{3.239\, V^{0.70}} \quad \textit{Eq. 150}$$

Where:

- $\upsilon = \upsilon(p_S)$ is the kinematic viscosity of the oil, evaluated at the suction control volume pressure [cSt].
- $V = \omega\, R_w$ is the tangential pitch line velocity [m/s].
- K is the load intensity in [N/mm^2], defined as :

$$K = \frac{1000\, T_1 (z_1 + z_2)}{2\, L_{axis}\, R_{w1}^2\, z_2} \quad \textit{Eq. 151}$$

For an external gear pump with identical gears, the load intensity simplifies to:

$$K = \frac{1000\, T_1}{L_{axis}\, R_w^2} \quad \textit{Eq. 152}$$

where L_{axis} is the gear axial length [mm].

The definition of the friction coefficient in Eq. 150 is valid for pitch line velocities in the rang $2\, m/s < V \leq 25\, m/s$ and for load intensities within $1.4\, N/mm^2 < K \leq 14\, N/mm^2$.

For the validation of the model, experimental tests were carried out using an external gear pump with a pitch radius R_w of approximately 15.95 mm. With this radius, the definition of the friction coefficient given in Eq. 150 is applicable only for rotational speeds above 1200 rpm. For this reason, the friction coefficient formulation proposed by ISO/TR-14719-1 was not adopted in the model. Instead, an alternative definition of the friction coefficient, which also remains valid at lower operating speeds, was selected from empirical formulations available in the literature.

C. Gurd and al. [29] compared different formulations of the friction coefficient to estimate the mesh power losses of a gearbox. The predicted mesh power losses were then compared with experimental data. Among these, the formulation proposed by Drozdov and Gavrikov [30] showed the best agreement with the experimental results and was therefore adopted in the gear pump model developed in this thesis.

The other formulations discussed in [29] were not considered, either because they are not applicable to identical gear meshing, or because they require additional information - such as tooth surface roughness - for the friction coefficient calculation, thereby increasing the complexity of the model.

The Drozdov and Gavrikov [30] formulation is based on experimental data obtained not from gears but from a pair of test disks. Various operating conditions were investigated, including disk rotational speed, lubricant type, contact force, and disk configurations. From these experimental results, the following equation for the definition of the friction coefficient was derived:

$$f_m = \frac{1}{0.8\, \upsilon^{\frac{1}{2}}\, V_s + V_\Sigma\ \phi(P_{max}, \upsilon) + 13.4} \qquad \textit{Eq. 153}$$

Where:

- $\phi(P_{max}, \upsilon) = 0.47 - 0.13 * 10^{-3}\, P_{max} - 0.4 * 10^{-3}\, \upsilon$.
- υ is the oil kinematic viscosity [cSt].
- V_s is the sliding velocity, calculated as the difference between the tangential velocities of the disks.
- V_Σ is the sum of the tangential velocities of the disks.
- P_{max} is the maximum contact pressure.

The definition of the friction coefficient in Eq. 153 is valid for the following ranges:

- Oil viscosity : $\upsilon \in [4\,, 500]$ cSt.
- Contact pressure: $P_{max} \in [4000\,, 20000]$ kg/cm^2.
- Summary rolling velocity : $V_\Sigma \in [3\,, 20]$ m/s.

In the case of an external gear pump, the diameter of the disks is approximated by the pitch radius of the gears, R_w. The tangential velocities of the driving and driven gears are denoted as $V_1 = R_w\, \omega$ and $V_2 = R_w\, \omega$, respectively.
The sliding velocity can be expressed as $V_s = |V_1 - V_2| = 0$, since the gears are identical and rotate at the same velocity. The sum of the velocities is expressed as $V_\Sigma = V_1 + V_2 = 2\, R_w\, \omega$.
The kinematic viscosity of the oil is evaluated at the suction control volume pressure, $\upsilon = \upsilon(p_S)$ [cSt].
The maximum contact pressure P_{max} is defined using Hertzian contact theory [31]. At the pitch point, the gear teeth are approximated as cylinders with a radius equal to the curvature radius of the tooth involute profile at the pitch point.
The maximum contact pressure, expressed in [kg/cm^2], is defined as :

$$P_{max} = \frac{4}{\pi} \frac{|F_{contact}|}{b\, L_{axis}} \frac{1}{98100} \quad \text{Eq. 154}$$

Where :

- $|F_{contact}|$ is the contact force [N].
- b is the width of the rectangular contact area [m].
- L_{axis} is the gear axial length [m].
- $\frac{1}{98100}$ is the factor used to convert the pressure from [Pa] to [kg/cm^2].

The width of the rectangular contact area is defined as:

$$b = 2\sqrt{\frac{4}{\pi}}\sqrt{\frac{|F_{contact}|}{L_{axis}} \frac{C}{r_1 + r_2}} \quad \text{Eq. 155}$$

Where:

- $C = 2\frac{1-\nu_{Poisson}^2}{E}$.
  - E is the elastic modulus of the gear material .
  - $\nu_{Poisson}$ is the Poisson's ratio.
- r_1 and r_2 are the curvature radii of the tooth involute profile at the pitch point, where $r_1 = r_2 = R_w \sin(\alpha_w)$.

In the model, the elastic modulus and Poisson's ratio are defined using the typical values for steel: $E = 210$ [GPa] and $\nu_{Poisson} = 0.3$.

Resuming, in the model the mesh torque loss is calculated using the Eq. 144 proposed by ISO/TR 14719-1 where the friction coefficient is defined using the Drozdov and Gavrikov formulation (Eq. 153).

3.8. Resultant Forces Acting on Gears and Pump Torque

The resultant forces acting on the gears are obtained as the sum of the pressure force and contact force contributions.
The components of the resultant force along the x- and y-axes, applied to the driving gear, are expressed as:

$$F1_x = F1p_x + F1c_x$$
$$F1_y = F1p_y + F1c_y \quad \text{Eq. 156}$$

For the driven gear, the components of the resultant force are expressed as:

$$F2_x = F2p_x + F2c_x$$
$$F2_y = F2p_y + F2c_y \quad \text{Eq. 157}$$

In the model, the definition of these resultant forces is crucial for calculating the gears' eccentricity. A more detailed explanation of this calculation is provided in the Sections 4.

For the pump to operate, it is necessary to supply adequate power from an external source. This power can be provided by an internal combustion engine (ICE) or an electric motor directly connected to the pump shaft. The torque supplied externally for the operation of the gear pump, as defined in the model, is:

$$M_{shaft} = -\left(M1_p + M1_{loss}\right) + \left(M2_p + M2_{loss}\right) + M_{mesh} \quad \textit{Eq. 158}$$

As the driving gear rotates counterclockwise, M_{shaft} is positive to ensure this direction of rotation.
For the pump to operate in steady-state conditions, M_{shaft} must balance the pressure and viscous losses applied to the driving gear, the pressure and viscous losses applied to the driven gear, and the mesh torque loss.
The definition of M_{shaft} is essential for estimating the hydro-mechanical efficiency of the external gear pump.

3.9. Hydro-Mechanical Efficiency

The hydro-mechanical efficiency of an external gear pump, as well as for other types of displacement pumps, is defined as:

$$\eta_{hm} = \frac{M_{th}}{M_{real}} \quad \textit{Eq. 159}$$

Where:

- M_{th} is the theoretical torque required to operate an ideal pump without losses.
- M_{real} is the actual torque required for the pump to operate. In this case, $M_{real} = M_{shaft}$.

The theoretical torque, expressed in [N·m], is given by::

$$M_{th} = \frac{V_d\,\Delta p}{20\,\pi} \quad \textit{Eq. 160}$$

Where:

- V_d is the pump displacement [cm^3/rev]
- $\Delta p = p_{DP} - p_{DS}$ is the pressure difference between delivery and suction ports [bar]

4. Journal Bearing Modelling

This section explains the modelling of journal bearings, which is crucial for defining the eccentricity of the gears.
The foundation of the journal bearing model is the ‘Mobility Method Theory’, proposed by J.K. Booker, to study the dynamic behaviour of journal bearings under variable forces [32], [33], [34], [35].

The first part presents the method applied to a dynamic case, where the force can vary in both magnitude and direction. Subsequently, the case of steady-state

conditions with a constant force is discussed, which is the approach used in the gear pump model.

4.1. Mobility Method

Consider a journal bearing subjected to a dynamic load F(t), which can vary in magnitude and whose direction changes with an angular velocity ω_{load}.

Under this force, the centre of the journal reaches a position defined by:

- ε , the eccentricity ratio, which is the ratio between the eccentricity e and the radial clearance C.
- ϕ, the attitude angle, which is the angle between the load direction and the line of centres (passing through the loci of maximum and minimum oil film thickness).

In this condition, the height of the clearance between the journal and the bearing is expressed as:

$$h = C(1 + \varepsilon\, cos\theta) \qquad \textit{Eq. 161}$$

where θ is the film coordinate (Figure 80).

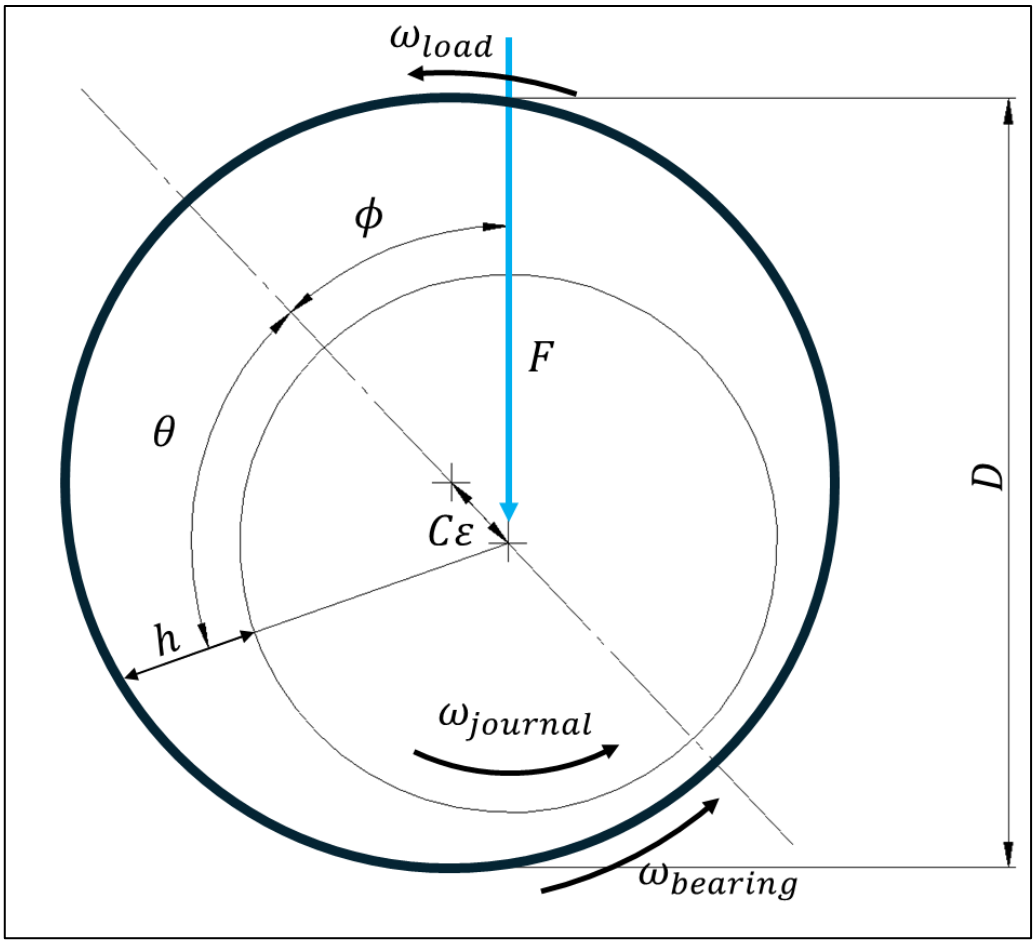

Figure 80 - Basic geometry of a journal bearing

The Reynolds equation is the fundamental equation of hydrodynamic lubrication. It describes how the pressure p is generated and distributed within a thin fluid film that separates two surfaces in relative motion—in this case, the gear shafts and the journal bearings.

The equation is derived by simplifying the Navier–Stokes equations under the "thin film" assumption, which includes the following hypotheses:

- The pressure gradient across the film thickness is negligible.
- The dominant velocities occur within the plane of the film.
- The Reynolds number within the film is low.
- The viscosity is often assumed to be constant.

In its incompressible, Newtonian, and constant-viscosity form, the Reynolds equation for a cylindrical bearing in local coordinates (z along the axis and θalong the circumference) is typically expressed as [32]:

$$\frac{\partial}{\partial\theta}\left[(1+\varepsilon\,cos\theta)^3\,\frac{\partial p}{\partial\theta}\right]+R^2\frac{\partial}{\partial z}\left[(1+\varepsilon\,cos\theta)^3\,\frac{\partial p}{\partial z}\right]= 12\,\mu\left(\frac{R}{C}\right)^2\left[\dot{\varepsilon}\,cos\theta+\,\varepsilon\left(\dot{\phi}-\bar{\omega}\right)sin\theta\right] \quad \textit{Eq. 162}$$

Where:

- $p(\theta,z)$ is the oil pressure within the clearance.
- z is the axial length coordinate, which varies in the range $\left[-\frac{L}{2},\frac{L}{2}\right]$.
- L is the axial length of the journal bearing.
- R is the bearing radius
- μ is the oil dynamic viscosity
- $\bar{\omega}=\frac{\omega_{journal}+\omega_{bearing}}{2}-\omega_{load}$ is the average angular velocity of the journal and bearing relative to the load F. In the following analysis, the case of a fixed bearing ($\omega_{\text{bearing}}=0$) is considered.

By applying the boundary conditions of atmospheric pressure at the extremities of the journal bearing, $p\left(\theta,z=\pm\frac{L}{2}\right)=0$, the Reynolds equation can be solved to determine the pressure distribution. However, analytical solutions to this equation do not exist. Therefore, certain simplifications can be introduced to obtain an approximate solution applicable under specific conditions.

Neglecting the axial flow variations in the Reynolds equation (Eq. 162) , assuming $R^2\frac{\partial}{\partial z}\left[(1+\varepsilon\,cos\theta)^3\,\frac{\partial p}{\partial z}\right]\approx 0$, the equation simplifies to:

$$\frac{\partial}{\partial\theta}\left[(1+\varepsilon\,cos\theta)^3\,\frac{\partial p}{\partial\theta}\right]+R^2\frac{\partial}{\partial z}\left[(1+\varepsilon\,cos\theta)^3\,\frac{\partial p}{\partial z}\right]= 12\,\mu\left(\frac{R}{C}\right)^2\left[\dot{\varepsilon}\,cos\theta+\,\varepsilon\left(\dot{\phi}-\bar{\omega}\right)sin\theta\right] \quad \textit{Eq. 163}$$

This approximation is known as the **Sommerfeld solution** or the **long bearing solution**, which is particularly applicable to journal bearings with$\frac{L}{D}$ >1.
Under this assumption, the Reynolds equation can be analytically integrated to obtain the pressure distribution:

$$p(\theta) = -6\,\mu\left(\frac{R}{C}\right)^2\left[\dot{\varepsilon}\,cos\theta + \left(\frac{2}{2+\varepsilon^2}\right)\,\varepsilon\left(\dot{\phi}-\bar{\omega}\right)sin\theta\right] \times\left[\frac{1}{(1+\varepsilon\,cos\theta)}+\frac{1}{(1+\varepsilon\,cos\theta)^2}\right] \qquad \textit{Eq. 164}$$

According to Eq. 164, the oil pressure inside the clearance can also assume negative values. However, under real conditions, the oil film ruptures in regions of low pressure, leading to aeration and cavitation of the oil. Therefore, to define a more realistic hydrodynamic lift force for the journal bearing, only the portion of the oil film with positive pressure is considered.

The portion of the oil film with positive pressure lies between the angles θ_1 and θ_2, which are determined by the following equations:

$$\begin{gathered}(2+\varepsilon^2)\,\dot{\varepsilon}\,cos\theta_1 + 2\;\varepsilon\left(\dot{\phi}-\bar{\omega}\right)sin\theta_1 = 0 \\ (2+\varepsilon^2)\,\dot{\varepsilon}\,sin\theta_1 - 2\;\varepsilon\left(\dot{\phi}-\bar{\omega}\right)cos\theta_1 \geq 0 \\ \theta_2 = \theta_1 + \pi\end{gathered} \qquad \textit{Eq. 165}$$

Another simplification of the Reynolds equation is the **Ocvirk solution**, or **short bearing solution**, which is applicable to journal bearings with $\frac{L}{D}$ <1.
In this approximation, the term representing variations in circumferential pressure flow is neglected, $\frac{\partial}{\partial\theta}\left[(1+\varepsilon\,cos\theta)^3\;\frac{\partial p}{\partial\theta}\right]=0$.
The Reynolds equation simplifies to:

$$R^2\frac{\partial}{\partial z}\left[(1+\varepsilon\,cos\theta)^3\;\frac{\partial p}{\partial z}\right] = 12\,\mu\left(\frac{R}{C}\right)^2\left[\dot{\varepsilon}\,cos\theta + \varepsilon\left(\dot{\phi}-\bar{\omega}\right)sin\theta\right] \qquad \textit{Eq. 166}$$

Under this assumption, the Reynolds equation can be analytically integrated to obtain the pressure distribution:

$$p(\theta,z) = -6\,\mu\left(\frac{R}{C}\right)^2\left(\frac{L}{D}\right)^2\left[1-\left(\frac{2z}{L}\right)^2\right]\times\left[\frac{\dot{\varepsilon}\,cos\theta+\varepsilon\left(\dot{\phi}-\bar{\omega}\right)sin\theta}{(1+\varepsilon\,cos\theta)^3}\right] \qquad \textit{Eq. 167}$$

In this case, the portion of the oil film with positive pressure lies between the angles θ_1 and θ_2, which are determined by the following equations:

$$\dot{\varepsilon}\, cos\theta_1 + \ \varepsilon\left(\dot{\phi} - \bar{\omega}\right) sin\theta_1 = 0$$

$$\dot{\varepsilon}\, sin\theta_1 - \ \varepsilon\left(\dot{\phi} - \bar{\omega}\right) cos\theta_1 \geq 0 \qquad \textit{Eq. 168}$$

$$\theta_2 = \theta_1 + \pi$$

4.2. Equations of motion

The force F applied to the journal is balanced by the hydrodynamic lift force generated by the oil in the journal bearing clearance. The equilibrium between these two forces, which are parallel and perpendicular to the line of centres (passing through the loci of maximum and minimum oil film thickness), can be expressed as:

$$F_\varepsilon = F\, cos\phi = \ -\int_A p \cos\theta \ dA \qquad \textit{Eq. 169}$$

$$F_\theta = -\, F\, cos\phi = \ -\int_A p \sin\theta \ dA$$

In the case of complete oil films, the integration is carried out over the entire bearing surface. For ruptured films, however, the integration is limited to the positive portions of the pressure distribution.

By substituting the pressure distribution expressions obtained from the long bearing solution (Eq. 164) or the short bearing solution (Eq. 167) into Eq. 169, and assuming the applied load F is known, the corresponding journal motion can be determined from the following inverted equations:

$$\dot{\varepsilon} = \frac{F\ (C/R)^2}{\mu\ L\ D}\ M_\varepsilon\left(\varepsilon, \phi, \frac{L}{D}, \theta_1, \theta_2\right) \qquad \textit{Eq. 170}$$

$$\varepsilon\left(\dot{\phi} - \bar{\omega}\right) = \frac{F\ (C/R)^2}{\mu\ L\ D}\ M_\phi\left(\varepsilon, \phi, \frac{L}{D}, \theta_1, \theta_2\right)$$

Here, θ_1 and θ_2 are equal to 0 and 2π , respectively, under the assumption of complete oil films. For ruptured films, $\theta_1$and θ_2 are determined by Eq. 165 when using the long bearing solution, and by Eq. 168 when using the short bearing solution

The terms M_ε and $M_\phi$are dimensionless functions of several variables, and their formulations are defined by J. Booker based on the simplifications adopted.

Given the applied force F, the definitions of M_ε and M_ϕ, and the initial conditions $\varepsilon(t=0)$and $\phi(t=0)$, the equations in Eq. 170 can be numerically integrated to determine the trajectory of the journal centre.

4.2.1. M_ε and M_ϕ – Long Journal Bearing Solution : General case

This section presents the formulation of the terms M_ε and M_ϕ for the **Sommerfeld solution** in the general case, where the load is dynamic in both magnitude and direction.

In general:

$$M_\varepsilon = \frac{B_{22}\cos\phi + B_{12}\sin\phi}{3\,(B_{11}\,B_{22} - B_{12}\,B_{21})\Pi}$$

$$M_\phi = -\frac{B_{21}\cos\phi + B_{11}\sin\phi}{3\,(B_{11}\,B_{22} - B_{12}\,B_{21})\Pi} \qquad \textit{Eq. 171}$$

Where:

$$B_{11} = (2\,J_2^{02} + \varepsilon\,J_2^{03})$$

$$B_{21} = (2\,J_2^{11} + \varepsilon\,J_2^{12})$$

$$B_{12} = \left(\frac{2}{2+\varepsilon^2}\right)(2\,J_2^{11} + \varepsilon\,J_2^{12}) \qquad \textit{Eq. 172}$$

$$B_{22} = \left(\frac{2}{2+\varepsilon^2}\right)(2\,J_2^{20} + \varepsilon\,J_2^{21})$$

The integrals $J_n^{lm}$are defined as [36]:

$$J_n^{lm} = \int_{\theta_1}^{\theta_2} \frac{\sin^l\theta\cos^m\theta}{(1+\varepsilon\cos\theta)^n}\,d\theta \qquad \textit{Eq. 173}$$

The term Π is given by:

$$\Pi = 1 - \frac{\tanh(\lambda\, L/D)}{\lambda\, L/D} \qquad \textit{Eq. 174}$$

where:

$$\lambda^2 = \frac{S^2\, A_1 + 2\, S\, A_2 + A_3}{S^2\, A_4 + 2\, S\, A_5 + A_6} \qquad \textit{Eq. 175}$$

and

$$S = -\frac{B_{22}\cos\phi + B_{12}\sin\phi}{B_{11}\sin\phi + B_{21}\cos\phi} \qquad \textit{Eq. 176}$$

The coefficients A_1, A_2, A_3, A_4, A_5, and $A_6$are defined as:

$$\begin{aligned} A_1 &= J_3^{20} \\ A_2 &= \frac{-3\varepsilon}{(2+\varepsilon^2)} J_3^{10} - J_3^{11} \\ A_3 &= \frac{9\varepsilon^2}{(2+\varepsilon^2)^2} J_3^{00} + \frac{6\,\varepsilon}{(2+\varepsilon^2)} J_3^{01} + J_3^{02} \\ A_4 &= \frac{1}{4}(J_1^{02} + 3\, J_0^{02} + \varepsilon\, J_0^{03}) \\ A_5 &= \frac{1}{2(2+\varepsilon^2)}(J_1^{11} + 3\, J_0^{11} + \varepsilon\, J_0^{12}) \\ A_6 &= \frac{1}{2(2+\varepsilon^2)^2}(J_1^{20} + 3\, J_0^{20} + \varepsilon\, J_0^{21}) \end{aligned} \qquad \textit{Eq. 177}$$

For the **2π film**, when $\theta_1 = 0$ and $\theta_2 = 2\pi$, the expressions for M_ε, M_ϕ, and λ^2 simplify as follows:

$$\begin{aligned} M_\varepsilon &= \frac{(1-\varepsilon^2)^{3/2}}{6\pi}\frac{\cos\phi}{\Pi} \\ M_\phi &= \frac{-(1-\varepsilon^2)^{\frac{1}{2}}}{6\pi}\left(\frac{2+\varepsilon^2}{2}\right)\frac{\sin\phi}{\Pi} \\ \lambda^2 &= 2\,(1-G^2)\left[\frac{2G^2\,\cot^2\phi\, + (3-G^2)}{G^4\,(2+G-3G^3)\,\cot^2\phi\, + G\,(1-G)(5+3G)}\right] \end{aligned} \qquad \textit{Eq. 178}$$

where:

$$G = (1-\varepsilon^2)^{1/2} \qquad \textit{Eq. 179}$$

For the **π film ,** $\theta_1$and θ_2 are determined by Eq. 165, and the general expression (Eq. 171-Eq. 177) apply.

4.2.2 M_ε and M_ϕ – Short Journal Bearing Solution : General case

This section presents the formulation of the terms M_ε and M_ϕ for the **Ocvirk solution** in the general case, where the load is dynamic in both magnitude and direction.

For the **2π film**, when $\theta_1 = 0$ and $\theta_2 = 2\pi$, M_ε and M_ϕ are defined as:

$$M_\varepsilon = \frac{(1-\varepsilon^2)^{5/2}\cos\phi}{2\pi\,(1+2\varepsilon^2)(L/D)^2}$$
$$M_\phi = \frac{-(1-\varepsilon^2)^{5/2}\sin\phi}{2\pi\,(L/D)^2} \qquad \textit{Eq. 180}$$

For the **π film ,** θ_1 and θ_2 are determined by Eq. 168, and M_ε and M_ϕ are defined as:

$$M_\varepsilon = \frac{(1-\xi)^{5/2}}{\pi(L/D)}\cos\phi - \frac{4\eta(1-\xi)^{3/2}}{\pi(L/D)}\sin\phi$$
$$M_\phi = -\frac{(1-\xi)^{5/2}}{\pi(L/D)}\sin\phi - \frac{4\eta(1-\xi)^{3/2}}{\pi(L/D)}\cos\phi \qquad \textit{Eq. 181}$$

where

$$\xi = \varepsilon\cos\phi$$
$$\eta = \varepsilon\sin\phi \qquad \textit{Eq. 182}$$

Eq. 181 is valid for $F \geq 0$. It can also be used for $F \leq 0$ if ξ and η are replaced by $(-\xi)$ and $(-\eta)$, respectively.

4.2.3. M_ε and M_ϕ – Long Journal Bearing Solution : Steady – State Conditions

This section presents the formulation of the terms M_ε and M_ϕ for the Sommerfeld solution under steady-state conditions, where the load is constant and $\dot{\varepsilon} = \dot{\phi} = 0$.

For the **2π film,** under steady-state conditions, the motion equation Eq. 170 simplifies to:

$$\phi = \frac{\pi}{2}$$ *Eq. 183*

The relationship between the applied load and the eccentricity is given by:

$$\frac{F(C/R)^2}{\bar{\omega}\mu LD} = \frac{6\pi\varepsilon}{(1-\varepsilon^2)^{1/2}}\left(\frac{2}{2+\varepsilon^2}\right)\Pi$$ *Eq. 184*

For the $\boldsymbol{\pi}$ **film,** under steady-state conditions, the portion of the oil film with positive pressure lies between the angles $\theta_1 = 0$and $\theta_2 = \pi$. In this case, the motion equation Eq. 170 gives:

$$\phi = \tan^{-1}\left(\frac{\pi}{2}\frac{(1-\varepsilon^2)^{1/2}}{\varepsilon}\right)$$ *Eq. 185*

The relationship between the applied load and the eccentricity is expressed as:

$$\frac{F(C/R)^2}{\bar{\omega}\mu LD} = \left(\frac{2}{2+\varepsilon^2}\right)\left(\frac{3\varepsilon}{1-\varepsilon^2}\right)[\pi^2\,(1-\varepsilon^2) + 4\varepsilon^2]^{1/2}\,\Pi$$ *Eq. 186*

The term Π of Eq. 184 and Eq. 186 are defined using Eq. 174, where:

$$\lambda^2 = \frac{2(1+G)(3-G^2)}{G\,(5+3G)}$$ *Eq. 187*

4.2.4. M_ε and M_ϕ – Short Journal Bearing Solution : Stady-State Conditions

This section presents the formulation of the terms $M_\varepsilon$and M_ϕ for the Ocvirk solution under steady-state conditions, where the load is constant and $\dot{\varepsilon} = \dot{\phi} = 0$.

For the **2**$\boldsymbol{\pi}$ **film,** under steady-state conditions, the motion equation Eq. 170 simplifies to:

$$\phi = \frac{\pi}{2}$$ *Eq. 188*

The relationship between the applied load and the eccentricity is given by:

$$\frac{F(C/R)^2}{\bar{\omega}\mu LD} = \frac{2\pi\varepsilon\,(L/D)^2}{(1-\varepsilon^2)^{3/2}}$$ *Eq. 189*

For the $\boldsymbol{\pi}$ **film,** under steady-state conditions, the portion of the oil film with positive pressure lies between the angles $\theta_1 = 0$and $\theta_2 = \pi$. In this case, the motion equation Eq. 170 gives:

$$\phi = \tan^{-1}\left(\frac{\pi}{4}\frac{(1-\varepsilon^2)^{1/2}}{\varepsilon}\right) \qquad \textit{Eq. 190}$$

The relationship between the applied load and the eccentricity is expressed as:

$$\frac{F(C/R)^2}{\bar{\omega}\mu LD} = \frac{\varepsilon\,(L/D)^2}{(1-\varepsilon^2)^2}[\pi^2\,(1-\varepsilon^2)+16\varepsilon^2]^{1/2} \qquad \textit{Eq. 191}$$

4.3. Use of the Mobility Method in the Gear Pump Model

One key assumption in the gear pump model is that the load applied to the gears, for determining their eccentricity, is constant.

During gear rotation, the resultant forces acting on the gears are periodic, with a period of $2\pi/(\omega z)$. Consequently, under steady-state conditions, the gear eccentricities also vary with the same period. Over one complete revolution of the gear, the gear centre traces a closed path that is repeated z times.

However, a fundamental assumption in the model is that, under steady-state conditions, the gear adopts a fixed eccentricity. This fixed eccentricity generates a hydrodynamic lift force in the journal bearing, which is assumed to balance the applied force on the gear. The applied force is considered constant and equal to the average force acting over one full rotation. This average force is equivalent to the mean force acting over $1/z$ of a rotation.

Based on this assumption, the formulation of the Mobility Method under steady-state conditions, as presented in Sections 0 and 0, is used to define the gear eccentricities.

The **long bearing solution** is applied when $L/D > 1$, while the **short bearing solution** is used when $L/D < 1$. The assumption of a π-film is preferred, as it provides more realistic results.

The modulus of the forces applied to the gears is expressed as:

$$F1 = \sqrt{F1_x^2 + F1_y^2} \qquad \textit{Eq. 192}$$

$$F2 = \sqrt{F2_x^2 + F2_y^2}$$

Figure 81 illustrates a typical trend of the forces $F1$, which is similar to the trend observed for $F2$, in the case of a gear pump operating under steady-state conditions with fixed eccentricities. The forces are defined for an 8.2 cc pump operating at $n = 1500$ rpm with a delivery pressure of 142 bar. Under these conditions, the gears complete one rotation in 0.04 seconds, and the period of the force is calculated as $\frac{60}{1500 \cdot 12} = 0.0333\ldots$ seconds, where 12 is the number of gear teeth.

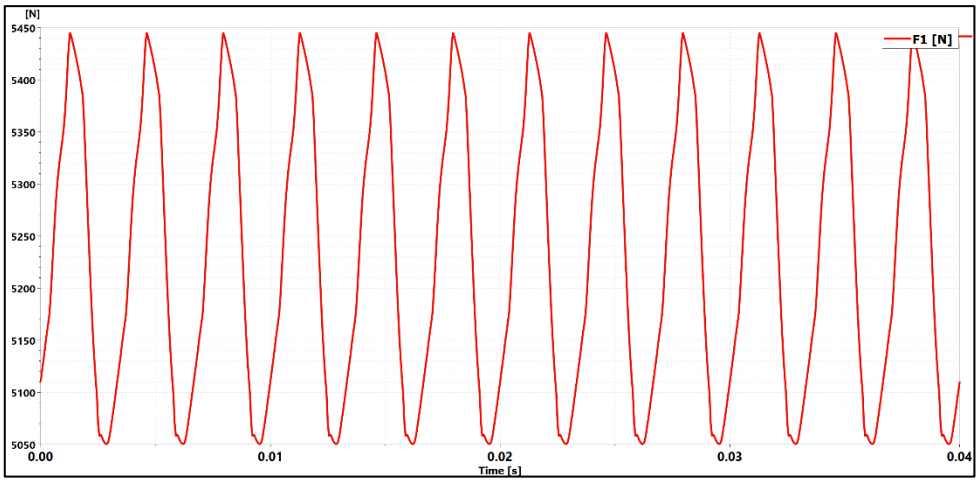

Figure 81 - Typical trend of the forces applied to the gears

The force values used for the application of the Mobility Method are:

- $F1_{\text{avg}}$: the average force applied to the driving gear over $1/z$ of a rotation.
- $F2_{\text{avg}}$: the average force applied to the driven gear over $1/z$ of a rotation.

Using the Mobility Method, the following parameters are obtained:

- ε_1: the eccentricity ratio of the driving gear.
- ϕ_1: the attitude angle of the driving gear, which is the angle between the direction of the load $F1_{\text{avg}}$ and the line of centres.
- ε_2: the eccentricity ratio of the driven gear.
- ϕ_2: the attitude angle of the driven gear, which is the angle between the direction of the load $F2_{\text{avg}}$and the line of centres.

With this information, the position of the gear centres relative to the applied load is determined. To define the centre positions of the driving gear (O_{g1}) and the driven gear (O_{g2}) in the reference systems $O_{jb1}x_{jb1}y_{jb1}$and $O_{jb2}x_{jb2}y_{jb2}$, refer to Figure 82.

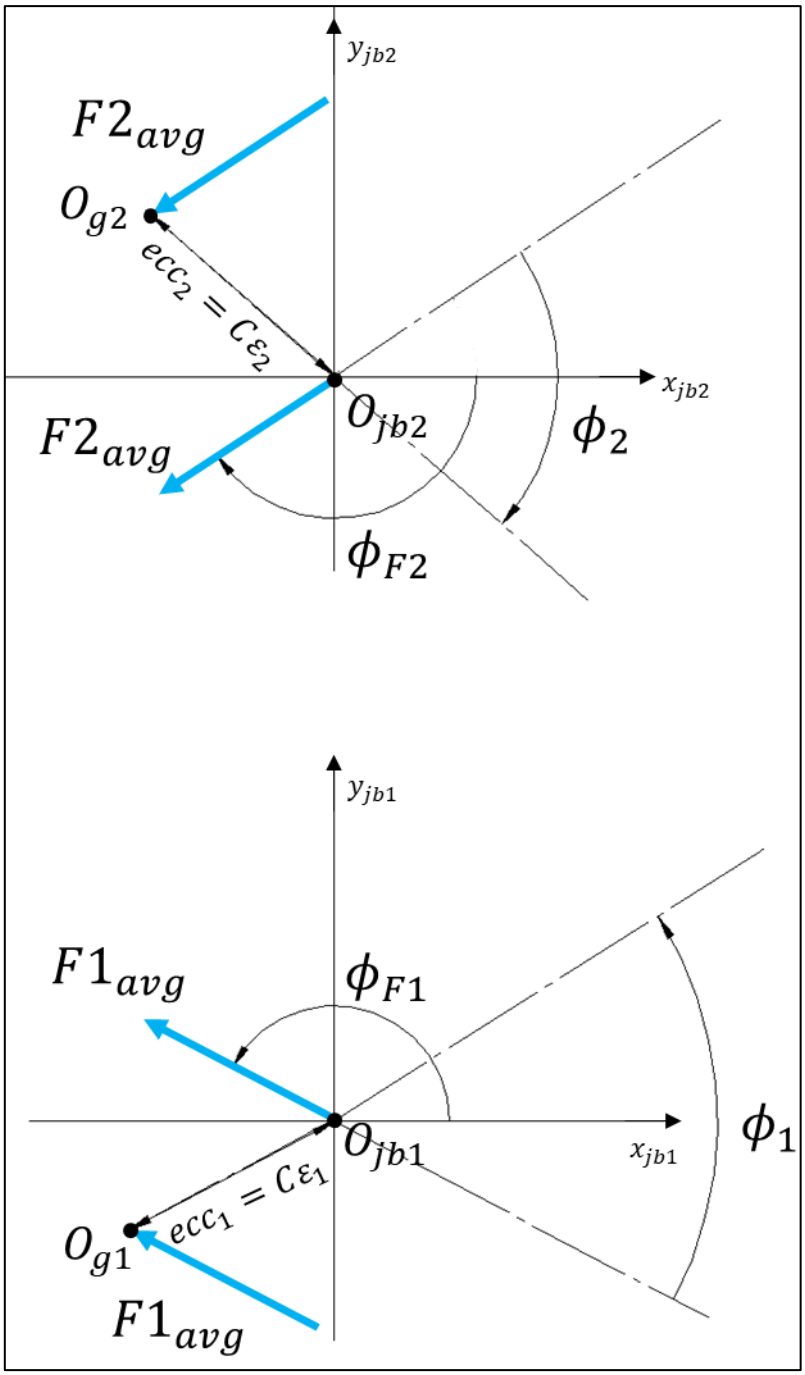

Figure 82 – Gears eccentricities in the reference systems $O_{jb1}x_{jb1}y_{jb1}$ and $O_{jb2}x_{jb2}y_{jb2}$

The term ϕ_{F1} represents the angle between the direction of the force $F1_{\text{avg}}$ and the x-axis (x_{jb1}), while ϕ_{F2} represents the angle between the direction of the force $F2_{\text{avg}}$ and the x-axis (x_{jb2}).

The centre position of the driving gear (O_{g1}) with respect to the reference system $O_{jb1}x_{jb1}y_{jb1}$ is expressed as:

$$ecc_{x1} = \varepsilon_1 \, c_{jb} \cos(\phi_{F1} + \phi_1)$$
$$ecc_{y1} = \varepsilon_1 \, c_{jb} \sin(\phi_{F1} + \phi_1)$$ *Eq. 193*

The centre position of the driven gear (O_{g2}) with respect to the reference system $O_{jb2}x_{jb2}y_{jb2}$is expressed as:

$$ecc_{x2} = \varepsilon_2 \, c_{jb} \cos(\phi_{F2} + \phi_2)$$
$$ecc_{y2} = \varepsilon_2 \, c_{jb} \sin(\phi_{F2} + \phi_2)$$ *Eq. 194*

The terms ϕ_{F1}, ϕ_{F2}, ϕ_1, and ϕ_2 are positive for counterclockwise rotation and negative otherwise.

4.4. Iterative Process for Eccentricity Definition in the Simcenter Amesim Model

The equation of the Mobility Method under steady-state conditions can be rewritten in a simplified form as:

$$\frac{F(C/R)^2}{\bar{\omega}\mu LD} = f(\varepsilon, L/D)$$ *Eq. 195*

Where $f(\varepsilon, L/D)$ can take different forms depending on the solution and the assumptions regarding the oil film extension, as presented in the previous Sections 0 and 0 .

From Eq. 195, it is evident that the gear eccentricity depends on the load F. In an external gear pump, the load is defined based on the oil pressure within the pump's chamber, which, in turn, depends on the working conditions and the volumetric leakage of the pump.

In particular, the volumetric leakage at the tooth tip is strongly influenced by the gear eccentricity. Consequently, the load on the gear is also dependent on the gear's eccentricity.
Eq. 195 can be rewritten to highlight this dependence:

$$\frac{F(\varepsilon)\,(C/R)^2}{\bar{\omega}\mu LD} = f(\varepsilon, L/D)$$ *Eq. 196*

As a result, defining the gear eccentricities requires an iterative process.

Figure 83 illustrates the layout of the external gear pump model implemented in Simcenter Amesim. The model is composed of various blocks, each performing a specific function and exchanging information with the others.

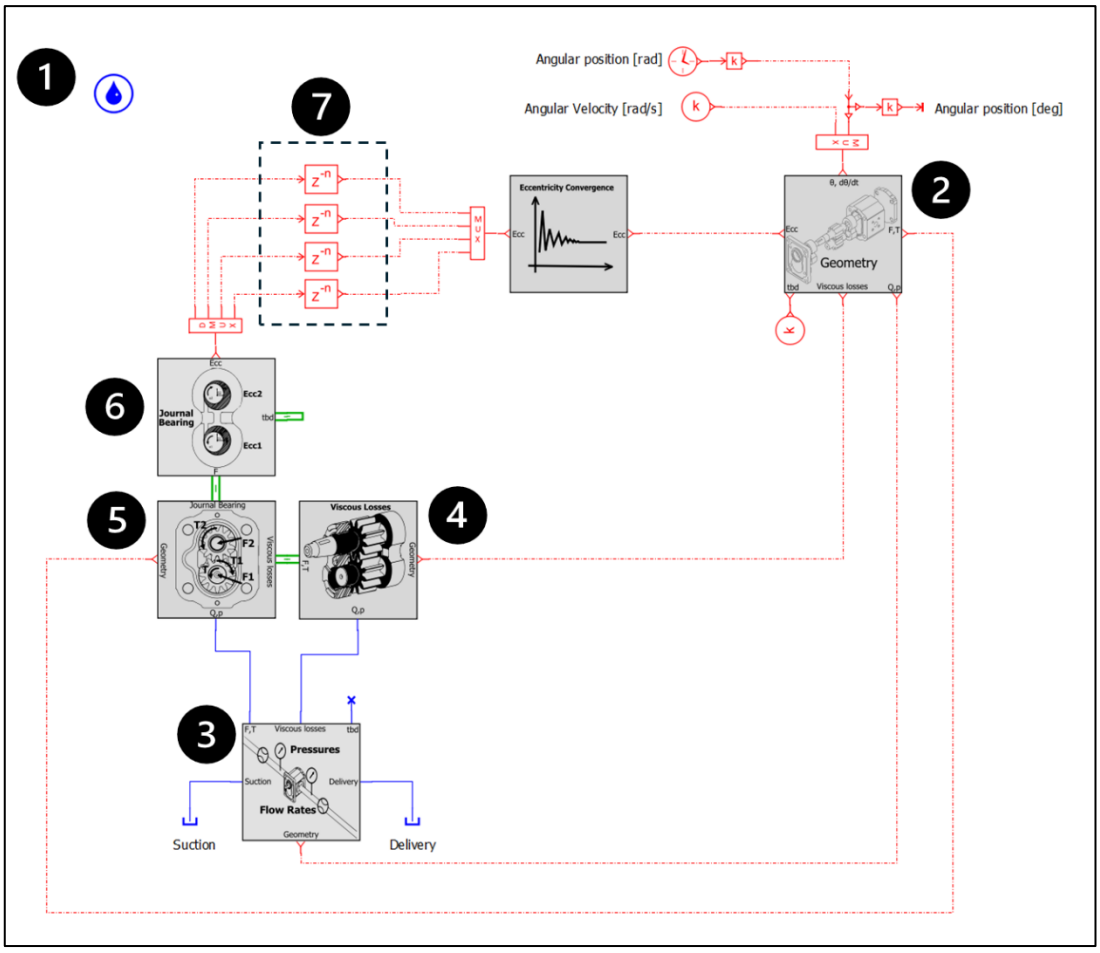

Figure 83 – Simcenter Amesim Model for Calculating Gears Eccentricities

Detailed descriptions of the blocks are provided below:

1. **Oil Model:**
   This block represents the properties and behaviour of the oil used in the pump.
2. **Geometry Block:**
   This element receives the pump velocity, angular position, and gear eccentricities as inputs. It calculates all the geometrical information necessary to evaluate the pump's performance.
3. **Fluid Dynamics Block:**
   This element takes the working conditions (pump speed, delivery pressure, and suction pressure) and the geometry data as inputs. It calculates the volumetric performance of the gear, including the flow rate at the suction and delivery ports, the pressure in the pump chambers, and all volumetric leakages.
4. **Viscous Losses Block:**
   This block receives the pump speed, the pressure in the pump control volume, and the geometric information of the gaps as inputs. It calculates the viscous losses of the pump.
5. **Forces and Torque Block**:
   This block receives as inputs the pressure in the control volume, the pump

speed, the viscous losses, and the geometrical information required to define the forces and torques generated by the oil pressure. As outputs, this element calculates the forces (pressure and contact forces) and the torques (pressure torque and meshing torque) acting on the gears. By summing the contributions of the different torques, it also determines the total torque required for the pump to operate.

6. **Journal Bearing Block**:
   This block receives as inputs the forces acting on the gears and the pump speed. Using the Mobility Method formulation under steady-state conditions, it evaluates the gear eccentricities.
7. **Delay Blocks**:
   These blocks introduce a time delay of $60/(nz)$ seconds between the eccentricity values calculated by the Journal Bearing Block and those sent to the Geometry Block. The purpose of this delay is explained in the following sections.

To introduce the iterative process, additional information is provided on the Journal Bearing Block.
This block specifically receives, from the Forces and Torque Block, the values of the forces applied to the driving and driven gears: $F1_x(t)$, $F1_y(t)$, $F2_x(t)$, and $F2_y(t)$.
It is important to highlight the time dependence of these forces. Simcenter Amesim integrates the equations underlying the model in the time domain, with a simulation time defined by the user.
In our case, $t \in [0, k \cdot 60/n]$ seconds, where k is a positive integer. Within this time range, the simulation executes k complete rotations.
The Journal Bearing Block calculates the eccentricities using the average force values over a period of $\frac{(60/n)}{z}$ seconds.
The average force values for the driving gear are defined as:

$$F1_{x,avg,i} = \left(\int_{T_{i-1}}^{T_i} F1_x\, dt - \int_0^{T_{i-1}} F1_x\, dt\right)\frac{1}{T_i - T_{i-1}}$$

$$F1_{y,avg,i} = \left(\int_{T_{i-1}}^{T_i} F1_y\, dt - \int_0^{T_{i-1}} F1_y\, dt\right)\frac{1}{T_i - T_{i-1}} \qquad \textit{Eq. 197}$$

$$F1_{avg,i} = \sqrt{F1_{x,avg,i}^2 + F1_{y,avg,i}^2}$$

Where:

- $T_i = \frac{60}{nz} \cdot i$ seconds. The i-th period refers to the time range $[T_i, T_{i+1}]$.
- $F1_{x,\mathrm{avg},i}$ is the average force along the x-axis applied to the driving gear during the i-th period, evaluated over the time range $[T_{i-1}, T_i]$.
- $F1_{y,\mathrm{avg},i}$ is the average force along the y-axis applied to the driving gear during the i-th period, evaluated over the time range $[T_{i-1}, T_i]$.

- $F1_{\text{avg},i}$ is the total average force applied to the driving gear during the i-th period, evaluated over the time range $[T_{i-1}, T_i]$.

For $i = 0$, as there is no preceding period, the average forces are defined as:

$$F1_{x,avg,0} = F1_x(t = 0)$$
$$F1_{y,avg,0} = F1_y(t = 0)$$
$$F1_{avg,0} = \sqrt{F1_{x,avg,0}^2 + F1_{y,avg,0}^2} \quad \textit{Eq. 198}$$

Similarly, the average force values for the driven gear are defined as:

$$F2_{x,avg,i} = \left(\int_{T_{i-1}}^{T_i} F2_x\, dt - \int_0^{T_{i-1}} F2_x\, dt\right)\frac{1}{T_i - T_{i-1}}$$
$$F2_{y,avg,i} = \left(\int_{T_{i-1}}^{T_i} F2_y\, dt - \int_0^{T_{i-1}} F2_y\, dt\right)\frac{1}{T_i - T_{i-1}} \quad \textit{Eq. 199}$$
$$F2_i = \sqrt{F2_{x,avg,i}^2 + F2_{y,avg,i}^2}$$

For $i = 0$, the average forces are defined as:

$$F2_{x,avg,0} = F2_x(t = 0)$$
$$F2_{y,avg,0} = F2_y(t = 0) \quad \textit{Eq. 200}$$
$$F2_{avg,0} = \sqrt{F2_{x,avg,0}^2 + F2_{y,avg,0}^2}$$

The Journal Bearing Block calculates the gear eccentricities using the previously defined average force values:

- $ecc_{x1,i}$:the x-axis component of the driving gear eccentricity during the i-th period, calculated using the average forces $F1_{x,avg,i}$ and $F1_{y,avg,i}$.
- $ecc_{y1,i}$: the y-axis component of the driving gear eccentricity during the i-th period, calculated using the average forces $F1_{x,avg,i}$ and $F1_{y,avg,i}$.
- $ecc_{x2,i}$: the x-axis component of the driven gear eccentricity during the i-th period, calculated using the average forces $F2_{x,avg,i}$ and $F2_{y,avg,i}$.
- $ecc_{y2,i}$ the y-axis component of the driven gear eccentricity during the i-th period, calculated using the average forces $F2_{x,avg,i}$ and $F2_{y,avg,i}$.

At the 0-th period, the eccentricities are fixed by the user as follows:

$$ecc_{x1,0} = \overline{ecc_{x1}}$$
$$ecc_{y1,0} = \overline{ecc_{y1}}$$
$$ecc_{x2,0} = \overline{ecc_{x2}} \quad \textit{Eq. 201}$$
$$ecc_{y2,0} = \overline{ecc_{y2}}$$

It is important to note that the eccentricity values for the i-th period $[T_i, T_{i+1}]$ are calculated using the average forces from the $(i-1)$-th period $[T_{i-1}, T_i]$.

The eccentricities defined by the Journal Bearing Block during the i-th period cannot be directly sent to the Geometry Block, as this would create an algebraic loop in Simcenter Amesim, significantly reducing simulation performance.

The term "algebraic loop" refers to a specific type of model topology where, at a given time, certain elements of the model cannot be evaluated due to the direction of information exchange at the ports. Algebraic loops are common in many Simcenter Amesim systems and arise from the interaction between the model topology (i.e., how submodels are interconnected) and the submodel I/O tables (i.e., how variables are defined at the ports of each submodel). This interaction can result in a direct feed-through effect, where some outputs require corresponding component inputs to be defined first, which themselves depend on the value of the desired output. The set of lines and components involved in this direct feed-through forms what is known as an algebraic loop.

A simple example of an algebraic loop is shown in Figure 84. In this case, the input of the model x is equal to the output of the model y, creating a direct connection between the input and output of the model. The equation defining the output is $y = f(x) = f(y)$.

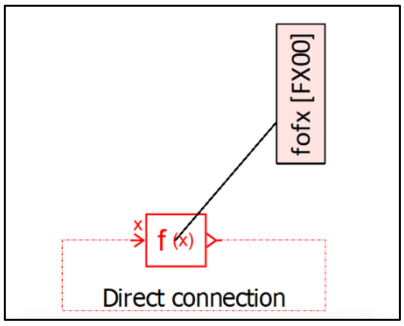

Figure 84 - Simple example of an algebraic loop

In the external gear pump model, to avoid algebraic loops and improve simulation performance, a discrete delay is introduced between the Journal Bearing Block and the Geometry Block using Delay Blocks.

Each element of the Delay Block receives one component of the gear eccentricities and introduces a delay of $60/(nz)$seconds. During the 0-th period, the Delay Block outputs the eccentricity values defined by the user (Eq. 201).

At the i-th period, the Geometry Block receives from the Delay Block the eccentricity values calculated by the Journal Bearing Block during the $(i-1)$-th period, which were based on the average forces from the $(i-2)$-th period.

In the simulation, each i-th period can be considered a step in the iterative process. For every gear rotation, there are z periods, corresponding to z steps of the iterative process.

By defining the total simulation time, it is possible to determine the total number of steps in the iterative process.

In Figure 85 and Figure 86, an example of the trend of the x-axis component of the driving gear eccentricity at different steps is shown. The example considers an 8.2 cc pump with gears having 12 teeth, operating at a delivery pressure of 142 bar and a speed of 1500 rpm. At this speed, the pump completes one rotation in 0.04 seconds. With a simulation time of 0.08 seconds, the number of iterative steps is 24.

Figure 85 illustrates the eccentricity along the x-axis of the driving gear. The red curve represents the eccentricity calculated by the Journal Bearing Block, while the blue curve shows the eccentricity received by the Geometry Block via the Delay Block. In this case, the time delay is $\frac{60}{1500/12} = 0.0033$ seconds. It is important to note that the curves exhibit a step-like trend, maintaining a constant value during each period.

In Figure 86, the red curve represents the x-axis component of the force applied to the driving gear, $F1_x$, while the blue curve represents the average force, $F1_{x,\text{avg}}$. In the time range from 0 to 0.0033 seconds, the average force is equal to $F1_x(t = 0)$. It is worth noting that the $F1_{x,\text{avg}}$ curve also exhibits a step-like trend, maintaining a constant value during each period.

As shown in the figure, after five steps, the eccentricities reach a stable value, as does the average force value. Meanwhile, the force $F1_x$ achieves a periodic trend.

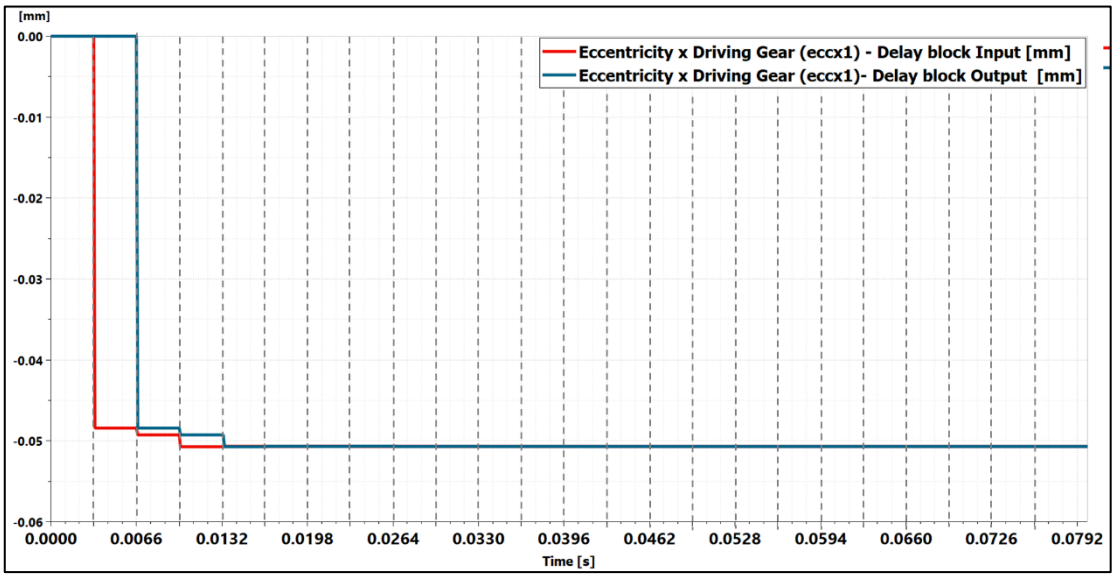

Figure 85 - Eccentricity Along the X-Axis of the Driving Gear During the Iterative Process: Input and Output of the Delay Block

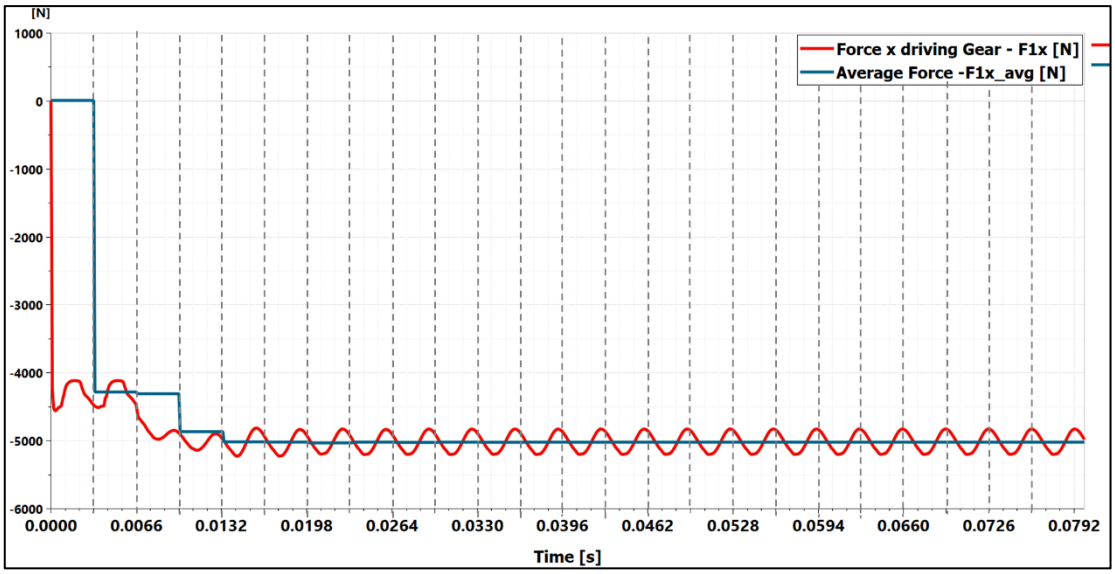

Figure 86 - X-Axis Component of the Force on the Driving Gear and Its Average Value During the Iterative Process

Figure 87 illustrates the convergence of the eccentricity components for both the driving and driven gears.

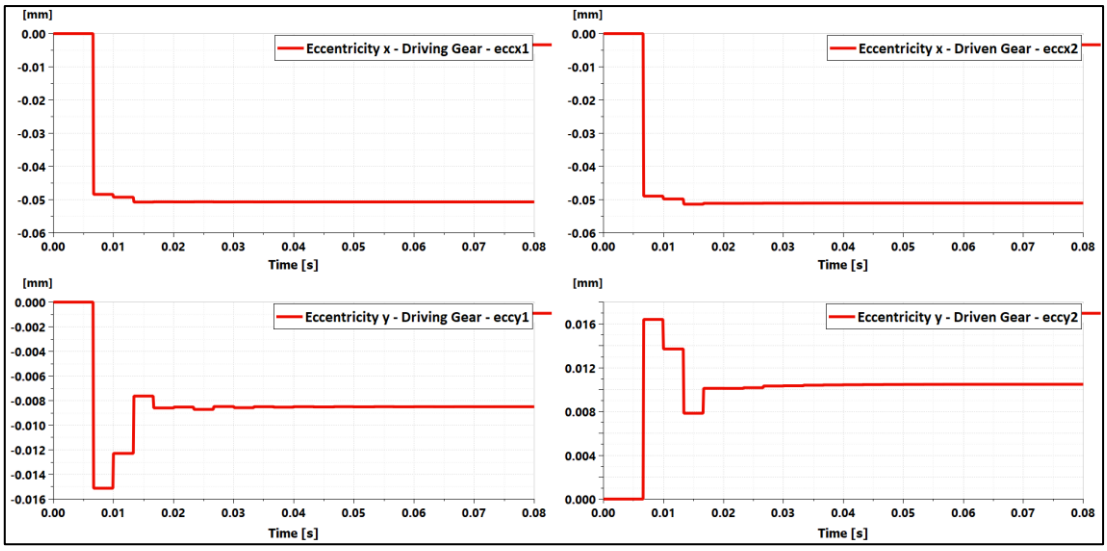

Figure 87 – Eccentricities convergence

In the iterative process implemented in the gear pump model, there is no convergence error threshold to automatically interrupt the simulation. Instead, the user defines the number of iterative steps and evaluates, at the end of the simulation, whether convergence has been achieved or if it is necessary to repeat the simulation with additional steps.

When the eccentricities of the gears are defined for a specific working condition, an additional simulation is required to evaluate the pump's performance under steady-state conditions. In this case, the eccentricity values input to the Geometry Block are fixed and set equal to the values obtained from the iterative process (see Figure 88).

In this simulation, the Delay Blocks are not included.

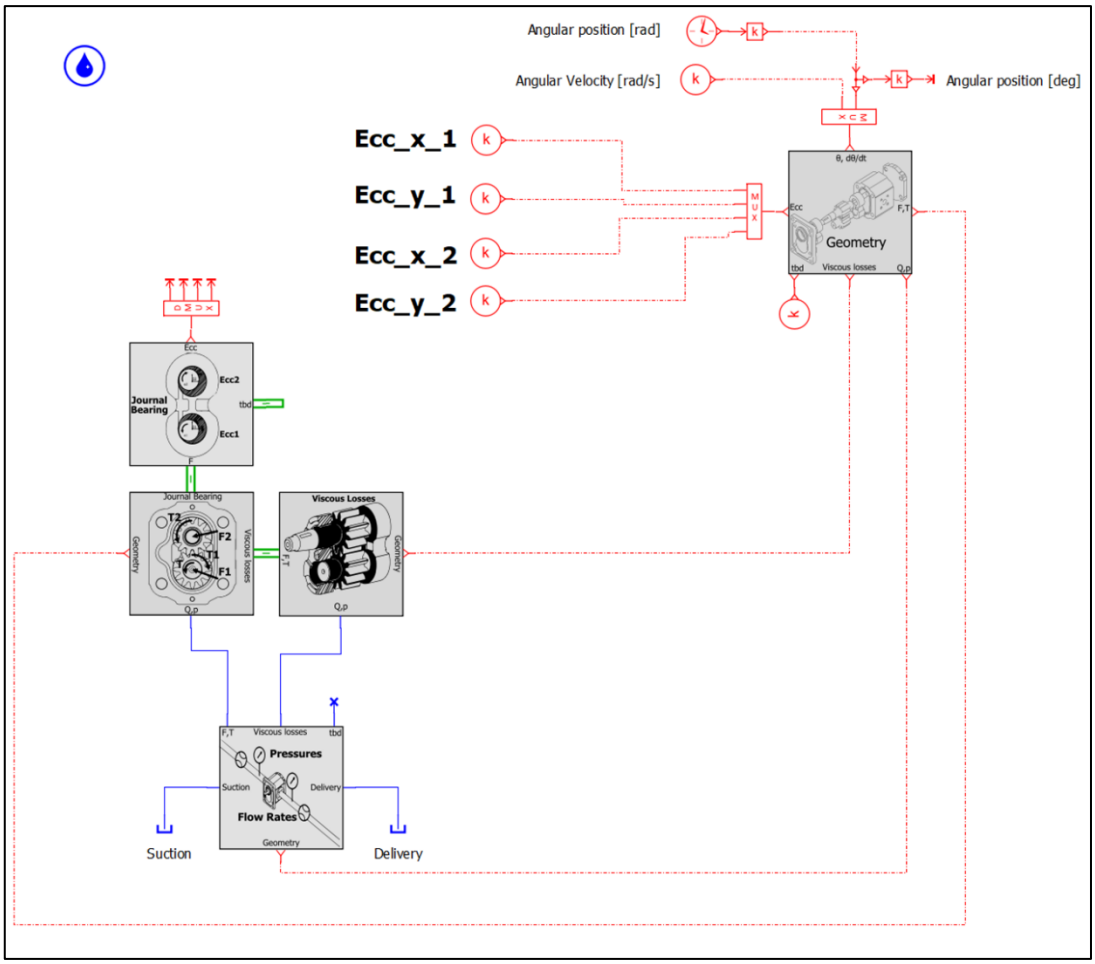

Figure 88 - Simcenter Amesim Model for Calculating Pump Performance in Stady State Condition

5. Run-In Process Modelling

The run-in process is a critical phase in the manufacturing of gear pumps, aimed at ensuring the proper operation of the pump.
During this phase, the correct coupling between the pump components is achieved, surface micro-asperities are reduced, the pump clearance is stabilised to minimise leakage, and long-term performance is guaranteed.

In the run-in process, the pressure of the fluid in the delivery line pushes the gears towards the suction port, creating contact between the gears and the pump housing. As a consequence, the wear of the pump housing occurs, ensuring proper coupling between the gear teeth and the pump housing. It is essential that the run-in process is performed before the pump is commissioned; otherwise, the metal residues removed during the process could contaminate the oil, compromising the operation of the system.

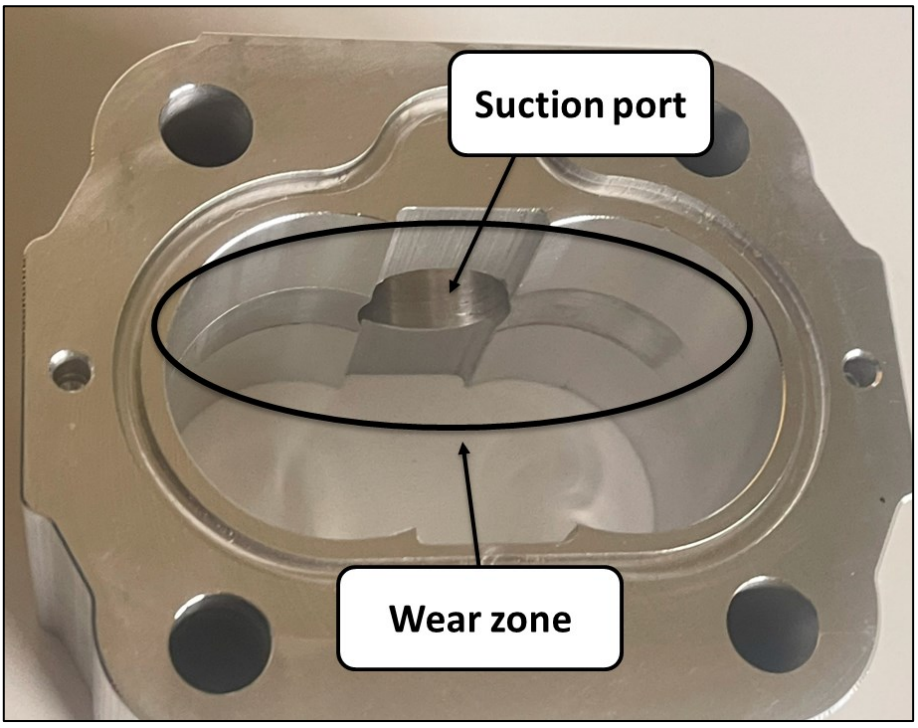

Figure 89 – Wear of the pump's housing due to the run-in process

Therefore, the run-in of the gear pump is carried out on a dedicated test bench equipped with an appropriate oil filtration system.

In general, to facilitate the run-in process, the pump housing is made from a more workable material than the gears, ensuring that wear occurs primarily in the housing. A typical combination is steel for the gears and aluminium for the pump housing. However, for pumps with large displacement and high-pressure applications, it may be necessary to use a different material for the housing, such as cast iron. In this case, the run-in process becomes more complex, as the gears and the pump housing have similar hardness properties.

To achieve a gradual removal of material from the pump housing, the pressure on the delivery line is increased incrementally.

A typical run-in process includes the following phases:

1. The pump speed is fixed.
2. Waiting time for pump stabilisation.
3. Application of a pressure ramp from 0 bar to $p_{\text{step},i}$ over $t_{1,i}$ seconds.
4. Operation at a pressure of $p_{\text{step},i}$ for $t_{2,i}$ seconds.
5. Decrease of the pressure from $p_{\text{step},i}$ to 0 bar over $t_{3,i}$ seconds.
6. Waiting time at 0 bar for $t_{4,i}$ seconds.
7. Repetition of phases 3, 4, 5, and 6 for $N - 1$ additional cycles, where N is the total number of steps in the run-in process.

The times $t_{1,i}$, $t_{2,i}$, $t_{3,i}$, and $t_{4,i}$ can either remain constant at each step or vary, depending on the type of pump and the manufacturer. Similarly, the pump speed, pressure increments, and the number of steps may also vary based on the pump type and the manufacturer's experience.

The maximum pressure is reached at the final step and, in general, exceeds the maximum continuous operating pressure of the pump as specified in the catalogue.

The definition of the pump housing profile is important to correctly estimate the dimensions of the tooth tip clearance. As mentioned earlier, the results of the run-in process are influenced not only by the running conditions but also by pump characteristics, such as clearances and the materials of the gears and housing.

To model the run-in process, a simplification is introduced: the housing profile is defined solely on the basis of geometric considerations, without taking the pump materials into account [3], [10]. This assumption has been shown to yield good results in many studies (insert references) and is applicable in cases where the gears are made of steel and the housing is made of aluminium. In such cases, the gears can easily penetrate the housing, and the wear is concentrated solely on the housing.

At the first step of the run-in process, the housing profile is approximated as an arc of a circle with radius r_{housing}, and the gear is modelled as a circle with radius r_e (see Figure 90). Due to the pressure force, the gear is pushed towards the suction side by a quantity $g_{\text{jb,h}} + \text{ecc}_{x1}$ along the x-direction and ecc_{y1} along the y-direction.

The term $g_{\text{jb,h}}$ represents the radial gap between the floating bearing blocks and the pump housing, while ecc_{x1} and ecc_{y1} are the gear eccentricities calculated for the working conditions of the specific run-in process step.

As a consequence of the micromotions of the gear, the gear penetrates the housing, and the extent of this penetration represents the material removed during that run-in process step. In this way, the new profile of the pump housing is defined as the union of arcs of circles.

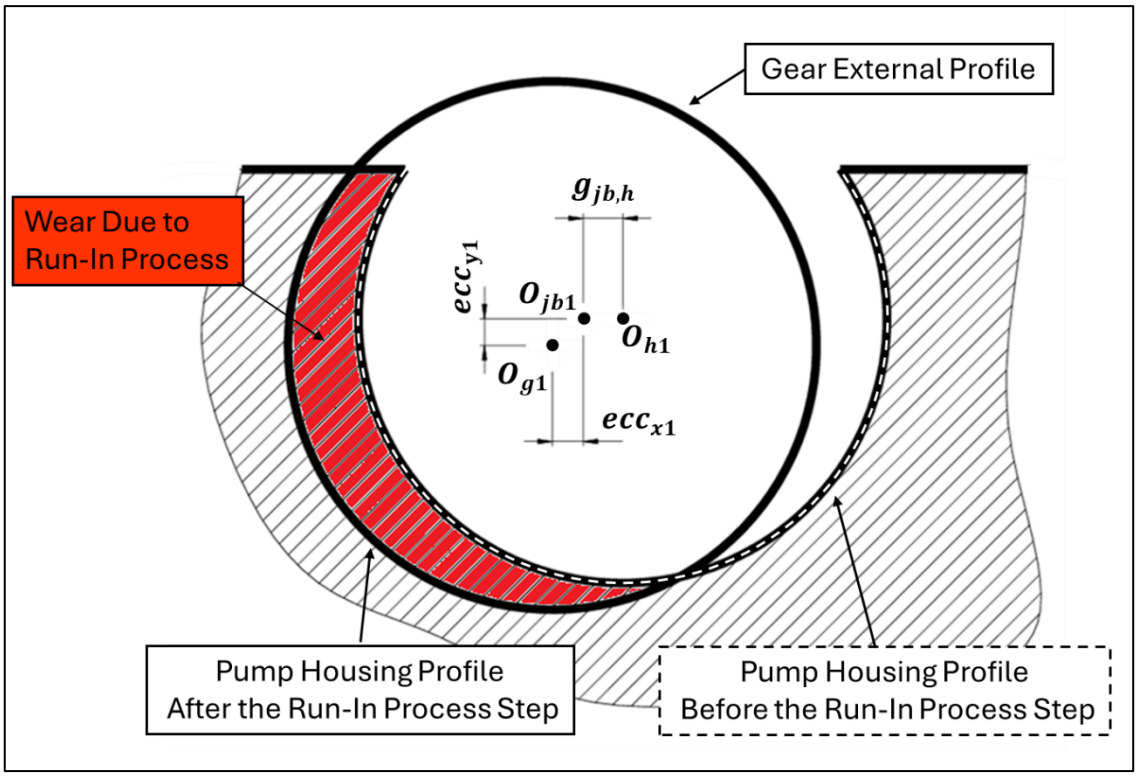

Figure 90 – Penetration of the gear due to the micromotions

The new pump housing profile is used as the basis for the simulation of the subsequent step.

In the run-in process model, each run-in step is simulated separately, excluding the phases of pressure increase, pressure hold, and pressure decrease.

At the beginning of the i-th step, the housing profile is equal to the profile obtained from the previous run-in step. During the simulation, the pump operates under steady-state conditions, with a pump speed equal to n and a delivery pressure of $p_{\text{step},i}$. Using the same model layout for defining the gear eccentricities (see Figure 83), the simulation time is set so as to ensure convergence of the gear eccentricities. The housing profile is then updated according to the gears position determined by this method.

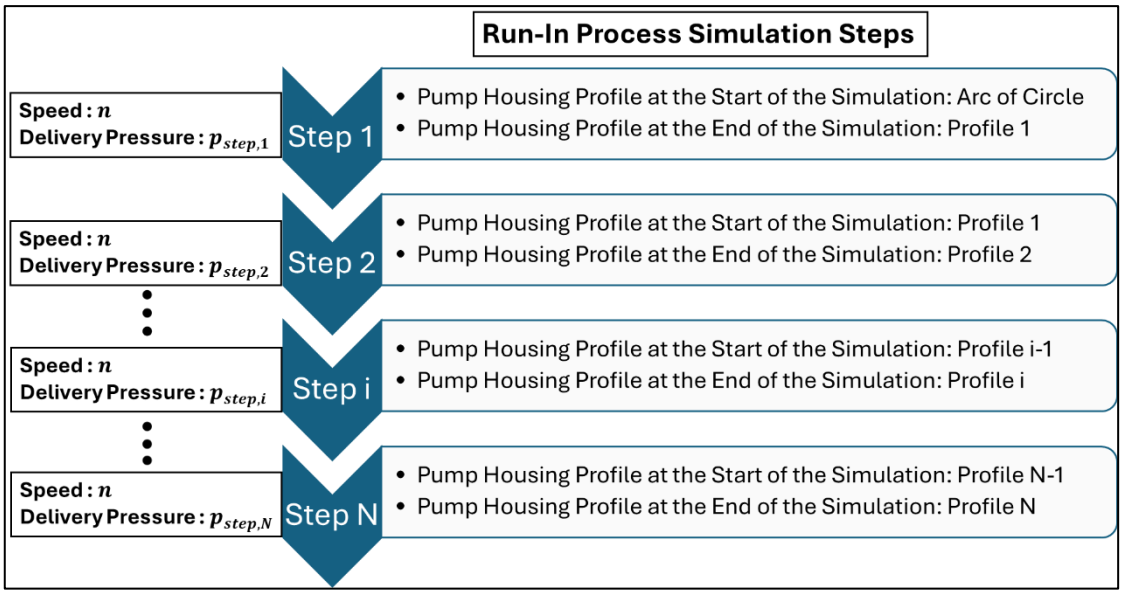

Figure 91 – Workflow of the Run-In Process Simulation

6. Experimental Activities for Model Validation

For the purpose of model validation, an experimental campaign was conducted at the Fluid Power Laboratory of Dana Motion Systems S.r.l. in Reggio Emilia. Two external gear pumps, manufactured by the same company, were tested: the OT200 model with a displacement of 8.2 cc (OT200P08D/B28P2) and 16 cc (OT200P16D/B28P2).

For each pump model, three samples were selected, resulting in a total of six pumps being tested.

The experimental activities were carried out in the following phases:

1. **Component Measurement Activities**: Prior to pump assembly, individual components were measured. Only the dimensions relevant to performance evaluation and model validation were recorded.
2. **Pump Run-in Process**: The pumps underwent a run-in process using the automated run-in bench available on the production line.
3. **Pump Housing Measurement**: Following the run-in process, the pumps were disassembled and the housings were measured to identify wear induced during the run-in phase.
4. **Pump Performance Testing**: The hydraulic efficiency, hydro-mechanical efficiency, flow rate, and torque of the pumps were measured.
5. **Pressure Ripple Testing**: The pressure ripple in the delivery line of the pumps was measured.

The experimental results and their comparison with the model results are presented in the dedicated sections, while further details on the measurement activities are provided in the following section.

6.1. Components Measurement Activities

Before pump assembly and the run-in process, pump components were measured. In the simulation, instead of using the clearances defined by the pump design drawings based on dimensional and geometric tolerances, the actual measured clearances were employed. This approach aimed to improve the accuracy of the model predictions. Among the components assessed (gears, floating bearing blocks, and housing), only the dimensions relevant to performance evaluation and model validation were recorded. These measurements allowed the actual pump clearances to be determined. The measurement activities were carried out by Zeiss S.r.l. of Reggio Emilia, a company specialised in metrology services for industrial applications.

The reported component dimensions are as follows:

Gears:

- Diameter of the tooth head.
- Axial length of the gear.

- Diameter and length of the gear shaft that interfaces with the bush of the floating bearing bushing.

Floating bearing blocks:

- External diameters of the bearing blocks.
- Axial length of the bearing blocks.
- Diameter and length of the bushes.
- Dimensions of the anti-noise recess.
- Distance between the centres of the bushes.

Pump Housing:

- Diameters of the internal housing profile.
- Distance between the centres of the housing profiles.
- Axial length of the housing.

Additional measurements were carried out on the pump housing to define its inner profile. The objective of these measurements was to quantify the housing wear resulting from the run-in process. Therefore, the measurements were performed both before and after the run-in process.

The housing profile was recorded using a coordinate measuring machine, with tests conducted along different circumferential paths (see Figure 92).

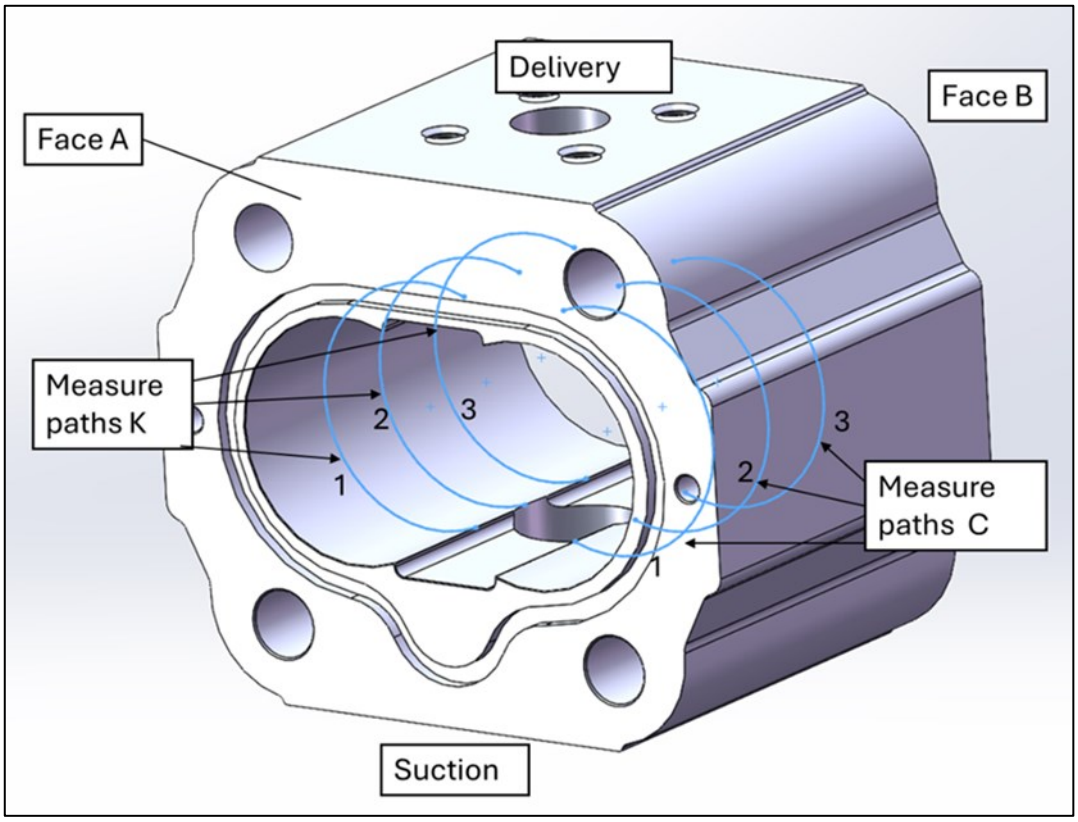

Figure 92 - Internal housing profile – Measurement paths

Three measurement paths were defined on the profile side **K**, and a further three on profile side **C**. The axial positions of these paths were determined according to Figure 93.

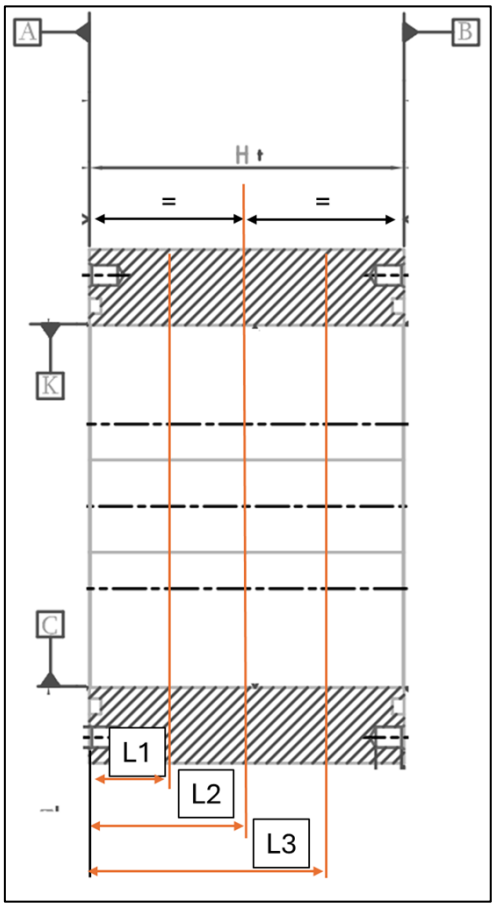

Figure 93- Measurement paths axial position

- Length L1: Corresponds to the axial length of the floating bearing blocks plus 2 mm.
- Length L2: Equals half the axial length of the pump housing.
- Length L3: Equals the axial length of the pump housing minus L1.

To compare the housing profiles before and after the run-in process, it was necessary to define the measurements with respect to the same reference system. The centre of this reference system was placed on a reference axis.

For side **K**, two housing profiles were considered: one located 10 mm from Face **A** and the other 10 mm from Face **B**. These profiles were approximated as circles, and the reference axis was defined by connecting the centres of these circles (see Figure 94).The same approach was applied to the profiles on side **C**.

The housing profiles used to define the reference axes were located in areas that were not in contact with the gears. This ensured that the reference axes remained unchanged before and after the run-in process.

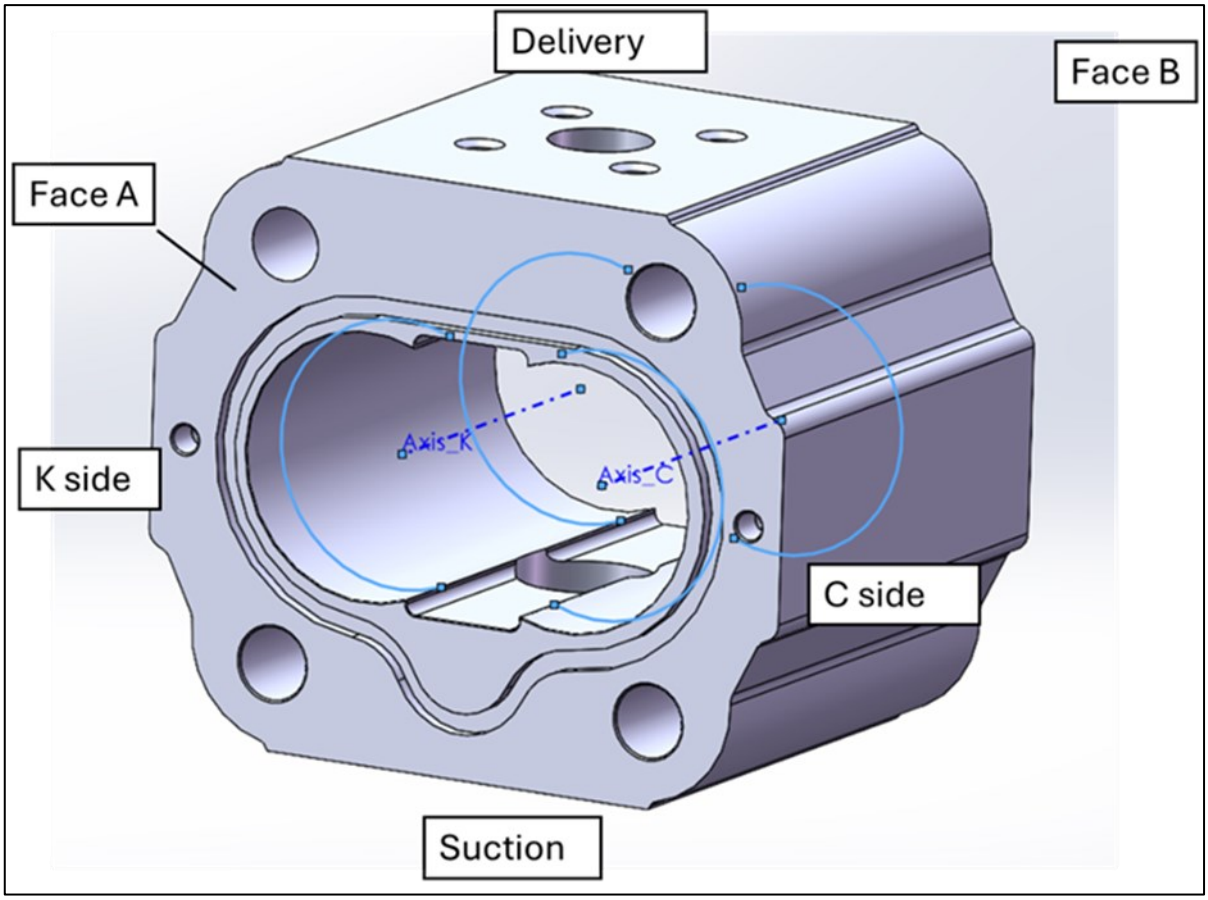

Figure 94 - Reference Axis for Internal Housing Measurements

7. Run-In Process: Comparison Between Model and Experimental Results

In this section, the experimental data obtained from the measurement campaign conducted on the inner profile of the pump housing are presented, with the aim of studying the wear caused by the run-in process.
The experimental data are also compared with the model results.

The measurements of the pump housing, obtained with a coordinate measuring machine (CMM), are provided as a `.txt` file containing the x-, y-, and z- coordinates of the points that define the housing profile.

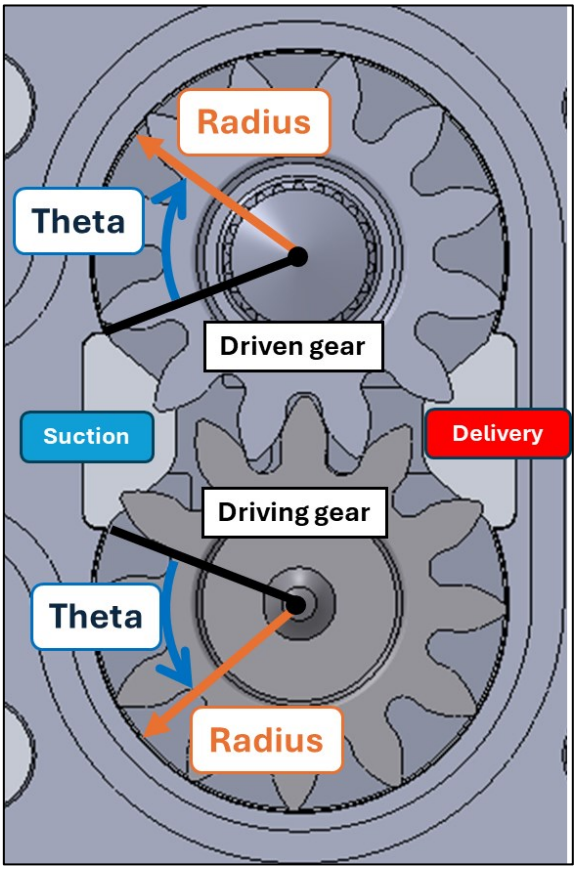

Figure 95 - Definition of the angular origin (θ = 0) for the radial profile measurements, located at the beginning of the suction port side of the pump housing

From these data, the radius of the housing profile is calculated. In the following sections, the radius of the pump housing profile is plotted as a function of the angular coordinate θ.
The origin of this angle is set at the beginning of the housing profile on the suction port side, as shown in Figure 95.

The run-in process is simulated using ISO VG 46 oil at a temperature of 40 °C. The

oil is modelled using the Simcenter Amesim Hydraulic library fluid model, with the parameters shown in Figure 96.

Title	Value	
type of fluid properties	**advanced using tables**	
fluid property file	**ISO VG 46 oil - Mobil DTE Medium**	
bulk modulus type	adiabatic	
index of hydraulic fluid	0	
temperature	40	degC
name of fluid	unnamed fluid	
▾ 🗀 Aeration		
absolute viscosity of air/gas	0.02	cP
saturation pressure (for dissolved air/gas)	1000	bar
air/gas content	0.1	%
polytropic index for air/gas/vapor content	1.4	null
▾ 🗀 Cavitation		
(advanced user) high saturated vapor pressure	-0.5	bar
(advanced user) low saturated vapor pressure	-0.6	bar
(advanced user) absolute viscosity of vapor	0.02	cP
(advanced user) effective molecular mass of vapor	200	null
(advanced user) air/gas density at atmospheric pressure 0 degC	1.2	kg/m**3

Figure 96 – Simcenter Amesim fluid model parameters

The speed and pressure conditions for the run-in process are as follows:

- Pump 8.2 cc: Speed: 2000 rpm; Pressure steps: 100, 200, 300 bar.
- Pump 16 cc: Speed: 1500 rpm; Pressure steps: 100, 220, 300 bar.

The short journal bearing hypothesis, with an oil film angular extent of π, was adopted for the simulation (see Section 0). The height of the lateral gaps was fixed at 0.01 mm.
For modelling of volumetric leakage through the tooth flanks, Formulation 1 was employed (see Section 2.6.5.1).

7.1. Model Results and Comparison with Experimental Data

7.1.1. Data Results: Pump 8.2 cc No.1

Figure 97 presents the experimental and model results for the gear pump with an 8.2 cc displacement, sample No.1.
Figure 97.(a) illustrates the housing radius data for the driving gear, while Figure 97.(b) shows the data for the driven gear side.
The curves Exp 1, Exp 2, and Exp 3 correspond to the three measurements performed at the three axial positions (see Figure 93), whereas the curve labelled 'Model' represents the results obtained from the external gear pump model.

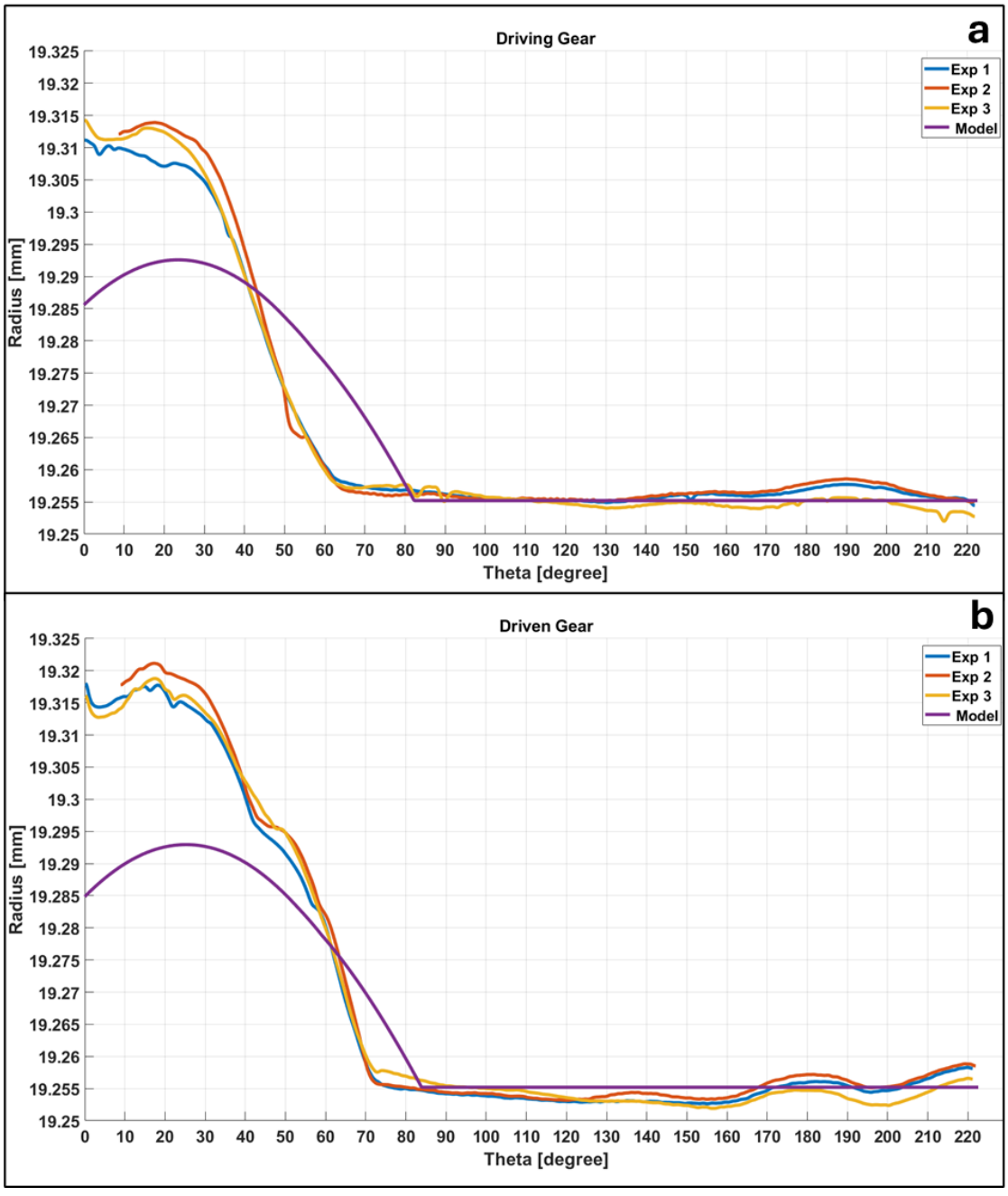

Figure 97 - Pump Housing Profile – Pump 8.2 cc No.1 – Experimental Data vs. Model: a) Driving Gear, b) Driven Gear

Table 1 contains the following parameters**:**

- **Wear Zone Extension:** Indicates the extent of the wear zone caused by the run-in process on the pump housing. For the experimental data, this is an approximated value, as it is not possible to define a precise boundary. In contrast, for the model data, the transition between the wear zone and the no-wear zone is more clearly defined.
- **Maximum Penetration:** Defined as the difference between the maximum radius value and the radius value measured prior to the run-in process.

Pump 8.2 cc n.1		**Exp Data 1**	**Exp Data 2**	**Exp Data 3**	**Model Data**
Driving Gear	**Wear Zone Extension [degree]**	70	66	67	82.4
	Maximum Penetration [mm]	0.055	0.058	0.057	0.037
Driven Gear	**Wear Zone Extension [degree]**	75	73	73	84
	Maximum Penetration [mm]	0.063	0.066	0.064	0.038

Table 1 – Wear Data - Pump 8.2 cc No.1 – Experimental Data vs. Model

The curves indicate that the housing radius is larger at lower values of θ, near the suction port where the wear is concentrated, and decreases until it reaches a stable value at higher θ, near the delivery port.
The wear on the driven gear side is greater than that on the driving gear side. This is evident from both the curves and Table 1, in terms of both wear zone extension and maximum penetration. This difference aligns with the load distribution on the gears: the pressure forces push the gears towards the suction port, while the contact forces are of equal magnitude but act in opposite directions. The contact force on the driven gear pushes it toward the suction port, whereas the contact force on the driving gear pushes it toward the delivery port.

The difference between the driving and driven sides is evident in the experimental data, whereas this difference is less pronounced in the model results.
The model overestimates the extension of the wear zone and underestimates the maximum penetration. Additionally, the model results for the driven gear side align better with the experimental data than those for the driving gear side.

Pump 8.2 cc n.1		**Error**
Driving Gear	**Wear Zone Extension [degree]**	14.7
	Maximum Penetration [mm]	-0.019
Driven Gear	**Wear Zone Extension [degree]**	10.3
	Maximum Penetration [mm]	-0.027

Table 2 – Model estimation error - Pump 8.2 cc No.1

The errors are defined as the difference between the model results and the average value of the experimental data obtained at the three different axial positions.

7.1.2. Data Results: Pump 8.2 cc No.2

Figure 98 presents the experimental and model results for the gear pump with an 8.2 cc displacement, sample No.2.

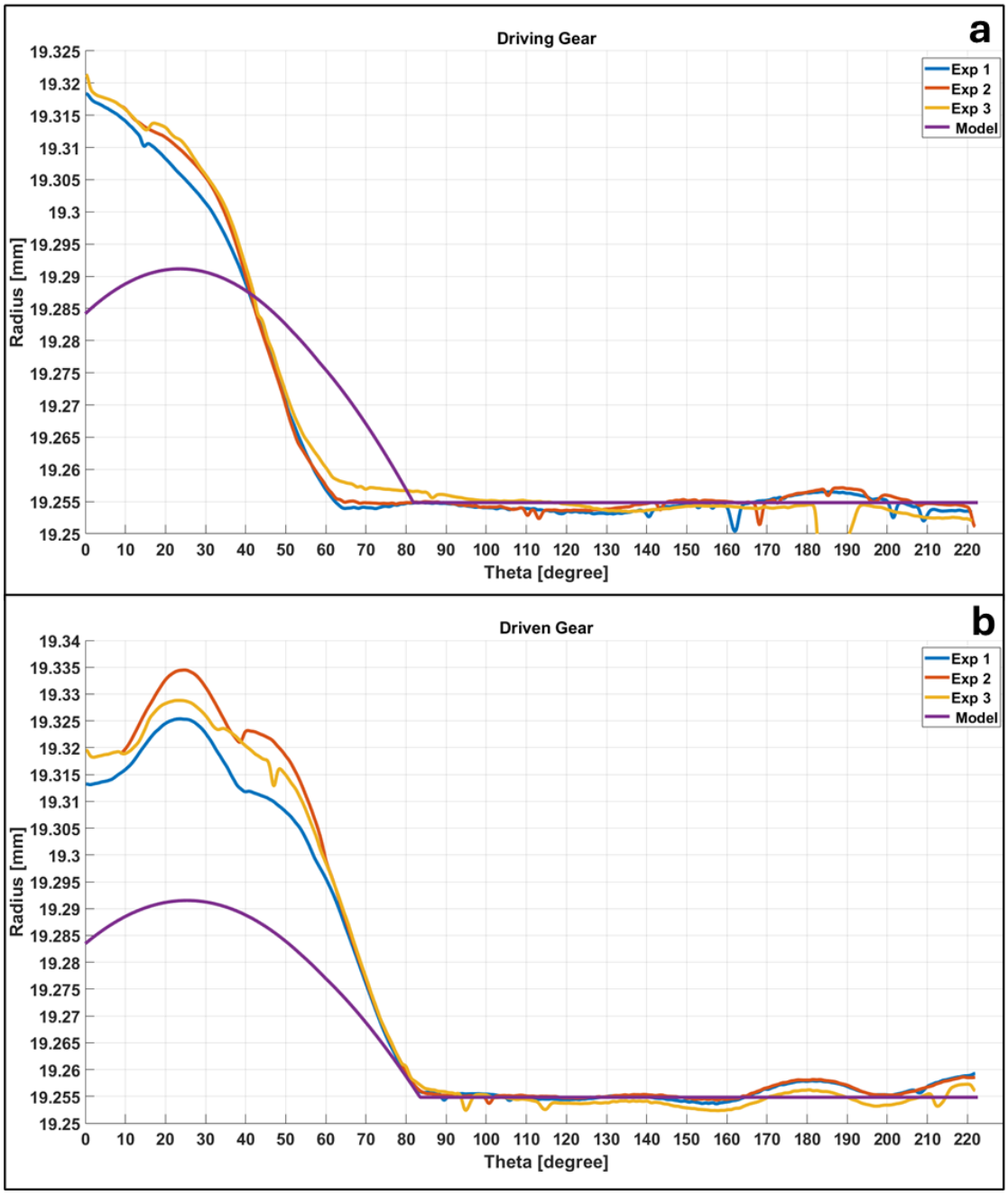

Figure 98 - Pump Housing Profile – Pump 8.2 cc No.2 – Experimental Data vs. Model: a) Driving Gear, b) Driven Gear

Considering the experimental data, the pump housing on the driven gear side exhibits a wear zone with greater extension and penetration depth than on the driving side.

However, this difference is less pronounced in the model results.

Pump 8.2 cc n.2		Exp Data 1	Exp Data 2	Exp Data 3	Model Data
Driving Gear	**Wear Zone Extension [degree]**	65	65	67	82
	Maximum Penetration [mm]	0.063	0.061	0.064	0.036
Driven Gear	**Wear Zone Extension [degree]**	84	85	85	83.5
	Maximum Penetration [mm]	0.070	0.080	0.074	0.037

Table 3- Wear Data - Pump 8.2 cc No.2 – Experimental Data vs. Model

On the driving gear side, the model overestimates the extension of the wear zone and underestimates the depth of the wear. Conversely, on the driven gear side, the model underestimates the depth of the wear but provides a good match for the wear zone extension.

Pump 8.2 cc n.2		Error
Driving Gear	**Wear Zone Extension [degree]**	16.3
	Maximum Penetration [mm]	-0.026
Driven Gear	**Wear Zone Extension [degree]**	-1.2
	Maximum Penetration [mm]	-0.038

Table 4 - Model estimation error - Pump 8.2 cc No.2

7.1.3. Data Results: Pump 8.2 cc No.3

Figure 99 presents the experimental and model results for the gear pump with an 8.2 cc displacement, sample No.3.

Based on the experimental data, the pump housing on the driven gear side exhibits a wear zone with greater extent that on the driving side, while the wear penetration depth is very similar on the two sides for this pump sample. However, this difference is less pronounced in the model results.

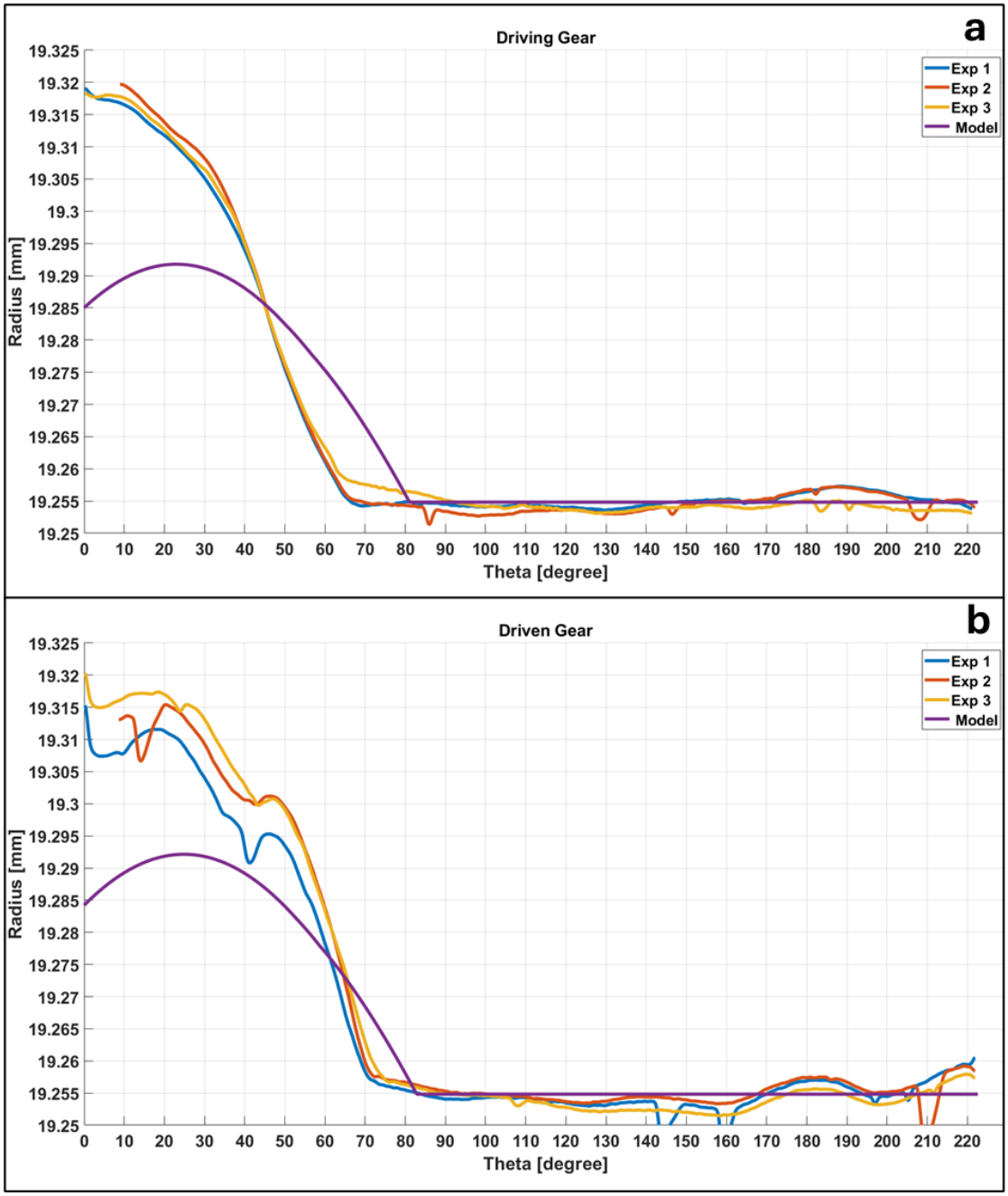

Figure 99 - Pump Housing Profile – Pump 8.2 cc No.3 – Experimental Data vs. Model: a) Driving Gear, b) Driven Gear

Pump 8.2 cc n.3		Exp Data 1	Exp Data 2	Exp Data 3	Model Data
Driving Gear	**Wear Zone Extension [degree]**	69	70	70	81
	Maximum Penetration [mm]	0.063	0.065	0.063	0.037
Driven Gear	**Wear Zone Extension [degree]**	72	73	76	83.0
	Maximum Penetration [mm]	0.057	0.061	0.063	0.037

Table 5 - Wear Data - Pump 8.2 cc No.3 – Experimental Data vs. Model

The model overestimates the extension of the wear zone and underestimates the maximum penetration for both the driving and driven gear sides. However, the error is less on the driven gear side.

Pump 8.2 cc n.3		Error
Driving Gear	**Wear Zone Extension [degree]**	11.3
	Maximum Penetration [mm]	-0.027
Driven Gear	**Wear Zone Extension [degree]**	9.3
	Maximum Penetration [mm]	-0.023

Table 6 - Model estimation error - Pump 8.2 cc No.3

7.1.4. Data Results: Pump 16 cc No.1

Figure 100 presents the experimental and model results for the gear pump with a 16 cc displacement, sample No.1.

Based on the experimental data, the pump housing on the driven gear side exhibits a wear zone with greater extension compared to the driving side, while the penetration depth of the wear between the driving and driven gear sides is very similar for this pump sample. However, this difference is less pronounced in the model results.

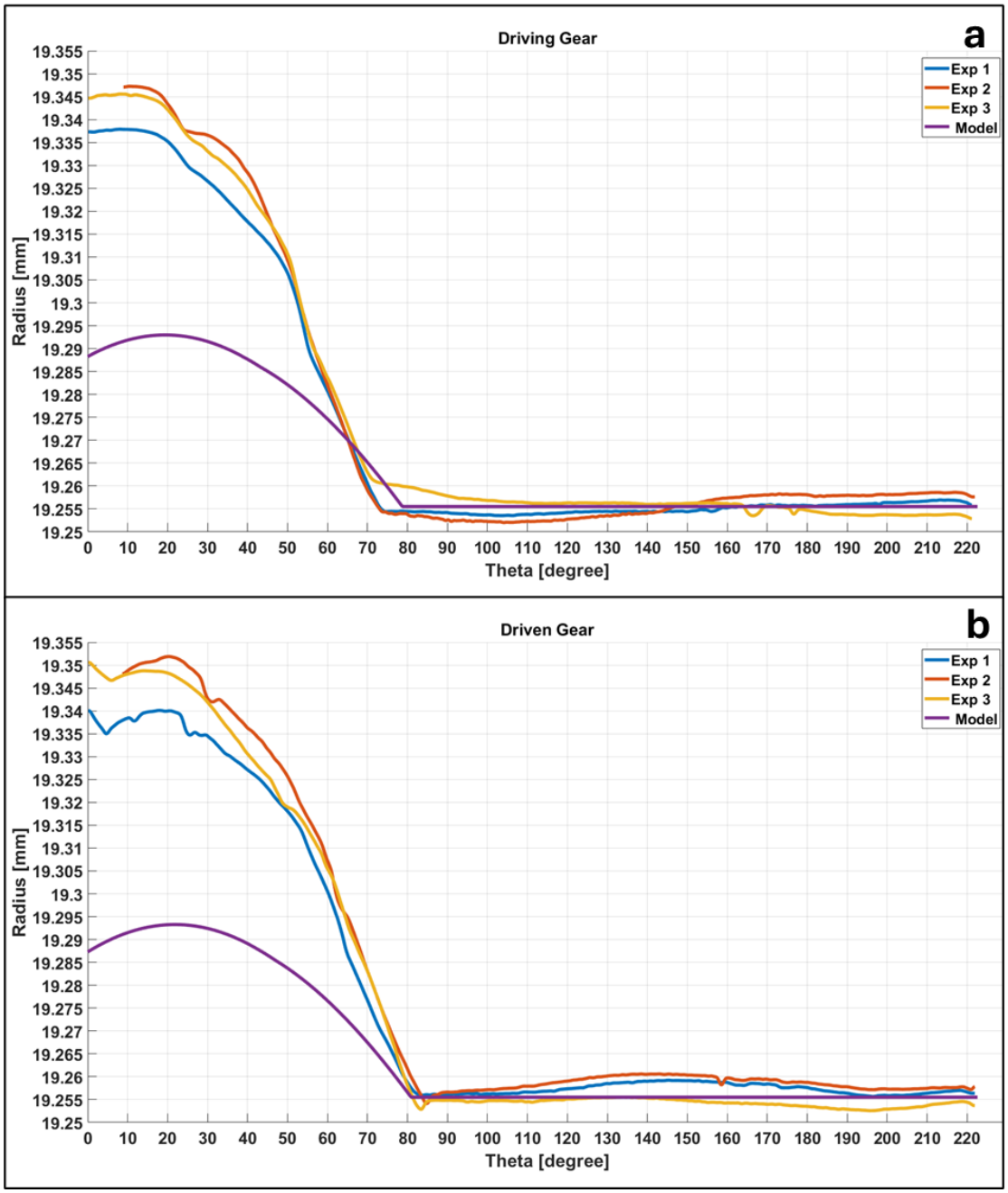

Figure 100 - Pump Housing Profile – Pump 16 cc No.1 – Experimental Data vs. Model: a) Driving Gear, b) Driven Gear

Pump 16 cc n.1		Exp Data 1	Exp Data 2	Exp Data 3	Model Data
Driving Gear	**Wear Zone Extension [degree]**	75	75	75	78.8
	Maximum Penetration [mm]	0.083	0.092	0.091	0.037
Driven Gear	**Wear Zone Extension [degree]**	83	85	83	81
	Maximum Penetration [mm]	0.084	0.096	0.093	0.038

Table 7 - Wear Data - Pump 16 cc No.1 – Experimental Data vs. Model

The model underestimates the depth of the wear but provides a good match for the wear zone extension for both the driving and driven gear sides.

Pump 16 cc n.1		Error
Driving Gear	**Wear Zone Extension [degree]**	3.8
	Maximum Penetration [mm]	-0.051
Driven Gear	**Wear Zone Extension [degree]**	-2.7
	Maximum Penetration [mm]	-0.053

Table 8 - Model estimation error - Pump 16 cc No.1

7.1.5. Data Results: Pump 16 cc No.2

Figure 101 presents the experimental and model results for the gear pump with a 16 cc displacement, sample No.2.

Based on the experimental data, the pump housing on the driven gear side exhibits a wear zone extension and penetration depth of the wear greatest compared to the driving side. However, this difference is less pronounced in the model results.

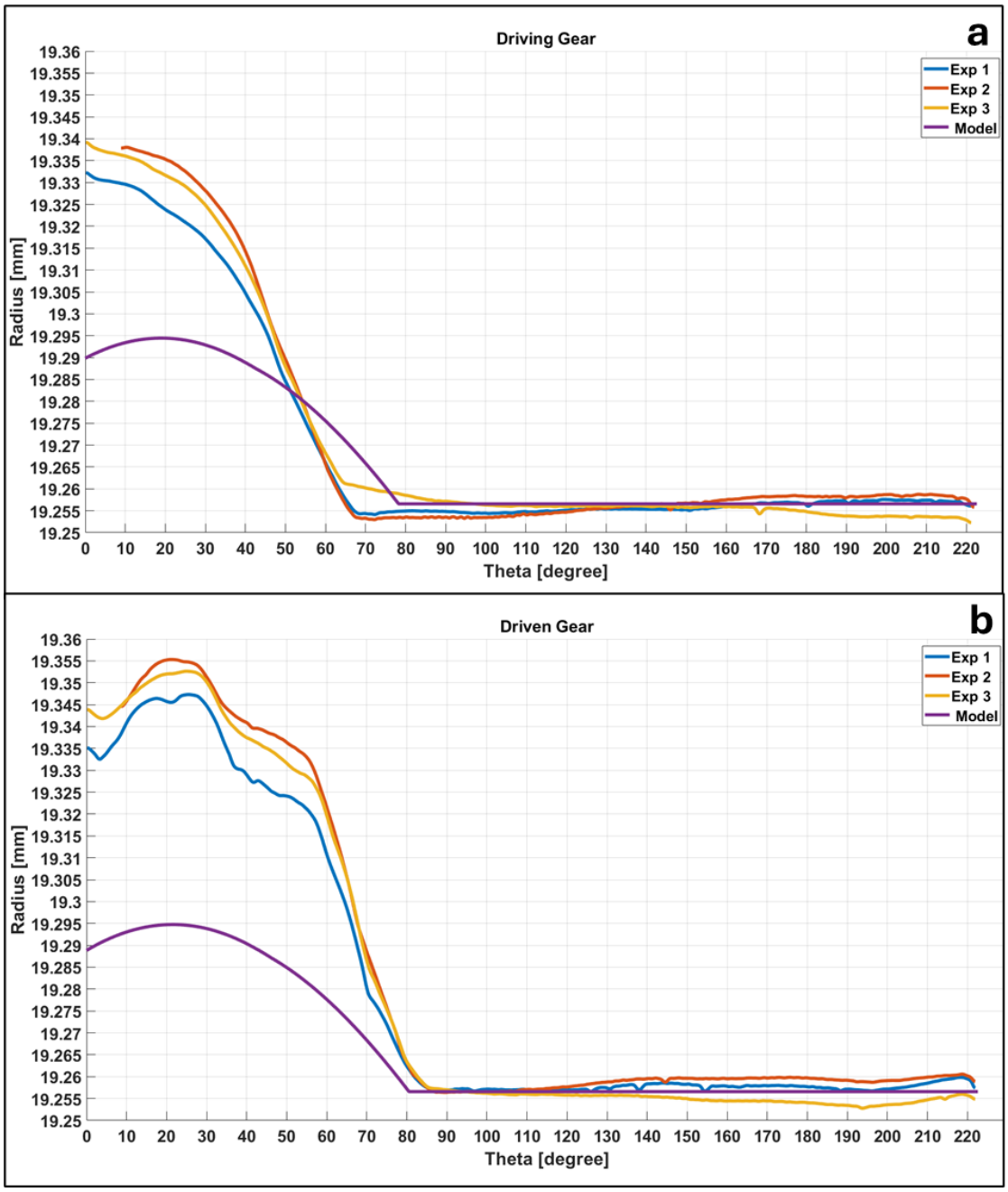

Figure 101 - Pump Housing Profile – Pump 16 cc No.2 – Experimental Data vs. Model: a) Driving Gear, b) Driven Gear

Pump 16 cc n.2		Exp Data 1	Exp Data 2	Exp Data 3	Model Data
Driving Gear	Wear Zone Extension [degree]	69	69	69	78.2
	Maximum Penetration [mm]	0.075	0.081	0.082	0.038
Driven Gear	Wear Zone Extension [degree]	86	86	86	80.5
	Maximum Penetration [mm]	0.091	0.099	0.096	0.038

Table 9 - Wear Data - Pump 16 cc No.2 – Experimental Data vs. Model

The model overestimates the extent of the wear zone on the driving gear side, while underestimating it on the driven gear side. Additionally, it underestimates the maximum penetration on both the driving and driven gear sides. However, the error is less pronounced on the driven gear side.

Pump 16 cc n.2		Error
Driving Gear	Wear Zone Extension [degree]	9.2
	Maximum Penetration [mm]	-0.041
Driven Gear	Wear Zone Extension [degree]	-5.5
	Maximum Penetration [mm]	-0.057

Table 10 - Model estimation error - Pump 16 cc No.2

7.1.6. Data Results: Pump 16 cc No.3

Figure 102 presents the experimental and model results for the gear pump with a 16 cc displacement, sample No.3.

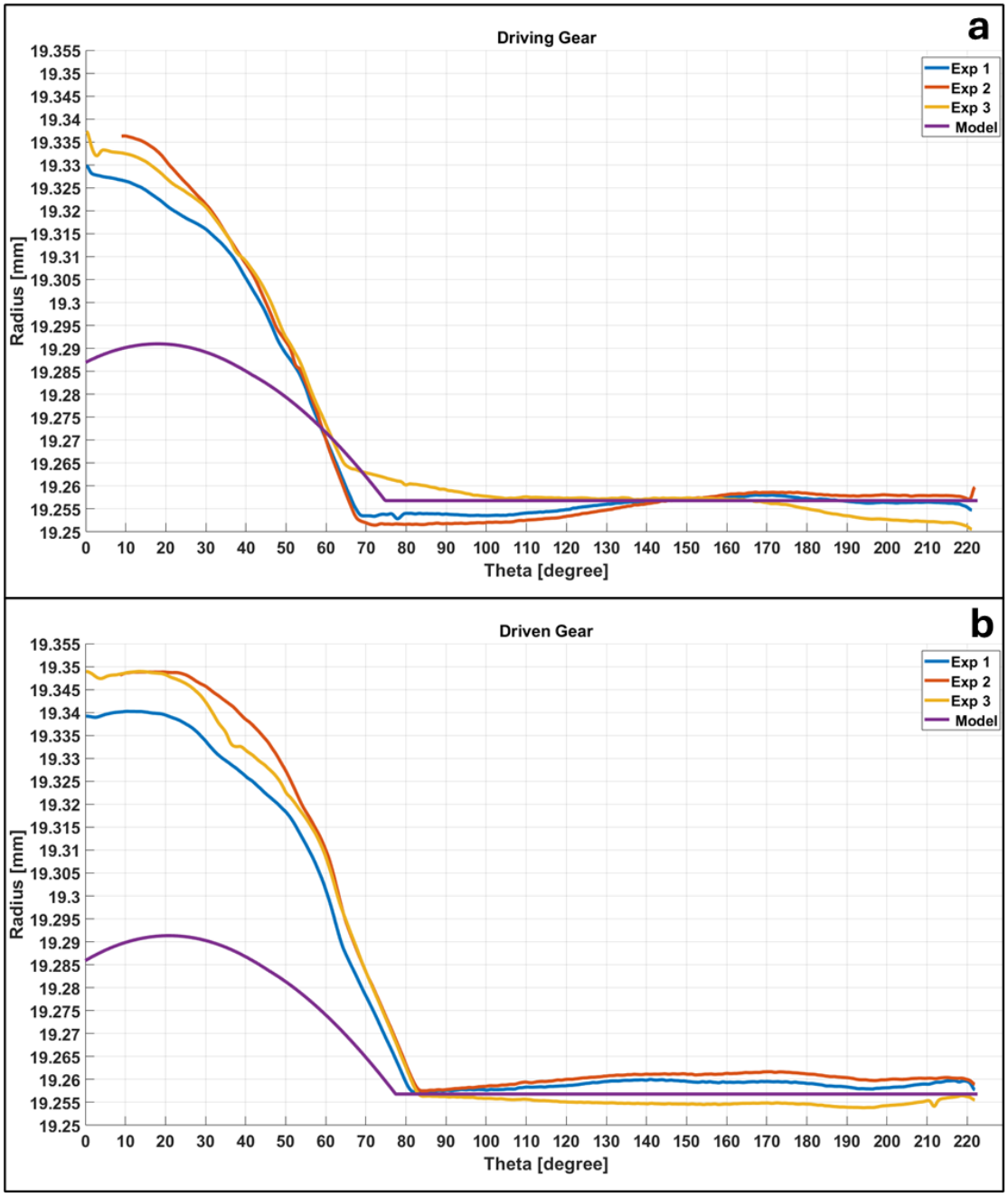

Figure 102 - Pump Housing Profile – Pump 16 cc No.3 – Experimental Data vs. Model : a) Driving Gear, b) Driven Gear

Based on the experimental data, the pump housing on the driven gear side exhibits a wear zone extension and penetration depth of the wear greatest compared to the driving side. However, this difference is less pronounced in the model results.

Pump 16 cc n.3		Exp Data 1	Exp Data 2	Exp Data 3	Model Data
Driving Gear	Wear Zone Extension [degree]	68	70	69	74.6
	Maximum Penetration [mm]	0.071	0.079	0.077	0.034
Driven Gear	Wear Zone Extension [degree]	82	84	84	77.4
	Maximum Penetration [mm]	0.083	0.092	0.092	0.034

Table 11 - Wear Data - Pump 16 cc No.3 – Experimental Data vs. Model

The model underestimates the maximum penetration on both the driving and driven gear sides. However, it overestimates the extent of the wear zone on the driving gear side, while underestimating the extent of the wear zone on the driven gear side.

Pump 16 cc n.3		Error
Driving Gear	Wear Zone Extension [degree]	5.6
	Maximum Penetration [mm]	-0.042
Driven Gear	Wear Zone Extension [degree]	-5.9
	Maximum Penetration [mm]	-0.055

Table 12 - Model estimation error - Pump 16 cc No.3

7.1.7. Conclusion

In this section, the conclusions derived from the experimental activities and the simulation of the run-in process are presented.

By comparing the experimental data for the pumps with displacements of 8.2 cc and 16 cc, the following observations emerged (see Table 13):

- The extent and depth of the wear zone are greater on the driven gear side than on the driving gear side for both displacements.
- The extent and depth of the wear zone are greater for the pump with a displacement of 16 cc compared to the pump with a displacement of 8.2 cc.

The bushes supporting the gears in both the 8.2 cc and 16 cc pumps are identical, as is the gear profile. The only difference between the two pumps lies in their axial length. The 16 cc pump has an axial length approximately twice that of the 8.2 cc pump.
The pressures used during the run-in process for both pumps are similar. Consequently, the forces applied to the 16 cc pumps are greater than those applied to the 8.2 cc pump due to its larger axial length. This increased force results in a greater extent and depth of the wear zone.

		Average Exp Data Pump 8.2 cc	Average Exp Data Pump 16 cc
Driving Gear	**Wear Zone Extension [degree]**	67.7	71.0
	Maximum Penetration [mm]	0.061	0.081
Driven Gear	**Wear Zone Extension [degree]**	77.3	84.3
	Maximum Penetration [mm]	0.066	0.092

Table 13 - Wear Data – Average Experimental Data- Pump 8.2 cc vs. Pump 16 cc

By comparing the model results for the pumps with displacements of 8.2 cc and 16 cc, the following observations were made (see Table 14):

- In terms of maximum wear depth between the driving and driven gear sides, no significant difference is observed.
- In terms of the extent of the wear zone, the difference between the driving and driven gear sides is less pronounced compared to the experimental data.

		Average Model Data Pump 8.2 cc	Average Model Data Pump 16 cc
Driving Gear	**Wear Zone Extension [degree]**	81.8	77.2
	Maximum Penetration [mm]	0.037	0.036
Driven Gear	**Wear Zone Extension [degree]**	83.5	79.6
	Maximum Penetration [mm]	0.037	0.037

Table 14 - Wear Data – Average Model Data- Pump 8.2 cc vs. Pump 16 cc

Considering the model's capability to estimate the wear zone resulting from the run-in process, the following observations were made (see Table 15):

- The model underestimates the maximum depth of the wear zone, regardless of the pump displacement.
- The error in estimating the extent of the wear zone is greater for the pump with a displacement of 8.2 cc. However, in general, the error is smaller on the driven gear side.

		Average Error Pump 8.2 cc	Average Error Pump 16 cc
Driving Gear	**Wear Zone Extension [degree]**	14.1	6.2
	Maximum Penetration [mm]	-0.024	-0.045
Driven Gear	**Wear Zone Extension [degree]**	6.1	-4.7
	Maximum Penetration [mm]	-0.029	-0.055

Table 15 - Average Error - Pump 8.2 cc vs. Pump 16 cc

In conclusion, the proposed model provides a reasonable approximation of the extent of the wear zone, particularly in the case of the 16 cc pump. However, with regard to the depth of the wear zone, the model tends to underestimate it.

The discrepancies between the model predictions and the experimental results can be attributed to the following factors:

- **Neglecting the deformation of pump components and thermal expansion**: The model does not account for the deformation of pump components caused by the applied forces, nor does it consider the thermal expansion of these components. These phenomena introduce variations in the pump geometry that are of the same order of magnitude as the housing wear. Studies by A. Pawar et al. [11] have demonstrated how these effects influence the accuracy of lumped parameter models for external gear pumps. Their research shows that 0D models that neglect deformation and thermal effects, such as the one proposed in this thesis, tend to underestimate the depth of the wear zone. Conversely, 0D models that include these effects often overestimate the wear depth. This highlights the inherent challenges in accurately modelling the run-in process, even when increasing the complexity of the model.
- **Coupling between the driving gear and the drive motor**:
  The model demonstrates good agreement with the experimental data regarding the estimation of the wear zone's extent, particularly on the driven gear side. In the model, both the driven and driving gears are assumed to move freely within the plane, constrained only by the radial clearance of the journal bearing. However, in the actual pump, the driving gear is mechanically coupled to the drive motor, and this connection can influence the driving gear’s mobility. This phenomenon, which is not accounted for in the model, may introduce inaccuracies in the estimation of the wear zone's extent within the pump housing.

8. Pump performance: Comparison Between Model and Experimental Results

This section presents the experimental data obtained from performance tests conducted on the pumps. The experimental results are also compared with the predictions of the gear pump model.

The performance tests were conducted using the test bench illustrated in Figure 103 and Figure 104.
Measurements were performed under steady-state conditions at various operating points (Figure 105, Figure 106).
Each operating point was recorded for 3 seconds during quasi-steady-state conditions, following a stabilisation period of 5 seconds.

The tests were carried out using ISO VG 46 oil at two different temperatures: 30 °C and 60 °C. The reference temperature corresponds to the oil temperature in the tank.

To evaluate the pump's steady-state performance (volumetric and hydro-mechanical efficiencies), the following parameters were measured:

- Angular speed (n)
- Torque (T)
- Tank oil temperature (T_{oil})
- Suction pressure (p_s)
- Delivery pressure (p_d)
- Delivery temperature (T_d)
- Delivery flow rate (Q)

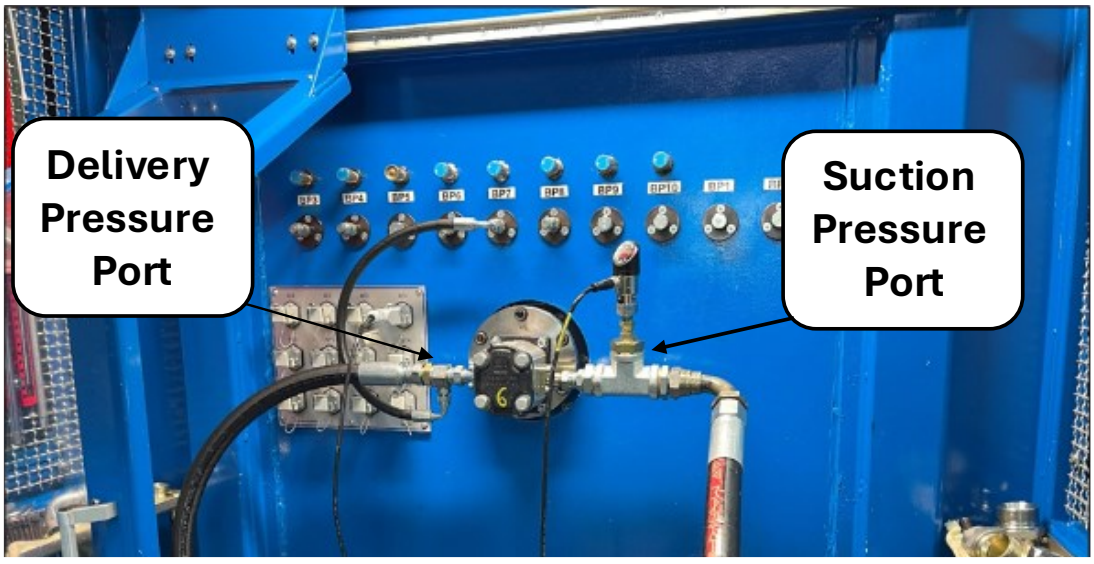

Figure 103 – BP99 test bench setup for performance test

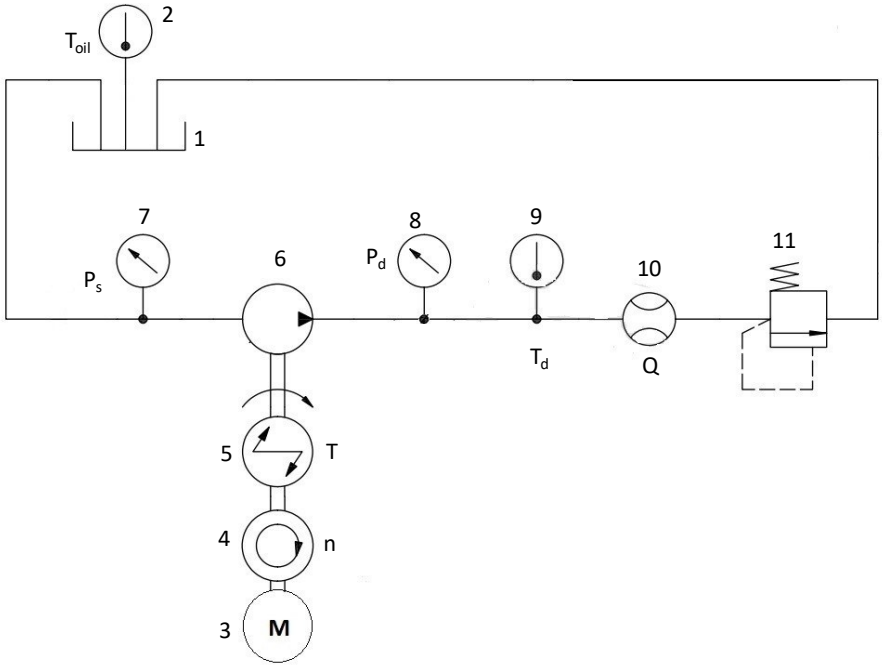

Figure 104 – Simplified ISO scheme test bench for the performance test

The components shown in Figure 104 are as follows:

- 1-Tank
- 2-Oil Temperature sensor
- 3- Electric drive motor
- 4-Speed sensor
- 5-Torque meter
- 6-Pump
- 7-Suction mean pressure sensor
- 8-Delivery mean pressure sensor.
- 9-Temperature delivery sensor
- 10-Flowmeter
- 11-Pressure valve

Sensor description	**Model**	**Range**	**Error**
Suction Pressure	Trafag 8380.26.5917	-1..10 bar	0.5% fs
Delivery Pressure	Wika S20	0-600bar	0.5 % fs
Flow rate	Kracht VC5-F1PS	250 L min^{-1}	0.3% fs
Torque	Kistler Torquemeter 4503B	1000 N·m	0.05% fs
Speed	Kistler 4503B1K0LP0B1KA2	8000 rpm	±2 rpm
Temperature	Termotech TR PT100 IEC 751	0-100 °C	± (0,15 + 0,002* | t |) Class A

Table 16 – Performance test sensors

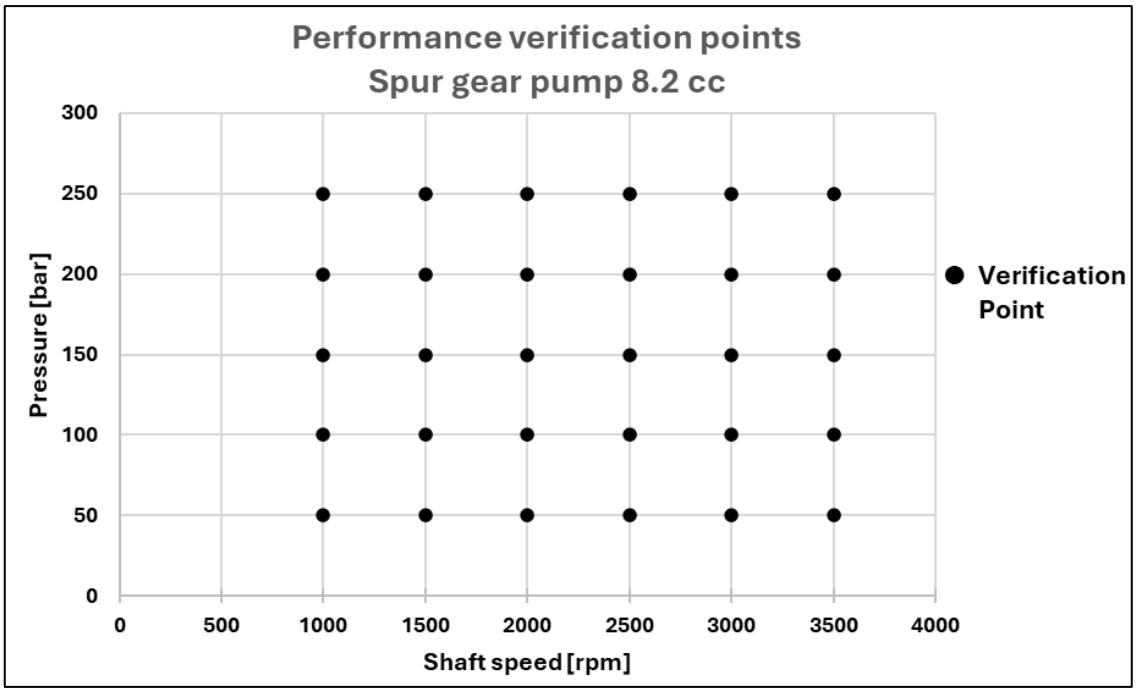

Figure 105 - Performance verification points of spur gear pump 8.2 cc

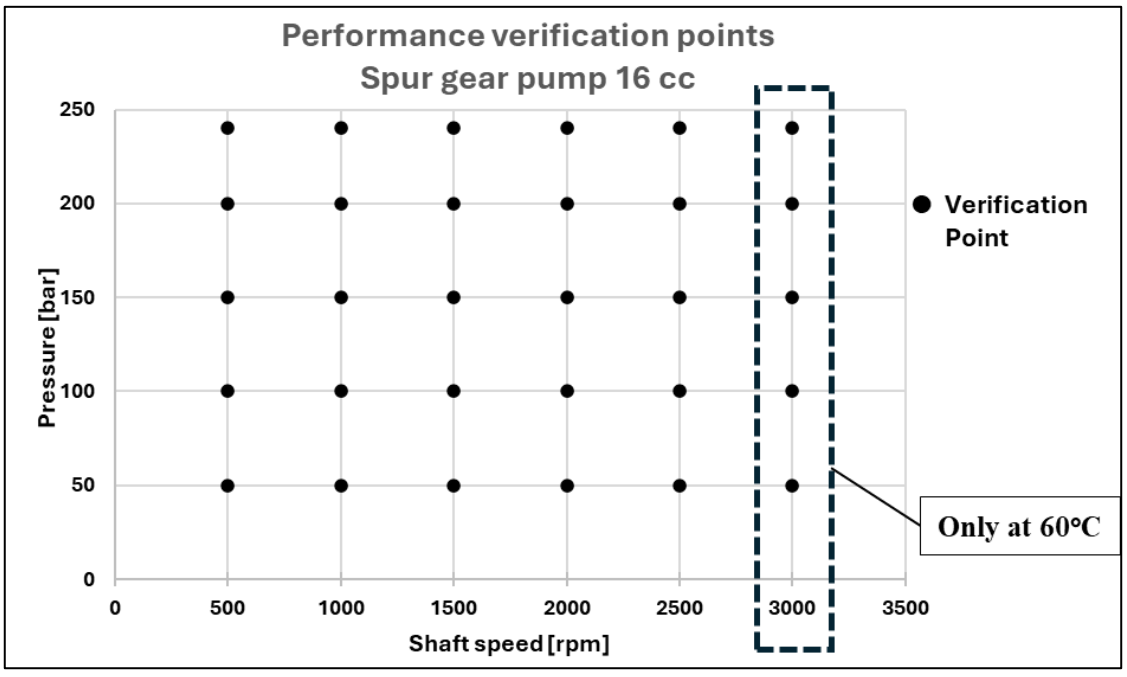

Figure 106 - Performance verification points of spur gear pump 16 cc

In the following, a comparison between the model and the experimental results is presented. For the sake of clarity, only the data for the 8.2 cc pump sample no. 1 and the 16 cc pump sample no. 3 are shown.

The simulations were conducted under the following assumptions and settings:

- The oil used was ISO VG 46, modelled with the Simcenter Amesim fluid model from the Hydraulic library, using the parameters shown in Figure 96 at the temperature of 30°C and 60°C.
- The short journal bearing hypothesis was adopted, with an oil film extension of π (see Section 0).
- The height of the lateral gaps was fixed at 0.01 mm.
- Volumetric leakage through the tooth flanks was modelled using Formulation 1 (see Section 2.6.5.1).

8.1. Pump 8.2 cc No.1 – Performance Results

The following sections present and analyse the experimental and model results for the 8.2 cc pump, sample No. 1, focusing on volumetric and hydro-mechanical performance at 30 °C and 60 °C.

8.1.1. Pump 8.2 cc No.1- Volumetric Performance – 30 °C

Figure 107 shows the flow rate of the 8.2 cc pump, sample No. 1, at different speeds at the temperature of 30 °C.
The solid line with square markers represents the experimental data, whereas the dotted line with triangular markers represents the model results.
The experimental data are plotted with the flowmeter measurement uncertainty, which is ±0.75 L min^{-1}.

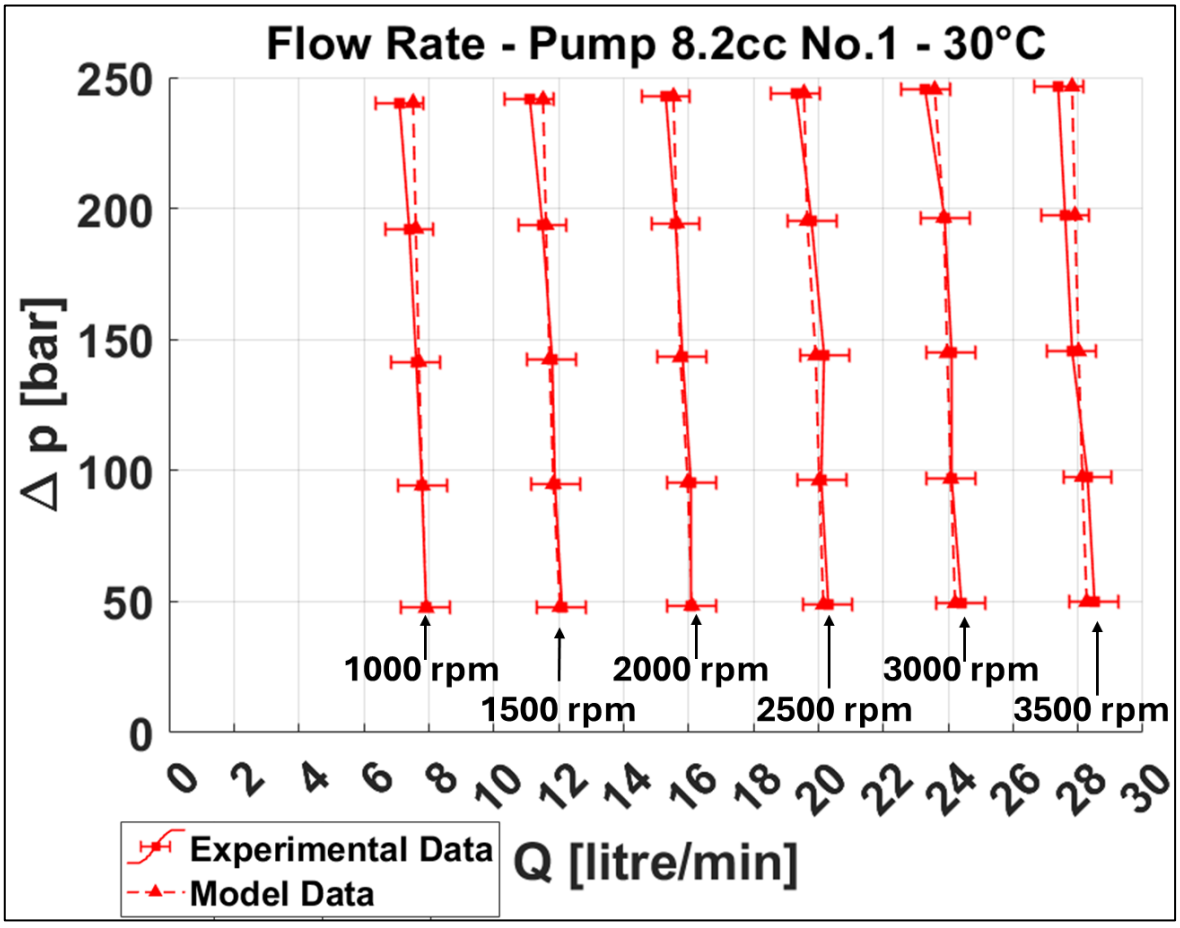

Figure 107 – Pump 8.2 cc No.1 Flow Rate - 30°

Figure 108 shows the model error in the estimation of the flow rate. Figure 108.(a) presents the relative error, defined as:

$$Error[\%] = \frac{|Q_{exp} - Q_{model}|}{Q_{exp}} \quad \text{Eq. 202}$$

Figure 108.(b) shows the absolute error, expressed in litres per minute, defined as:

$$Error[l/min] = \left|Q_{exp} - Q_{model}\right| \qquad \textit{Eq. 203}$$

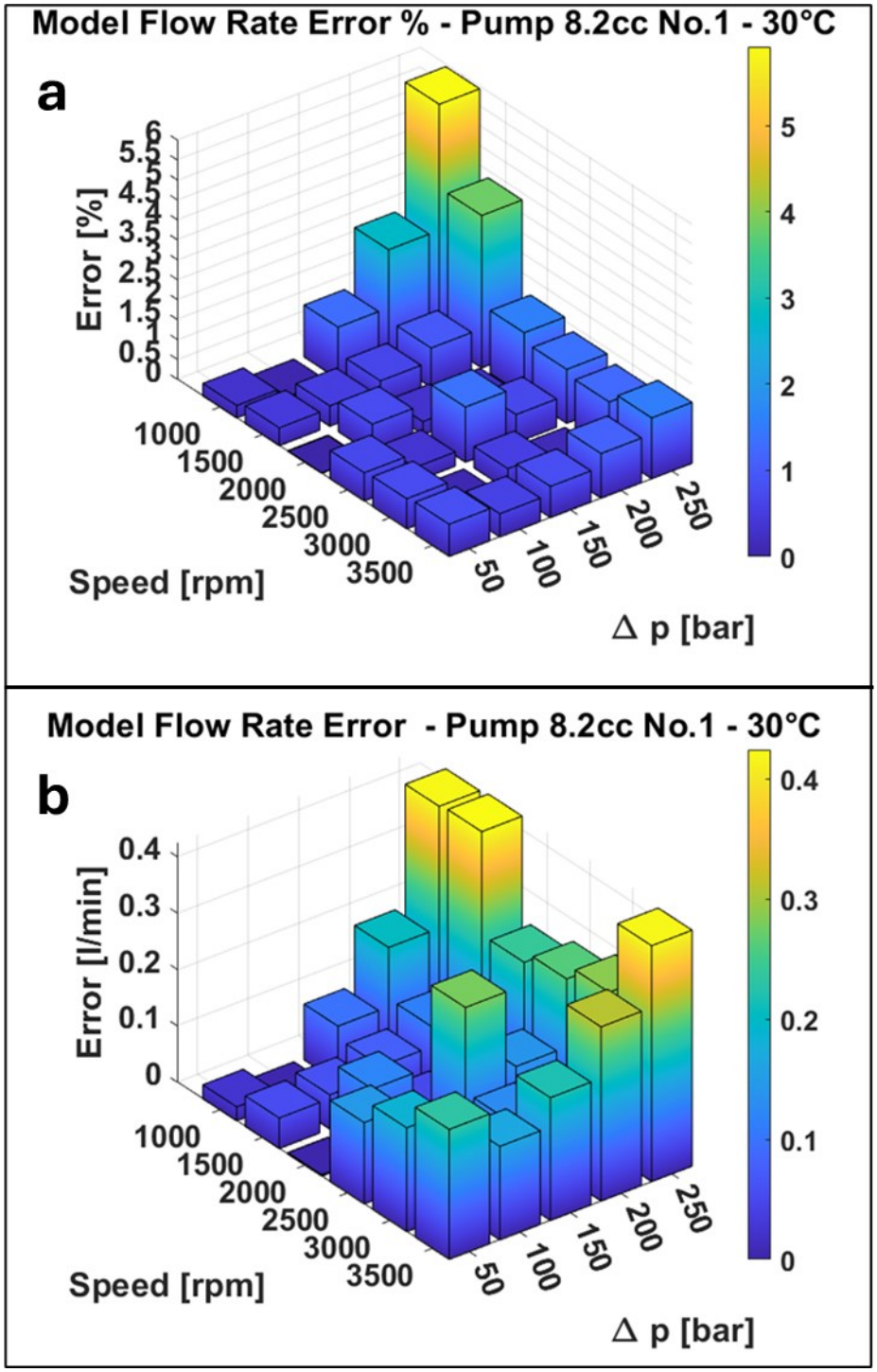

Figure 108 – Model flow-rate estimation error: (a) relative error [%]; (b) absolute error [L min⁻¹] Pump 8.2 cc No.1 30°

From the comparison, the model demonstrates good capability in estimating the flow rate at 30 °C for the 8.2 cc pump. The largest error occurs at high pressure and low

speed, with a relative magnitude of approximately 6%; however, in absolute terms the error is always less than 0.43 L min⁻¹. In all cases, the error lies within the flowmeter measurement uncertainty.

Figure 109 and Figure 110 compare the volumetric efficiency obtained experimentally with that predicted by the model. The volumetric efficiency is defined as:

$$\eta_{vol} = \frac{Q_{exp}}{Q_{th}} \qquad \textit{Eq. 204}$$

Where Q_{exp} is the experimental flow rate in L min⁻¹, and Q_{th} is the theoretical flow rate in L min⁻¹ expressed as:

$$Q_{th} = \frac{V_d\, n}{1000} \qquad \textit{Eq. 205}$$

Where:

- n is the pump speed in rpm.
- V_d is the pump displacement in cm^3.

The measurement uncertainty of the volumetric efficiency is evaluated using standard uncertainty propagation:

$$\delta\eta_{vol} = \sqrt{\left(\frac{\partial \eta_{vol}}{\partial Q_{exp}}\ \delta Q_{exp}\right)^2 + \left(\frac{\partial \eta_{vol}}{\partial n}\ \delta n\right)^2} \qquad \textit{Eq. 206}$$

Where:

- $\delta\eta_{vol}$ is the volumetric efficiency measurement uncertainty.
- δQ_{exp}= ±0.75 L min⁻¹, is the flowmeter uncertainty.
- δn = ±2 rpm, is the speed measurement uncertainty.

Substituting the definition of η_{vol} yields:

$$\delta\eta_{vol} = \frac{1000}{V_d}\ \sqrt{\left(\frac{\delta Q_{exp}}{n}\right)^2 + \left(\frac{Q_{exp}}{n^2}\ \delta n\right)^2} \qquad \textit{Eq. 207}$$

In this case, the measurement uncertainty is not constant. As evident from Figure 110 it is primarily influenced by the pump speed n, due to the $1/n$ and $1/n^2$ dependencies; consequently, the uncertainty increases at lower speeds.

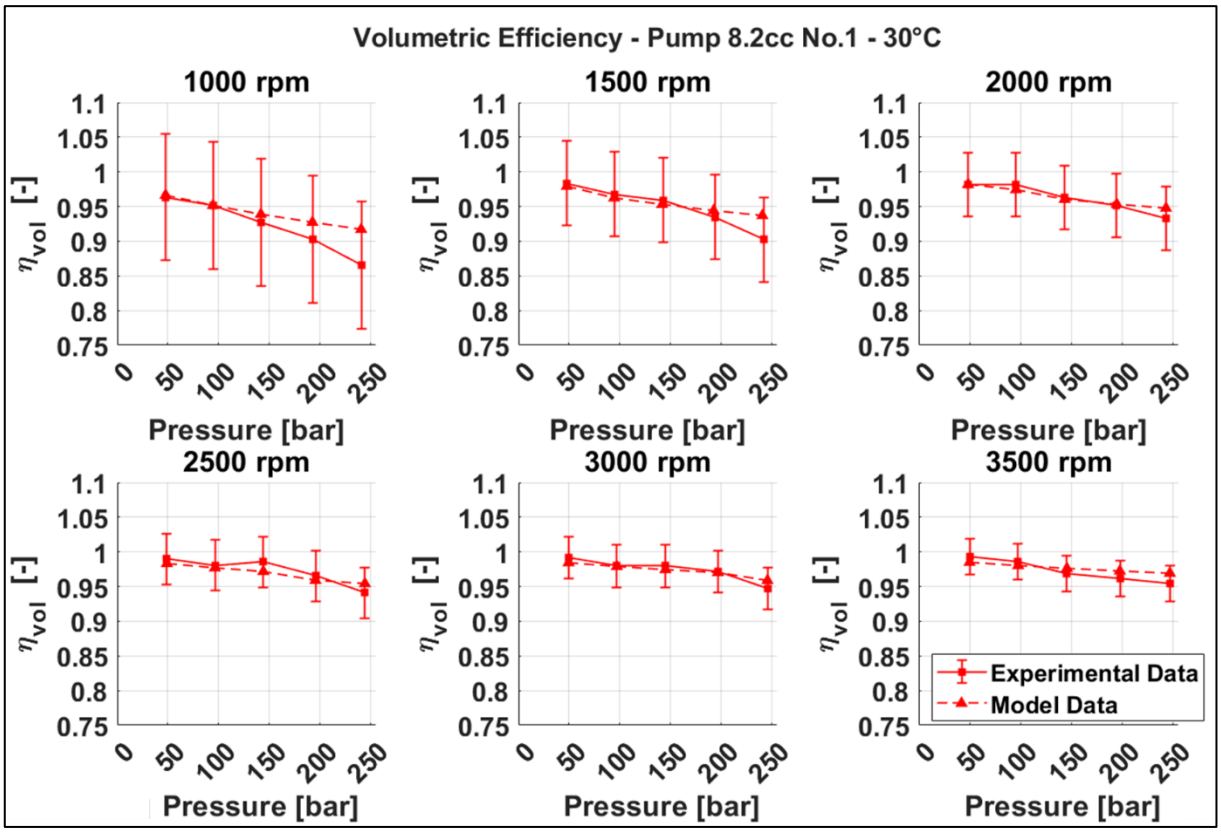

Figure 109 – Pump 8.2 cc No.1 30° – Volumetric Efficiency vs Pressure

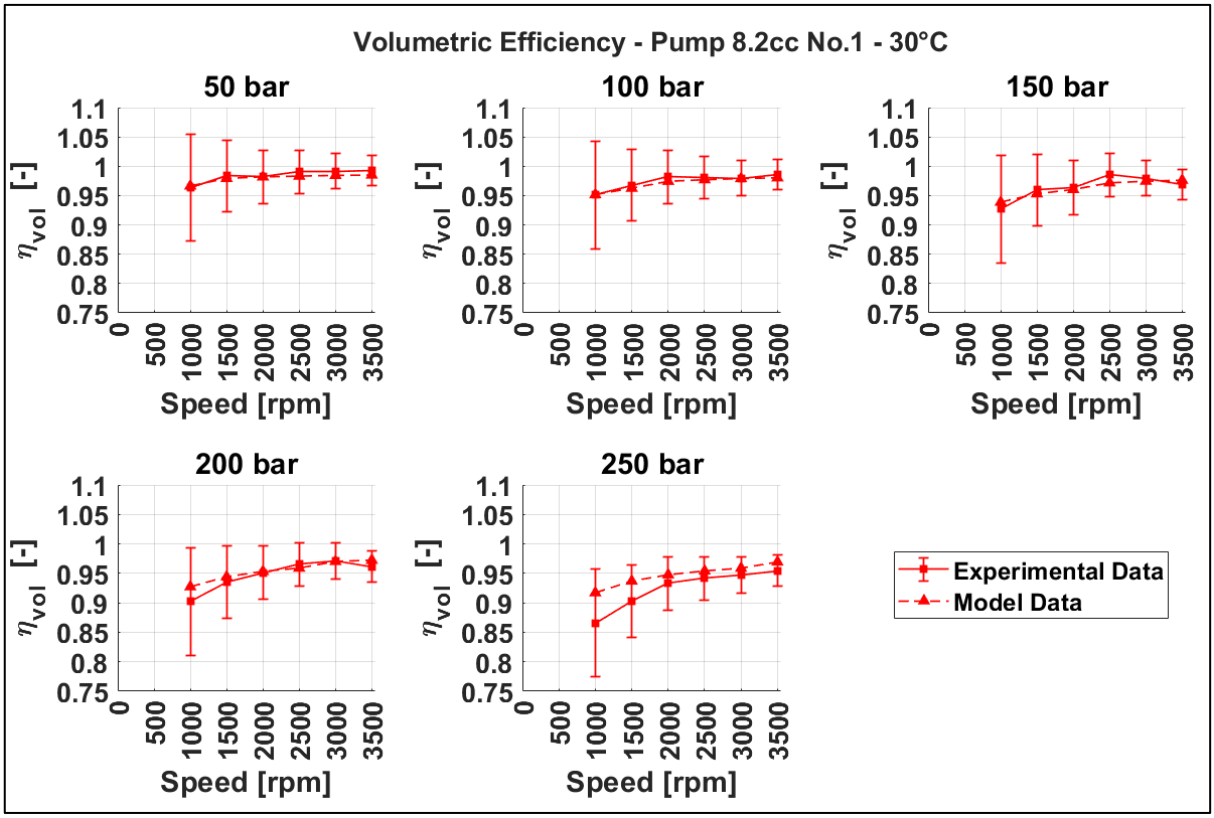

Figure 110 - Pump 8.2 cc No.1 30° – Volumetric Efficiency vs Speed

8.1.2. Pump 8.2 cc No.1- Volumetric Performance – 60 °C

Figure 111 illustrates the flow rate of the 8.2 cc pump sample No. 1 at various rotational speeds at a temperature of 60 °C, while Figure 112 presents the model error in the estimation of the flow rate, expressed both relatively and absolutely.

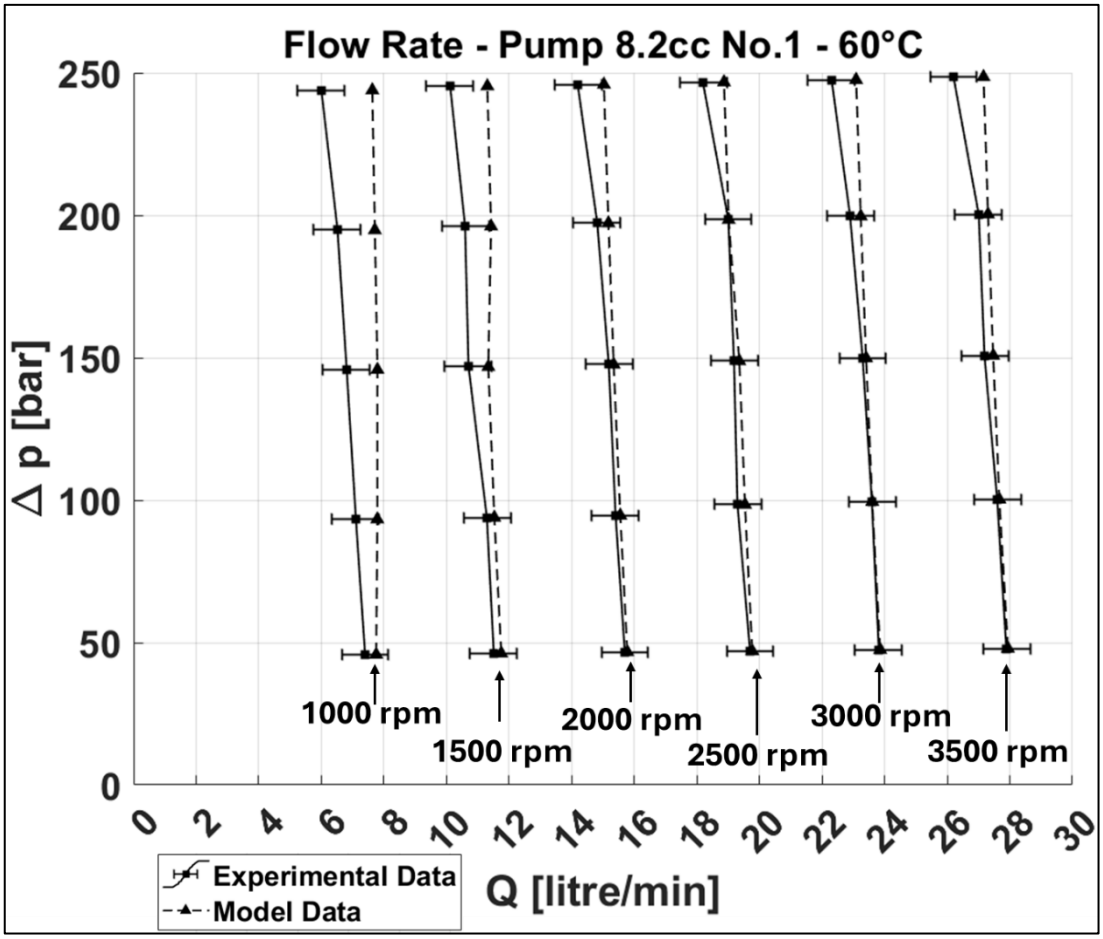

Figure 111 - Pump 8.2 cc No.1 Flow Rate - 60°

The comparison indicates that the model provides accurate flow-rate estimates within the speed range 2000–3500 rpm. As speed decreases, the discrepancy with respect to the experimental data increases, and is most pronounced at 1000 rpm.

In terms of error, within 2000–3500 rpm the maximum relative error is 5.8%; at 1500 rpm it reaches 11.9%, and at 1000 rpm 27.1%. In absolute terms, within 2000–3500 rpm the maximum error is 0.96 L min^{-1}; at 1500 rpm it is 1.21 L min^{-1}, and at 1000 rpm 1.63 L min^{-1}. Considering the flowmeter measurement uncertainty of ±0.75 L min^{-1}, these results confirm good estimation capability in the 2000–3500 rpm range and an acceptable estimation at 1500 rpm.

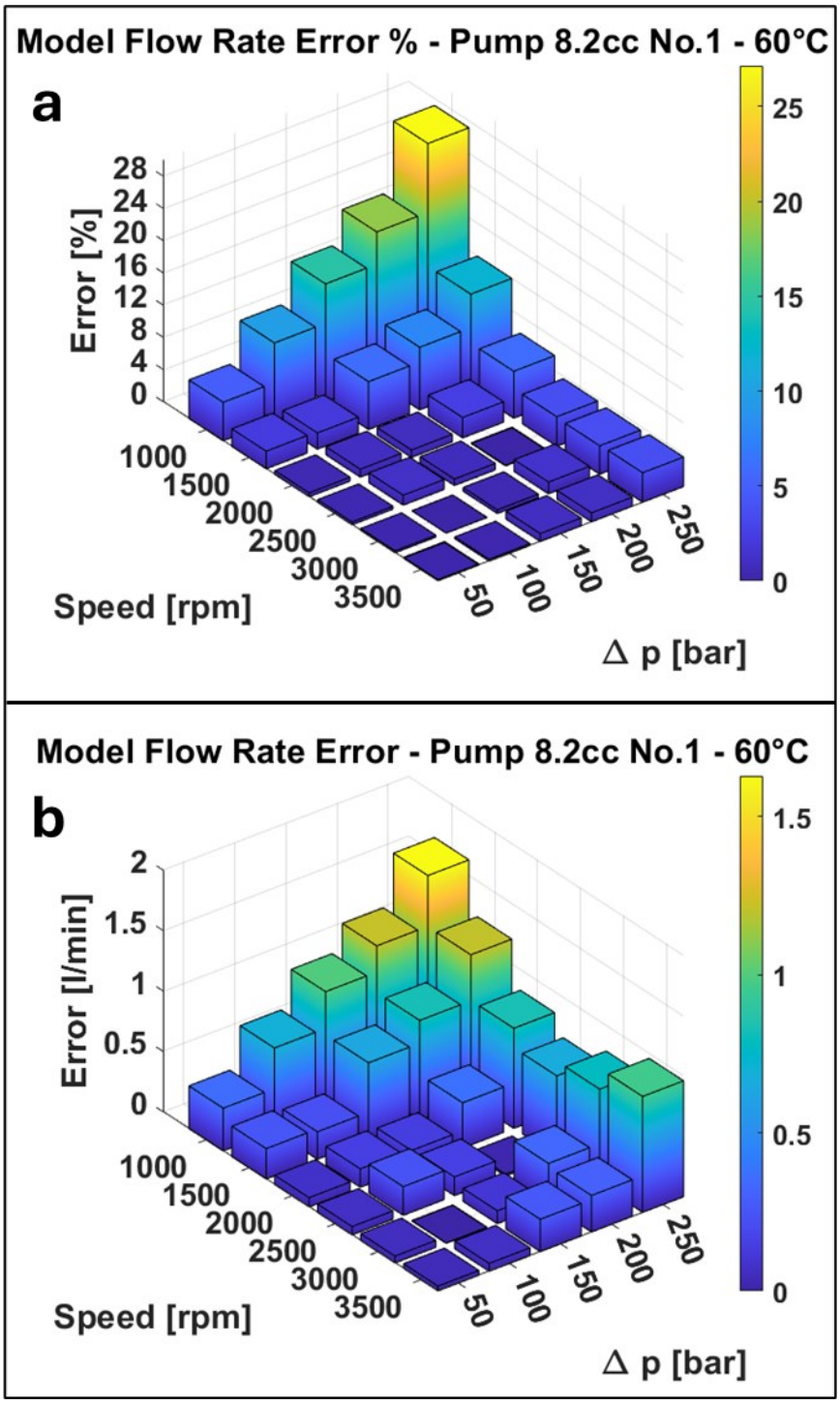

Figure 112 - Model flow-rate estimation error: (a) relative error [%]; (b) absolute error [L min^{-1}] Pump 8.2 cc No.1 60°

Figure 113 shows the volumetric efficiency as a function of pressure. Within the speed range 2000–3500 rpm, the model follows the experimental trend more closely, whereas at 1000 rpm it overestimates the volumetric efficiency. At this lower speed, the experimental volumetric efficiency decreases markedly with increasing pressure, while the model curve is only weakly affected by the increase in pressure.

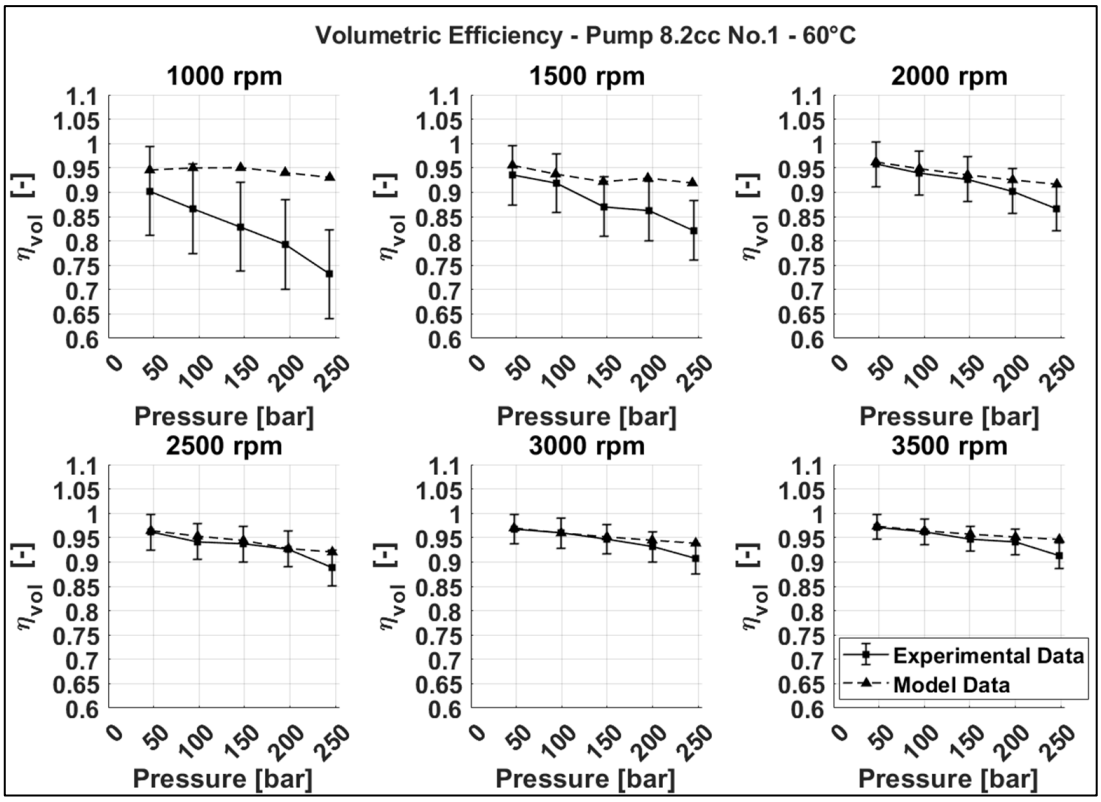

Figure 113- Pump 8.2 cc No.1 60° – Volumetric Efficiency vs Pressure

Figure 114 shows the volumetric efficiency as a function of speed. The experimental volumetric efficiency increases with increasing speed; however, this trend is not reproduced by the model due to its overestimation of volumetric efficiency at 1000-1500 rpm.

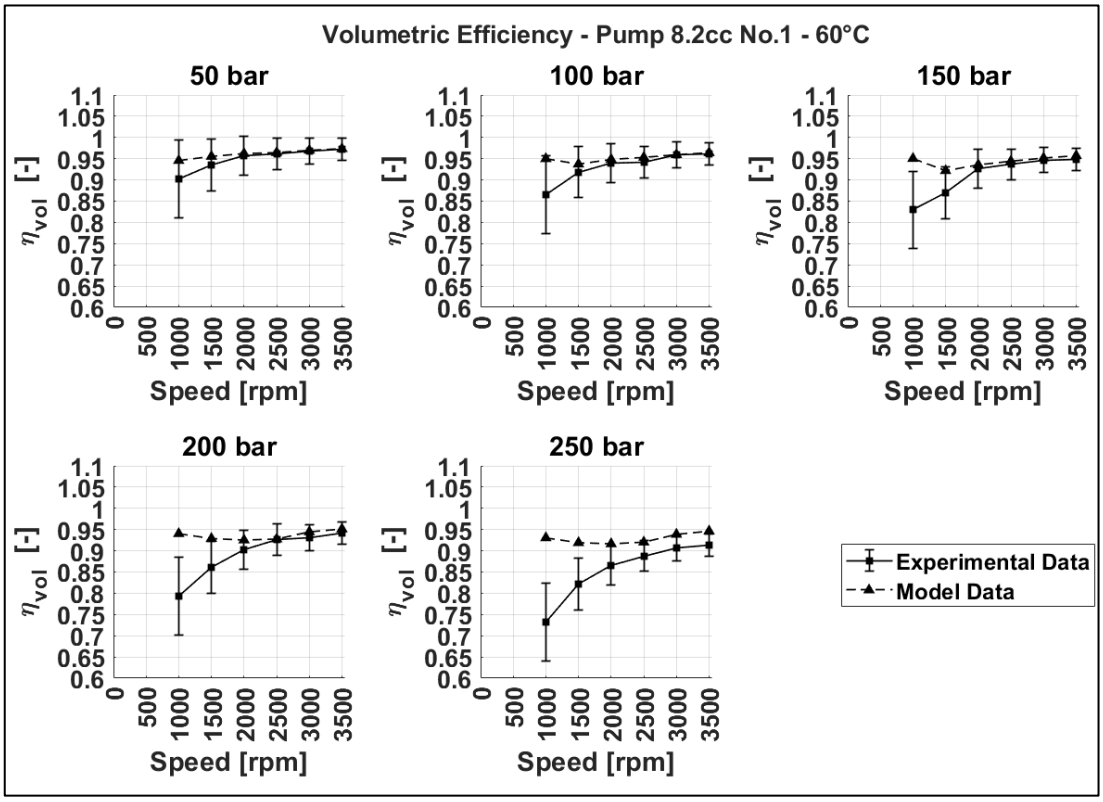

Figure 114 - Pump 8.2 cc No.1 60° – Volumetric Efficiency vs Speed

8.1.3. Pump 8.2 cc No. 1 - Comparative Volumetric Performance at 30 °C and 60 °C

Figure 115 illustrates the flow rate of the 8.2 cc pump (sample No. 1) at various rotational speeds at temperatures of 30 °C (red curves) and 60 °C (black curves). Considering the experimental data, at the same speed the pump flow rate at 60 °C is lower than at 30 °C. This behaviour is attributable to the increase in temperature, which reduces the oil viscosity and promotes volumetric leakage.
This difference between the 30 °C and 60 °C flow-rate curves is also reproduced by the model within the speed range 1500–3500 rpm.
At 1000 rpm, however, the modelled flow-rate curves at the two temperatures are very similar, with the 60 °C curve slightly higher than the 30 °C curve, an aspect not observed in the experimental data.

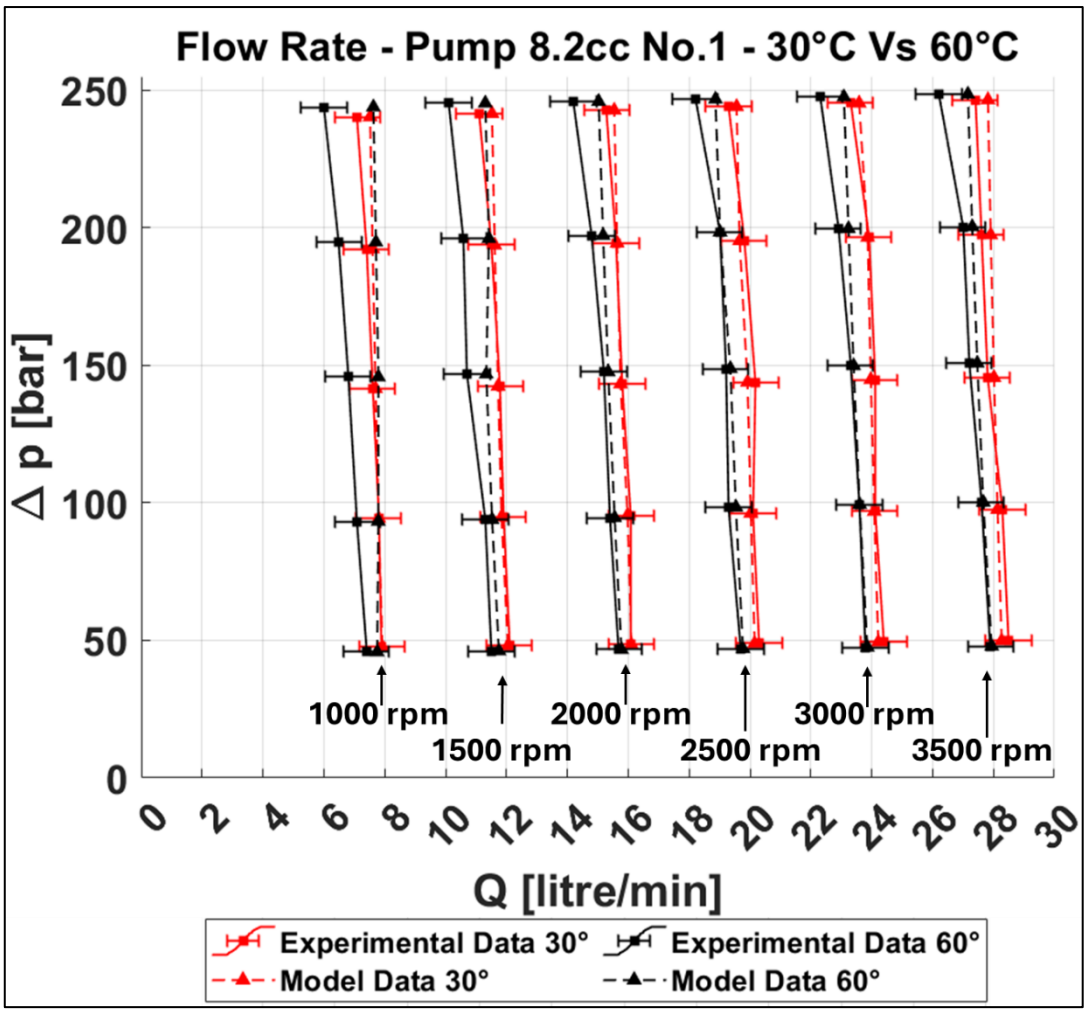

Figure 115 - Pump 8.2 cc No.1 Flow Rate - 30°C and 60°C

Figure 116 shows the flow rate ripple of the 8.2 cc pump (sample No. 1) at 1000 rpm and a delivery pressure of approximately 250 bar, at the two temperatures.

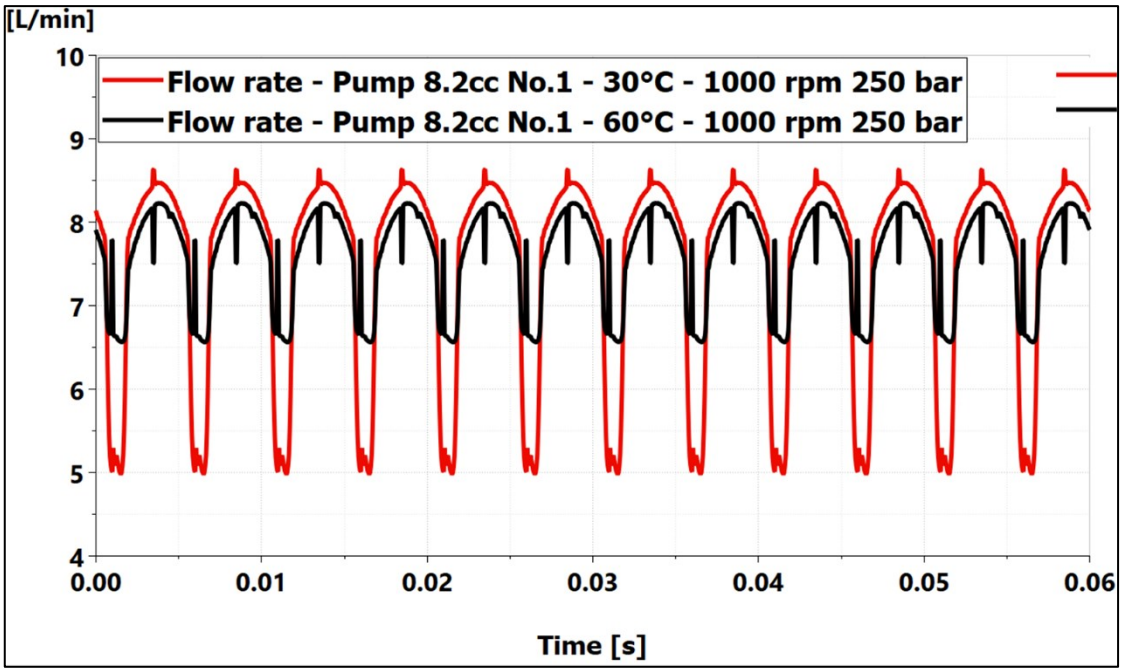

Figure 116 - Pump 8.2 cc No.1- Model Flow Rate - 30° and 60° - 1000 rpm and 250bar

The flow rate oscillation at 60 °C is lower than at 30 °C; consequently, the mean flow rate value is higher at 60 °C. This reduced ripple at 60 °C is attributed to the gear eccentricity estimated by the model under these operating conditions. Specifically, at 60 °C the inter-axis distance of the gears is 31.929 mm according to the model, whereas at 30 °C it is 31.989 mm.

A lower inter-axis distance at 60 °C implies a smaller gap height between the tooth flanks and reduced bypass between delivery and suction during meshing. This bypass is one of the main volumetric leakage paths influencing both flow and pressure ripple at the delivery port.
At 60 °C, the flank-gap height is 0.020 mm, whereas at 30 °C it is 0.063 mm.

To improve the model's capability to estimate the flow rate at high temperature and low speed, a more detailed modelling of the journal bearings is required.

8.1.4. Pump 8.2 cc No.1- Hydro-Mechanical Performance – 30 °C

Figure 117 shows the torque of the 8.2 cc pump, sample No. 1, at different pressures at 30 °C.
The solid line with square markers represents the experimental data, whereas the dotted line with triangular markers represents the model results.
The experimental data are plotted with the torque meter measurement uncertainty, which is ±0.5 N·m .

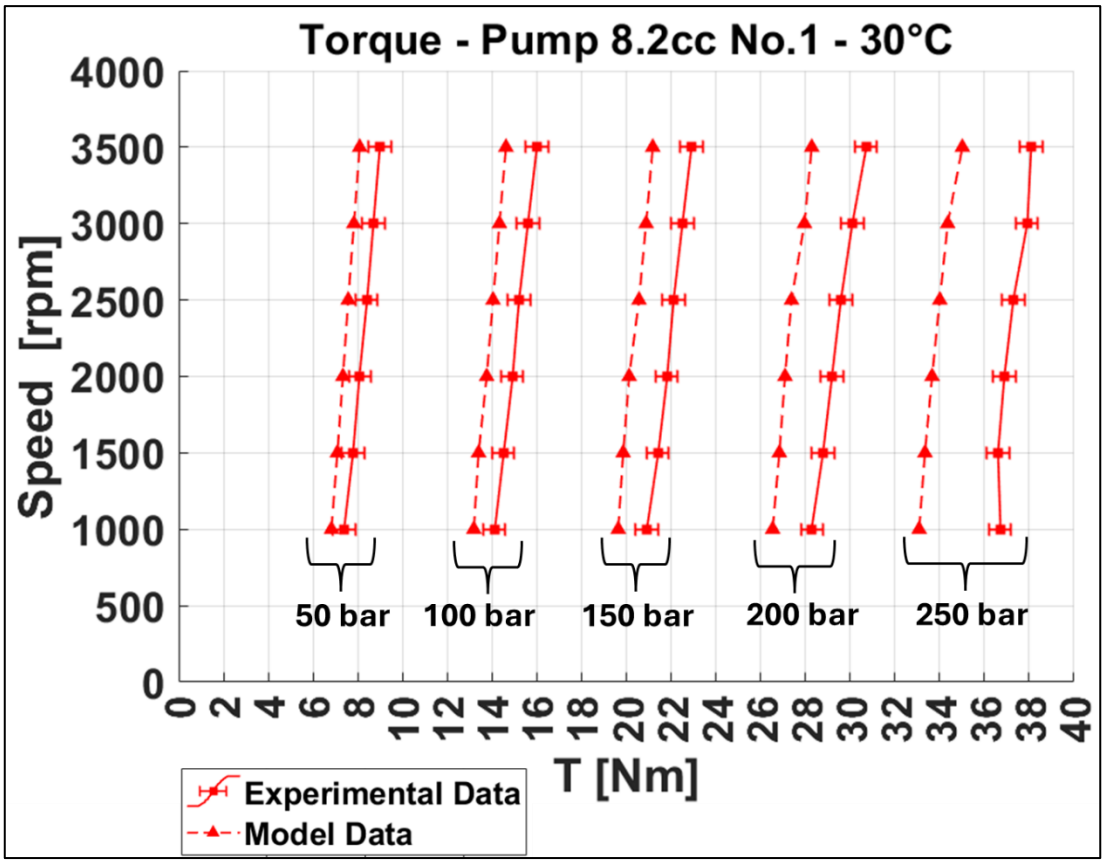

Figure 117- Pump 8.2 cc No.1 Torque - 30°C

From Figure 117, the model follows the experimental trend reasonably well: torque increases with increasing speed. It should be noted, however, that the model underestimates the torque across all operating conditions.

Figure 118 presents the model error in the estimation of torque. Figure 118.(a) presents the relative error, expressed as:

$$Error[\%] = \frac{|M_{exp} - M_{model}|}{M_{exp}} \qquad \textit{Eq. 208}$$

Figure 118.(b) shows the absolute error, expressed in N·m , as:

$$Error[Nm] = |M_{exp} - M_{model}| \qquad \textit{Eq. 209}$$

Considering the relative error, the maximum occurs at 50 bar with a value of 10.1%. Within the 100–200 bar range, the relative error decreases, with a maximum value of 8.6%, and then increases slightly at 250 bar to a maximum of 9.8%.

Considering the absolute error, at constant pressure it is weakly influenced by speed variation, whereas at constant speed the variation in pressure strongly affects the error. The minimum absolute error is 0.57 N·m at 50 bar and 1000 rpm, while the maximum absolute error is 3.62 N·m at 250 bar and 1000 rpm The torque meter measurement uncertainty is ±0.5 N·m.

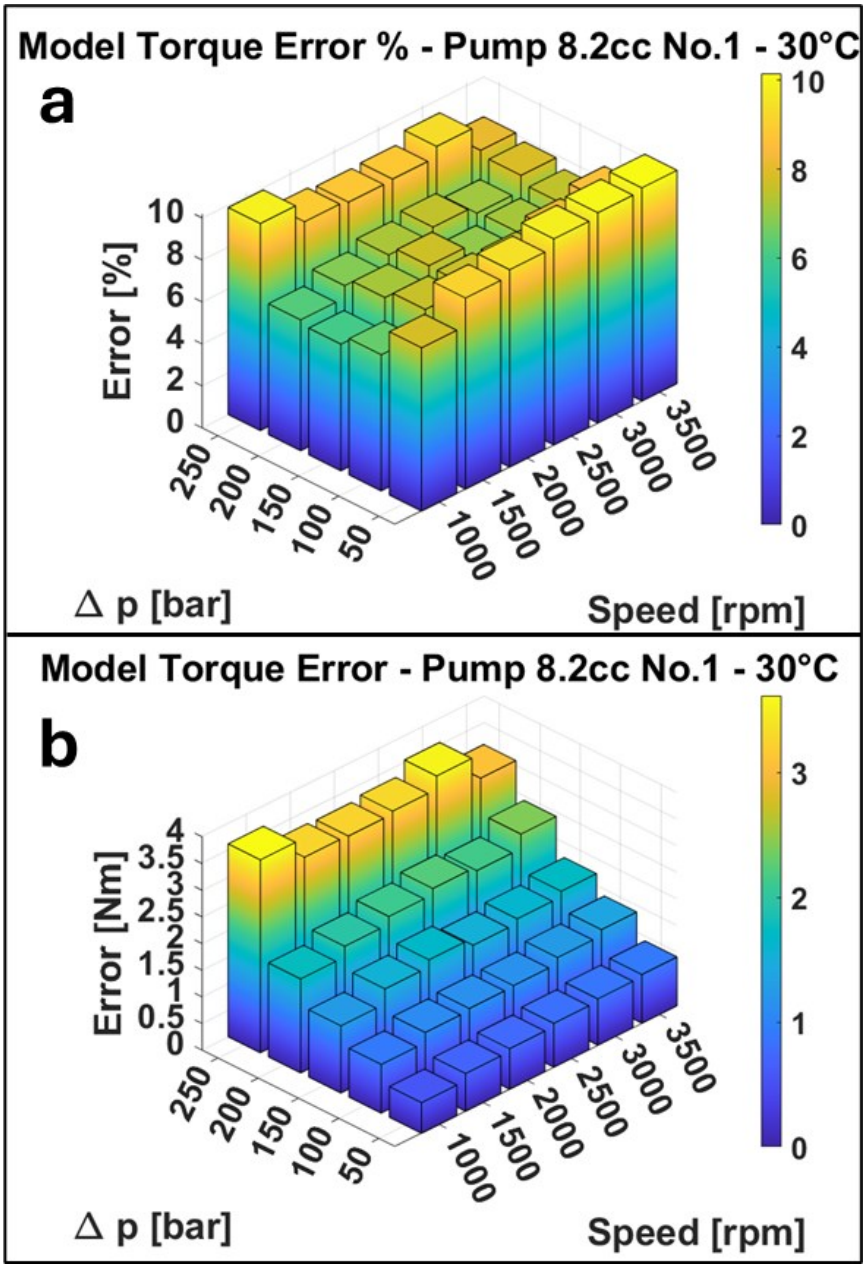

Figure 118 - Model torque estimation error: (a) relative error [%]; (b) absolute error [N·m]
Pump 8.2 cc No.1 30°C

Figure 119 and Figure 120 compare the hydro-mechanical efficiency obtained experimentally with that predicted by the model. The hydro-mechanical efficiency is defined as

$$\eta_{hm} = \frac{M_{th}}{M_{exp}} \qquad \textit{Eq. 210}$$

Where M_{exp} is the experimental torque in N·m, and M_{th} is the theoretical torque in N·m express as:

$$M_{th} = \frac{V_d\ (p_d - p_s)}{20\ \pi} \qquad \textit{Eq. 211}$$

Where:

- p_d is the delivery pressure in bar.
- p_s is the suction pressure in bar.
- V_d is the pump displacement in cm^3.

The measurement uncertainty of the hydro-mechanical efficiency is evaluated using standard uncertainty propagation:

$$\delta\eta_{hm} = \sqrt{\left(\frac{\partial\eta_{hm}}{\partial M_{exp}}\ \delta M_{exp}\right)^2 + \left(\frac{\partial\eta_{hm}}{\partial p_d}\ \delta p_d\right)^2 + \left(\frac{\partial\eta_{hm}}{\partial p_s}\ \delta p_s\right)^2} \qquad \textit{Eq. 212}$$

Where:

- $\delta\eta_{vol}$ is the hydro-mechanical efficiency measurement uncertainty.
- δM_{exp}= ±0.5 N·m, is the torquemeter uncertainty.
- δp_d = ±3 bar, is the delivery pressure measurement uncertainty.
- δp_s = ±0.05 bar, is the suction pressure measurement uncertainty.

Substituting the definition of η_{hm} yields:

$$\delta\eta_{hm} = \frac{V_d}{20\ \pi}\sqrt{\left(\frac{(p_d - p_s)}{M_{exp}^2}\ \delta M_{exp}\right)^2 + \left(\frac{\delta p_d}{M_{exp}^2}\right)^2 + \left(\frac{\delta p_s}{M_{exp}^2}\right)^2} \qquad \textit{Eq. 213}$$

Figure 119 plots the hydro-mechanical efficiency as a function of pressure. The experimental data indicate that hydro-mechanical efficiency increases with pressure in the range 50–200 bar, and then decreases at 250 bar. This trend is generally captured by the model, except at 250 bar where the modelled hydro-mechanical efficiency continues to increase.

Figure 120 plots the hydro-mechanical efficiency as a function of speed. With increasing speed, the experimental hydro-mechanical efficiency decreases; however, at 250 bar it is only weakly influenced by speed. The model follows the experimental data over most conditions, but at 250 bar the modelled hydro-mechanical efficiency exhibits a stronger dependence on speed than observed experimentally.

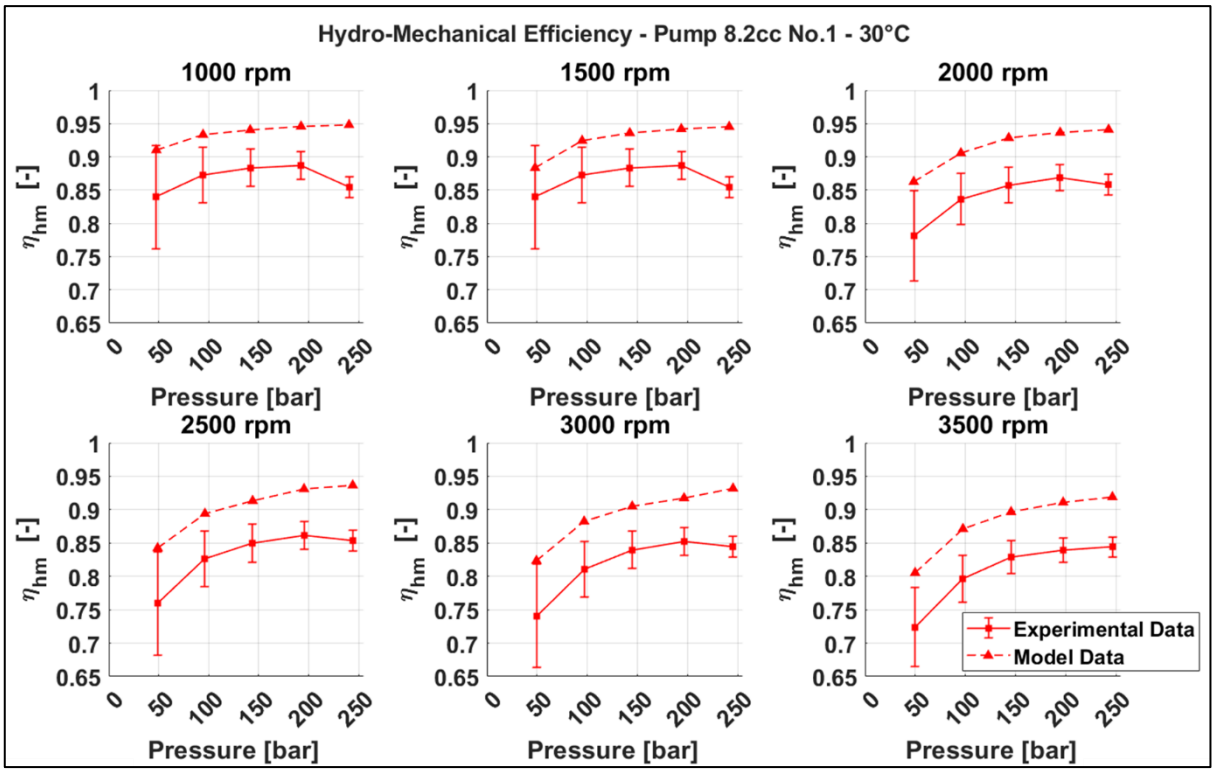

Figure 119 - Pump 8.2 cc No.1 30° – Hydro-Mechanical Efficiency vs Pressure

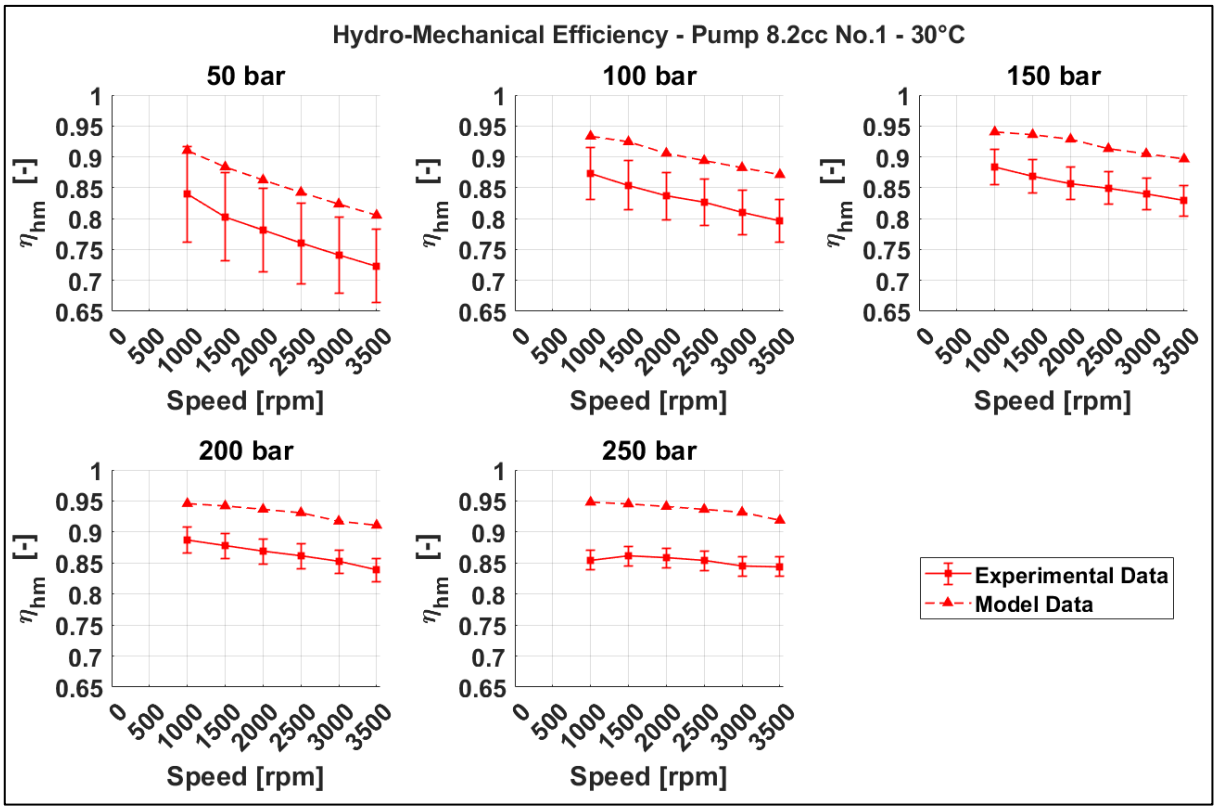

Figure 120 - Pump 8.2 cc No.1 30° – Hydro-Mechanical Efficiency vs Speed

8.1.5. Pump 8.2 cc No.1- Hydro-Mechanical Performance – 60 °C

Figure 121 shows the torque of the 8.2 cc pump, sample No. 1, at different pressure at 60 °C.
The solid line with square markers represents the experimental data, whereas the dotted line with triangular markers represents the model results.
The experimental data are plotted with the torque-meter measurement uncertainty, which is ±0.5 N·m.

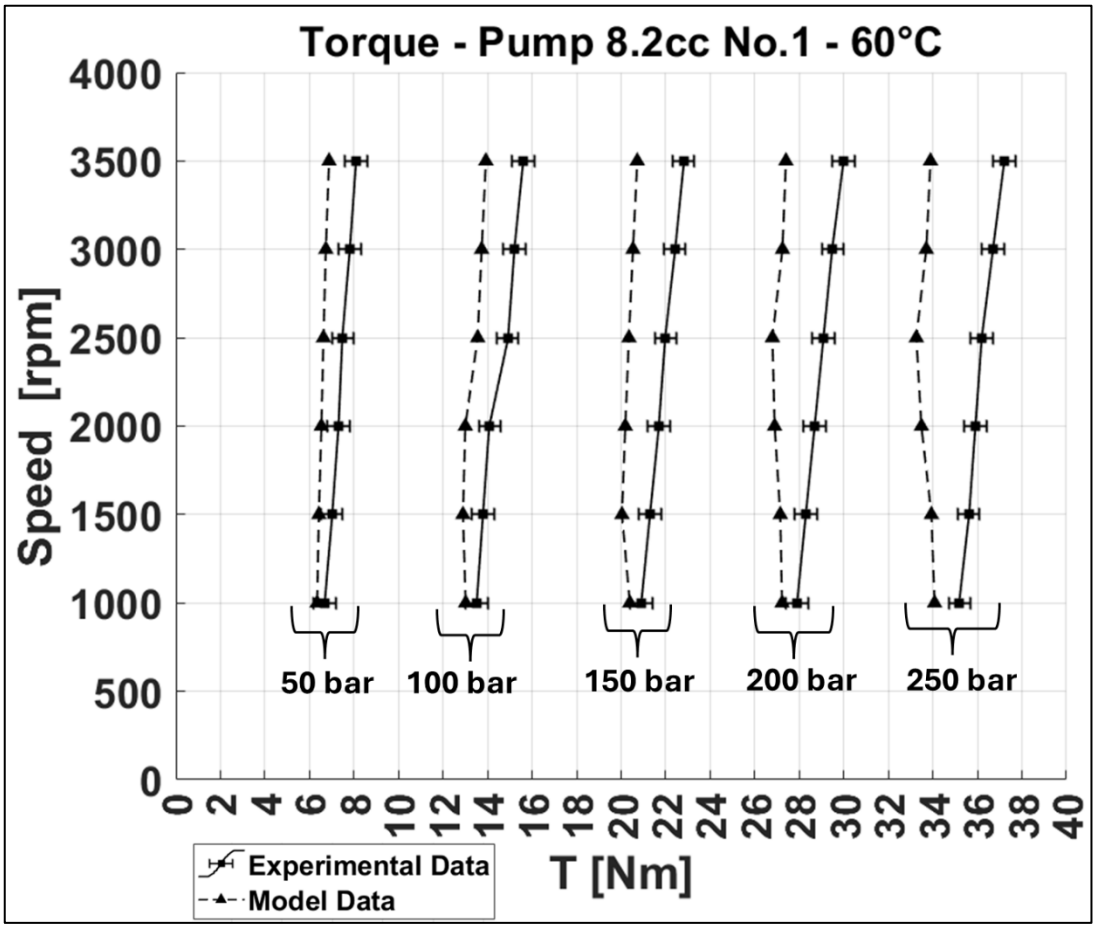

Figure 121 - Pump 8.2 cc No.1 Torque – 60°C

Figure 121 shows that the model reproduces the experimental trend well in the pressure range 50-150 bar. At 200 and 250 bar, however, the modelled torque exhibits a phase of reduction with increasing speed from 1000 to 2500 rpm, followed by a phase of increase from 2500 to 3500 rpm, whereas the experimental torque increases monotonically with speed.

Figure 122.(a) presents the relative error, while Figure 122.(b) shows the absolute error, expressed in N·m .
In terms of relative error, the maximum value is 15.1% at 50 bar; within the 100–250 bar range, the maximum relative error is 10.7%.
Considering the absolute error, the maximum value is 3.3 N·m at 250 bar and 3500 rpm. Compared with the relative error, the absolute error at 50 bar is lower than at the other pressure conditions.

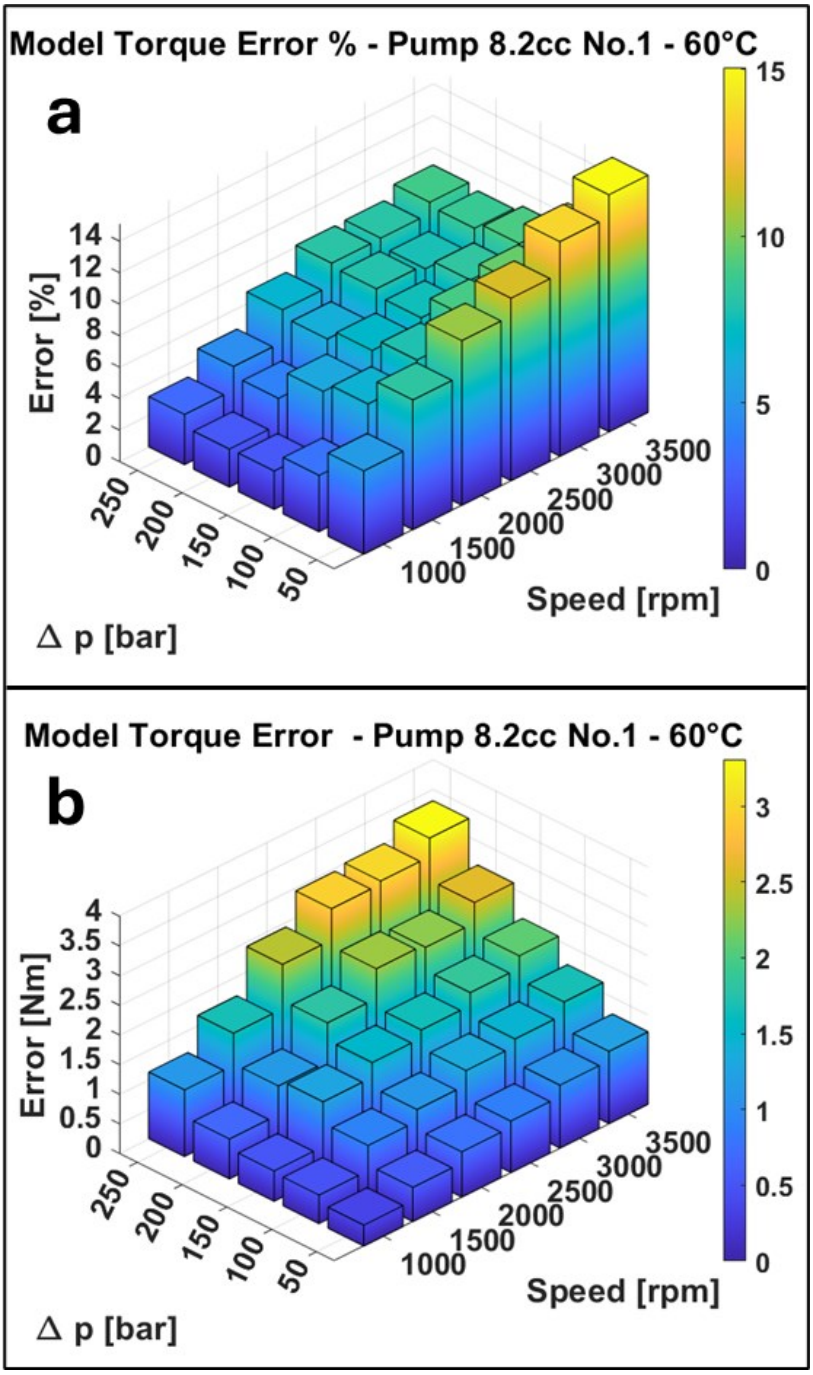

Figure 122 - Model torque estimation error: (a) relative error [%]; (b) absolute error [N·m] Pump 8.2 cc No.1 60°C

Figure 123 plots the hydro-mechanical efficiency as a function of pressure. In this case, the modelled hydro-mechanical efficiency follows the experimental trend well. By contrast, Figure 124 plots the hydro-mechanical efficiency as a function of speed, and here the model does not reproduce the experimental behaviour.

Experimentally, hydro-mechanical efficiency decreases with increasing speed. In the model, however, the efficiency at 100 and 150 bar is nearly constant with speed, whereas at 200 and 250 bar it increases and then decreases with speed. Only at 50 bar does the modelled hydro-mechanical efficiency follow the experimental data closely.

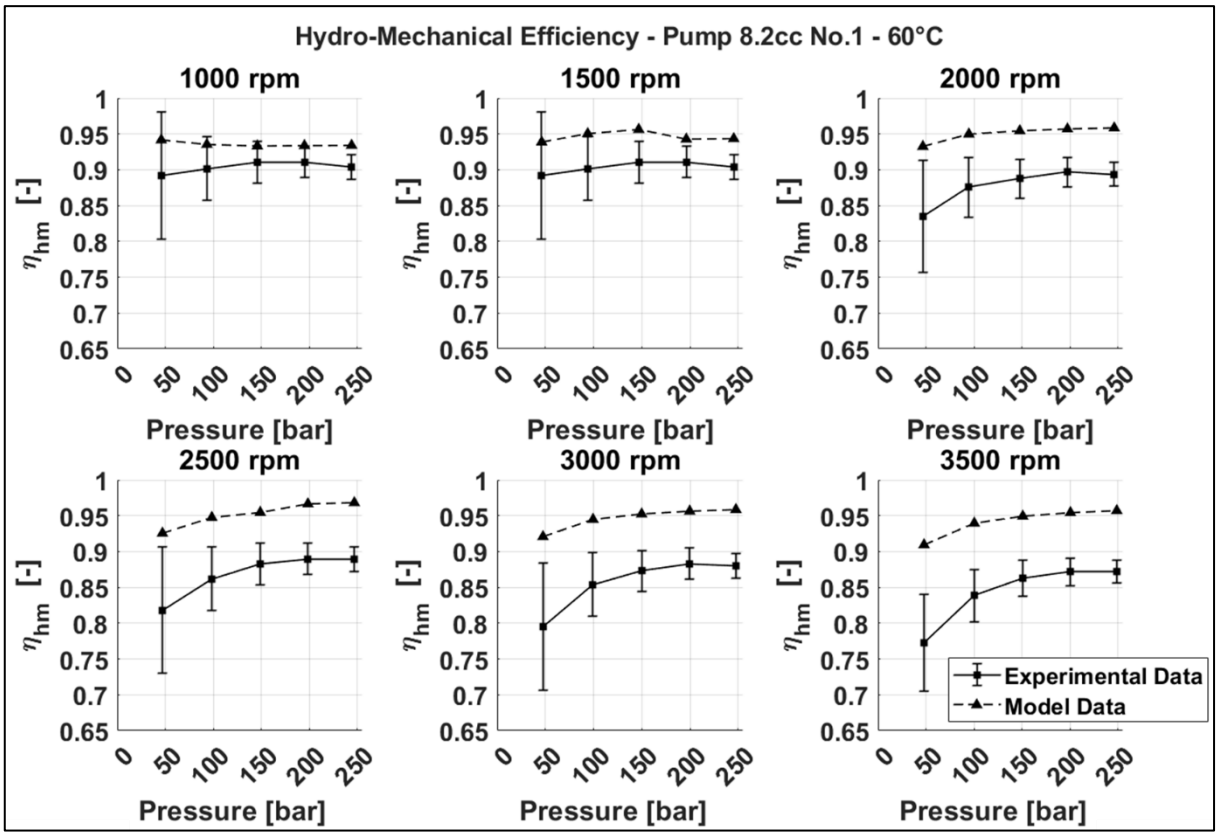

Figure 123 - Pump 8.2 cc No.1 60° – Hydro-Mechanical Efficiency vs Pressure

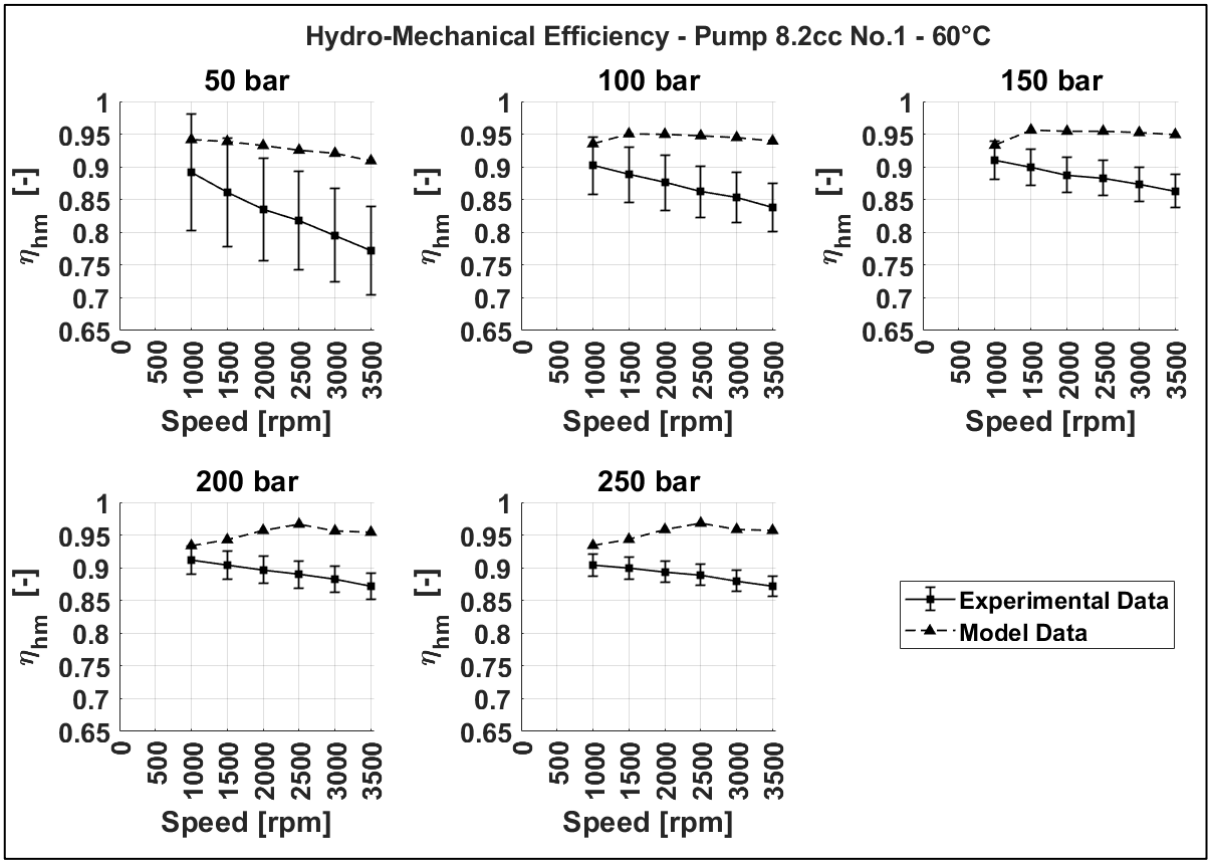

Figure 124 - Pump 8.2 cc No.1 60° – Hydro-Mechanical Efficiency vs Speed

8.1.6. Pump 8.2 cc No. 1 - Comparative Hydro-Mechanical Performance at 30 °C and 60 °C

Figure 125 illustrates the torque of the 8.2 cc pump (sample No. 1) as a function of pressure, at various rotational speeds and at temperatures of 30 °C (red curves) and 60 °C (black curves).

The experimental data show that increasing the temperature reduces the torque required to drive the pump. This behaviour can be attributed to the decrease in oil viscosity with increasing temperature, which in turn reduces viscous losses.
This phenomenon is also reproduced by the model within the speed range 2000–3500 rpm. At 1500 rpm, however, the modelled torques at 30 °C and 60 °C are very similar, and at 1000 rpm, from 100 to 250 bar, the modelled torque at 60 °C is higher than at 30 °C (see Figure 125).

The modelled torque is obtained as the sum of two contributions: the torque due to fluid pressure and the torque due to viscous–mechanical losses.
Figure 126 shows the torque attributable solely to fluid pressure as estimated by the model.

Within the 1500–3500 rpm range, the pressure-induced torque at 30 °C and 60 °C is very similar; in some cases, the torque at 30 °C is slightly higher than at 60 °C. The pressure torque is governed primarily by the chamber pressures in the meshing zone. Figure 127 shows the chamber pressure predicted by the model under operating conditions of 1000 rpm and about 250 bar.

It emerges that, in the meshing zone, the chamber pressures at 60 °C are higher than at 30 °C. This behaviour is attributed to the gear eccentricity predicted by the model under these conditions. Specifically, the inter-axis distance is 31.929 mm at 60 °C and 31.989 mm at 30 °C. A smaller inter-axis distance at 60 °C implies a reduced flank-gap height and lower chamber volumetric leakage, leading to higher chamber pressures than at 30 °C.

The higher average torque and the reduced flow rate ripple are consistent with the higher chamber pressures and the reduced volumetric leakage.

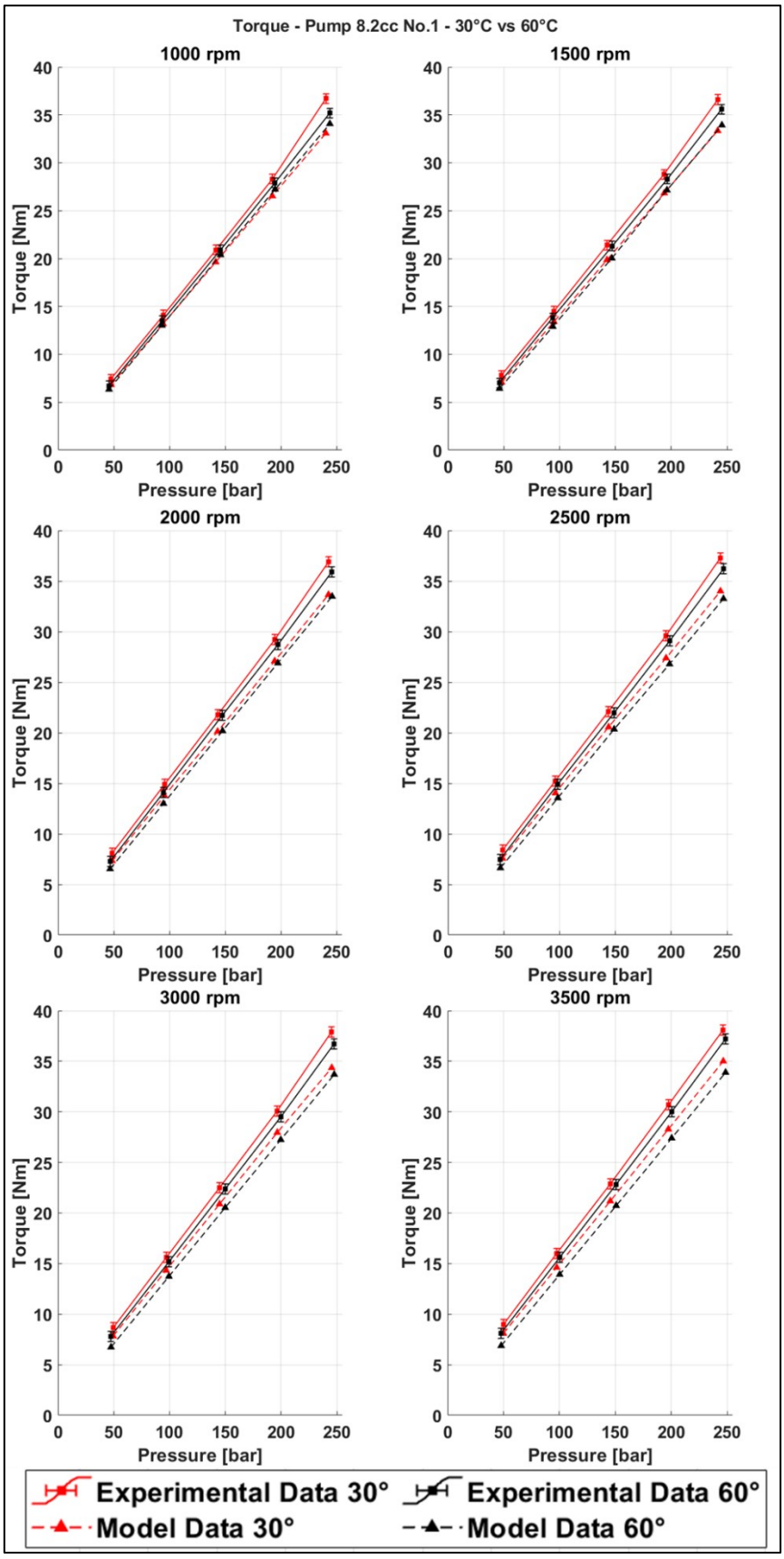

Figure 125 - Pump 8.2 cc No.1 Torque - 30°C and 60°C

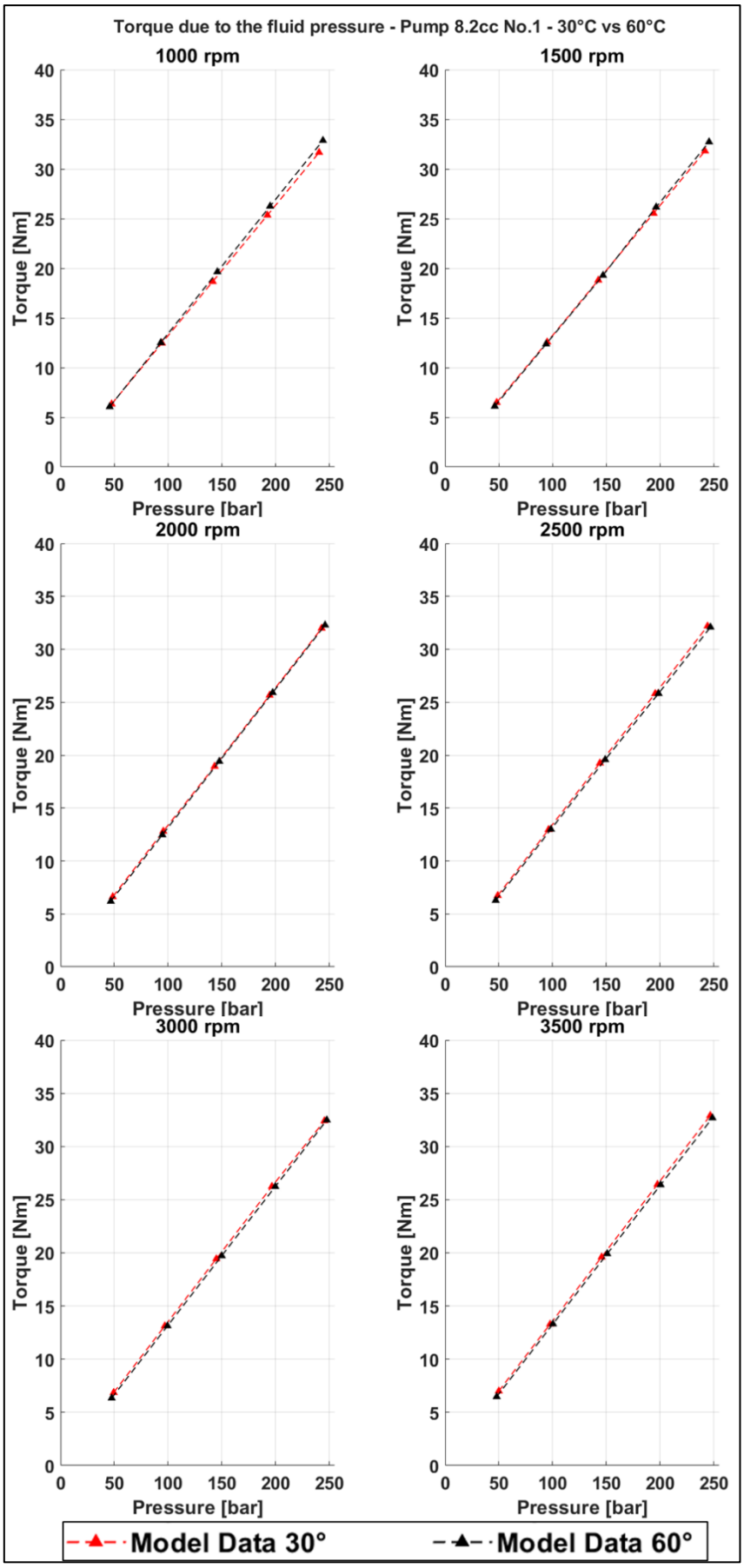

Figure 126 - Pump 8.2 cc No.1 Torque due to the fluid pressure - 30°C and 60°C

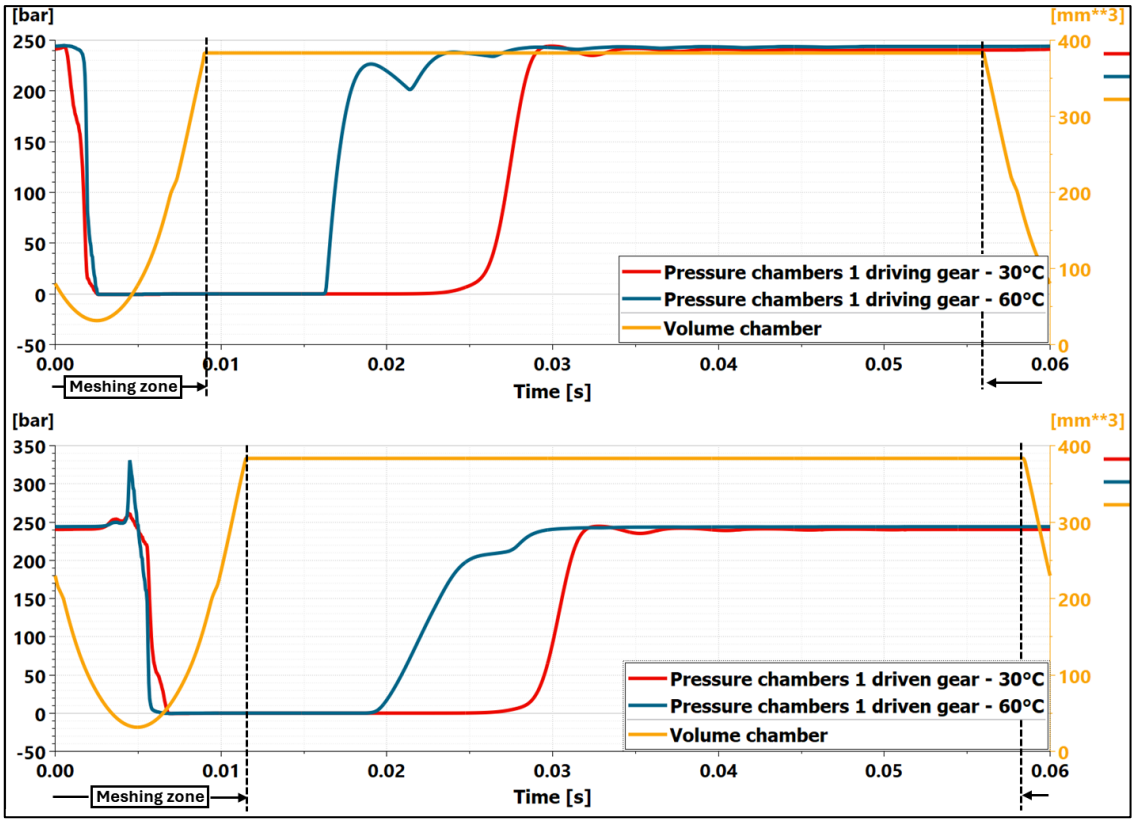

Figure 127 – Pressure in the first chamber of the driving and driven gear at 30°C and 60°C - Pump 8.2 cc No.1

Figure 128 illustrates the torque losses of the 8.2 cc pump (sample No. 1) as a function of pressure, evaluated at multiple rotational speeds and at temperatures of 30 °C (red curves) and 60 °C (black curves). The torque losses estimated by the model at 30 °C are higher than at 60 °C. Consequently, the discrepancy between the model and the experimental data at 1000 rpm is attributed to the estimation of the pressure-induced torque, and more specifically to the definition of gear eccentricity at 60 °C.

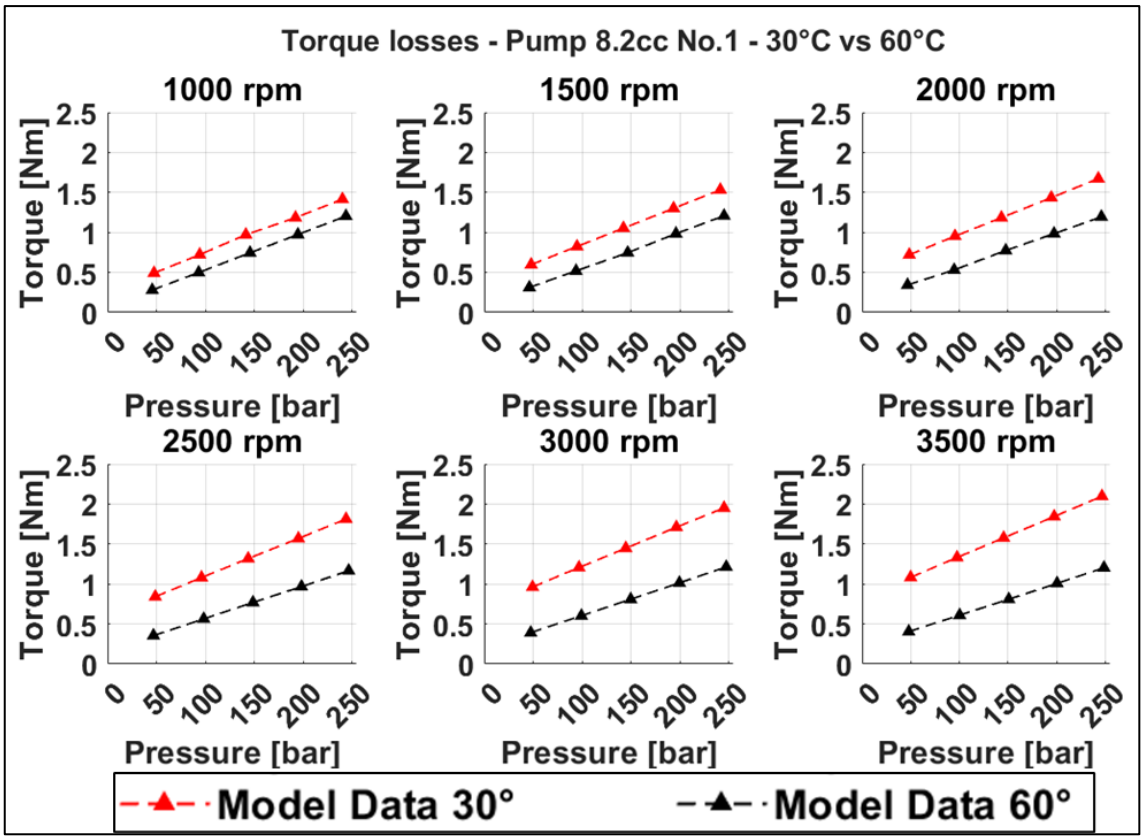

Figure 128 - Pump 8.2 cc No.1 Torque losses - 30°C and 60°C

Figure 129 shows the individual contributions to the torque losses:

- viscous losses arising from the journal bearings, the clearance between the tooth tips and the pump housing, and the lateral gap.
- mechanical losses due to gear meshing.

An increase in speed primarily affects the viscous losses, which rise with speed, whereas the meshing losses decrease slightly. By contrast, increasing pressure has little influence on the viscous losses but substantially increases the meshing losses. Increasing temperature predominantly affects the viscous losses, which decrease with temperature, while the meshing losses are only weakly influenced.

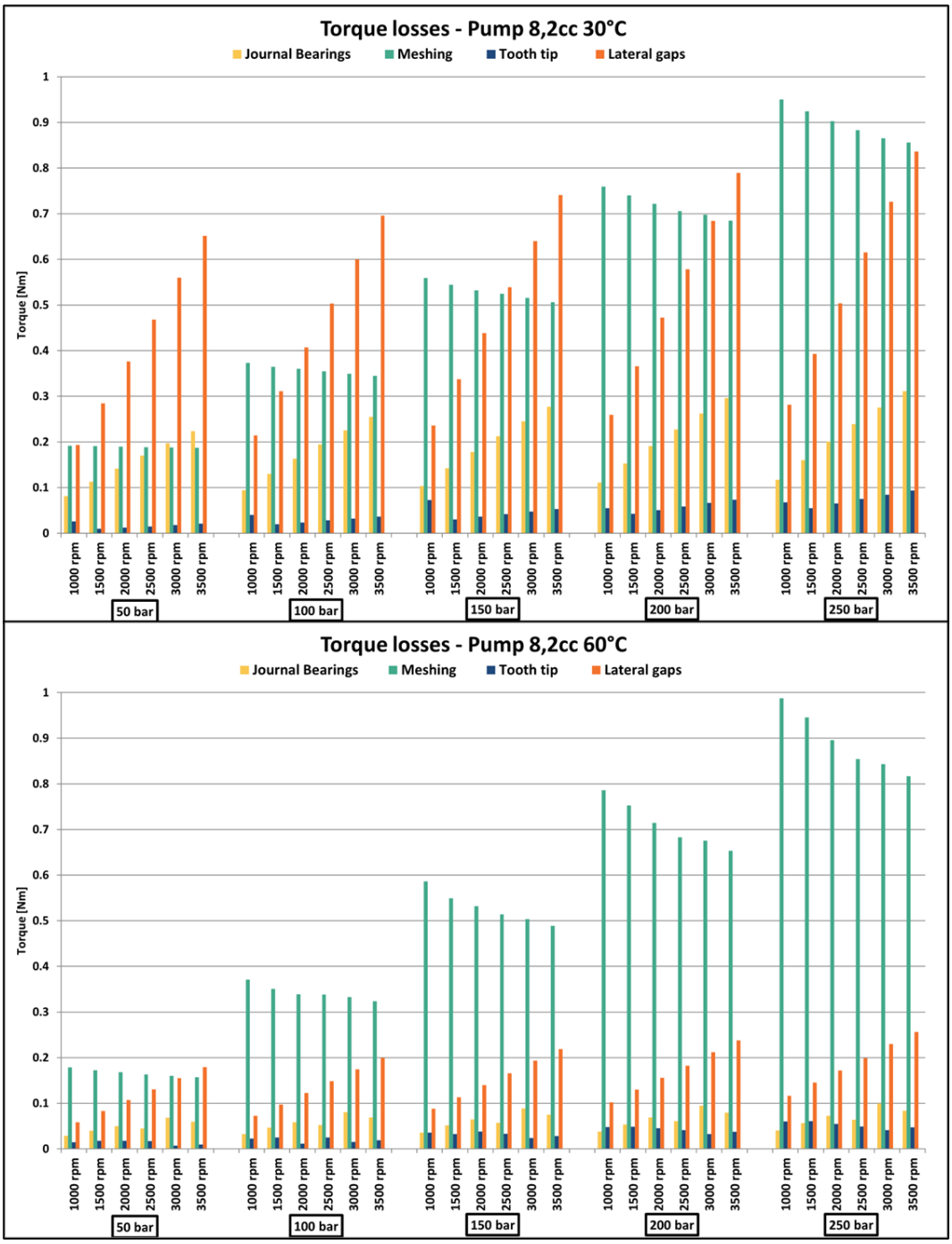

Figure 129 - Pump 8.2 cc No. 1 - Contributions to torque losses at 30 °C and 60 °C

Figure 130 shows the relative contributions of the different loss components to the total torque losses.

At 30 °C, the losses due to the journal bearings and the lateral gap play a significant role in determining the overall torque losses; however, with increasing pressure, the meshing losses also become more prominent. The losses associated with the tooth-tip clearance are small compared with the other contributions.

At 60 °C, by contrast, the torque losses are dominated primarily by the meshing losses.

Figure 130 - Pump 8.2 cc No. 1 - Percentage contributions to torque losses at 30 °C and 60 °C

8.2. Pump 16 cc No.3 – Performance Results

The following sections present and analyse the experimental and model results for the 16 cc pump, sample No. 3, focusing on volumetric and hydro-mechanical performance at 30 °C and 60 °C.

8.2.1. Pump 16 cc No.3- Volumetric Performance – 30 °C

Figure 131 shows the flow rate of the 16 cc pump, sample No. 3, at different speeds at 30 °C. The solid line with square markers represents the experimental data, whereas the dotted line with triangular markers represents the model results. The experimental data are plotted with the flow-meter measurement uncertainty, which is ±0.75 L min⁻¹.

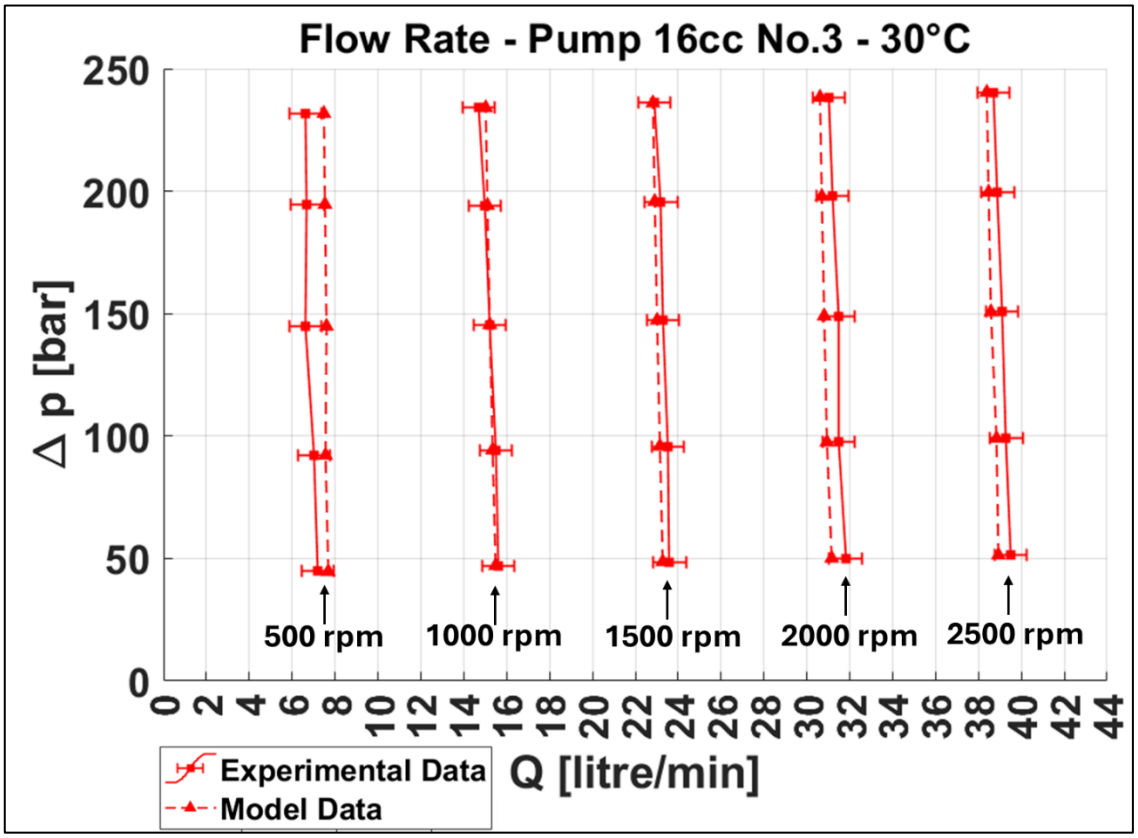

Figure 131 - Pump 16 cc No.3 Flow Rate - 30°

Figure 132.(a) shows the relative error in the estimation of the flow rate, whereas Figure 132.(b) presents the absolute error.
presents the absolute error. The comparison indicates that the model exhibits strong capability in estimating the flow rate at 30 °C for the 16 cc pump within the 1000–2500 rpm range. In this speed interval, the model's maximum relative error is 2.2%, corresponding to a maximum absolute error of 0.69 L min⁻¹.

At 500 rpm, the model predictions deviate most from the experimental data, with a maximum relative error of 15.2% and an absolute error of approximately 1 L min⁻¹.

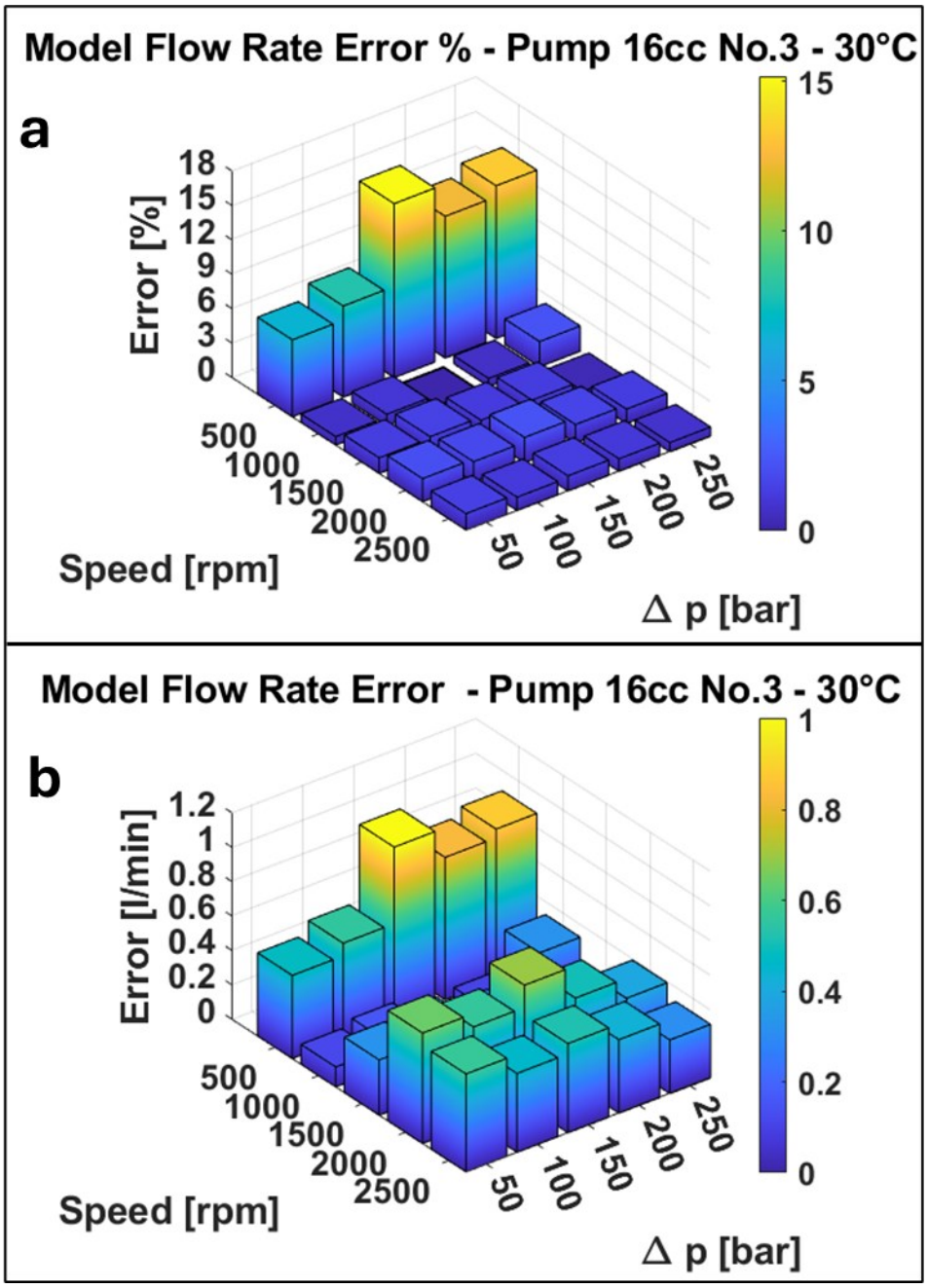

Figure 132 - Model flow-rate estimation error: (a) relative error [%]; (b) absolute error [L min^{-1}] Pump 16 cc No.3 30°

Figure 133 compares the volumetric efficiency obtained experimentally with that predicted by the model as a function of pressure. The model reproduces the experimental trend well.
While Figure 134 shows the volumetric efficiency as a function of rotational speed, where the largest discrepancy between experimental and model data is observed at 500 rpm.

It should be noted that, at 500 rpm, the measurement uncertainty of volumetric efficiency is greater than at other angular velocities. The adoption of a more suitable flowmeter for flow-rate detection at 500 rpm could be a possible future work to more rigorously evaluate the model's performance at low speeds.

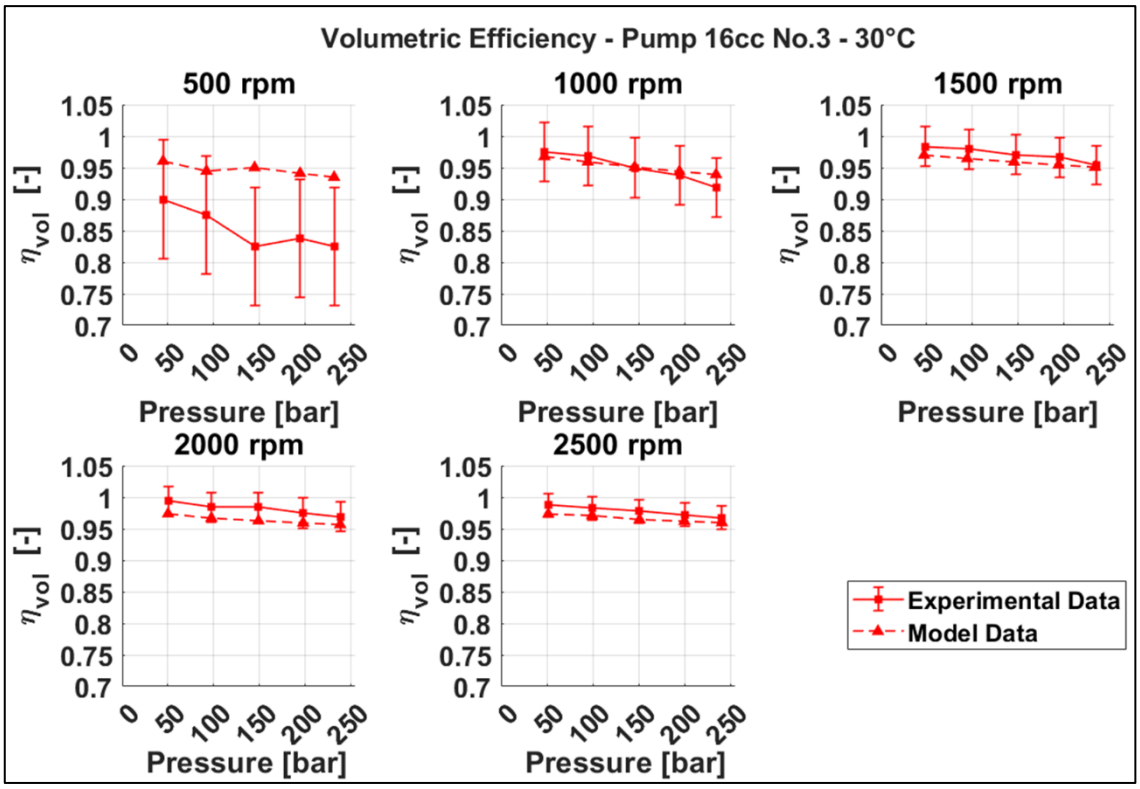

Figure 133 - Pump 16 cc No.3 30° – Volumetric Efficiency vs Pressure

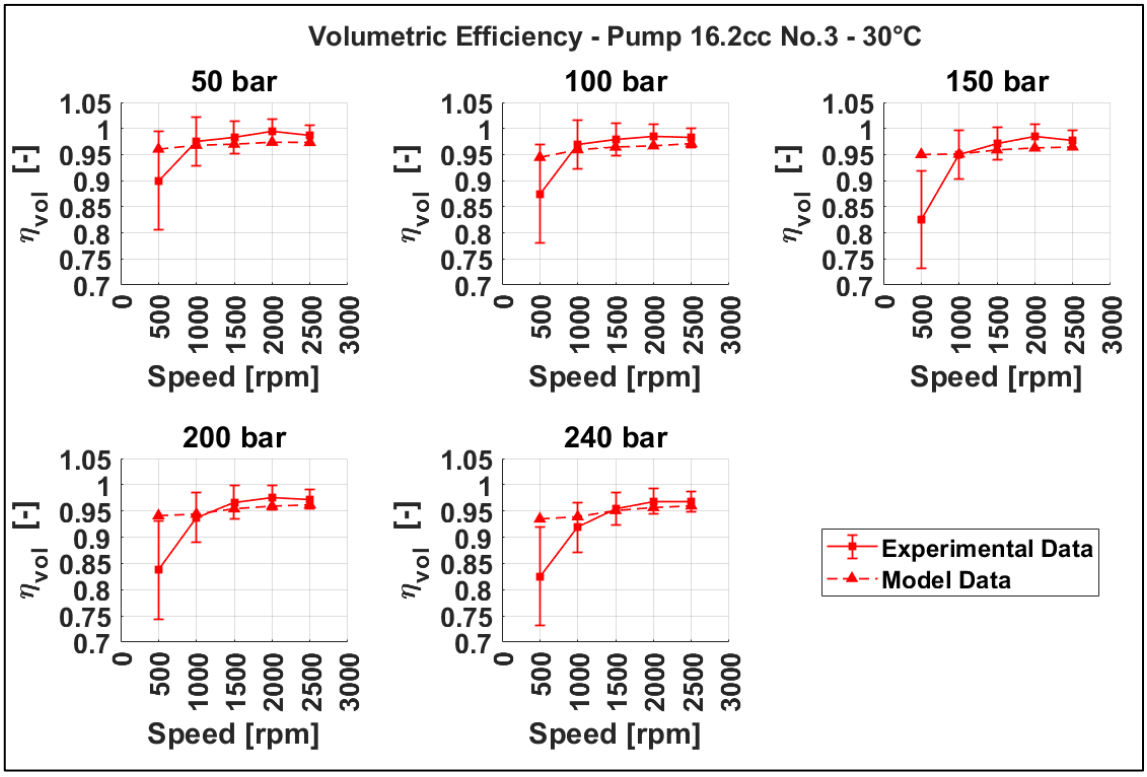

Figure 134 - Pump 16 cc No.3 30° – Volumetric Efficiency vs Speed

8.2.2. Pump 16 cc No.3- Volumetric Performance – 60 °C

Figure 135 illustrates the flow rate of the 16 cc pump sample No. 3 at various rotational speeds at 60 °C, while Figure 136 presents the model error in the estimation of the flow rate, expressed both relatively and absolutely.

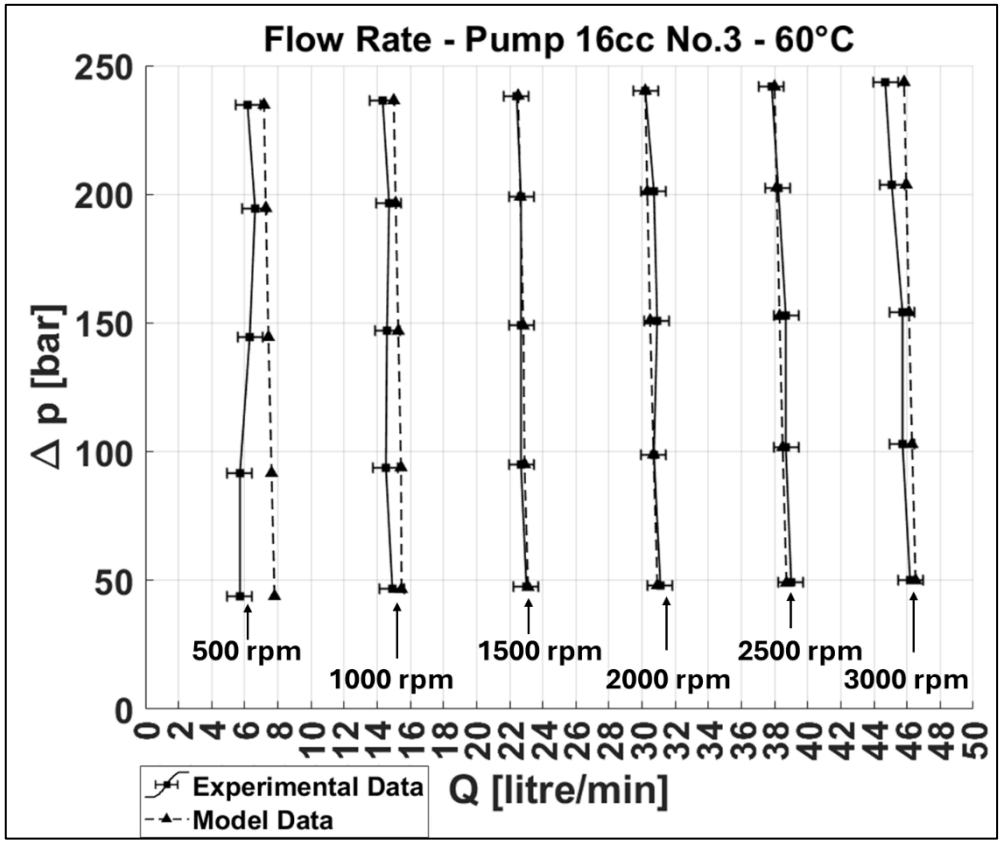

Figure 135 - Pump 16 cc No.3 Flow Rate - 60°

The comparison indicates that the model provides accurate flow rate estimates within the speed range 1000–3000 rpm. As speed decreases, the discrepancy with respect to the experimental data increases, and is most pronounced at 500 rpm.

In terms of error, within 1500–3000 rpm the maximum relative error is 2.5%; at 1000 rpm it reaches 4.9%, and at 500 rpm 36.8%.
In absolute terms, within 1500–3000 rpm the maximum error is 1.1L min^{-1}; at 1000 rpm it is 0.7 L min^{-1}, and at 500 rpm 2.1 L min^{-1}. Considering the flowmeter measurement uncertainty of ±0.75 L min^{-1}, these results confirm good estimation capability in the 1000–3000 rpm range.

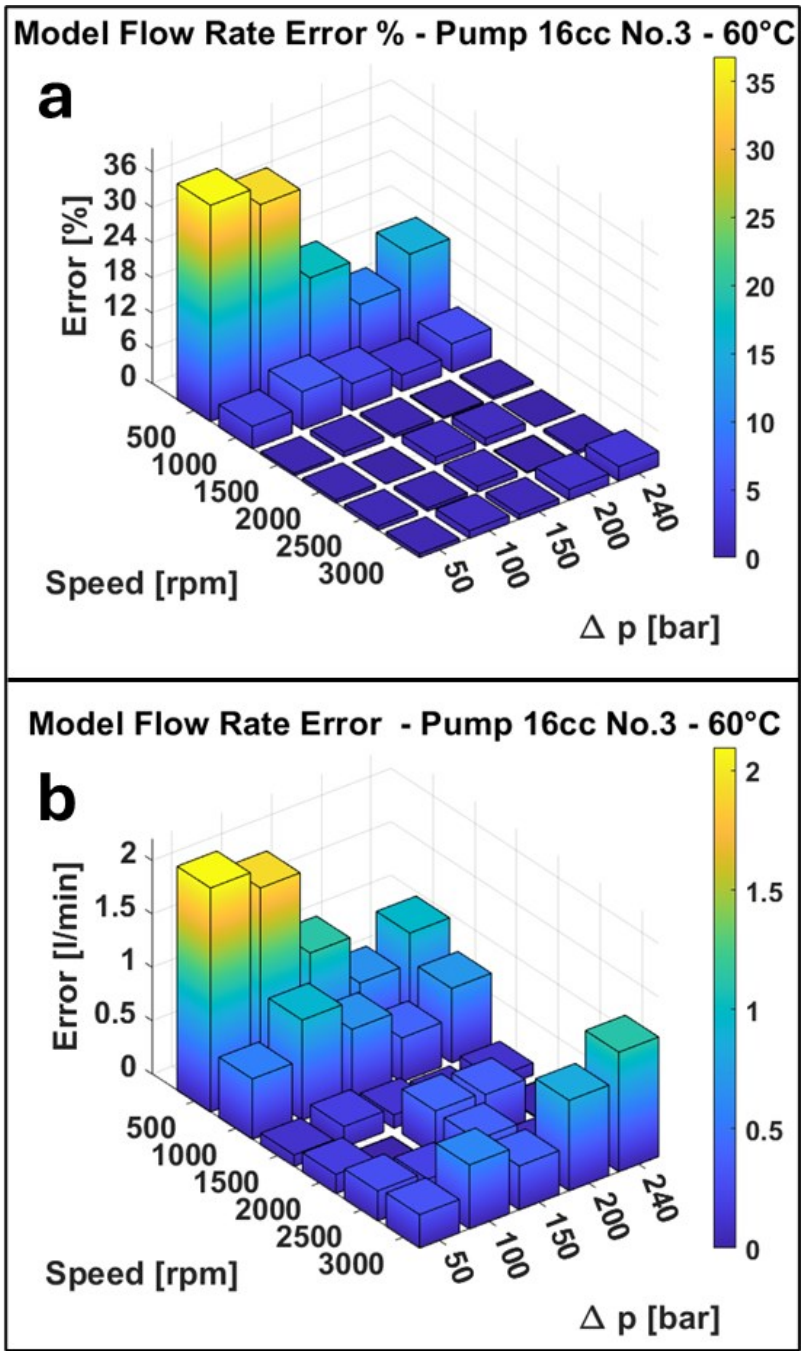

Figure 136 - Model flow-rate estimation error: (a) relative error [%]; (b) absolute error [L min^{-1}] Pump 16 cc No.3 60°

Figure 137 shows the volumetric efficiency as a function of pressure. Within the speed range 1500–3000 rpm, the model follows the experimental trend more closely, whereas at 1000 rpm it overestimates the volumetric efficiency. At the lower speed, the experimental volumetric efficiency and the model data have very different trends. It is worth noting that the experimental curve at 500 rpm has a very different trend from the other experimental volumetric efficiency curves at other angular velocities. As mentioned for the case of 30 °C, the use of a more adequate flowmeter at low speed is necessary to evaluate the pump behaviour under this condition.

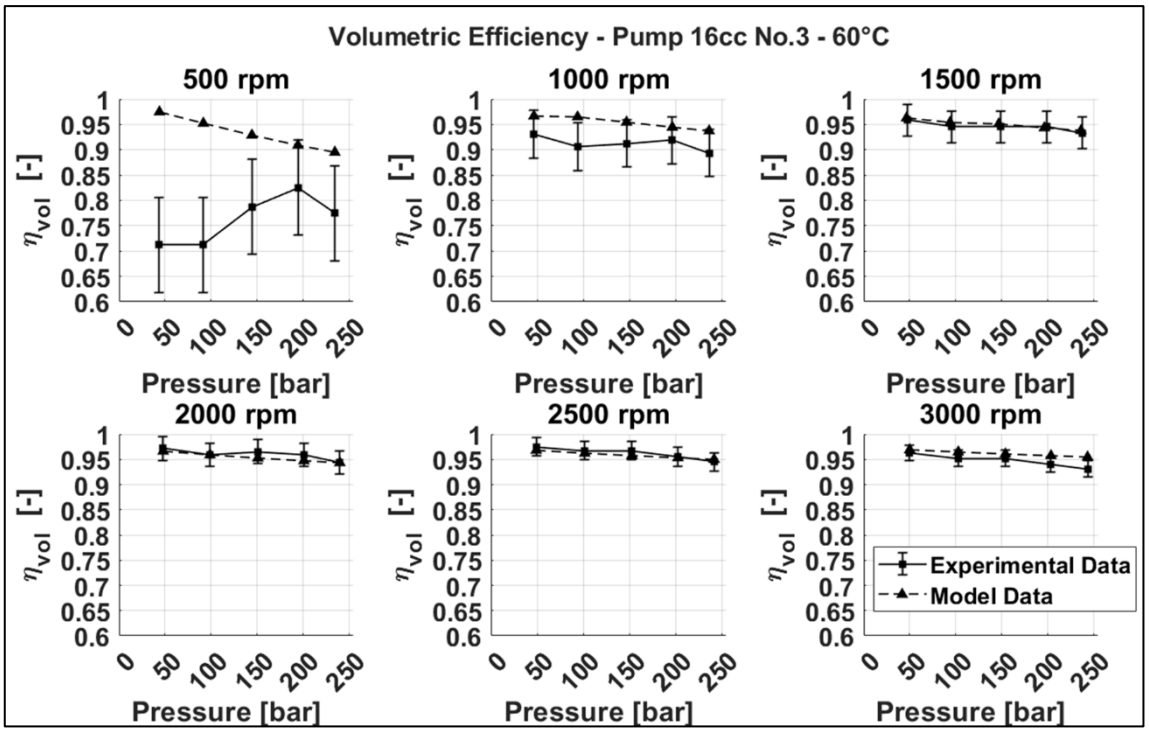

Figure 137 - Pump 16 cc No.3 60° – Volumetric Efficiency vs Pressure

Figure 138 shows the volumetric efficiency as a function of speed. The experimental volumetric efficiency increases with increasing speed; however, this trend is reproduced by the model at in the pressure range of 150-240bar.

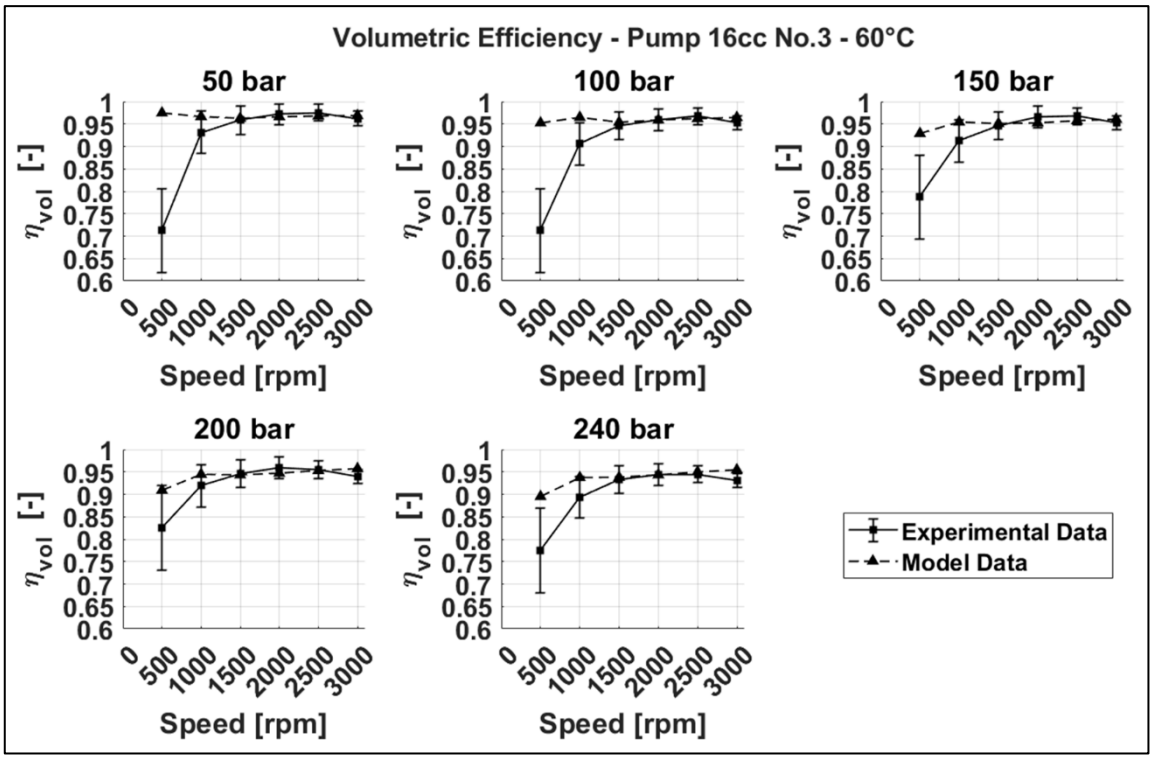

Figure 138 - Pump 8.2 cc No.1 60° – Volumetric Efficiency vs Speed

8.2.3. Pump 16 No. 3- Comparative Volumetric Performance at 30 °C and 60 °C

Figure 139 illustrates the flow rate of the 16 cc pump (sample No. 1) at various rotational speeds at 30 °C (red curves) and 60 °C (black curves). Considering the experimental data, at the same speed the pump flow rate at 60 °C is lower than at 30 °C. This behaviour is attributable to the increase in temperature, which reduces the oil viscosity and promotes volumetric leakages. This difference between the 30 °C and 60 °C flow-rate curves is also reproduced by the model, until at 1000 rpm, where the modelled flow-rate curves at the two temperatures are very similar, an aspect not observed in the experimental data

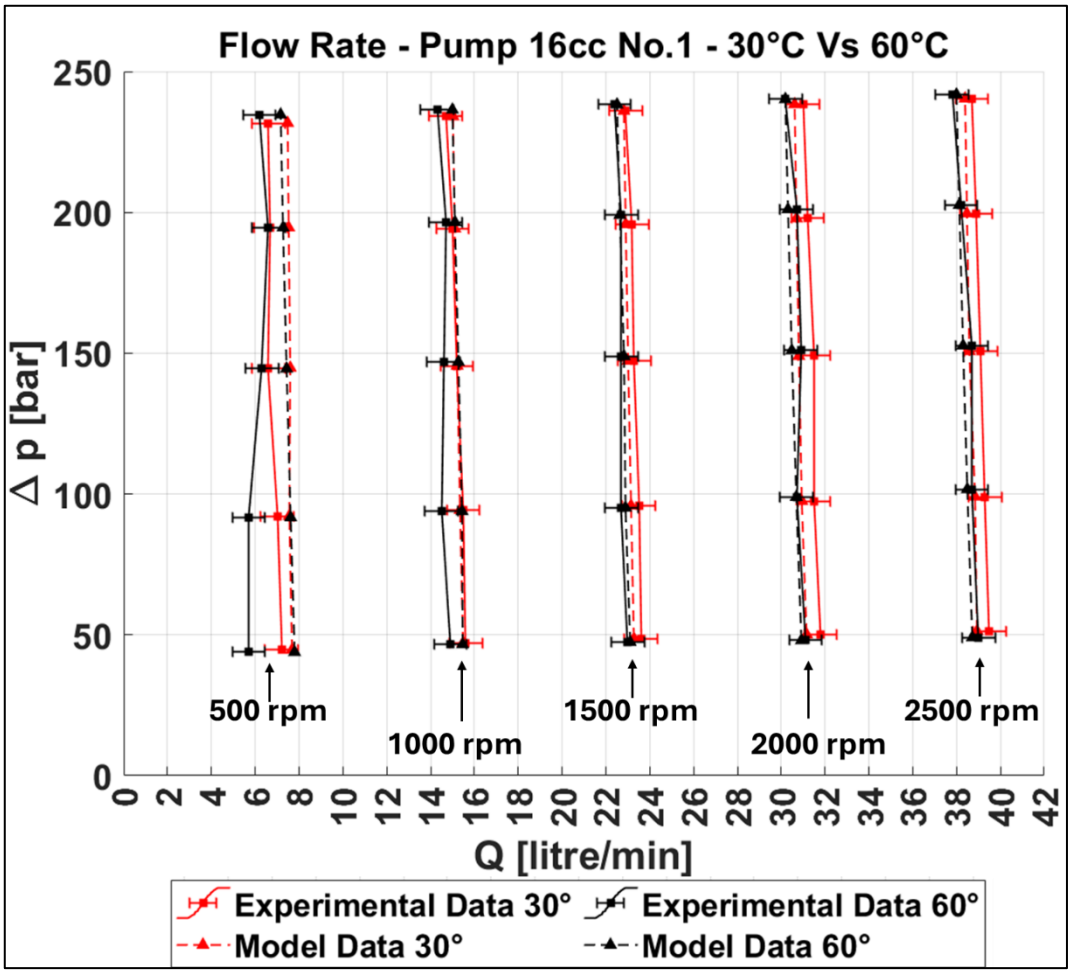

Figure 139 - Pump 16 cc No.3 Flow Rate - 30°C and 60°C

8.2.4. Pump 16 cc No.3 - Hydro-Mechanical Performance – 30 °C

Figure 140 shows the torque of the 16 cc pump, sample No. 3, at different pressures at 30°C. The solid line with square markers represents the experimental data, whereas the dotted line with triangular markers represents the model results. The experimental data are plotted with the torque-meter measurement uncertainty, which is ±0.5 N·m .

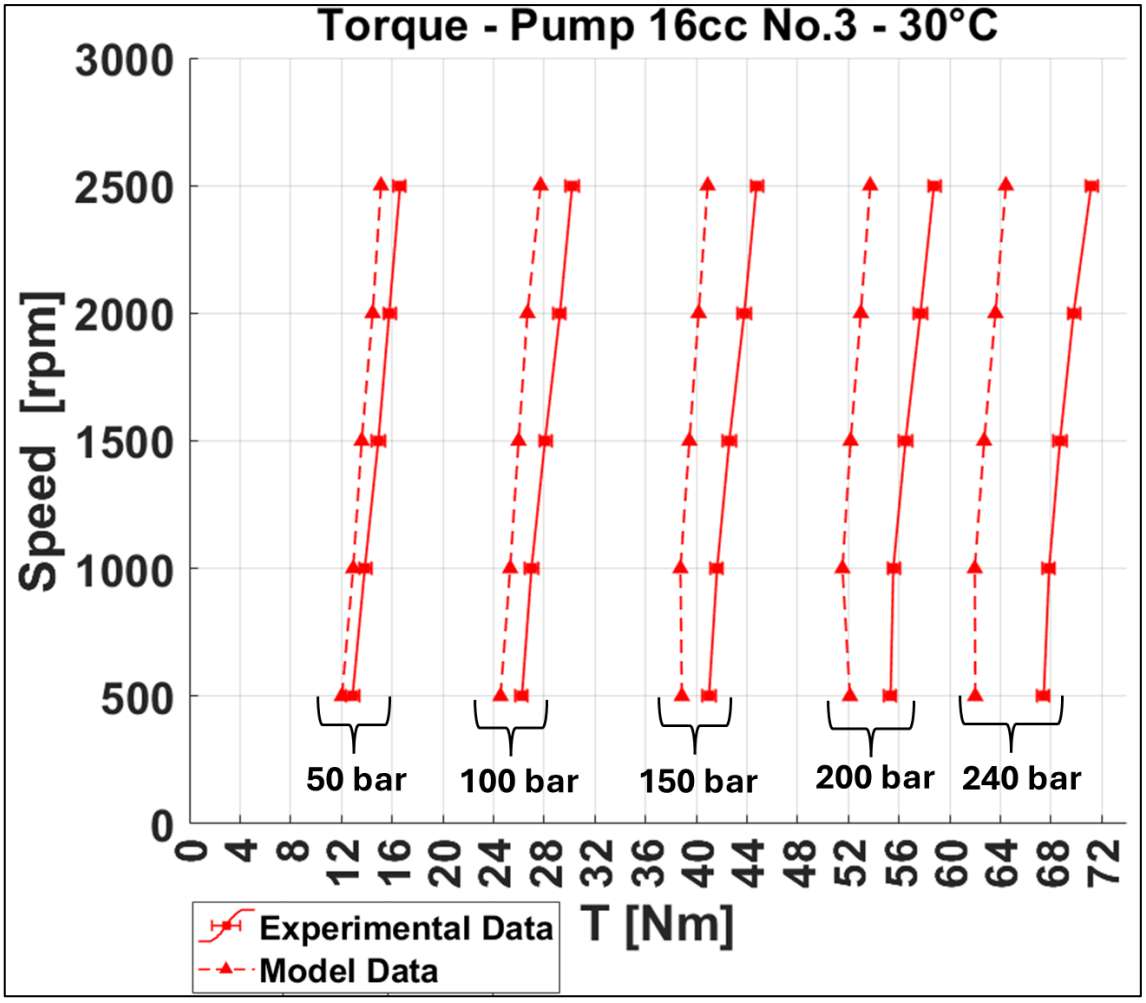

Figure 140 - Pump 16 cc No.3 Torque - 30°C

From Figure 140, the model follows the experimental trend reasonably well: torque increases with increasing speed. It should be noted, however, that the model underestimates the torque across all operating conditions.

Considering the relative error (see Figure 141(a)), it varies between a minimum value of 5.2% at 500 rpm and 150 bar, and a maximum value of 9.5% at 2500 rpm and 240 bar.

The absolute torque errorr (see Figure 141(b)) is most influenced by the increase in pressure, while it is only slightly influenced by the increase in speed. It varies between a minimum value of 0.86 N·m at 500 rpm and 50 bar, and a maximum value of 6.8 N·m at 2500 rpm and 240 bar.

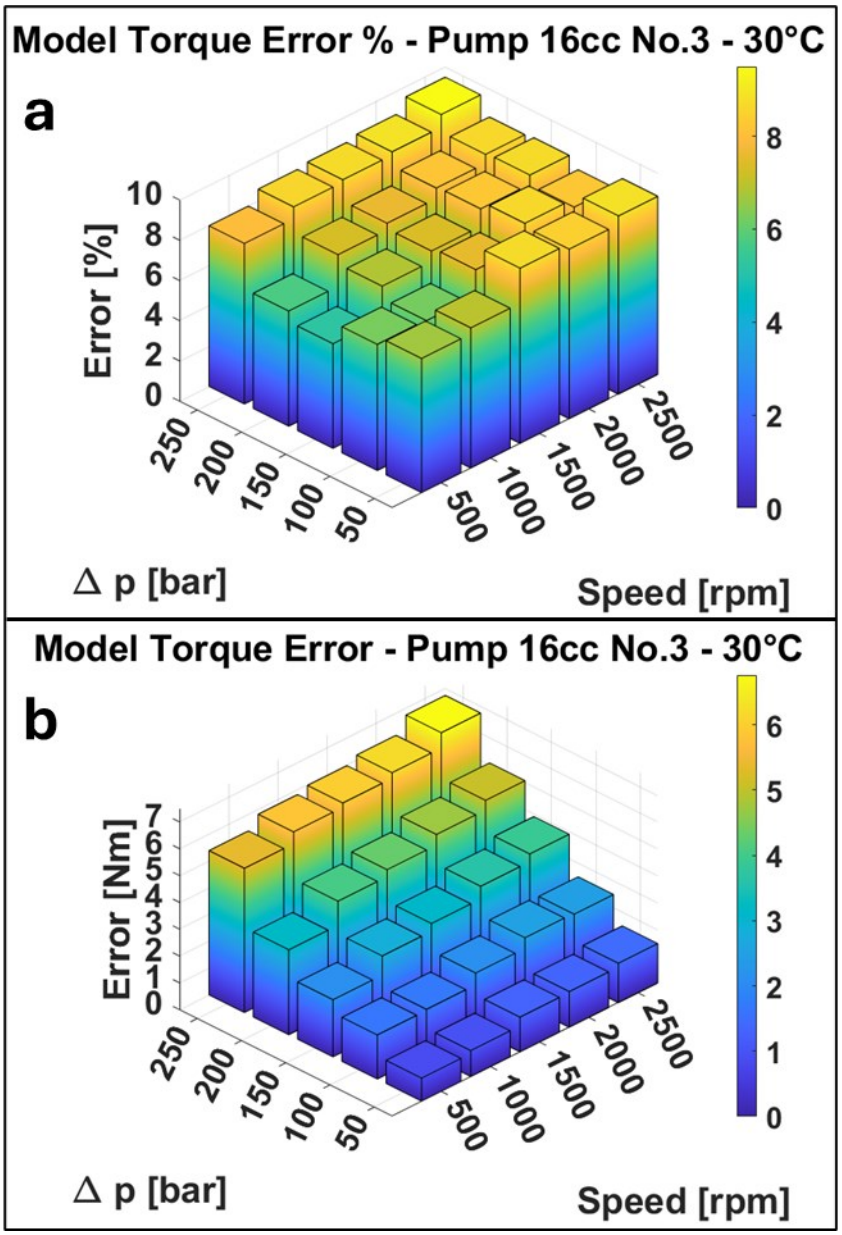

Figure 141 - Model torque estimation error: (a) relative error [%]; (b) absolute error [N·m] Pump 16 cc No.3 30°C

Figure 142 plots the hydro-mechanical efficiency as a function of pressure. The experimental data indicate that hydro-mechanical efficiency increases with pressure in the range 50–200 bar and then decreases at 240 bar. This trend is generally captured by the model, except at 240 bar where the modelled hydro-mechanical efficiency continues to increase.

Figure 143 plots the hydro-mechanical efficiency as a function of speed. With increasing speed, the experimental hydro-mechanical efficiency decreases; this type of trend is also followed by the model.

It should be noted, however, that the model overestimates the hydro-mechanical efficiency across all operating conditions.

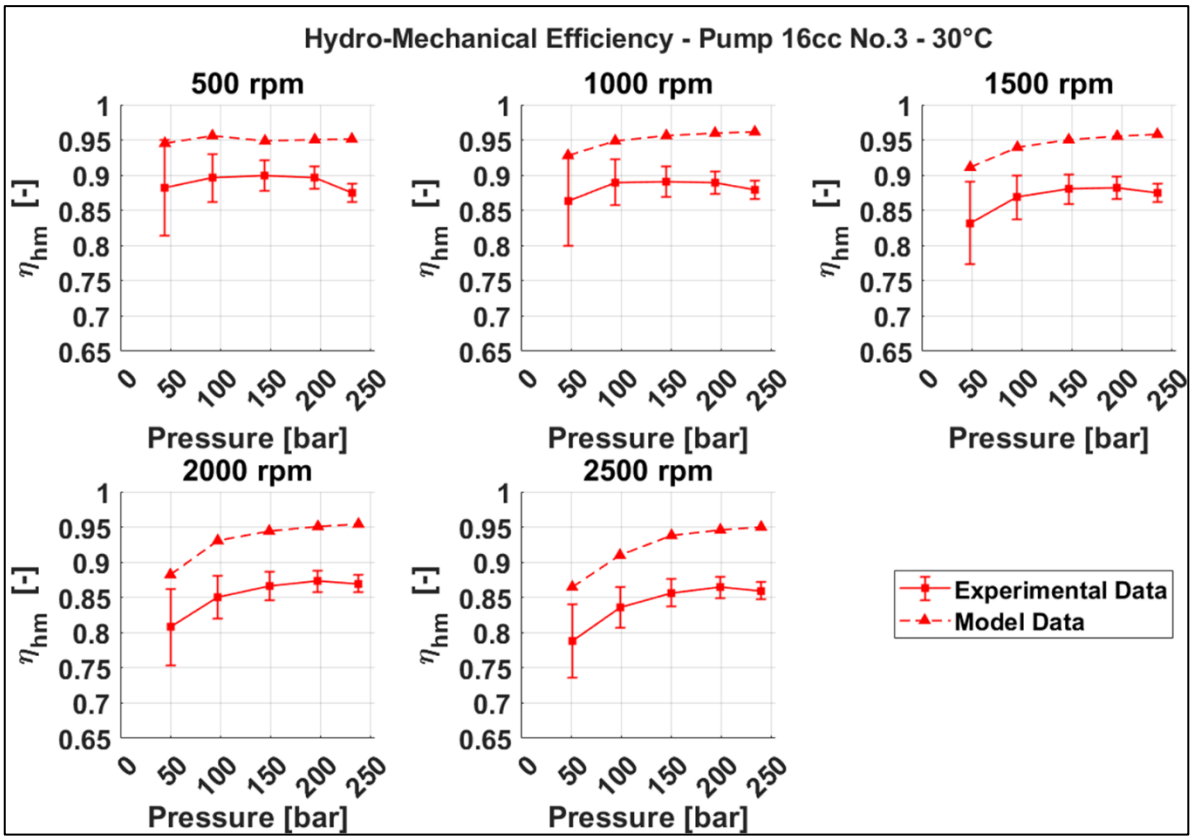

Figure 142 – Pump 16 cc No.3 30° – Hydro-Mechanical Efficiency vs Pressure

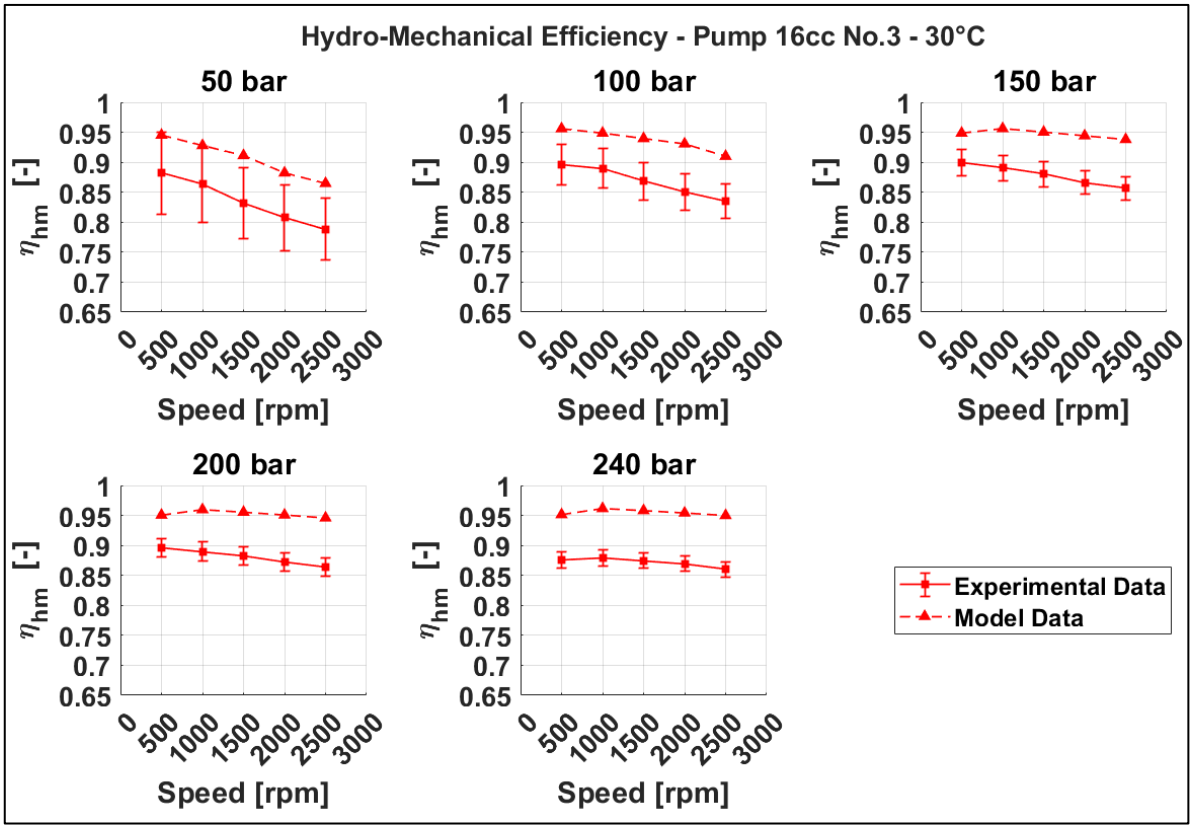

Figure 143 - Pump 16 cc No.3 30° – Hydro-Mechanical Efficiency vs Speed

8.2.5. Pump 16 cc No.3- Hydro-Mechanical Performance – 60 °C

Figure 144 shows the torque of the 16 cc pump, sample No. 3, at different pressures at 60°C. The solid line with square markers represents the experimental data, whereas the dotted line with triangular markers represents the model results. The experimental data are plotted with the torque-meter measurement uncertainty, which is ±0.5 N·m .

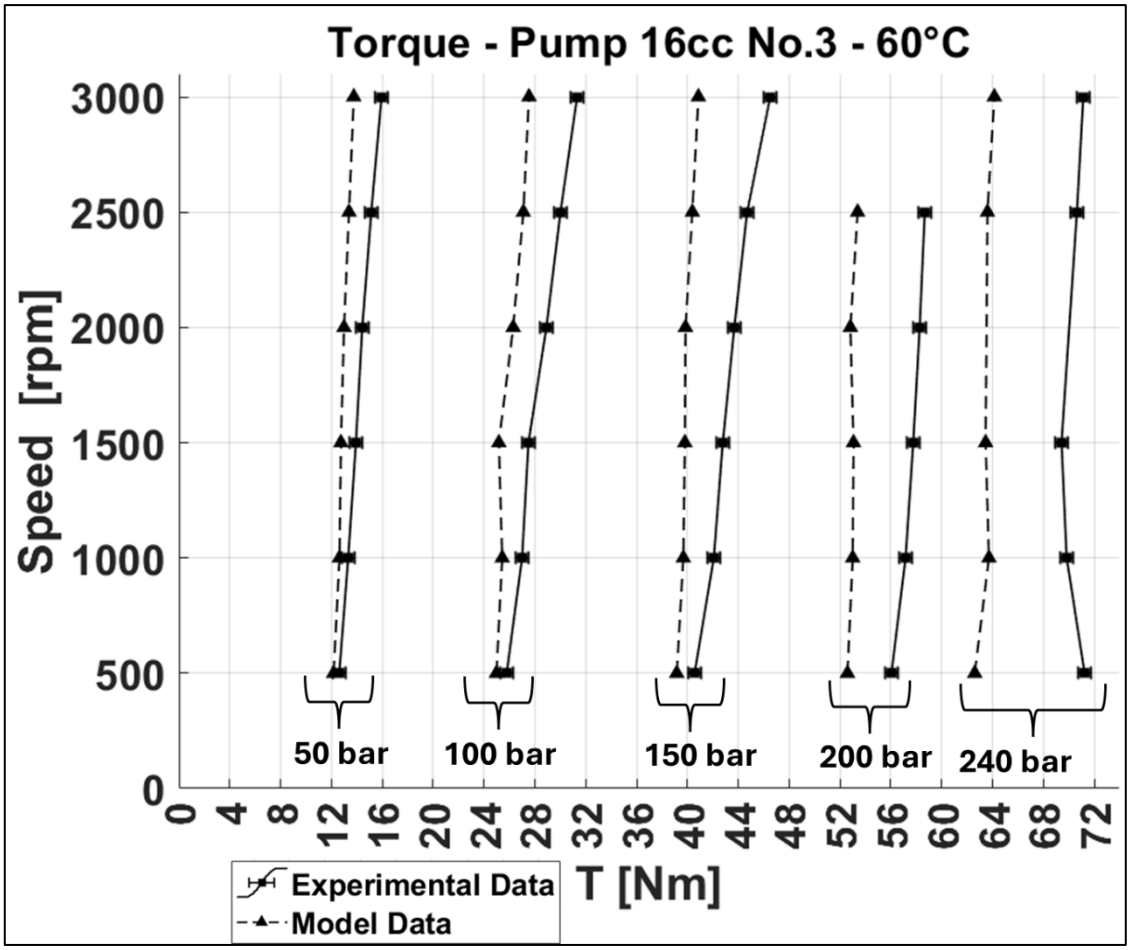

Figure 144 - Pump 16 cc No.3 Torque – 60°C

Figure 144 shows that the model reproduces the experimental trend, but it underestimates the torque across all operating conditions. The experimental data at 240 bar/3000 rpm and 240 bar/2000 rpm are not plotted because of a data-acquisition problem during the test.

Figure 145(a) presents the relative error, while Figure 145(b) shows the absolute error, expressed in N·m.
In terms of relative error, the maximum value is 13.5% at 50 bar and 3000 rpm, while the minimum value of 3.2% is obtained at 100 bar and 500 rpm.
Considering the absolute error, the maximum value is 8.6 N·m at 240 bar and 500 rpm, while the minimum value of 0.42 N·m is obtained at 50 bar and 500 rpm.

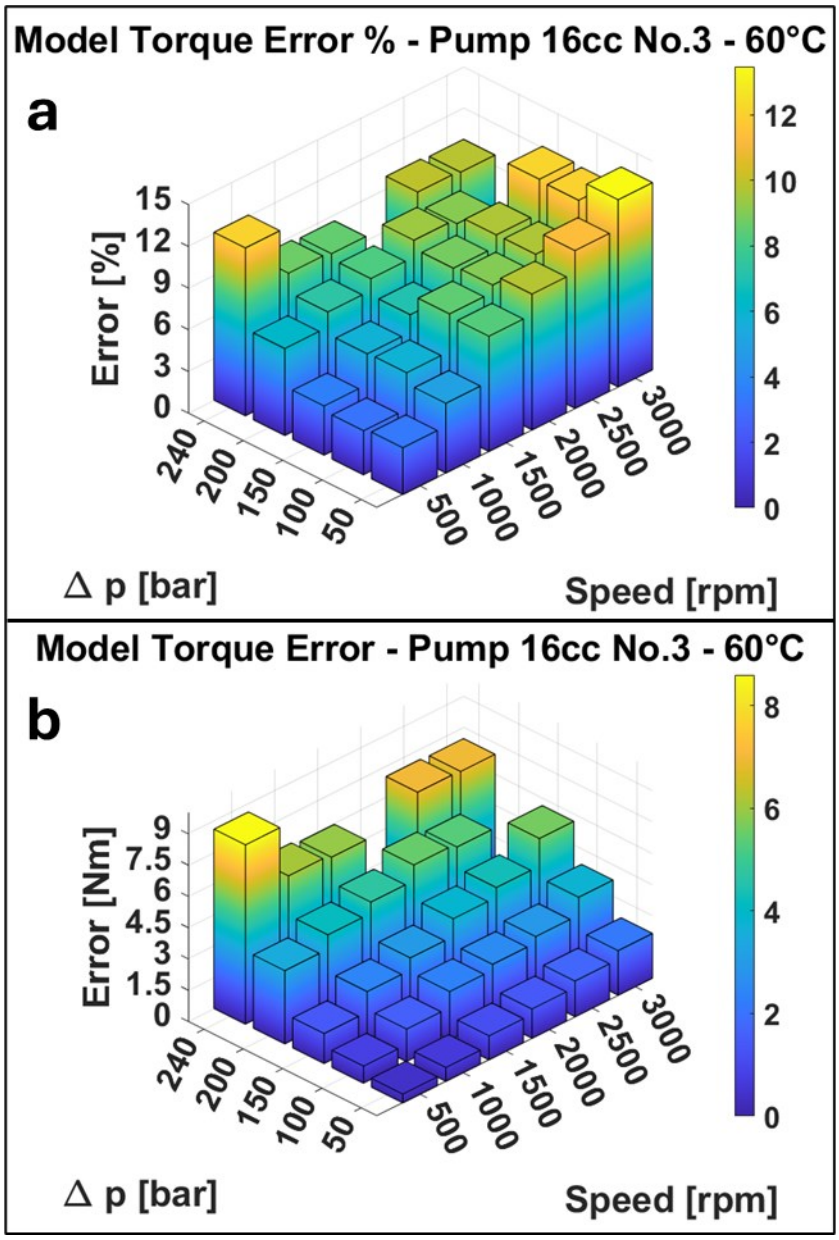

Figure 145 - Model torque estimation error: (a) relative error [%]; (b) absolute error [N·m] Pump 16 cc No.3 60°C

Figure 146 plots the hydro-mechanical efficiency as a function of pressure.
At 500 rpm, the experimental data exhibit an initial increase followed by a subsequent decrease, whereas the model predicts a monotonic increase with pressure.
At 1000 rpm, the experimental data decrease with increasing pressure, while the model predictions increase.
Within the 1500–3000 rpm range, the model follows the experimental trend.

Figure 147 plots the hydro-mechanical efficiency as a function of speed. At 50 bar, the model follows the experimental trend, although the efficiency reduction with increasing speed is less pronounced in the model than in the experimental data.
In the 100–200 bar range, the experimental hydro-mechanical efficiency decreases with pressure, while the model curve increases slightly.
At 240 bar, the model follows the experimental data more closely.

However, the model overestimates the hydro-mechanical efficiency across all operating conditions.

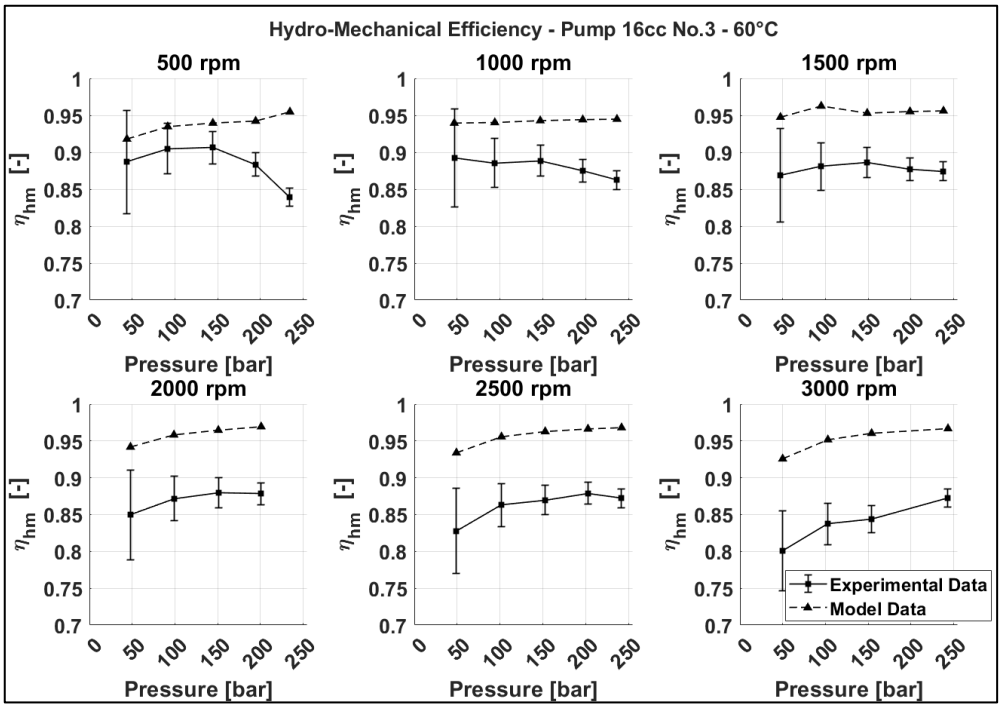

Figure 146 - Pump 16 cc No.3 60° – Hydro-Mechanical Efficiency vs Pressure

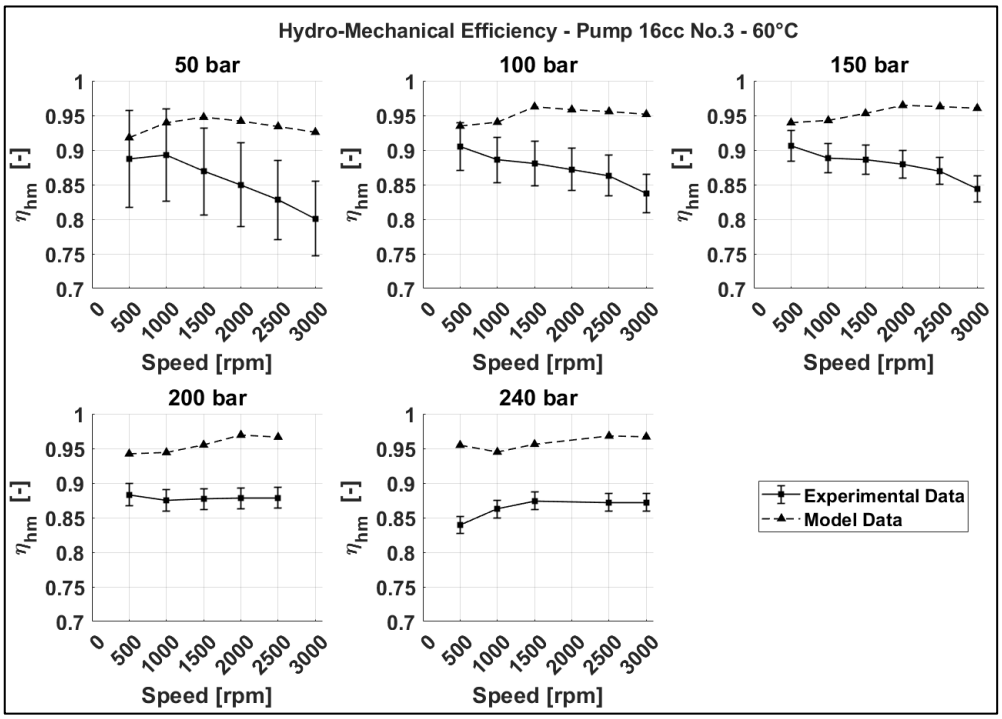

Figure 147 - Pump 16 cc No.3 60° – Hydro-Mechanical Efficiency vs Speed

8.2.6. Pump 16 cc No. 3 - Comparative Hydro-Mechanical Performance at 30 °C and 60 °C

Figure 148 illustrates the torque of the 16 cc pump (sample No. 3) as a function of pressure, at various rotational speeds and at temperatures of 30 °C (red curves) and 60 °C (black curves). The following observations emerge:

- 500 rpm: In the 50-150 bar range, the torque at 30 °C is higher than at 60 °C, whereas at higher pressures the torque at 60 °C exceeds that at 30 °C. The model does not reproduce this behaviour; it predicts higher torque at 60 °C across the range.
- 1000 rpm: Only at 50 bar is the torque at 30 °C higher than at 60 °C. At this speed, the model follows the experimental trend.
- 1500 rpm: In the 50-150 bar range, the torque at 30 °C is higher than at 60 °C, while at higher pressures the 60 °C torque surpasses the 30 °C torque. The model captures this trend, although at high pressure the difference between 30 °C and 60 °C is less pronounced than in the experimental data.
- 2000 rpm: In the 50-150 bar range, the torque at 30 °C is higher than at 60 °C, with the relationship reversing at higher pressures in the experiments. The model does not follow this reversal; it predicts the 30 °C torque to be higher than the 60 °C torque at all pressures.
- 2500 rpm: The torque at 30 °C is higher than at 60 °C across the entire pressure range. The model shows the same behaviour.

The experimental data indicate that, at low pressure, the torque at 30 °C is generally higher than at 60 °C. A plausible explanation is the increase in viscous losses at lower temperature due to the higher oil viscosity. Conversely, at higher pressure, it is hypothesised that the lower viscosity at 60 °C may not ensure adequate lubrication, potentially leading to partial lubrication (and occasional contact) between components; this could account for the higher torque observed at 60 °C.

The modelled torque is obtained as the sum of two contributions: the torque due to fluid pressure and the torque due to viscous–mechanical losses.
Figure 149 shows the torque attributable solely to fluid pressure, as estimated by the model. The following observations emerge:

- 500-1000 rpm: The pressure-induced torque at 60 °C is higher than at 30 °C, with maximum differences of 0.7 N·m at 500 rpm and 1.3 N·m at 1000 rpm.
- 1500 rpm: In the 50–150 bar range, the torques at 30 °C and 60 °C are very similar; at higher pressures, the 60 °C torque exceeds the 30 °C torque, with a maximum difference of about 0.5 N·m.
- 2000-2500 rpm: The pressure-induced torque at 30 °C is higher than at 60 °C, with maximum differences of 0.5 N·m at 2000 rpm and 0.7 N·m at 2500 rpm.

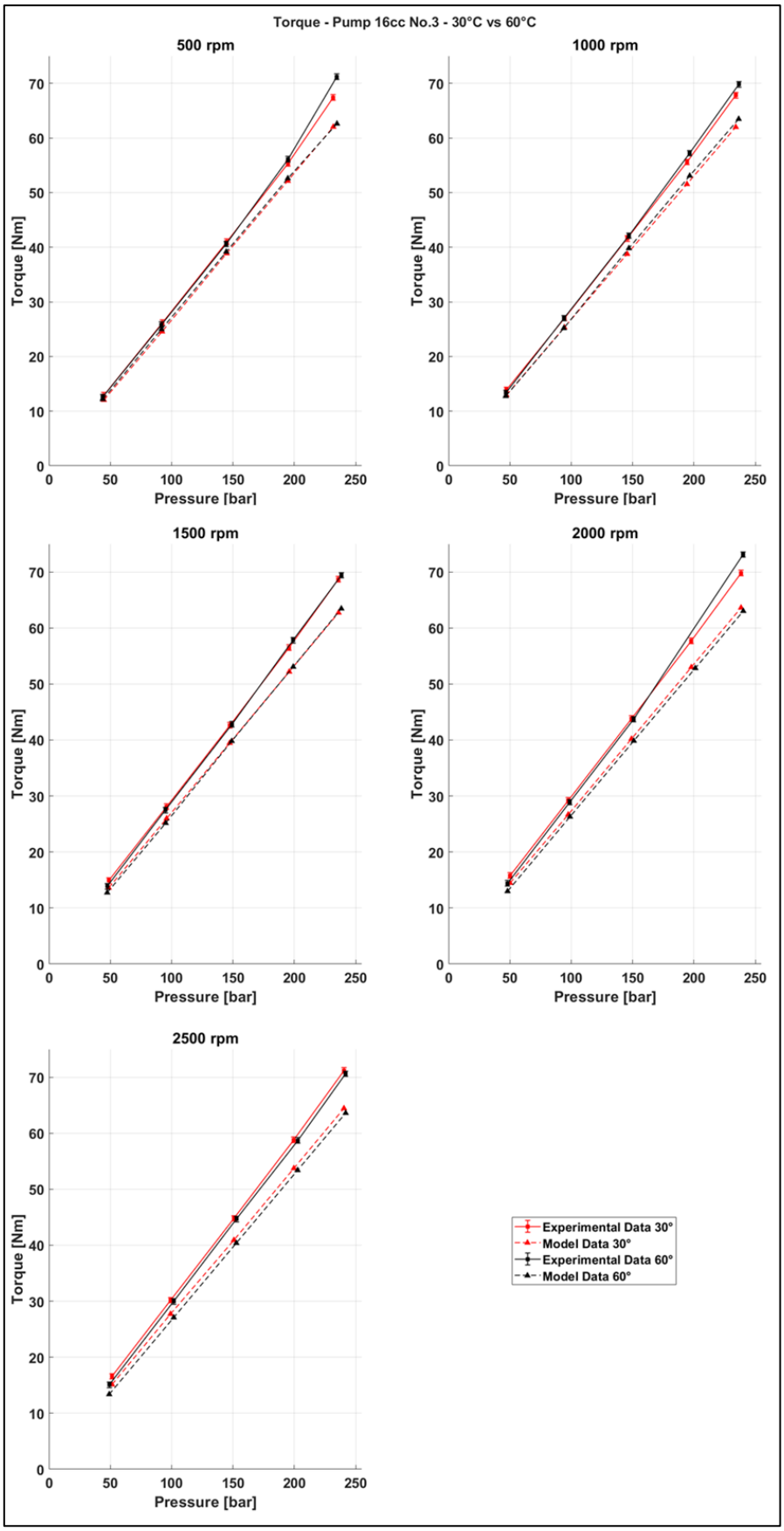

Figure 148 - Pump 16 cc No.3 Torque - 30°C and 60°C

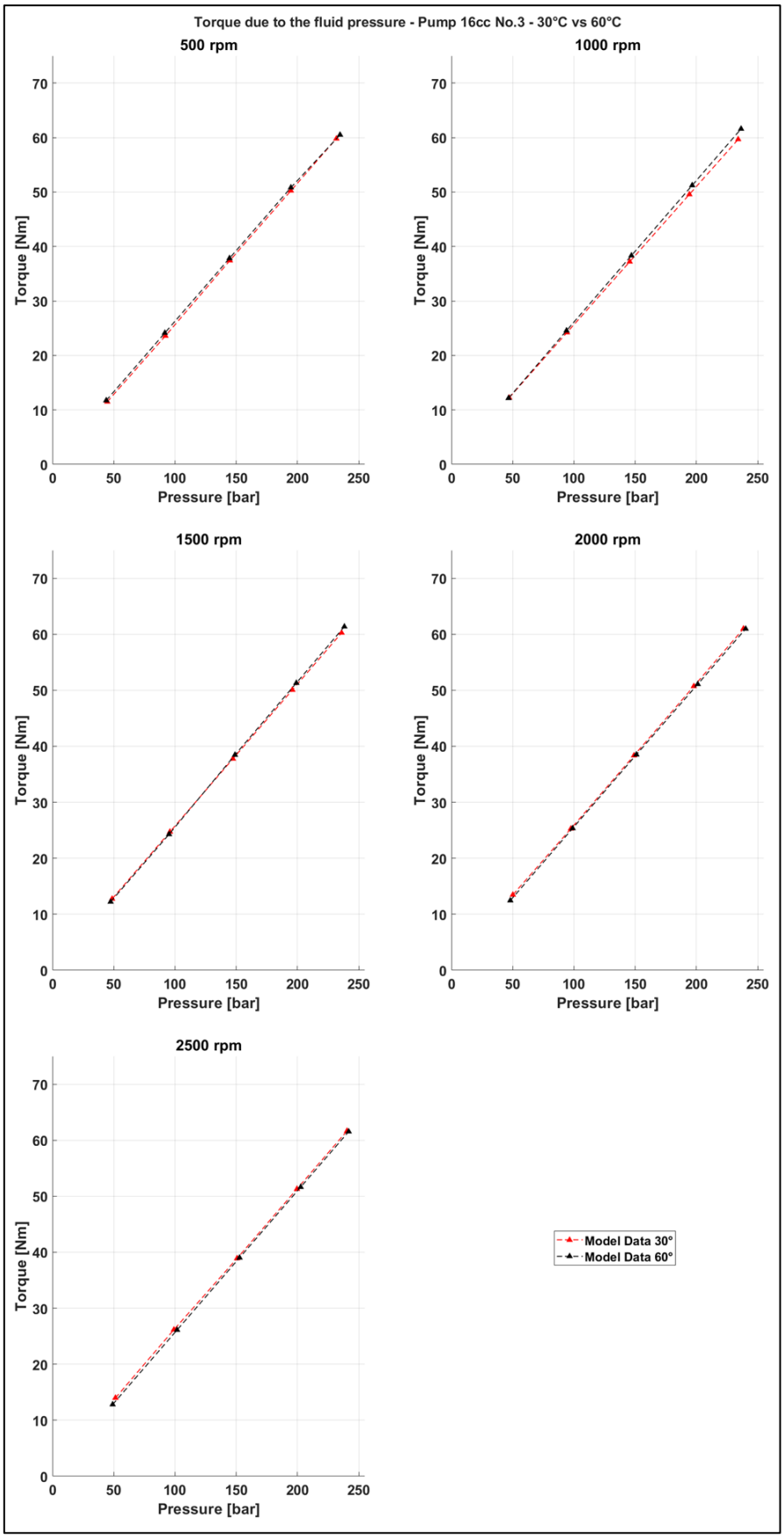

Figure 149 - Pump 16 cc No.3 Torque due to the fluid pressure - 30°C and 60°C

Figure 150 illustrates the torque losses of the 16 cc pump (sample No. 3) as a function of pressure, evaluated at multiple rotational speeds and at temperatures of 30 °C (red curves) and 60 °C (black curves). The modelled torque losses at 30 °C are higher than those at 60 °C. Consequently, the operating conditions under which the modelled torque at 60 °C exceeds that at 30 °C (Figure 148) can be attributed solely to the pressure-induced torque contribution.

The model does not account for mixed-lubrication phenomena.

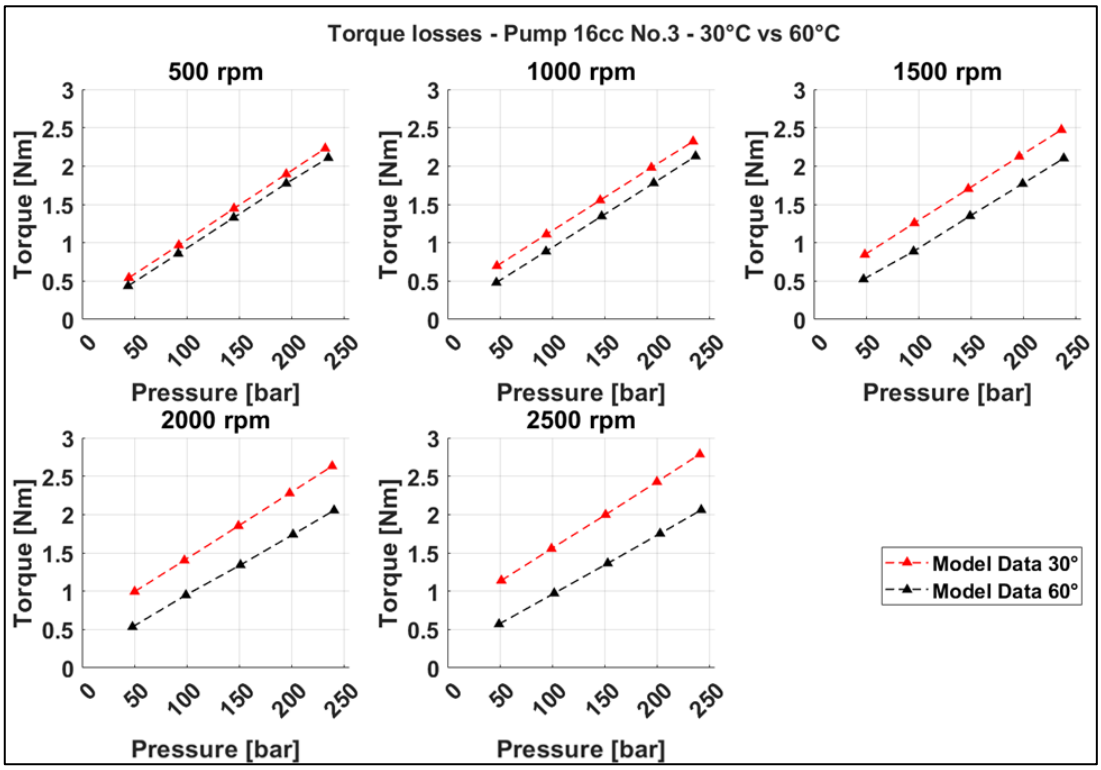

Figure 150 - Pump 16 cc No.3 Torque losses - 30°C and 60°C

Figure 151 shows the individual contributions to the torque losses:

- viscous losses arising from the journal bearings, the clearance between the tooth tips and the pump housing, and the lateral gap; and
- mechanical losses due to gear meshing.

An increase in speed primarily affects the viscous losses, which rise with speed, whereas the meshing losses decrease slightly. By contrast, increasing pressure has little influence on the viscous losses but substantially increases the meshing losses. Increasing temperature predominantly affects the viscous losses, which decrease with temperature, while the meshing losses are only weakly influenced.

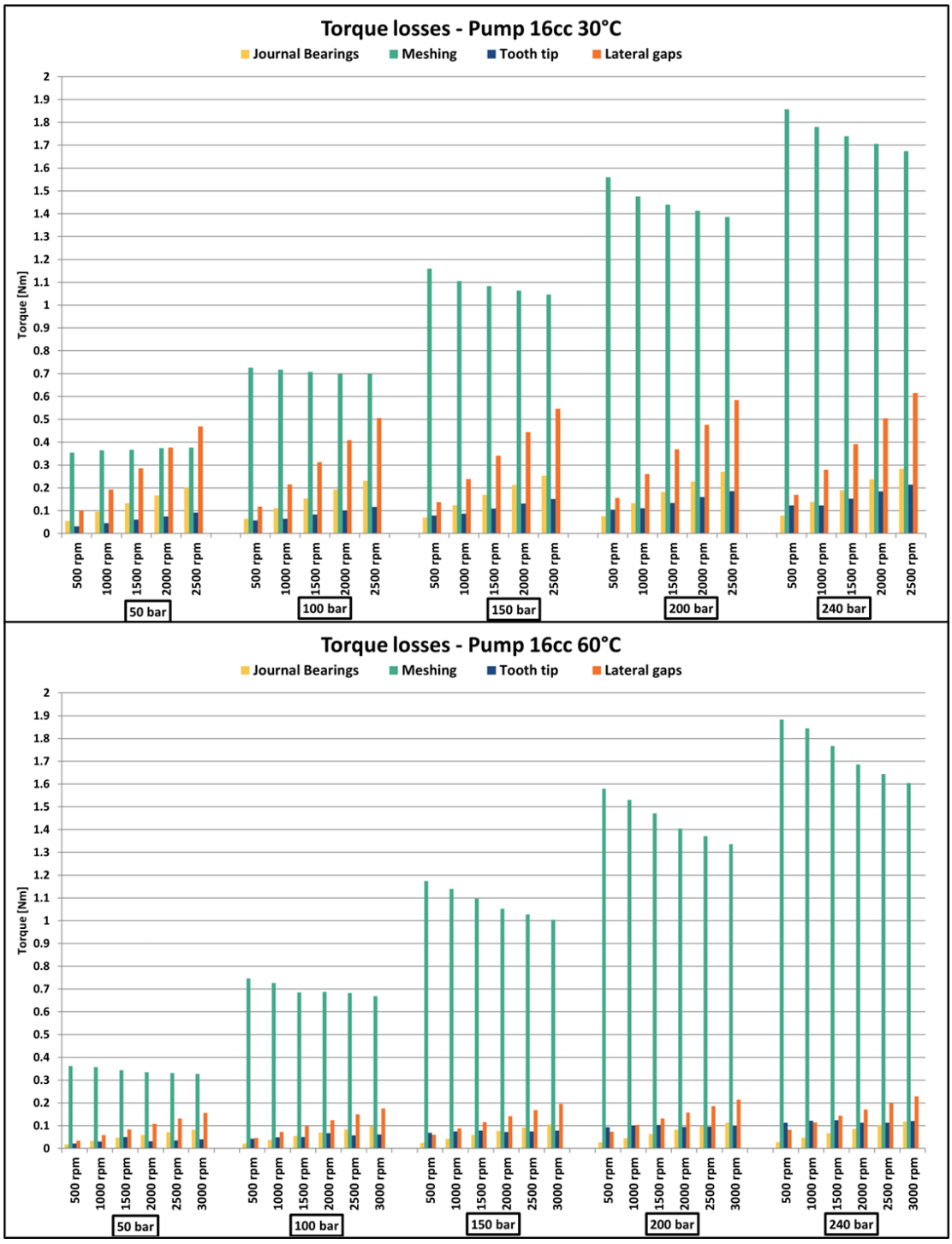

Figure 151 - Pump 16 cc No. 3 - Contributions to torque losses at 30 °C and 60 °C

Figure 152 shows the relative contributions of the different loss components to the total torque losses.

At 30 °C, the losses due to the gear meshing and the lateral gap play a significant role in determining the overall torque losses; however, with increasing pressure, the meshing losses also become more prominent.

At 60 °C, the torque losses are dominated primarily by the meshing losses.

Figure 152 - Pump 16 cc No. 3 - Percentage contributions to torque losses at 30 °C and 60 °C

8.3. Conclusion

This chapter has presented a validation of the model against experimental data. Two external spur gear pumps were tested and modelled: an 8.2 cc unit and a 16 cc unit, with the working fluid at 30 °C and 60 °C. What follows is a concise account of the model's performance, organised by volumetric and hydro-mechanical behaviour, highlighting the operating ranges, error magnitudes, and principal discrepancies observed.

Volumetric performance

- Pump 8.2 cc
    - 30 °C: The model estimates the volumetric flow rate very well, with low errors; the relative error lies in the range 0.3-6%.
    - 60 °C: The model performs well over 1500-3500 rpm, with a relative error in the range 0.1-12%. At 1000 rpm the model overestimates the flow rate more substantially, with a relative error in the range 4.5-27%.
    - The model captures the effect of temperature on volumetric performance over 1500-3500 rpm; at 1000 rpm, however, the temperature effect on flow rate is not well reproduced.
- Pump 16 cc
    - 30 °C: Very good agreement over 1000-2500 rpm, with relative error in the range 0.1-2.5%.
    - 60 °C: Good agreement over 1000-3000 rpm, with relative error in the range 0.1-7.5%. At 500 rpm the model tends to overestimate the flow rate, with relative error in the range 15-37%.
    - The model reproduces the temperature effect on volumetric performance over 1500-2500 rpm; at 500-1000 rpm the temperature effect on flow rate is not captured satisfactorily.

Overall, comparison with the experiments confirms a good capability in estimating the volumetric flow rate, with a deterioration in accuracy at the lowest speeds. Future work should include the use of a flowmeter with a lower full-scale range (the instrument employed has a 250 L min^{-1} full scale) to resolve low flows more accurately at low speeds; this would support further refinement of the model in this operating region.

Hydromechanical performance

- Pump 8.2 cc
    - 30 °C: The model follows the experimental torque trends but underestimates the torque across all operating conditions; the relative error is in the range 6-10%.
    - 60 °C: The model again underestimates torque, with relative error in the range 2.5-15%. The largest discrepancies occur at high speed and low pressure.
    - The effect of temperature on torque is well reproduced over 2000-3500 rpm.
- Pump 16 cc

- 30 °C: The model follows the experimental trends yet underestimates the torque in all conditions; the relative error is 5-10%.
- 60 °C: The model underestimates torque throughout, with relative error 3-14%.
- The temperature-induced variation in torque is generally well captured.

In summary, the comparison with experimental data demonstrates that the model provides a good description of hydro-mechanical performance, although it systematically underestimates torque. A plausible explanation - stated as a hypothesis - is the absence of mixed-lubrication phenomena in the current model. A simplifying assumption in the model is that the lateral clearances are constant and the floating bearing blocks are parallel to the gear faces. In practice, the clearance varies with operating conditions and the bushings may tilt, giving rise to mixed-lubrication regimes between gears and bushings that increase mechanical losses. Incorporating these effects is expected to improve torque prediction, particularly under operating conditions prone to partial or mixed lubrication.

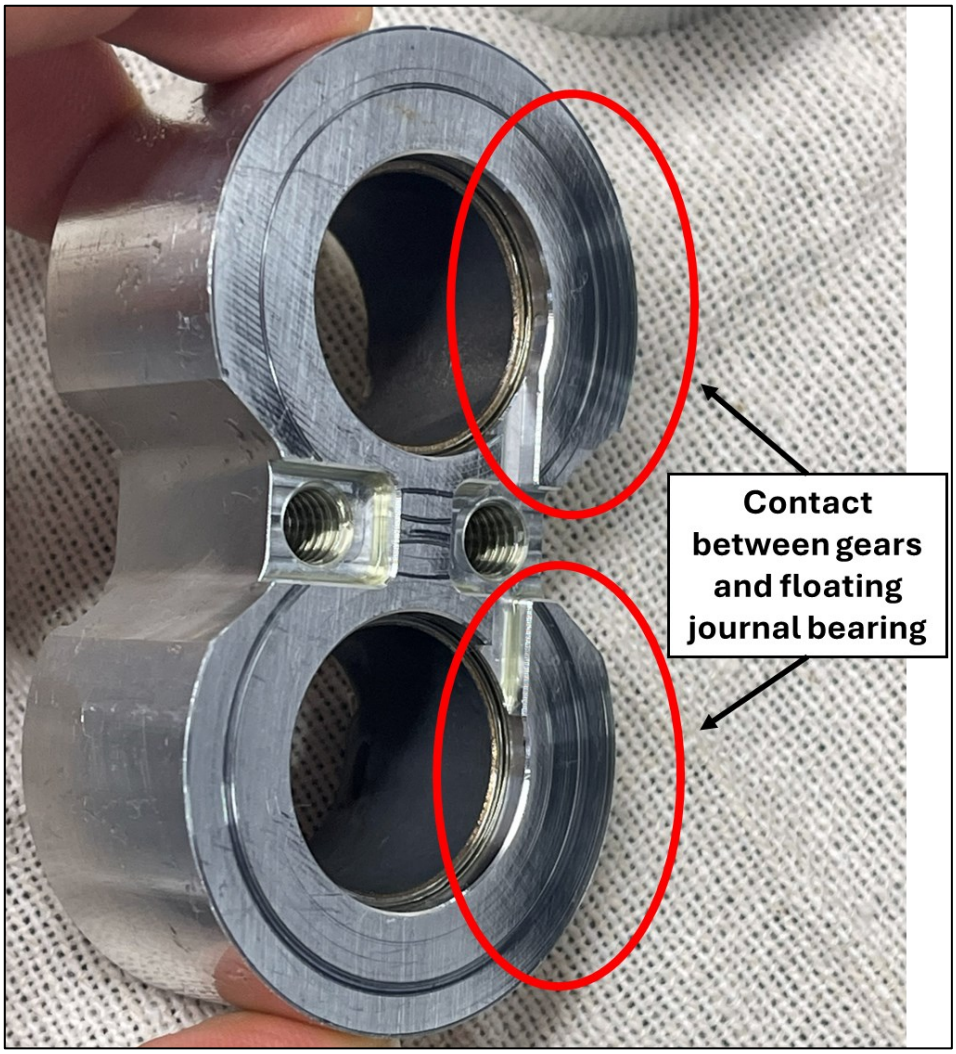

Figure 153 – Contact zone between gears and floating bearing bushing

9. Pressure Ripple: Comparison Between Model and Experimental Results

This section presents the experimental data obtained from pressure ripple tests conducted on the pumps. The experimental results are also compared with the predictions of the gear pump model.

The performance tests were carried out using the test bench illustrated in Figure 154. Measurements were performed under steady-state conditions at various operating points (see Figure 156 and Figure 157). For the pressure ripple tests, only one sample of each pump was tested: an 8.2 cc displacement pump (sample No.1) and a 16 cc displacement pump (sample No.3). The data were recorded using the HIDROTECHNIK Multisystem 5070 acquisition system, for 10 seconds at a sampling frequency of 10 kHz.

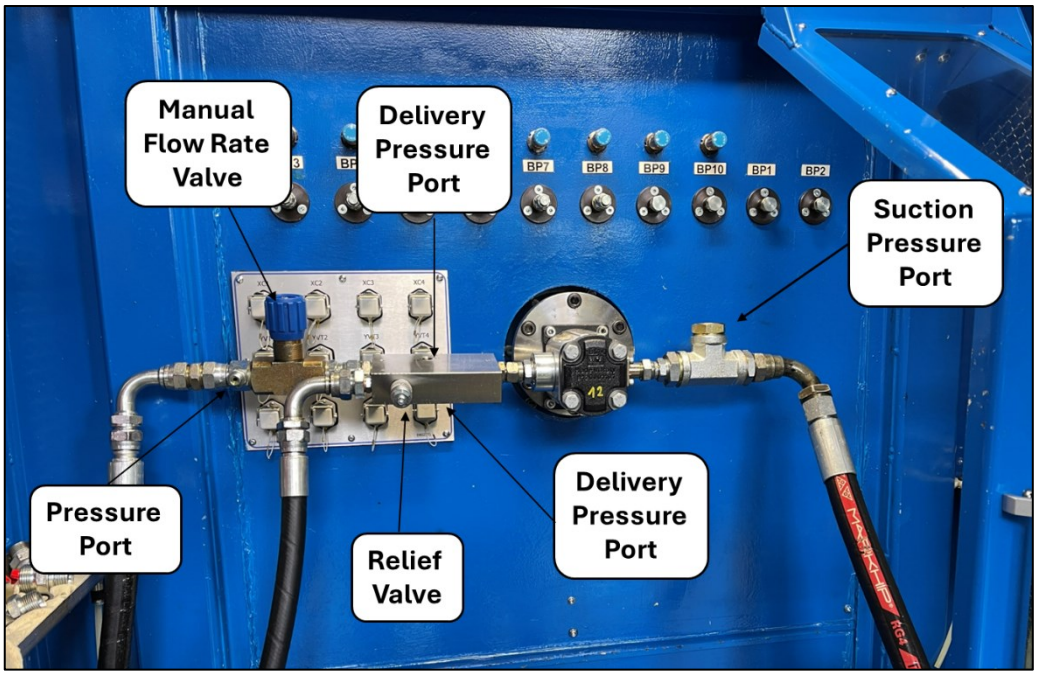

Figure 154 - BP99 test bench setup for pressure ripple test

For the pressure ripple tests, a rigid pipe was installed on the pump delivery side. A high-frequency pressure transducer was used to measure the pressure oscillations at the delivery, while an additional pressure sensor was placed to measure the mean pressure value. The specifications of the sensors used for the tests are provided in Table 17.

Sensor description	Model	Range	Error
Suction Pressure	Trafag 8380.26.5917	-1-10 bar	0.5% fs
Delivery Pressure (High frequency)	Trafag 8254.82.2317.32.GS	0-600 bar	0.5% fs
Delivery Pressure (Mean pressure)	Hydrotechnik 3403-15-D1.39S	0-400 bar	0.5% fs
Pressure after flow rate valve	Hydrotechnik 3403-21-L5.37S	0-60 bar	0.5% fs
Flowmeter	Kracht VC5-F1PS	250 L min^{-1}	0.3% fs
Torque	Kistler Torquemeter 4503B	1000 N·m	(0.5) 0.05% fs
Speed	Kistler 4503B1K0LP0B1KA2	8000 rpm	+-2 rpm
Temperature	Termotech TR PT100 IEC 751	0-100 °C	± (0,15 + 0,002* | t |) Class A

Table 17 – Pressure ripple test sensors

The rigid pipe on the delivery side was constructed using a custom manifold and commercial pipe fittings. The manifold (see Figure 155) included two pressure ports for the sensors and a seat for the relief valve (Aron CMP10C3002). The delivery pressure was regulated using a manual flow rate control valve.

All pipe fittings used during the tests were measured to ensure accurate reproduction of the test conditions in the simulation.

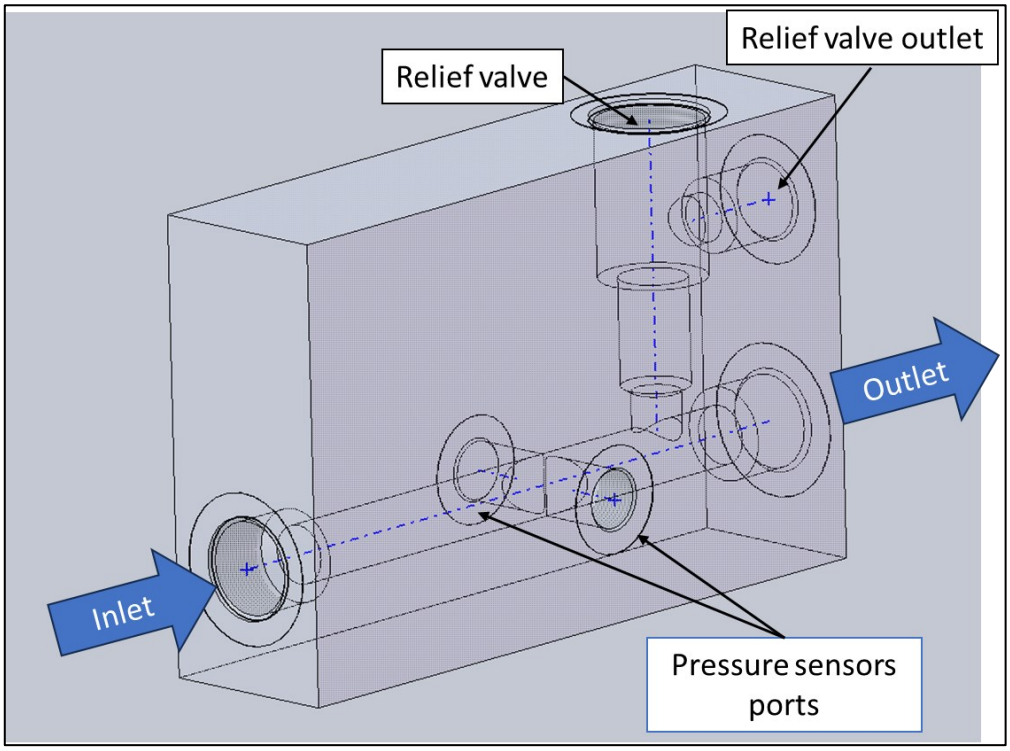

Figure 155 – Manifold used for the pressure ripple test

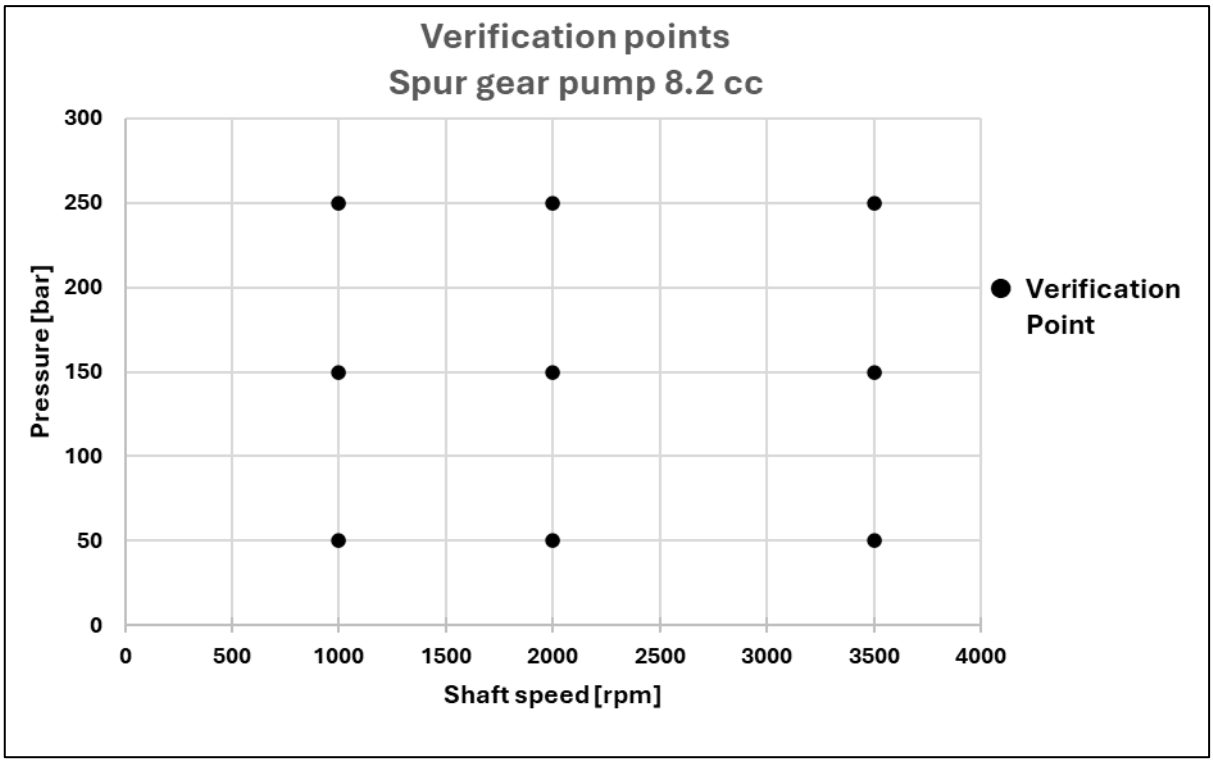

Figure 156 – Pressure ripple verification points of spur gear pump 8.2 cc

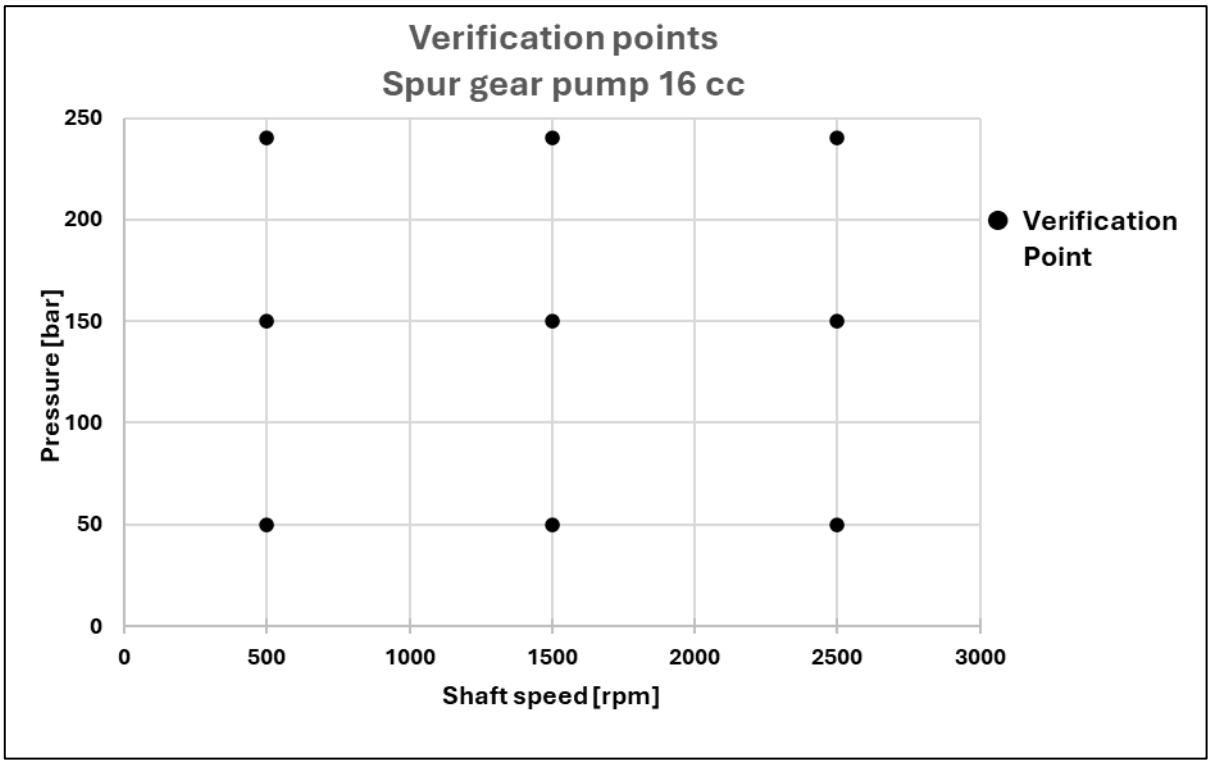

Figure 157 – Pressure ripple verification points of spur gear pump 16 cc

9.1. Simcenter Amesim Model – Pressure Ripple Simulation

Figure 158 shows the layout of the Simcenter Amesim model used to simulate the pressure-ripple tests. Prior to simulating the pressure ripple on the pump delivery line, the gear eccentricities at the various operating conditions were defined using the model shown in Figure 83.

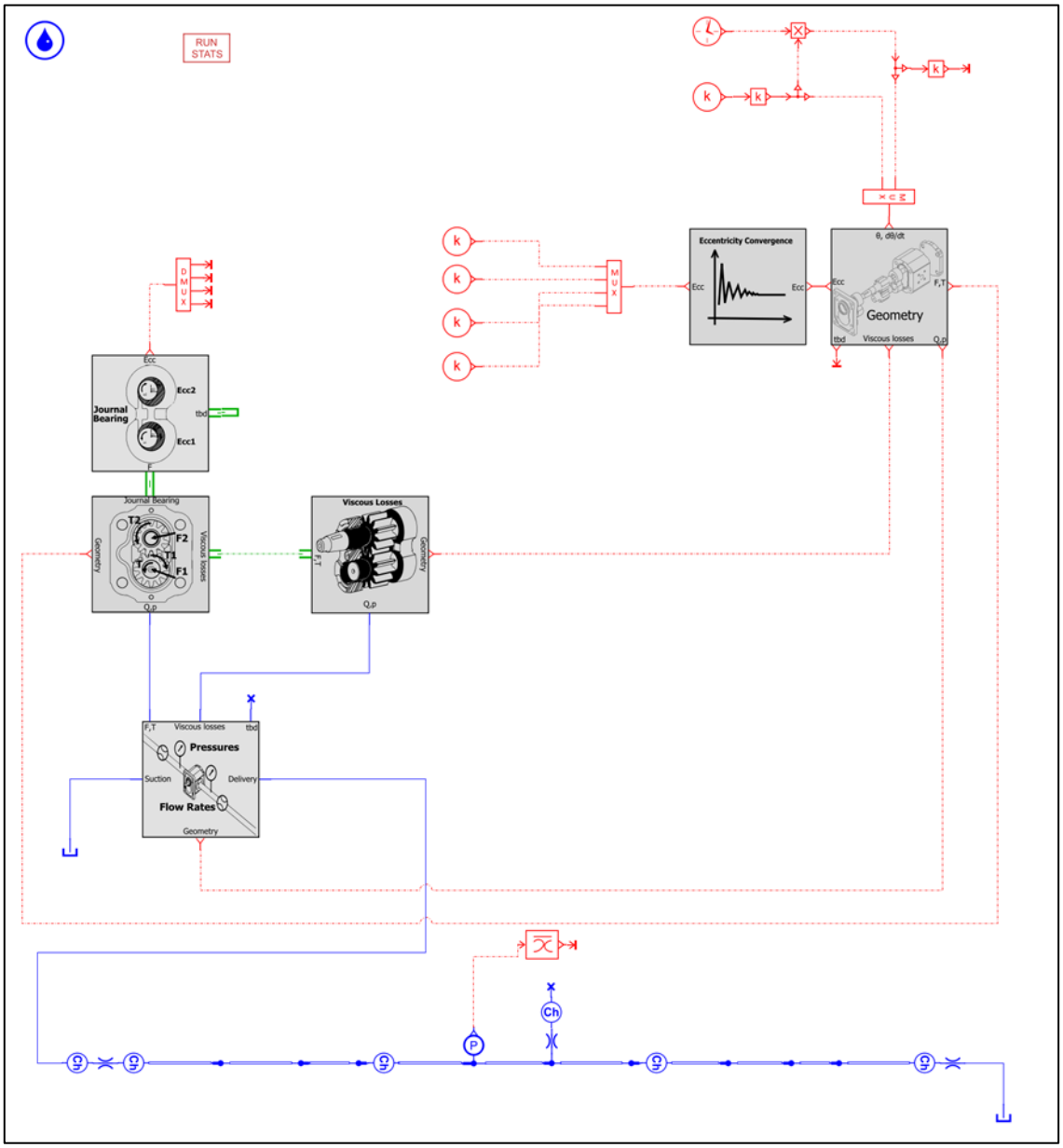

Figure 158 – Pressure Ripple Model

The simulations were conducted under the following assumptions and settings:

- The working fluid was ISO VG 46, modelled with the Simcenter Amesim hydraulic-library fluid model, using the parameters shown in Figure 94 at temperatures of 30 °C and 60 °C.
- The short-journal-bearing hypothesis was adopted, with an oil-film angular extent of π (see Section 0).

- The lateral-gap height was fixed at 0.01 mm.
- Volumetric leakage through the tooth flanks was modelled using Formulation 1 (see Section 2.6.5.1).

Figure 158 shows the model of the delivery line, which was represented using fixed-area orifices and lumped volumes, and, primarily, the CFD-1D hydraulic straight-pipe Amesim component (model name: HLLW0). This model is based on a one-dimensional mesh for which the continuity and momentum equations are solved. The resulting set of partial differential equations is integrated in time and space using the dedicated CFD-1D solver. The correlation between the model and the physical delivery line parts is reported in Figure 159.

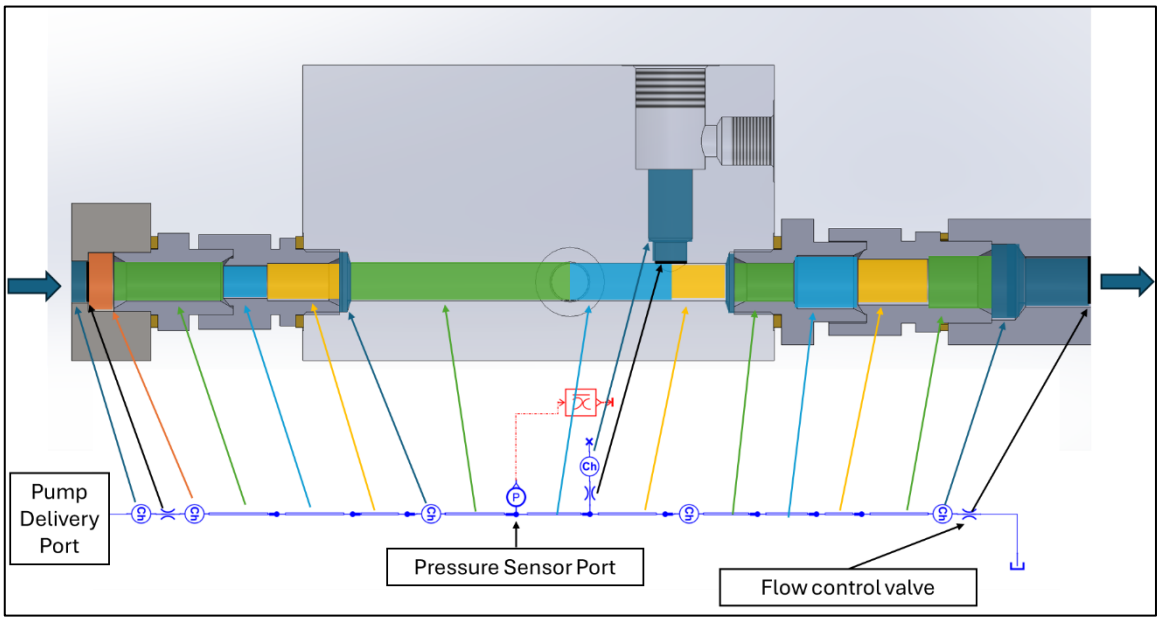

Figure 159 – Delivery line model

The delivery-line pressure was set experimentally using a manually actuated flow-control valve. In the model, this valve was represented by a fixed-area orifice whose area was adjusted for each simulated operating condition. To determine the orifice area in Simcenter Amesim, the required inputs are the flow rate through the orifice and the corresponding pressure drop; both quantities were measured experimentally. The orifice area A is computed as:

$$A = \frac{Q}{0.7\sqrt{2\frac{\Delta p}{\rho(0)}}} \qquad \textit{Eq. 214}$$

where:

- A is the orifice cross-sectional area,
- Q is the experimentally measured flow rate,
- Δp is the experimentally measured pressure drop, and
- $\rho(0)$ is the oil density at atmospheric pressure at the test temperature.

The definition of the flow rate Q affects the model's estimate of the average pressure in the delivery line. The flow rate value is measured experimentally with a measurement uncertainty of ±0.75 L min^{-1}. Consider, for example, the 16 cc pump (sample No. 3) used for the pressure ripple test. Under the operating condition of 2500 rpm and a delivery pressure of 240 bar, the measured flow rate is 39.6 L min^{-1}. Figure 160 shows the delivery line pressure predicted by the model when different flow rate values are assigned to the orifice representing the manual flow-control valve. The three flow-rate values are obtained by adding to or subtracting from the measured value the stated measurement uncertainty. The results indicate that the chosen flow rate input alters the average delivery line pressure predicted by the model.

Figure 161 shows the amplitude spectrum of the delivery pressure obtained by applying the Fast Fourier Transform (FFT) [17] [37] to the delivery pressure time history estimated by the model. It is possible to notice that the definition of the flow rate has a negligible effect on the pressure amplitude.

In the following section, the model and experimental results are compared. Since, under different operating conditions, there are differences in the average delivery pressure between the model and the experiments, it can be difficult to observe the pressure oscillations when they are plotted on the same chart. To avoid this problem, the pressure ripple curves are plotted net of the average pressure, allowing a clearer distinction between the model and experimental curves.

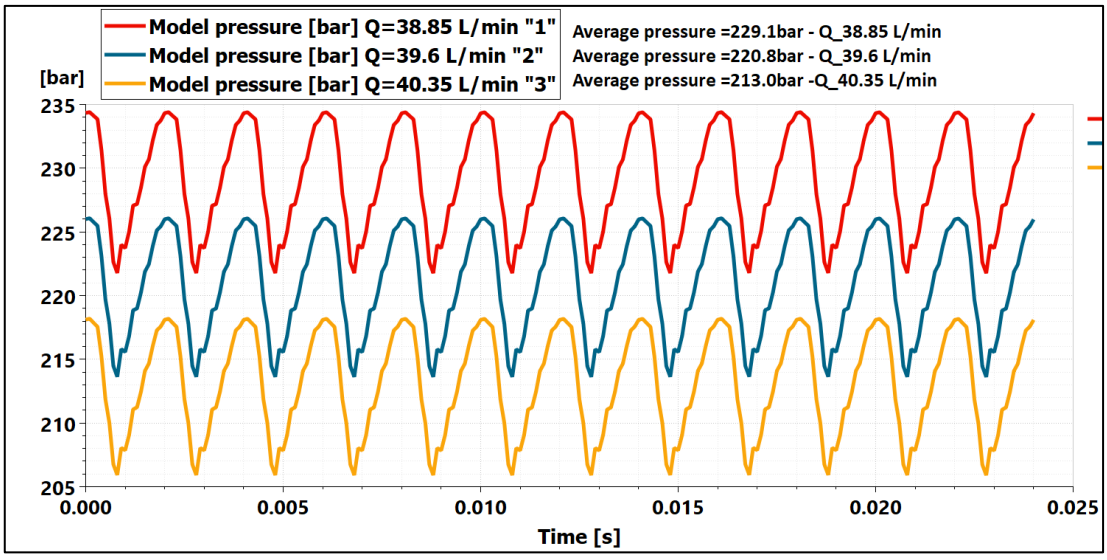

Figure 160 – Effect of the flow-rate input parameter on the delivery pressure predicted by the model

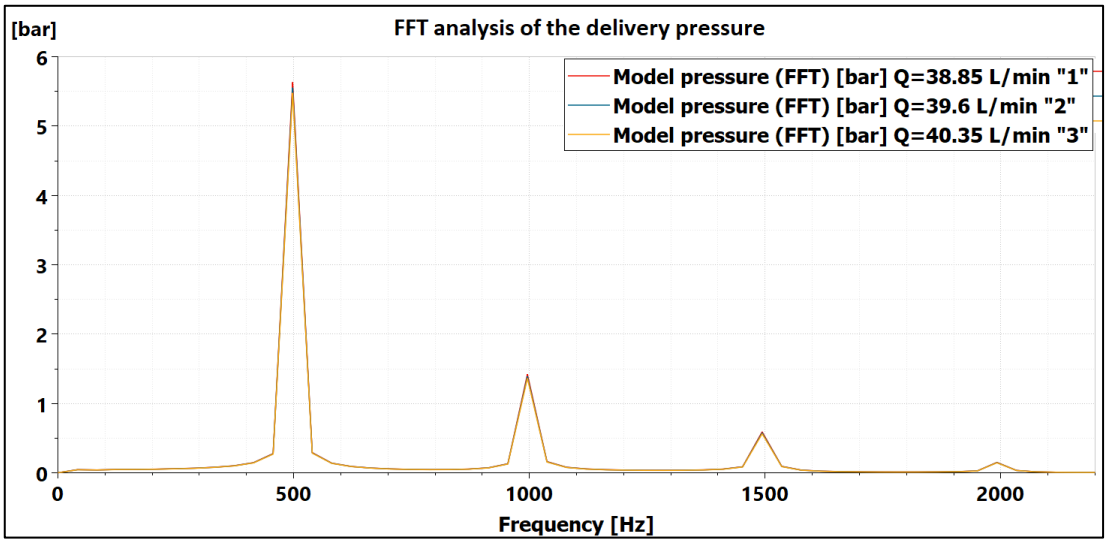

Figure 161 - Effect of the flow-rate input parameter on the amplitude of delivery-pressure oscillations

9.2. Pump 8.2 cc No.1 – Pressure Ripple: Experimental and Model Results

In this section, the experimental and model results for the 8.2 cc pump (sample No. 1) are analysed under different speed, pressure, and oil temperature conditions.

9.2.1. Pump 8.2 cc No.1 – Pressure ripple at 1000 rpm

Figure 162 shows the pressure ripple of the 8.2 cc pump at 1000 rpm and 50 bar over one gear revolution.

The experimental curve exhibits a pressure oscillation with a period of one gear revolution; this oscillation is likely due to a micro-error in the coupling between the pump and the test bench, or to a gear manufacturing error. As the model assumes nominal gear geometry and perfect coupling between the pump and the test bench, this oscillation is not present in the modelled pressure curve.

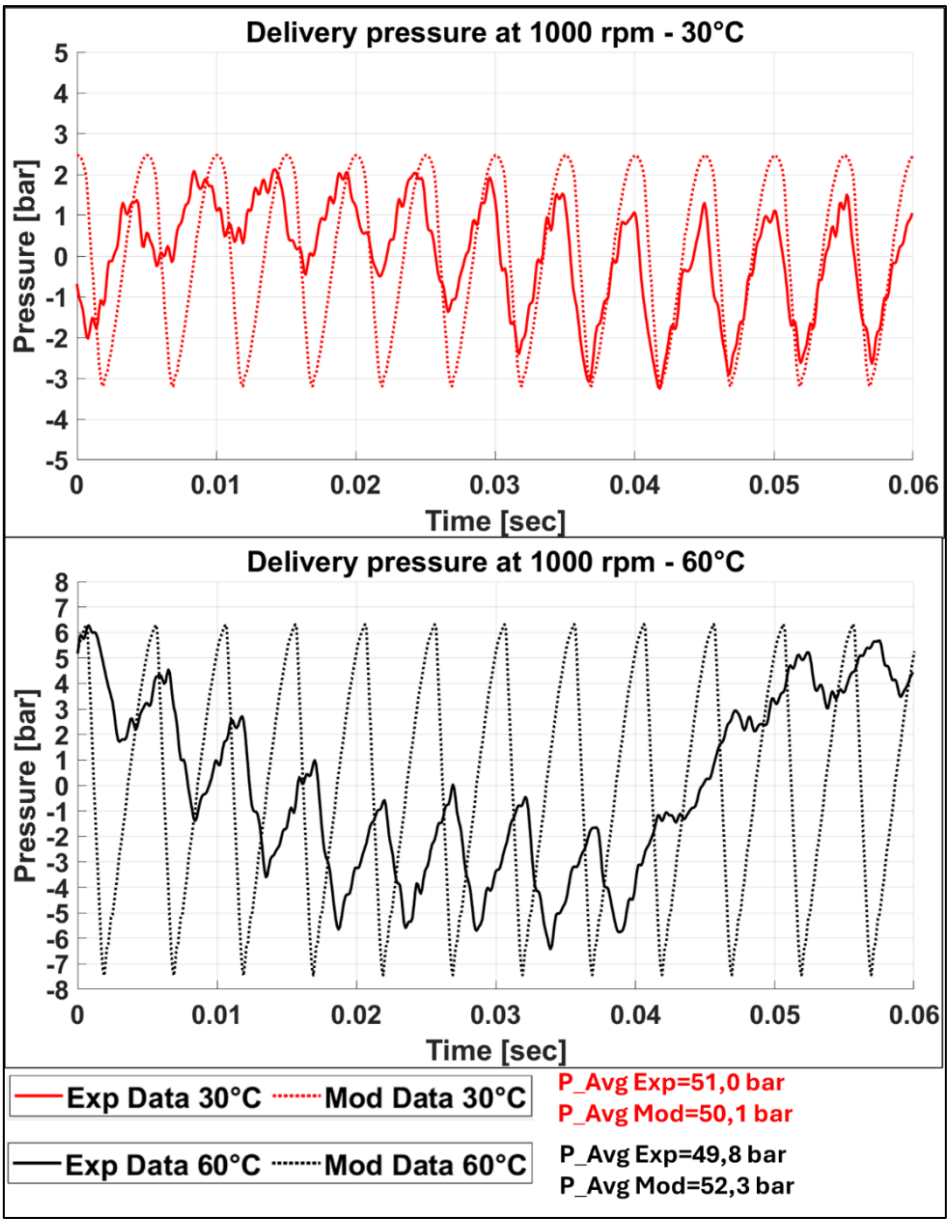

Figure 162 – Pressure ripple Pump 8.2 cc No.1 at 1000rpm and 50 bar

This type of pressure oscillation is also reported in other experimental studies in the literature [38], [39], [40].

In addition to this oscillation, the experimental pressure curves exhibit an oscillation with a period equal to 1/12 of one gear revolution. Thus, within one revolution, the pressure shows 12 oscillations. The number of oscillations equals the number of gear teeth, which, for the tested pump, is 12. These pressure oscillations also appear in the modelled curve, but with a different amplitude.
Under these conditions, the average pressure estimated by the model is similar to the experimental average pressure at 30°C and 60°C.

Figure 163 shows the pressure ripple of the 8.2 cc pump at 1000 rpm and 150 bar over one gear revolution. In this case too, the average pressure estimated by the model is similar to the experimental average pressure at 30 °C and 60 °C.

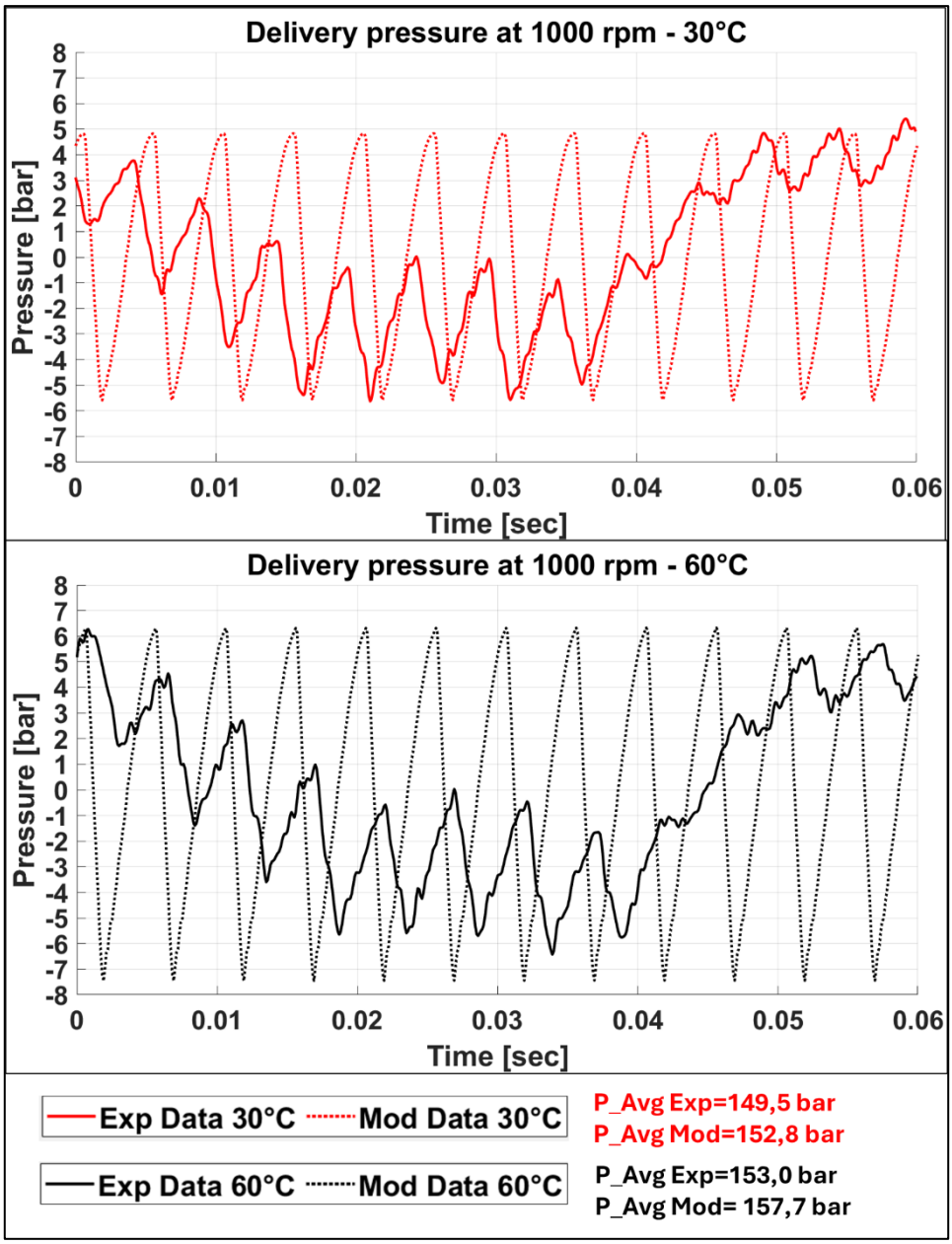

Figure 163 – Pressure ripple Pump 8.2 cc No.1 at 1000rpm and 150 bar

Figure 164 shows the pressure ripple of the 8.2 cc pump at 1000 rpm and 250 bar over one gear revolution. Under these operating conditions, the differences between the model and experimental average pressures are more significant. At 30°C, there is a difference of about 37 bar between the model and experimental average pressures, increasing to about 93 bar at 60°C.

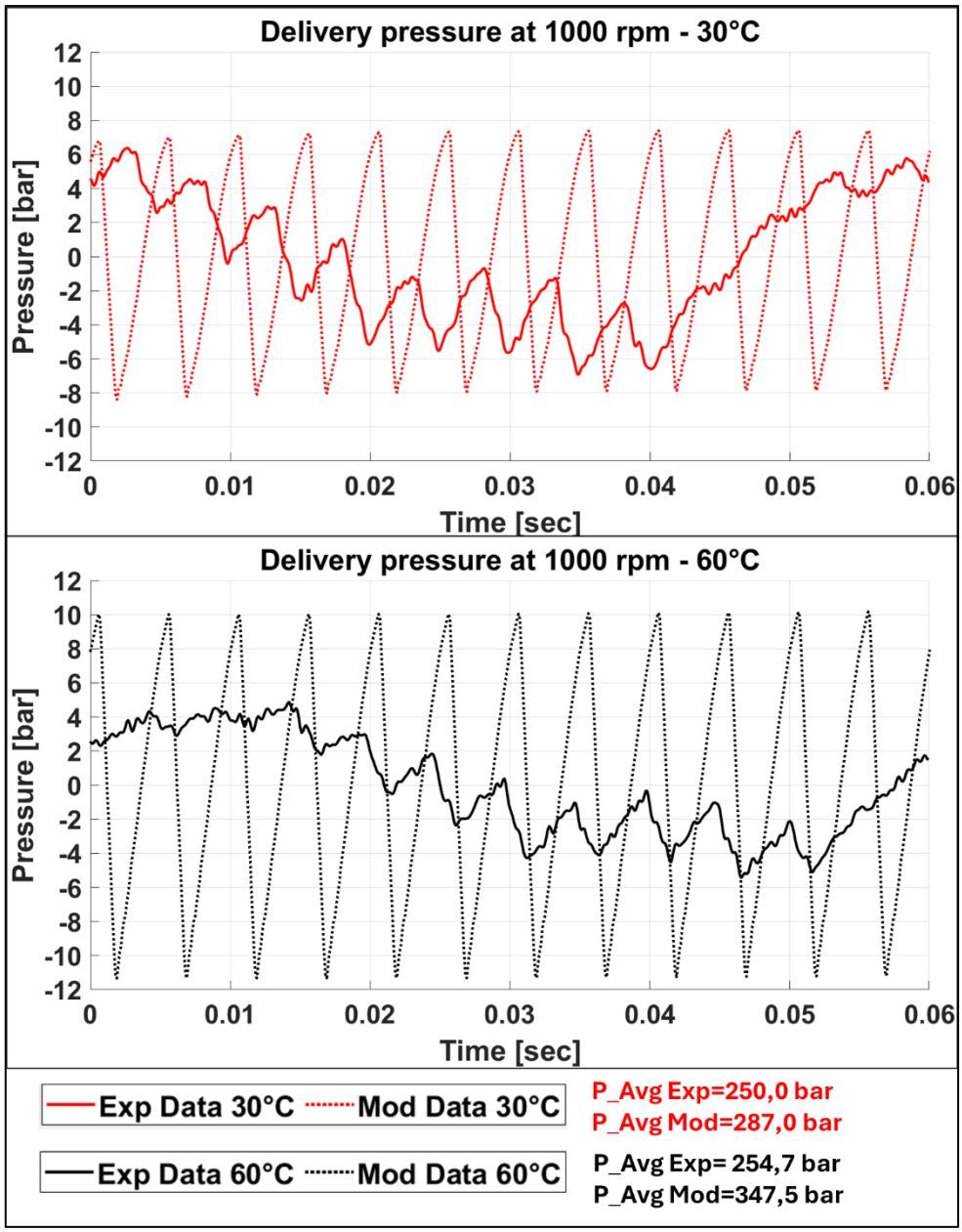

Figure 164 – Pressure ripple Pump 8.2 cc No.1 at 1000rpm and 250 bar

To facilitate a better comparison between the model and the experimental results, the Fast Fourier Transform (FFT) is applied to the pressure signal, converting it from the time domain to the frequency domain. For the experimental signal, although 10 seconds of data were recorded, only one second is considered.
The results of the FFT analysis are shown in Figure 165. Only the first five fundamental frequencies are plotted.

The fundamental frequency associated with one gear revolution is defined as:

$$f_{shaft} = \frac{n}{60} \qquad \textit{Eq. 215}$$

where the frequency f_{shaft} is expressed in Hz and n is the pump speed in rpm.

The other fundamental frequencies are defined as:

$$f_i = f_{shaft} * z * i = \frac{n}{60} * z * i \qquad \textit{Eq. 216}$$
$$i = 1,2,3,4, \ldots$$

where z is the number of gear teeth.

The component at f_{shaft} is zero in the model data and non-zero in the experimental curve.

From the analysis of the experimental data, the following observations emerge:

- The amplitude of the oscillation at the frequency f_{shaft} increases with increasing average delivery pressure at 30°C, whereas at 60°C it first increases and then slightly decreases as the average delivery pressure increases.
  With temperature variation, the amplitude sometimes slightly increases (e.g., at 150 bar) or slightly decreases (e.g., at 250 bar).
- The amplitude of the oscillation associated with the frequency f_1 at 30°C first increases and then decreases as the average delivery pressure increases. At 60°C, increasing delivery pressure reduces the oscillation amplitude.
  With temperature variation, the amplitude sometimes slightly increases (e.g., at 150 bar) or slightly decreases (e.g., at 250 bar).
  Anyway, the magnitude of this variations are of limited significance
- The amplitudes associated with the remaining frequencies are negligible.

From the analysis of the model data, a clearer trend can be identified:

- Increasing the average delivery pressure causes an increase in amplitude at all frequencies.
- Increasing the temperature increases the oscillation amplitude at all frequencies.

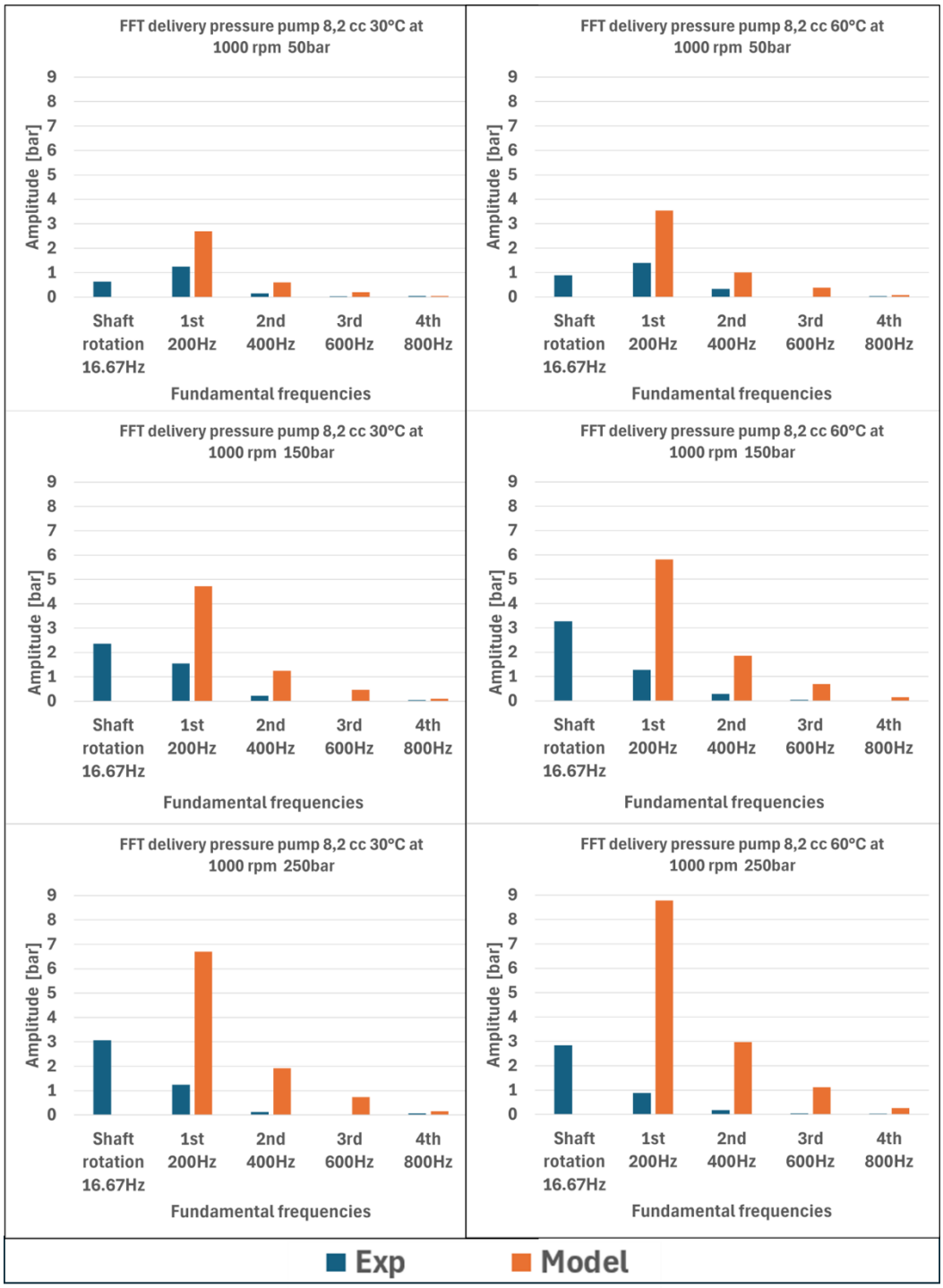

Figure 165 – FFT Pressure Ripple – Pump 8.2 cc No.1 at 1000rpm

9.2.2. Pump 8.2 cc No.1 – Pressure ripple at 2000 rpm

Figure 166 shows the pressure ripple of the 8.2 cc pump at 2000 rpm and 50 bar over one gear revolution. Under these conditions, the average pressure estimated by the model is similar to the experimental average pressure at 30°C and 60°C.

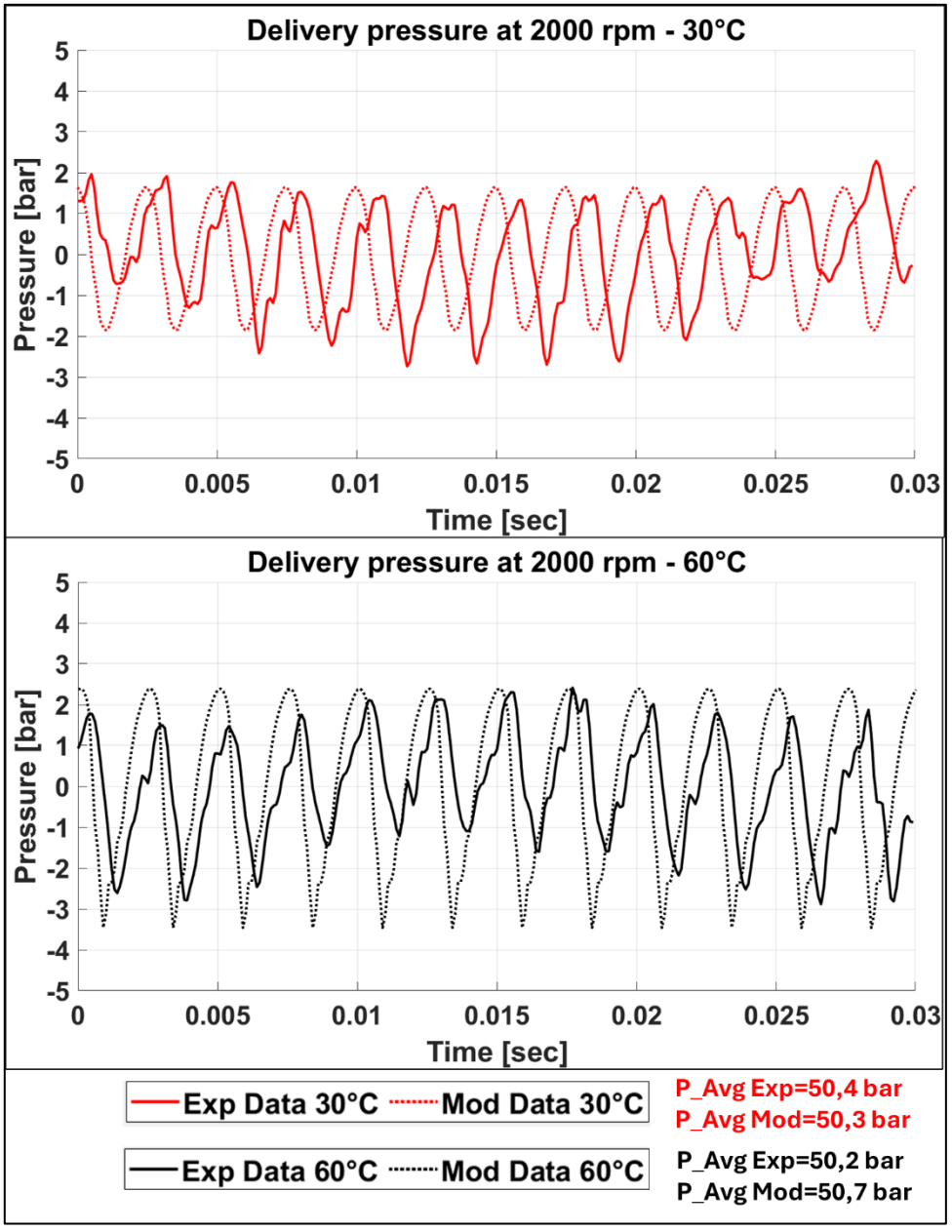

Figure 166 – Pressure ripple Pump 8.2 cc No.1 at 2000rpm and 50 bar

Figure 167 shows the pressure ripple of the 8.2 cc pump at 2000 rpm and 150 bar over one gear revolution. Also in these conditions, the average pressure estimated by the model is similar to the experimental average pressure at 30°C and 60°C.

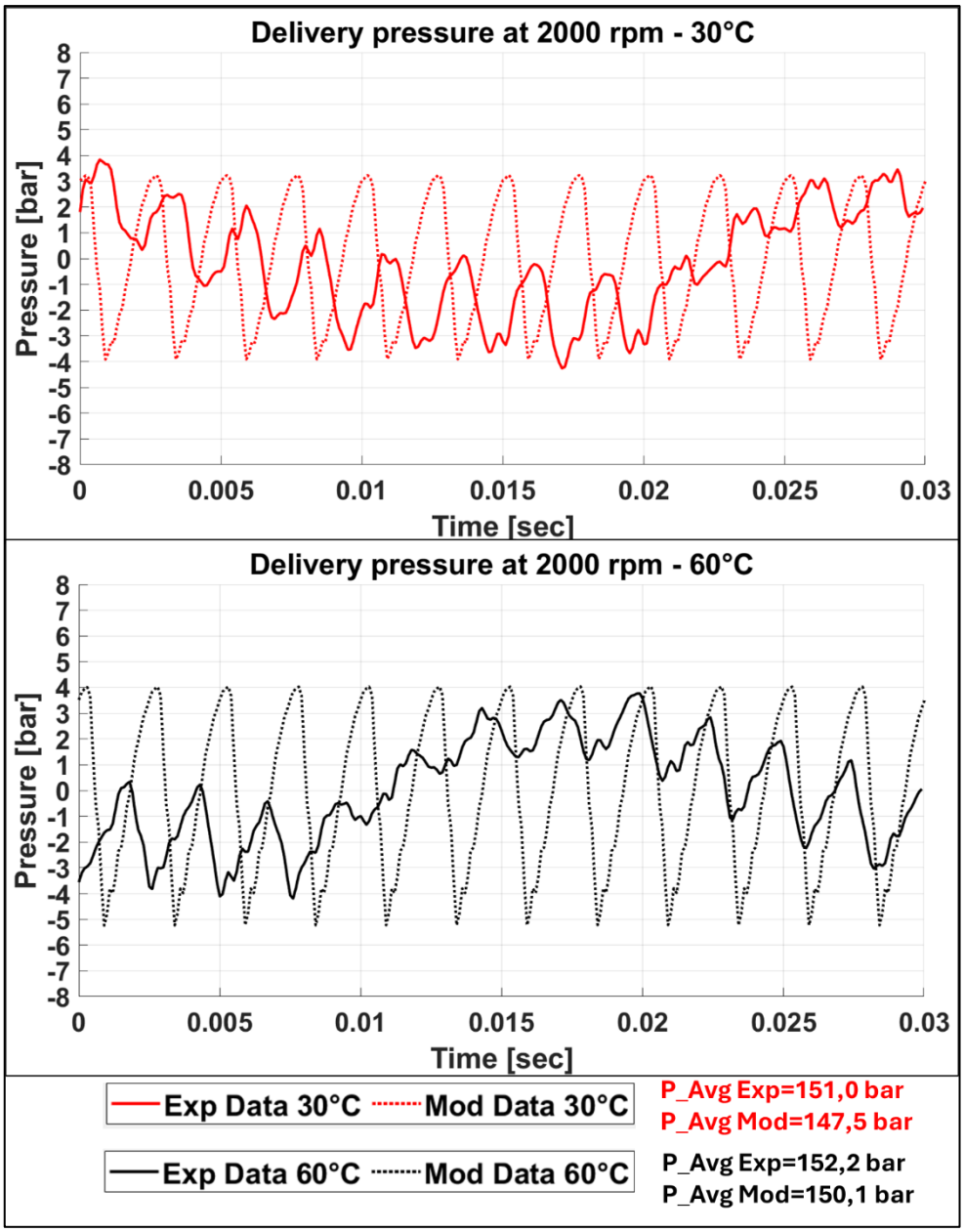

Figure 167 – Pressure ripple Pump 8.2 cc No.1 at 2000rpm and 150 bar

Figure 168 shows the pressure ripple of the 8.2 cc pump at 2000 rpm and 240 bar over one gear revolution. Under these operating conditions, the differences between the model and experimental average pressures are more significant at 60°C, where the difference is about 27 bar between the model and experimental average pressures.

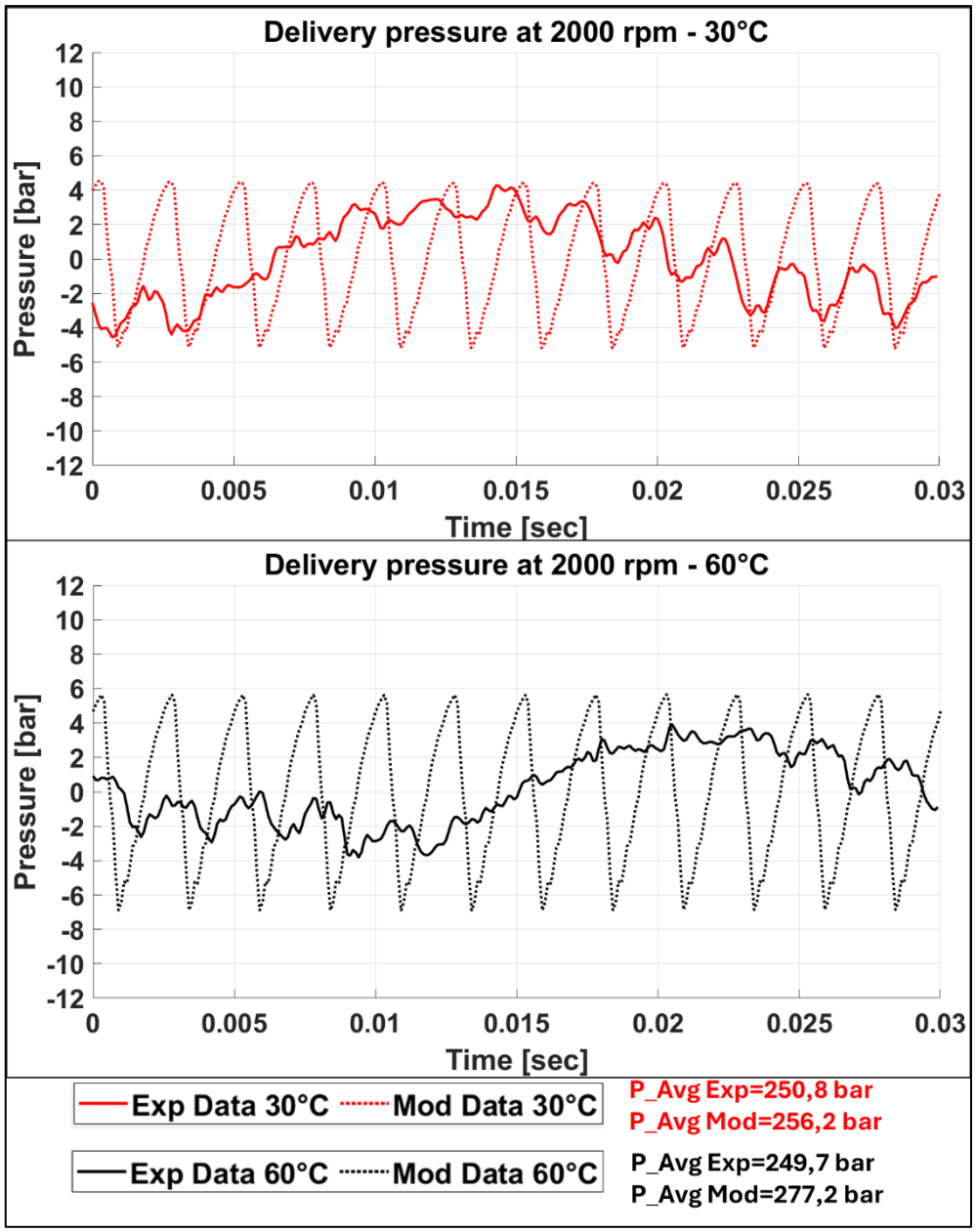

Figure 168 – Pressure ripple Pump 8.2 cc No.1 at 2000rpm and 250 bar

Figure 169 show the result of FFT analysis applied to the experimental and model pressure signal at the speed of 2000rpm.

From the analysis of the experimental data, the following observations emerge:

- The amplitude of the oscillation at the frequency f_{shaft} increases with increasing average delivery pressure at 30°C, whereas at 60°C it first increases and then slightly decreases as the average delivery pressure increases.
  With temperature variation, the amplitude decreases.
- The amplitude of the oscillation associated with the frequency f_1 at 30°C first increases and then decreases as the average delivery pressure increases. At 60°C, increasing delivery pressure reduces the oscillation amplitude.

With temperature variation, the amplitude sometimes slightly increases (e.g., at 50 bar) or slightly decreases (e.g., at 250 bar).
Although the magnitude of these variations are of limited significance

- The amplitudes associated with the remaining frequencies are negligible.

From the analysis of the model data, the following observations emerge:

- Increasing the average delivery pressure causes an increase in amplitude at all frequencies.
- Increasing the temperature increases the oscillation amplitude at all frequencies.

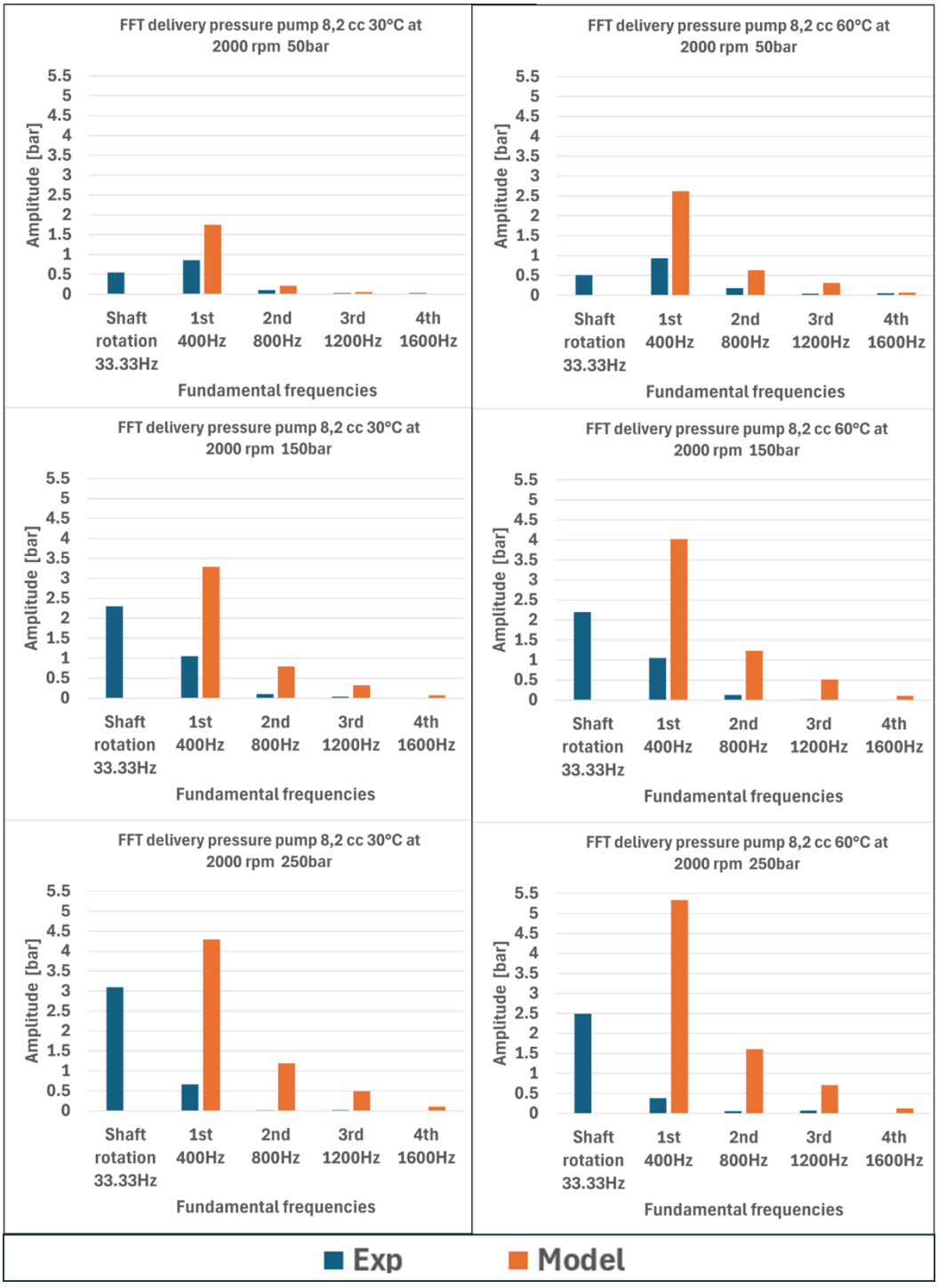

Figure 169 – FFT Pressure Ripple – Pump 8.2 cc No.1 at 2000rpm

9.2.3. Pump 8.2 cc No.1 – Pressure ripple at 3500 rpm

Figure 170 shows the pressure ripple of the 8.2 cc pump at 3500 rpm and 50 bar over one gear revolution. Under these conditions, the average pressure estimated by the model is similar to the experimental average pressure at 30°C and 60°C.

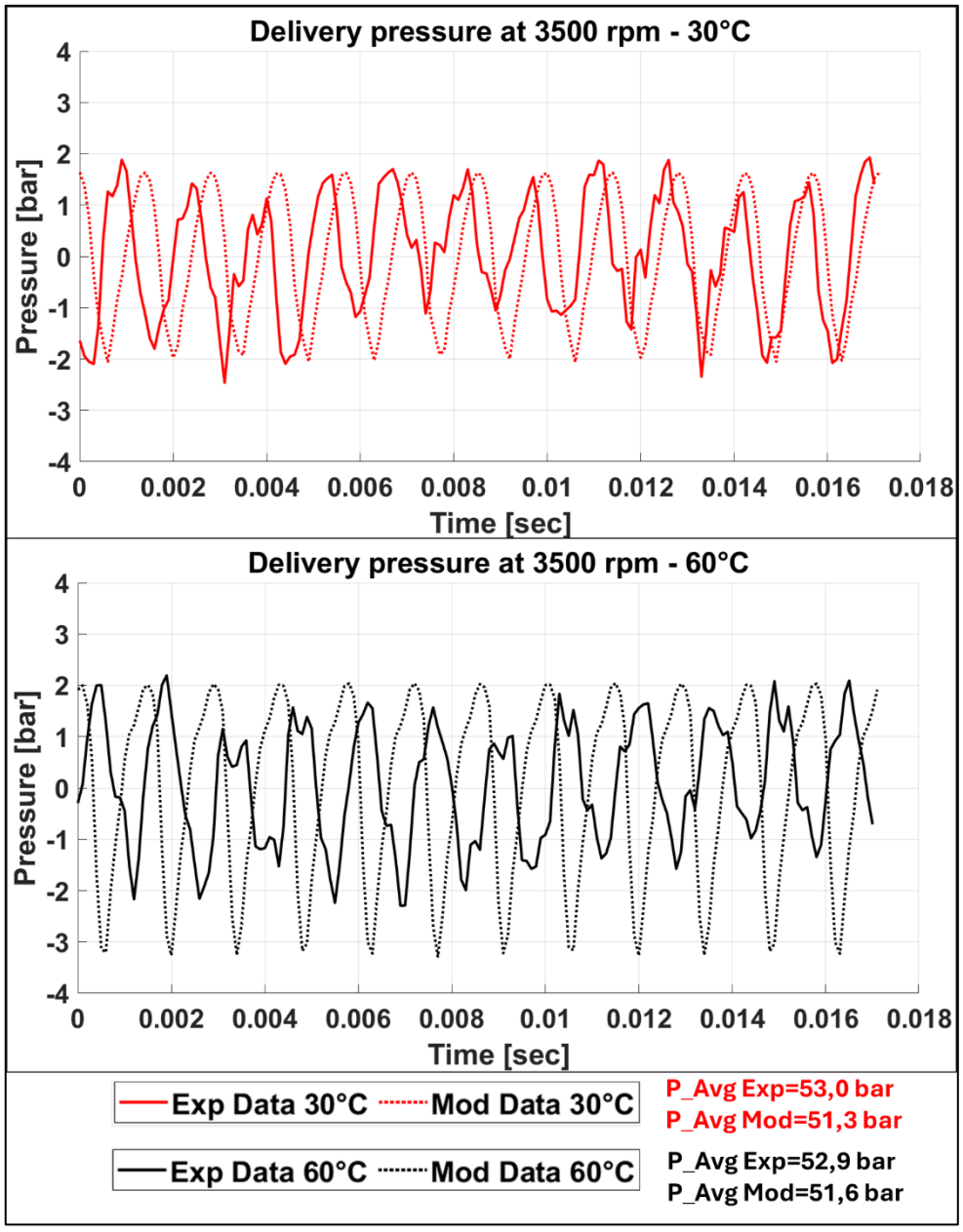

Figure 170 - Pressure ripple Pump 8.2 cc No.1 at 3500rpm and 50 bar

Figure 171 shows the pressure ripple of the 8.2 cc pump at 3500 rpm and 150 bar over one gear revolution. Also at these conditions, the average pressure estimated by the model is similar to the experimental average pressure at 30°C and 60°C.

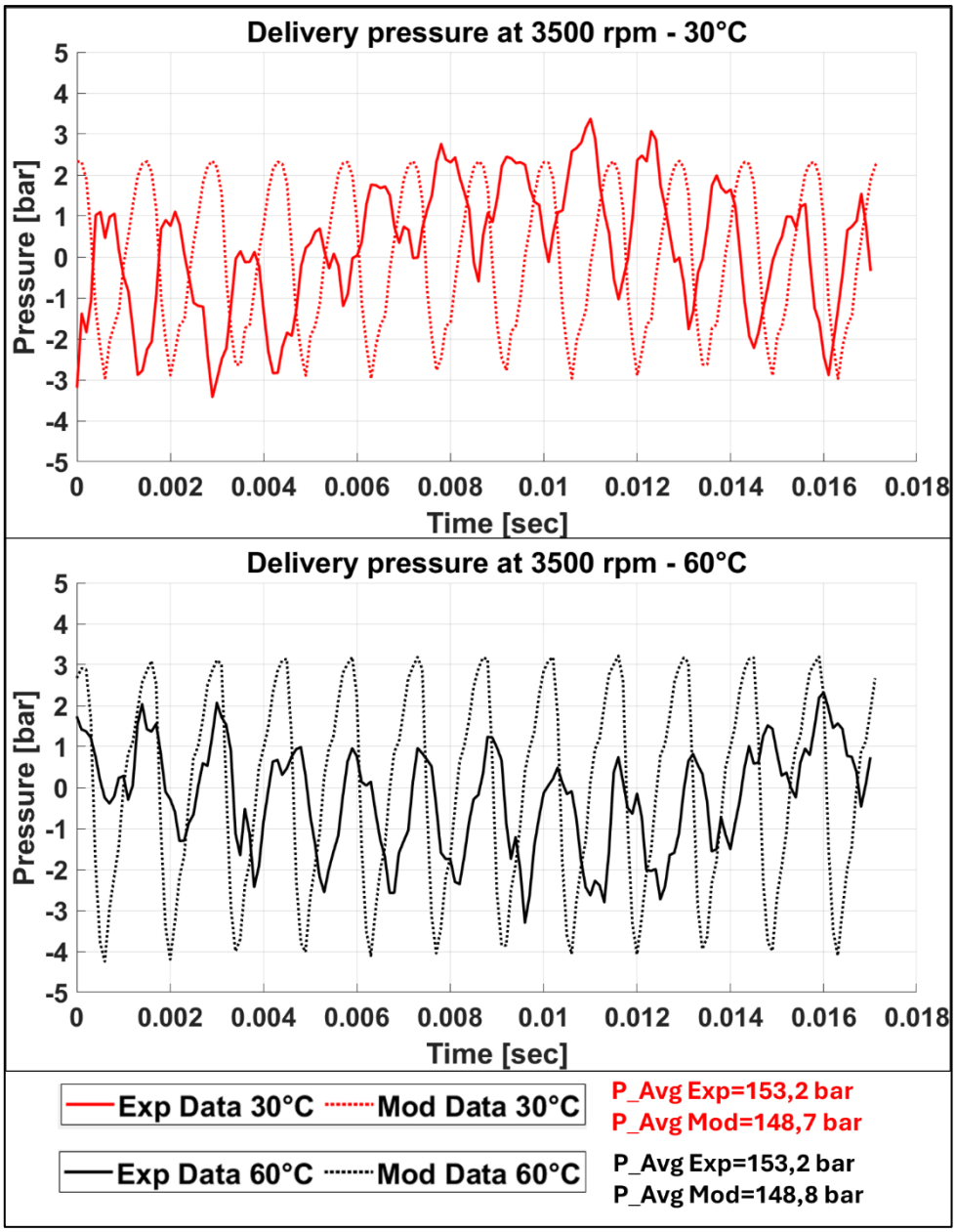

Figure 171 - Pressure ripple Pump 8.2 cc No.1 at 3500rpm and 150 bar

Figure 172 shows the pressure ripple of the 8.2 cc pump at 3500 rpm and 250 bar over one gear revolution. Under these conditions, the average pressure estimated by the model is similar to the experimental average pressure at both 30°C and 60°C, unlike at 1000 rpm and 2000 rpm, where at 240 bar there are substantial differences.

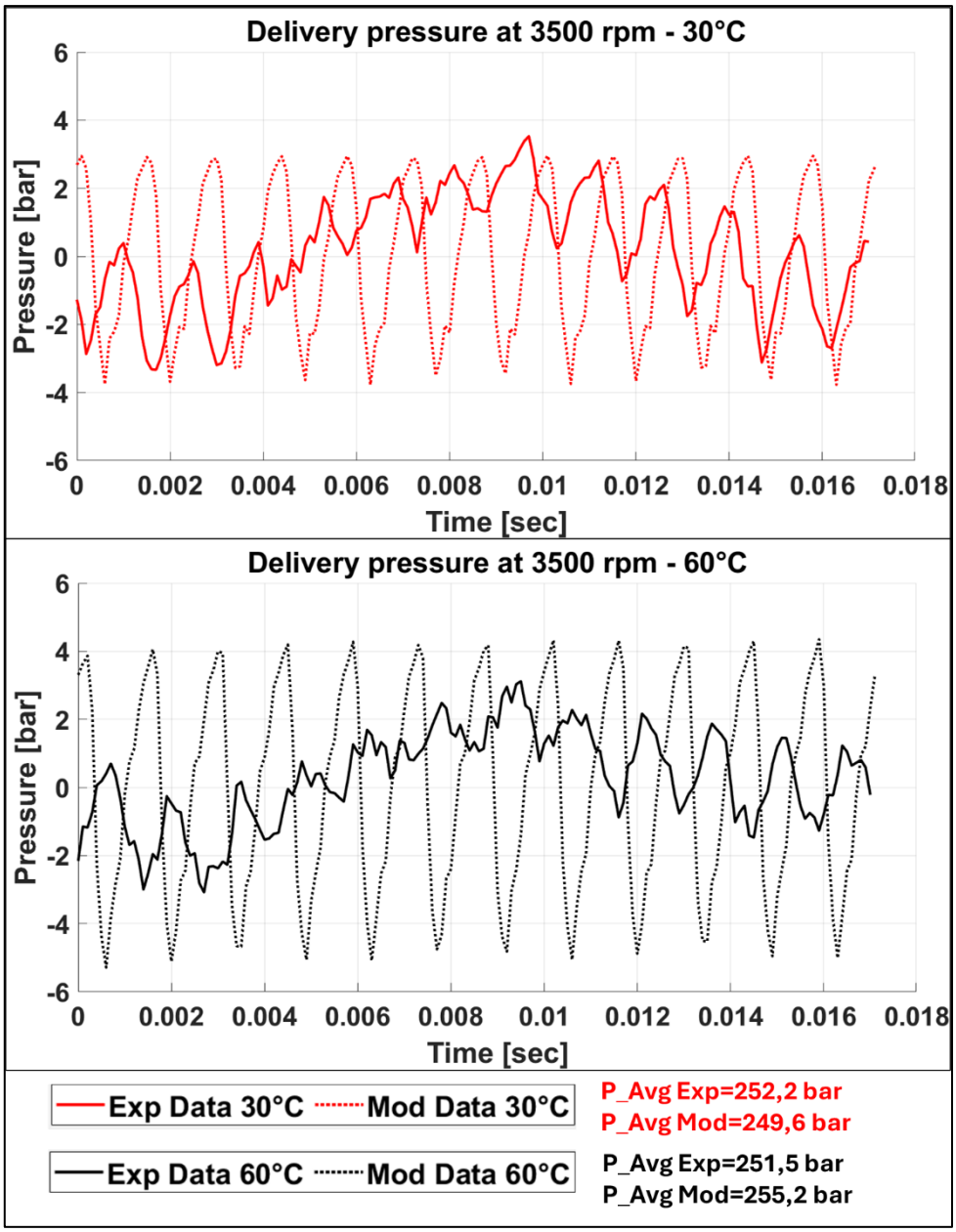

Figure 172 - Pressure ripple Pump 8.2 cc No.1 at 3500rpm and 250 bar

Figure 173 shows the results of FFT analysis applied to the experimental and model pressure signals at 3500rpm.

From the analysis of the experimental data, the following observations emerge:

- The amplitude of the oscillation at the frequency f_{shaft} increases with increasing average delivery pressure at 30°C and 60°C.
  With temperature variation, the amplitude decreases.
- The amplitude of the oscillation associated with the frequency f_1 at 30°C first decreases and then increases as the average delivery pressure increases. At 60°C, increasing delivery pressure reduces the oscillation amplitude.
  With temperature variation, the amplitude sometimes slightly increases (e.g.,

at 50 bar) or slightly decreases (e.g., at 250 bar).
Although these magnitude of these variations is of limited significance

- The amplitudes associated with the remaining frequencies are negligible.

From the analysis of the model data, the following observations emerge:

- Increasing the average delivery pressure causes an increase in amplitude at all frequencies.
- Increasing the temperature increases the oscillation amplitude at all frequencies.

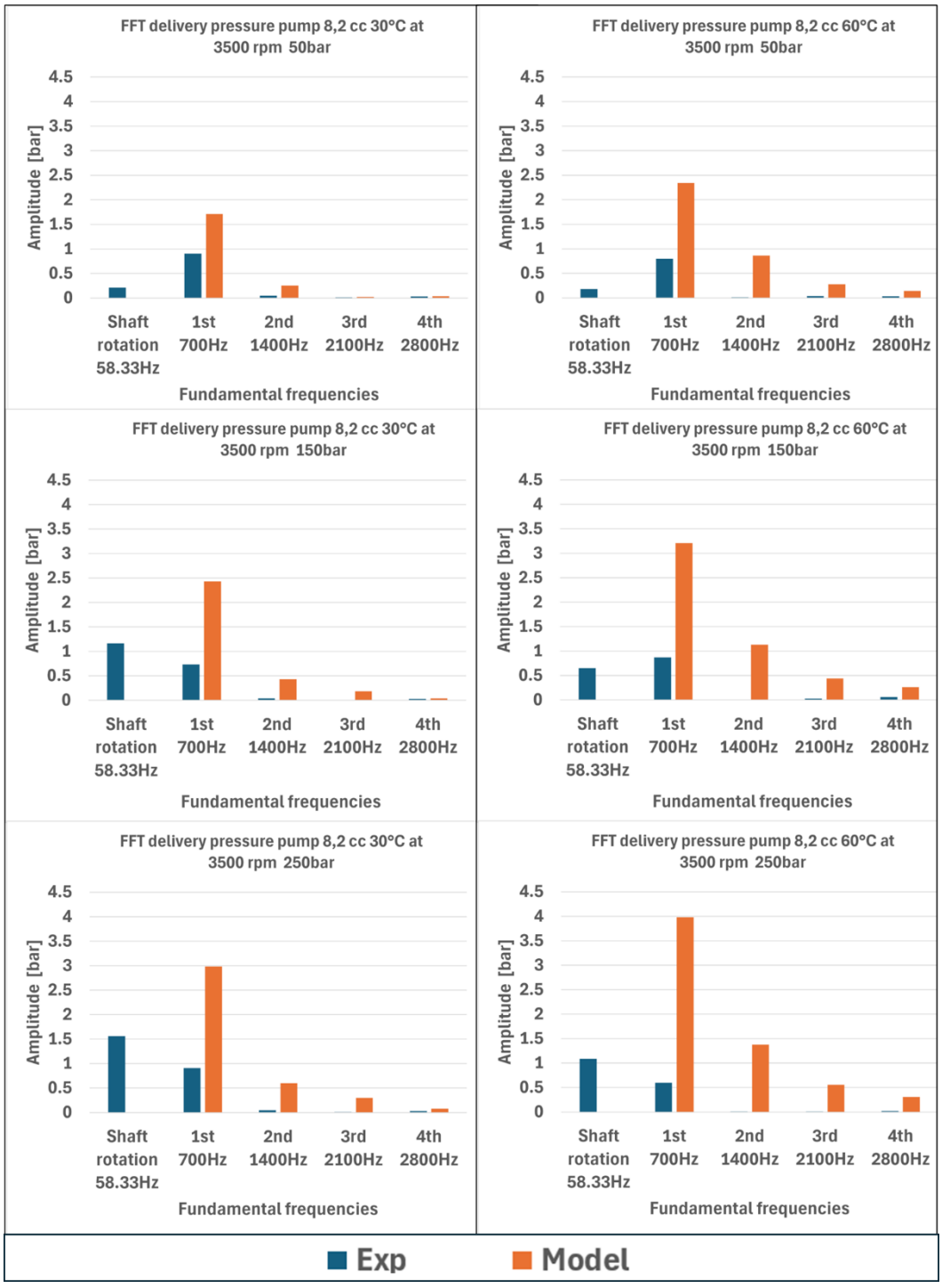

Figure 173 - FFT Pressure Ripple - Pump 8.2 cc No.1 at 3500rpm

9.3. Pump 16 cc No.3 – Pressure Ripple: Experimental and Model Results

In this section, the experimental and model results for the 16 cc pump (sample No. 3) are analysed under different speed, pressure, and oil temperature conditions.

9.3.1. Pump 16 cc No.3 – Pressure ripple at 500 rpm

Figure 174 shows the pressure ripple of the 16 cc pump at 500 rpm and 50 bar over one gear revolution. Under these operating conditions, the differences between the model and experimental average pressures are more significant at 60°C, where the difference is about 36 bar between the model and experimental average pressures.

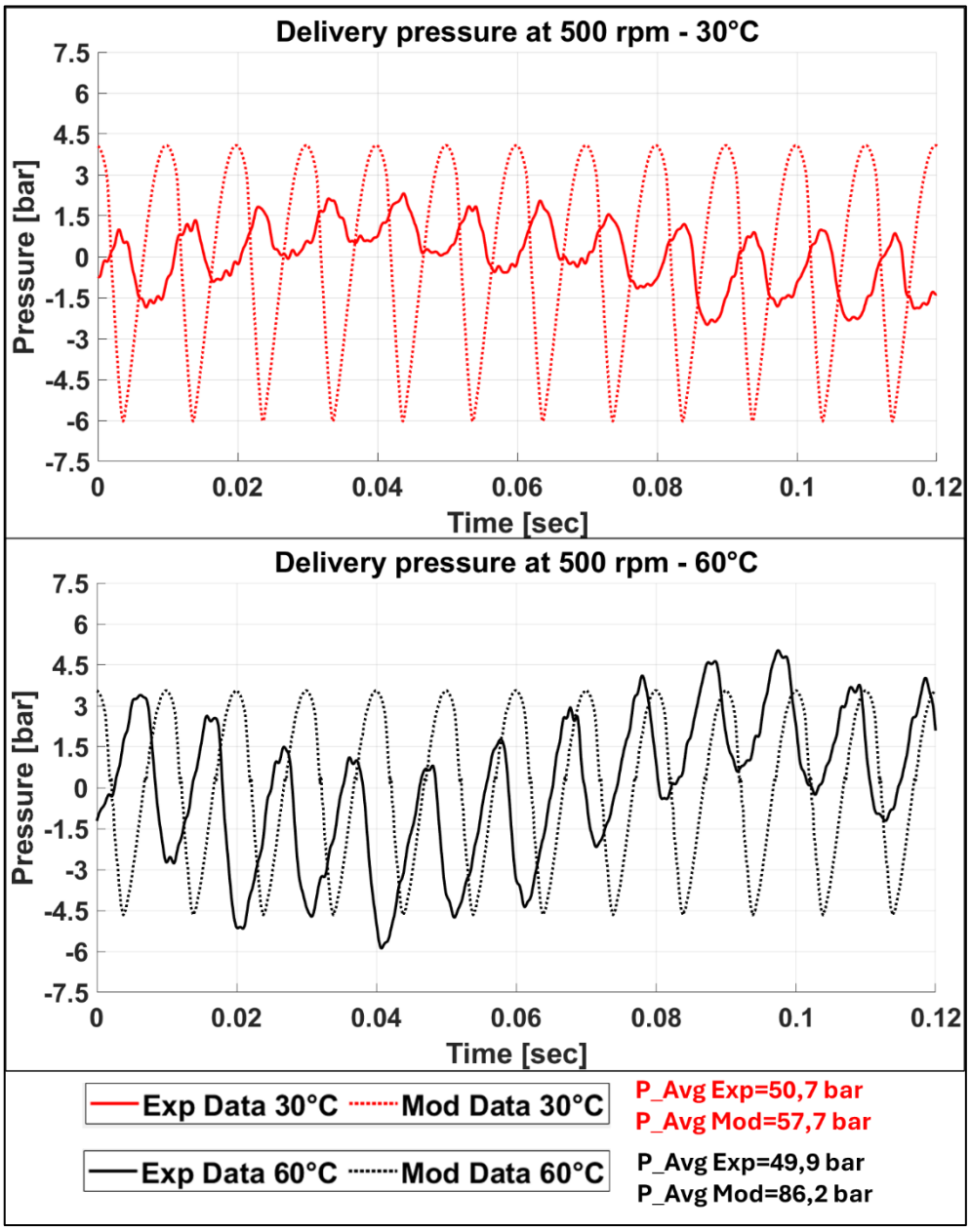

Figure 174 – Pressure ripple Pump 16 cc No.3 at 500rpm and 50 bar

Figure 175 shows the pressure ripple of the 16 cc pump at 500 rpm and 150 bar over one gear revolution. Under these operating conditions, the differences between the

model and experimental average pressures are more significant. At 30°C, there is a difference of about 47 bar between the model and experimental average pressures, increasing to about 234 bar at 60°C.

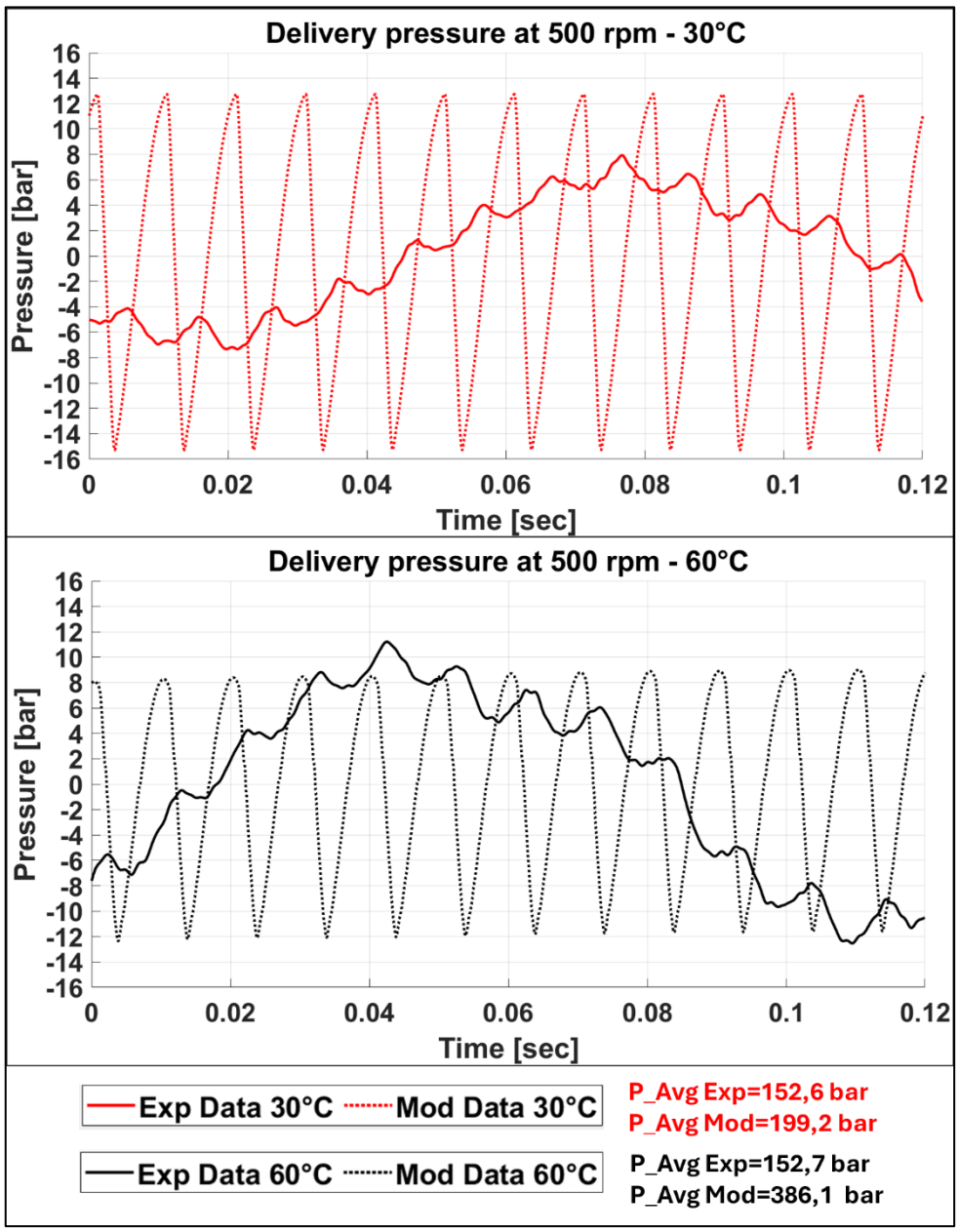

Figure 175 – Pressure ripple Pump 16 cc No.3 at 500rpm and 150 bar

Figure 176 shows the pressure ripple of the 16 cc pump at 500 rpm and 240 bar over one gear revolution. Only the curves at 30°C are shown because there was a problem with data acquisition at 60°C. At 30°C, the difference between the modelled average delivery pressure and the experimental data is about 65 bar.

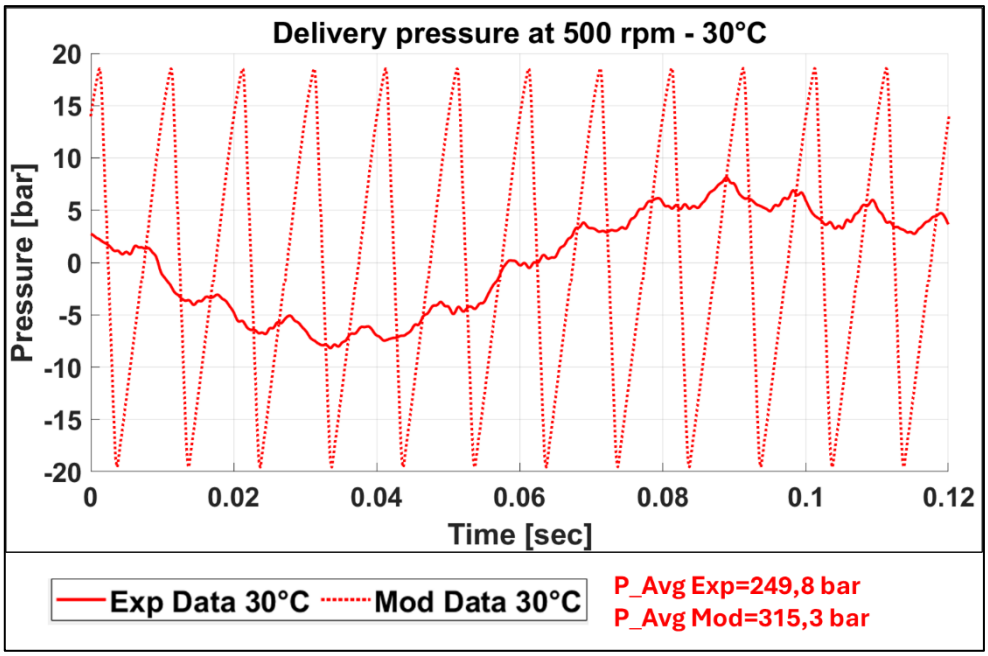

Figure 176 – Pressure ripple Pump 16 cc No.3 at 500rpm and 240 bar

Figure 177 shows the results of FFT analysis applied to the experimental and model pressure signals at the speed of 500 rpm.

From the analysis of the experimental data, the following observations emerge:

- The amplitude of the oscillation at the frequency f_{shaft} increases with increasing average delivery pressure at 30°C and 60°C.
  With temperature variation, the amplitude increases.
- The amplitude of the oscillation associated with the frequency f_1 is influenced only marginally by variations in average delivery pressure and temperature.
- The amplitudes associated with the remaining frequencies are negligible.

From the analysis of the model data, the following observations emerge:

- Increasing the average delivery pressure causes an increase in amplitude at all frequencies.
- Increasing the temperature decreases the oscillation amplitude at all frequencies.

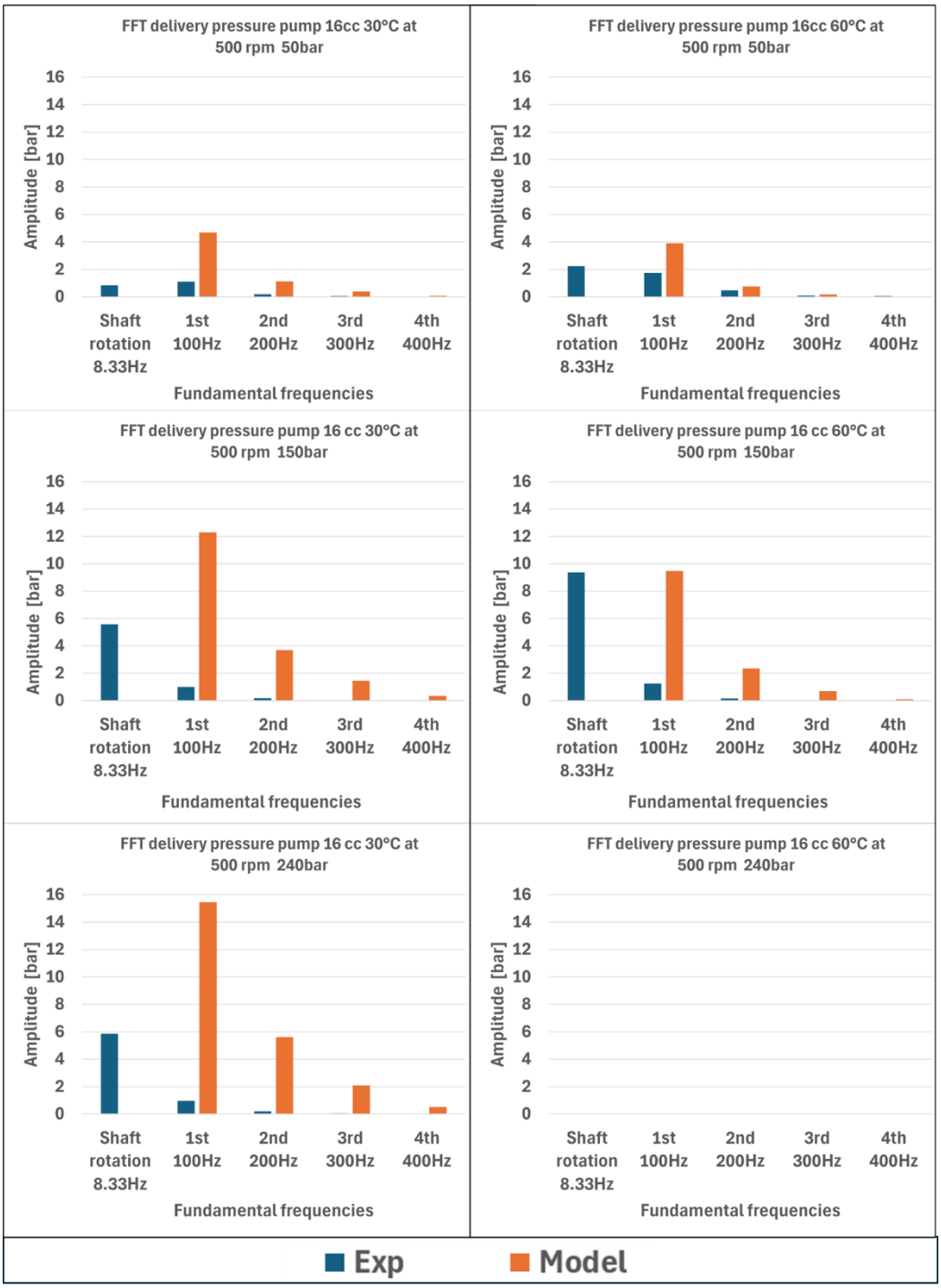

Figure 177 – FFT Pressure Ripple – Pump 16 cc No.3 at 500rpm

9.3.2. Pump 16 cc No.3 – Pressure ripple at 1500 rpm

Figure 178 shows the pressure ripple of the 16 cc pump at 1500 rpm and 50 bar over one gear revolution. Also at these conditions, the average pressure estimated by the model is similar to the experimental average pressure at 30°C and 60°C.

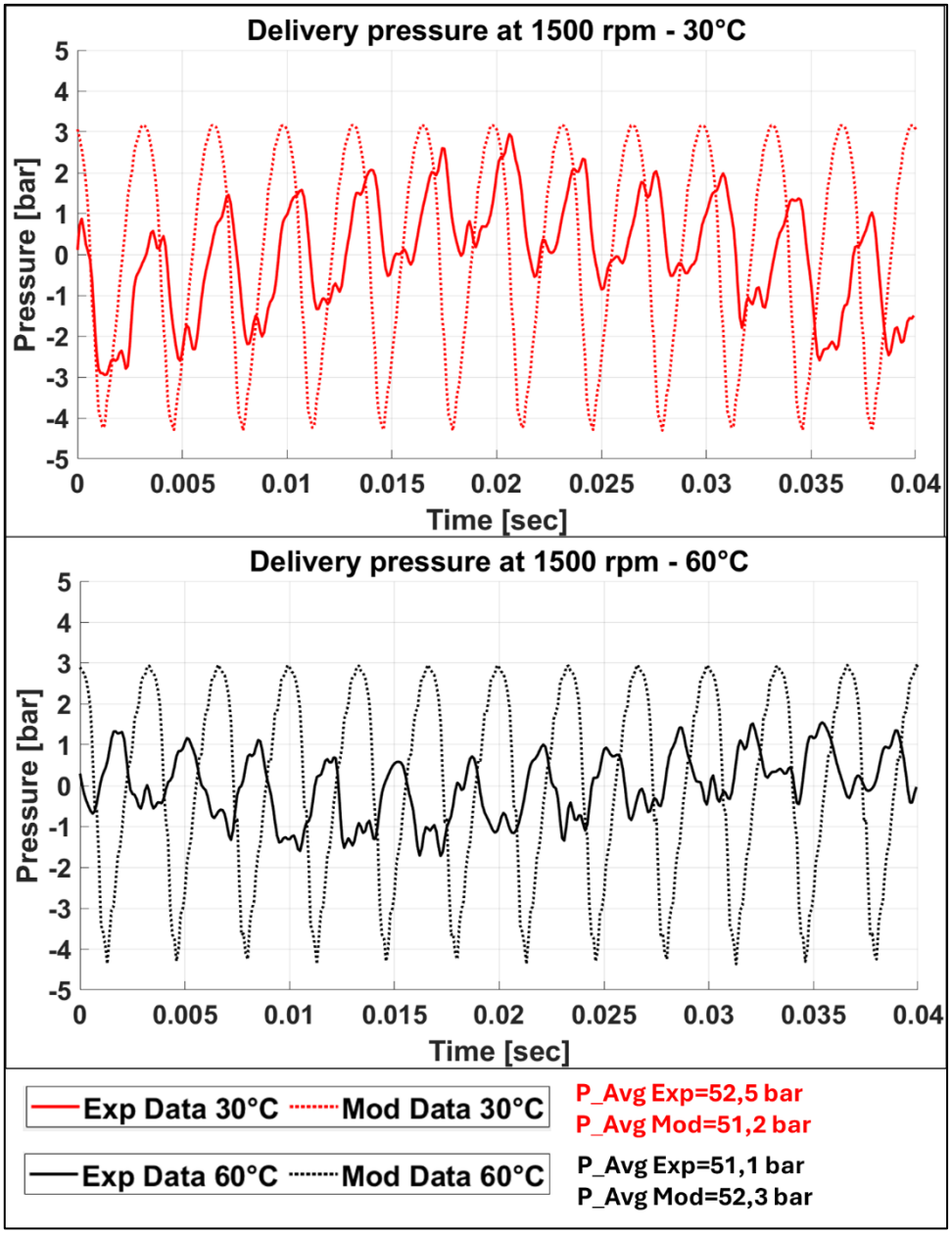

Figure 178 – Pressure ripple Pump 16 cc No.3 at 1500rpm and 50 bar

Figure 179 shows the pressure ripple of the 16 cc pump at 1500 rpm and 150 bar over one gear revolution. Also at these conditions, the average pressure estimated by the model is similar to the experimental average pressure at 30°C, while at 60°C the difference between the modelled average delivery pressure and the experimental data is about 43 bar.

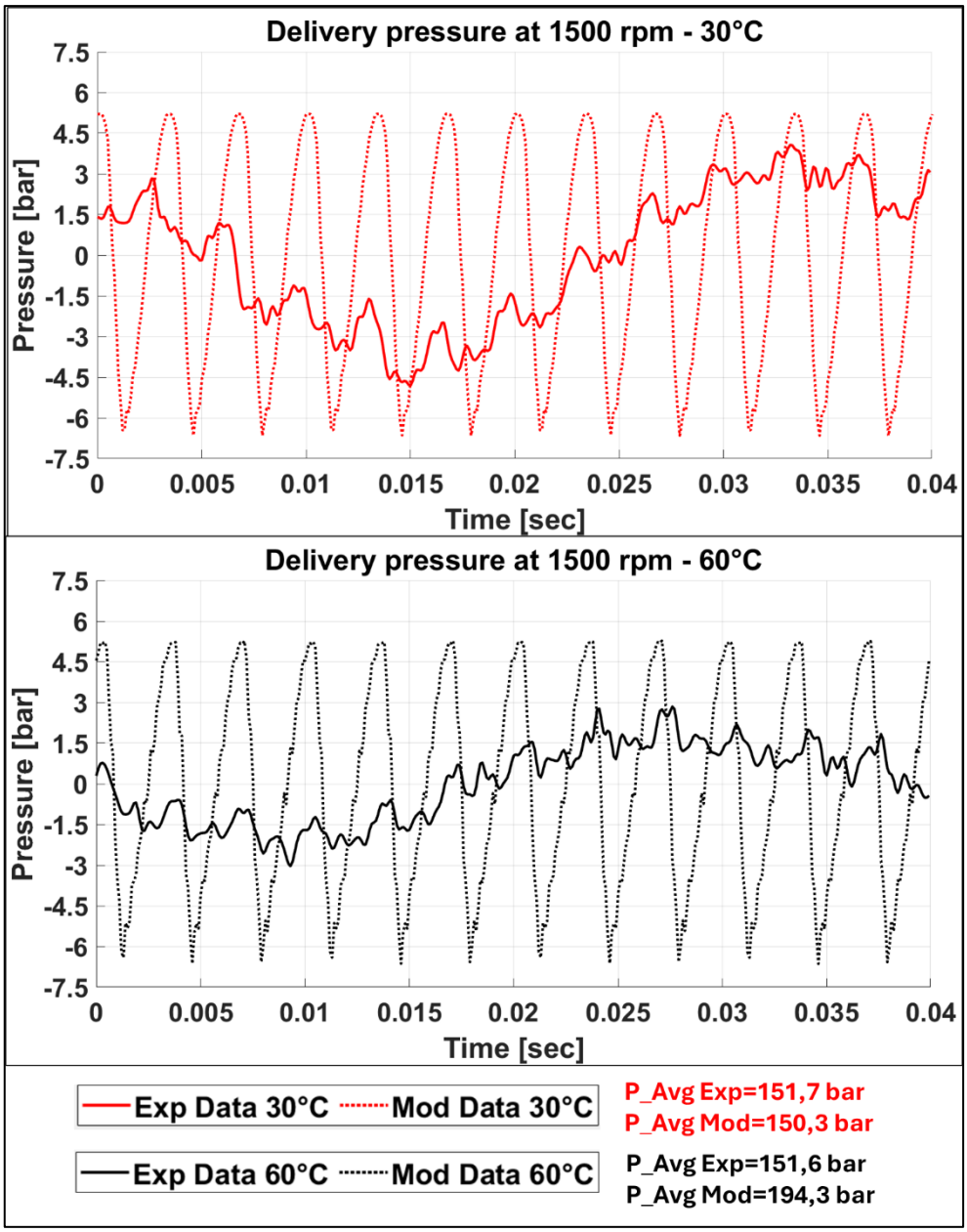

Figure 179 – Pressure ripple Pump 16 cc No.3 at 1500rpm and 150 bar

Figure 180 shows the pressure ripple of the 16 cc pump at 1500 rpm and 240 bar over one gear revolution. At these conditions, the average pressure estimated by the model is similar to the experimental average pressure at 30°C, while at 60°C the difference between the modelled average delivery pressure and the experimental data is about 43 bar.

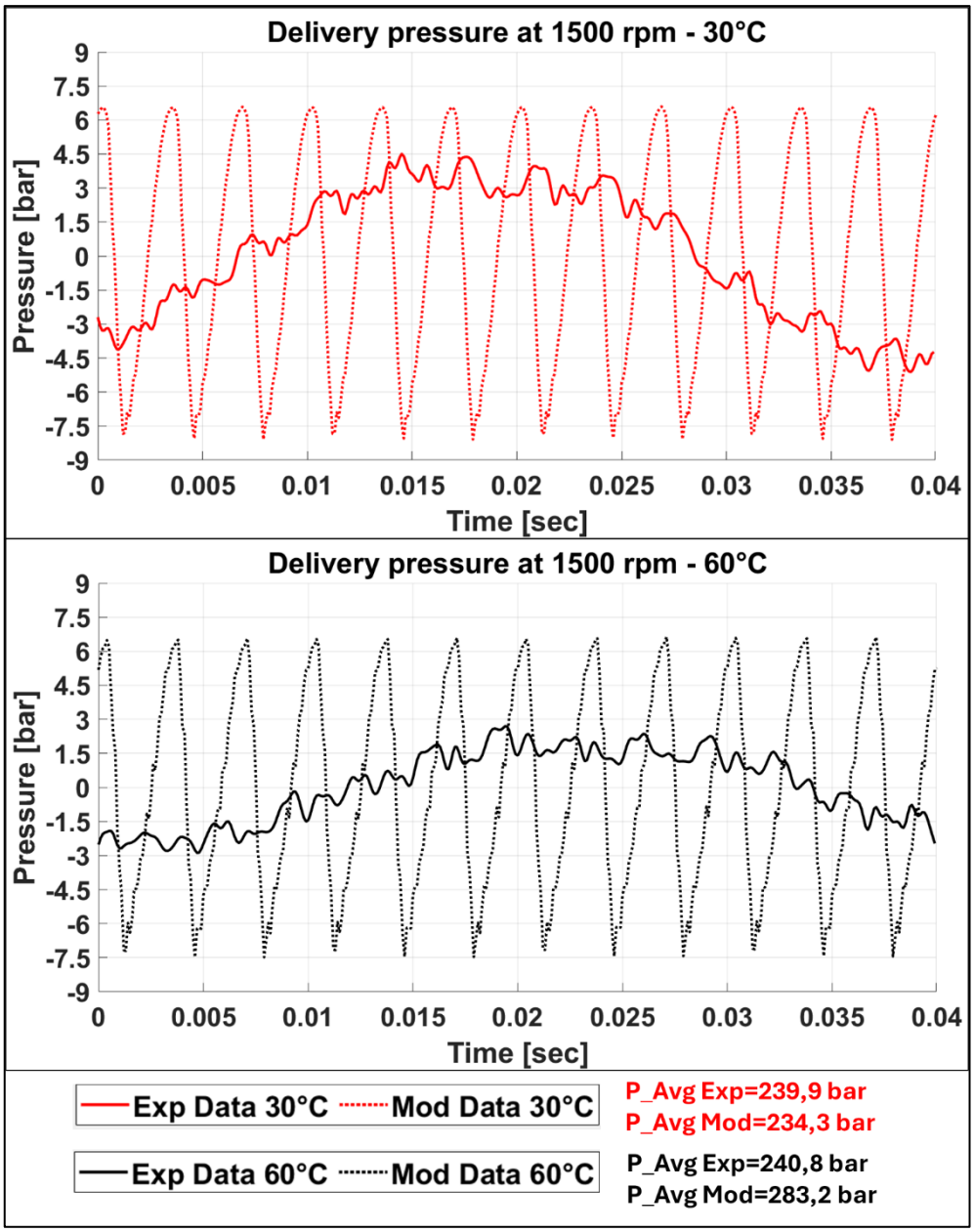

Figure 180 – Pressure ripple Pump 16 cc No.3 at 1500rpm and 240 bar

Figure 181 shows the result of FFT analysis applied to the experimental and model pressure signals at the speed of 1500 rpm.

From the analysis of the experimental data, the following observations emerge:

- The amplitude of the oscillation at the frequency f_{shaft} increases with increasing average delivery pressure at 30°C and 60°C.
  With temperature variation, the amplitude decreases.
- The amplitude of the oscillation associated with the frequency f_1 is only marginally influenced by variations in average delivery pressure and temperature.
- The amplitudes associated with the frequency f_2 become more relevant, unlike the other working condition.

- The amplitudes associated with the remaining frequencies are negligible.

From the analysis of the model data, the following observations emerge:

- Increasing the average delivery pressure causes an increase in amplitude at all frequencies.
- Increasing the temperature decreases the oscillation amplitude at all frequencies.

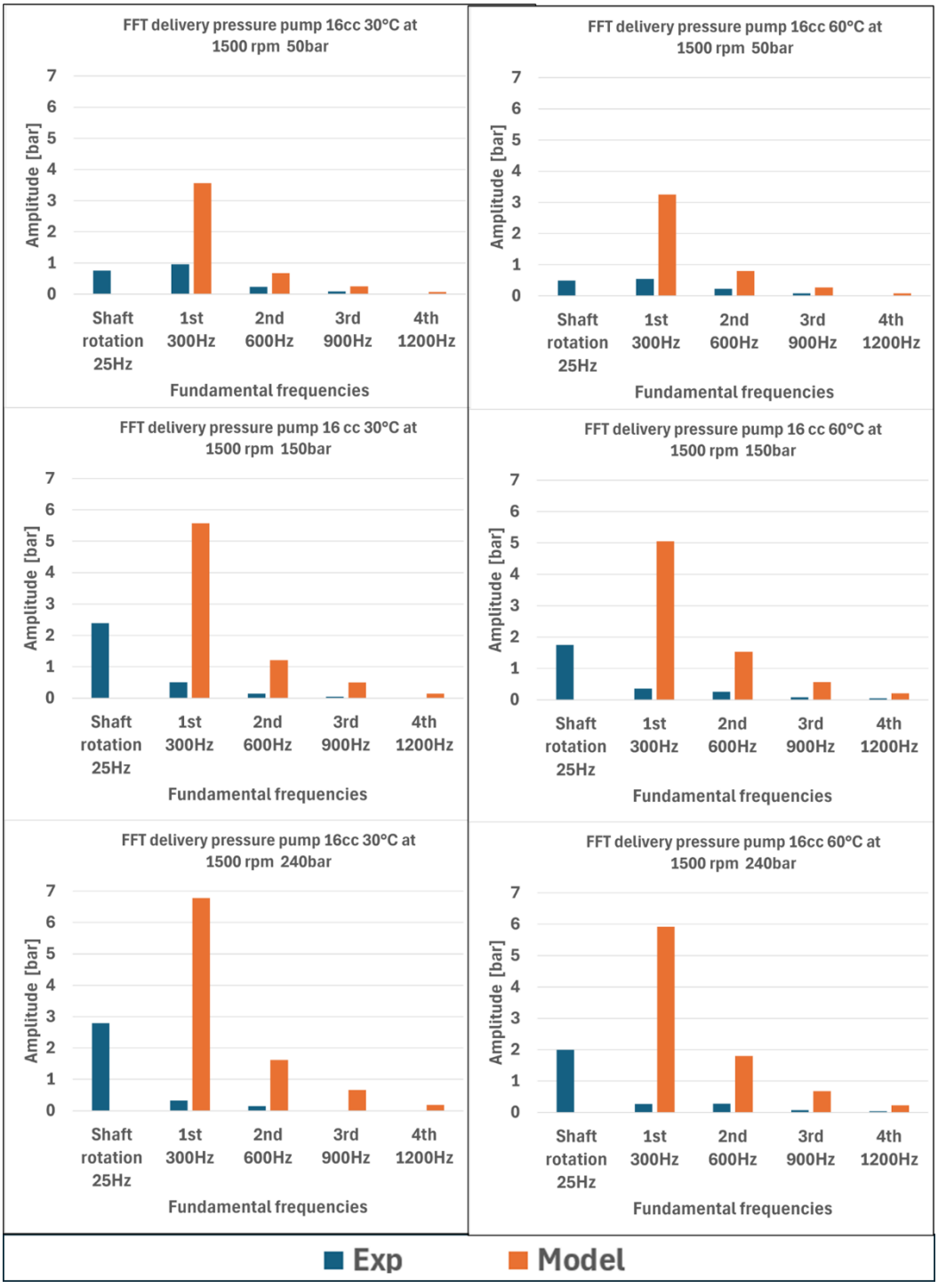

Figure 181 – FFT Pressure Ripple – Pump 16 cc No.3 at 1500rpm

9.3.3. Pump 16 cc No.3 – Pressure ripple at 2500 rpm

Figure 182 shows the pressure ripple of the 16 cc pump at 2500 rpm and 50 bar over one gear revolution. At these conditions, the average pressure estimated by the model is similar to the experimental average pressure at 30°C and 60°C.

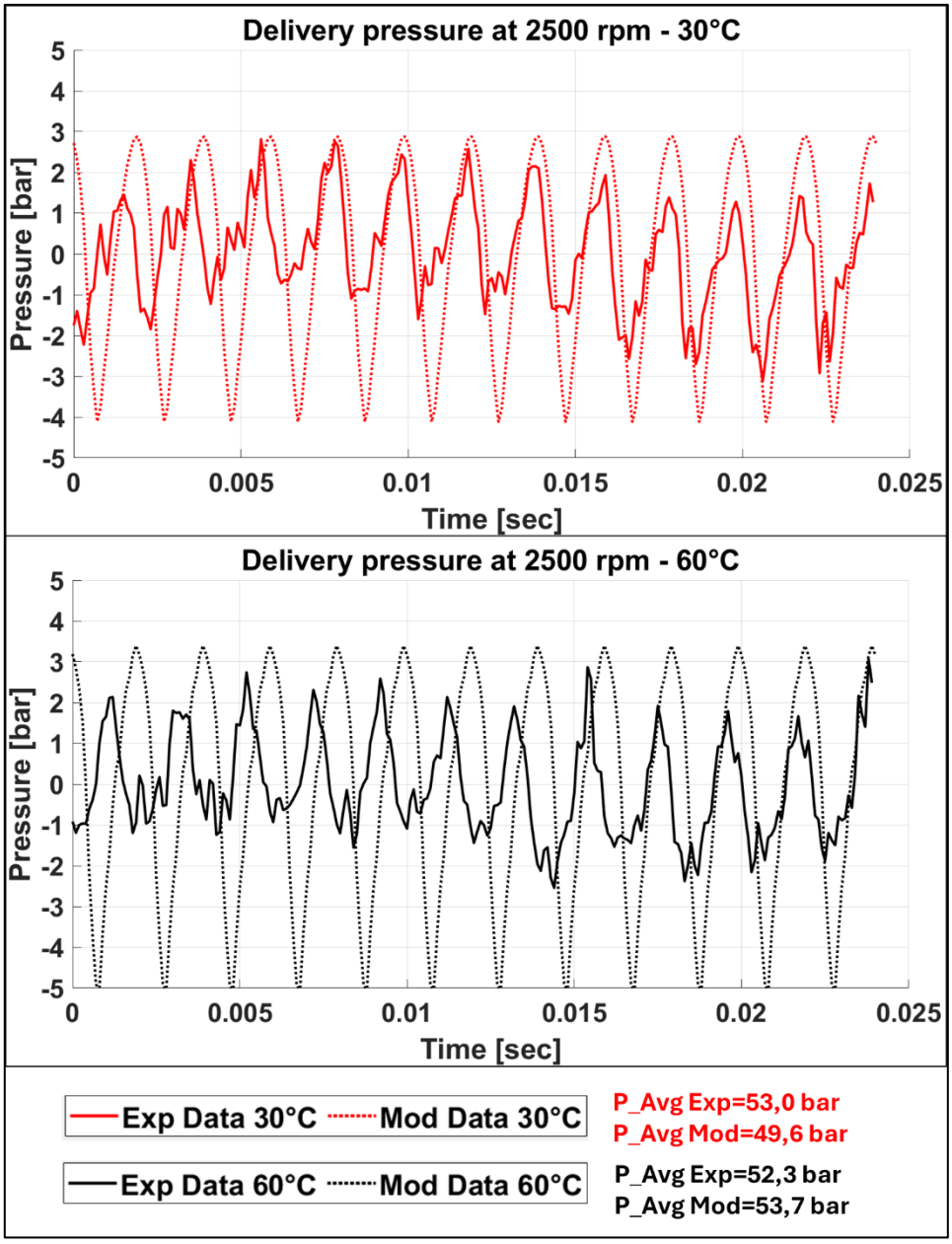

Figure 182 - Pressure ripple Pump 16 cc No.3 at 2500rpm and 50 bar

Figure 183 shows the pressure ripple of the 16 cc pump at 2500 rpm and 150 bar over one gear revolution. Also at these conditions, the average pressure estimated by the model is similar to the experimental average pressure at 30°C and 60°C.

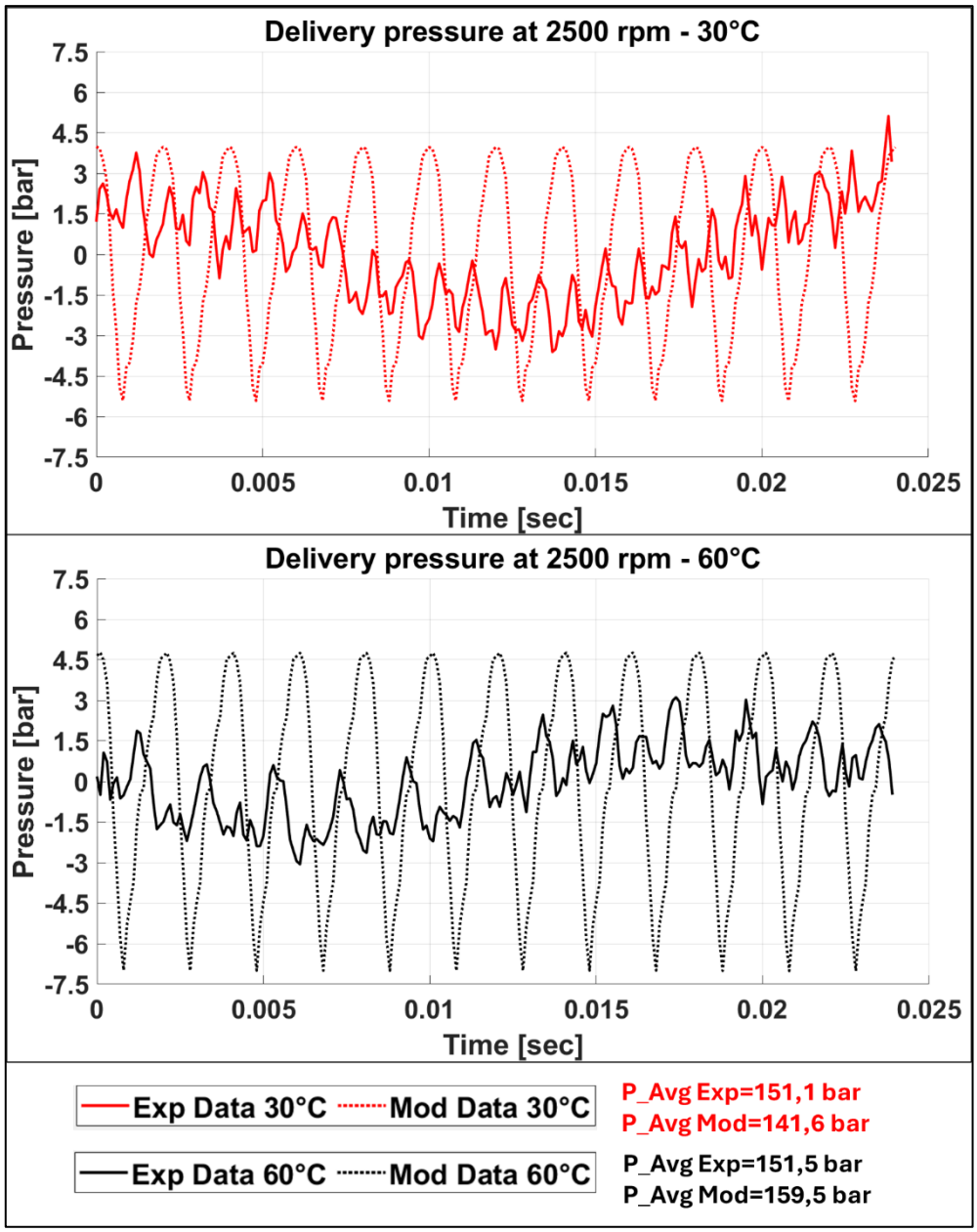

Figure 183 - Pressure ripple Pump 16 cc No.3 at 2500rpm and 150 bar

Figure 184 shows the pressure ripple of the 16 cc pump at 2500 rpm and 240 bar over one gear revolution. Also at these conditions, the average pressure estimated by the model is similar to the experimental average pressure at 30°C and 60°C.

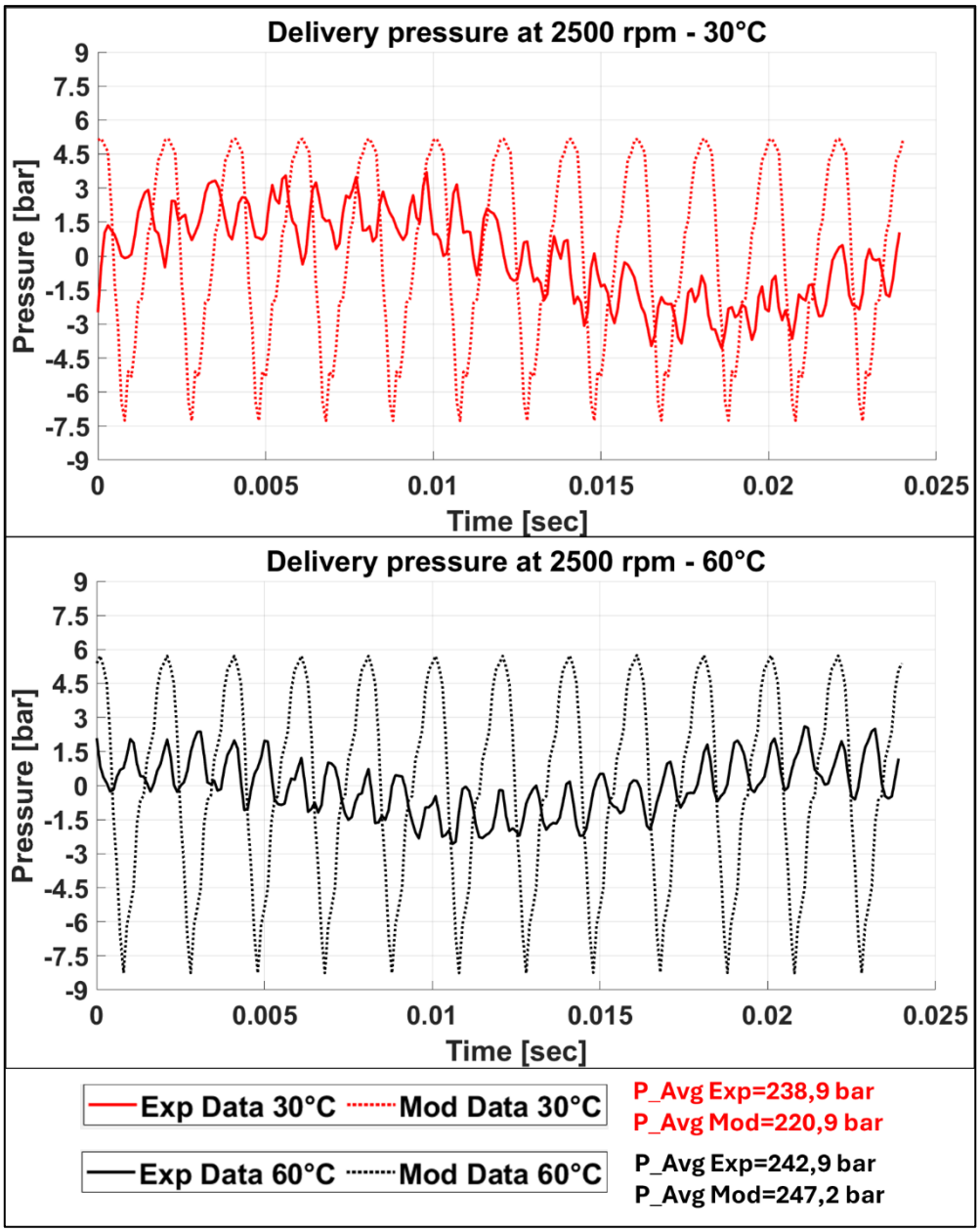

Figure 184 - Pressure ripple Pump 16 cc No.3 at 2500rpm and 240 bar

Figure 185 shows the results of FFT analysis applied to the experimental and model pressure signals at the speed of 2500 rpm.

From the analysis of the experimental data, the following observations emerge:

- The amplitude of the oscillation at the frequency f_{shaft} increases with increasing average delivery pressure at 30°C and 60°C.
  With temperature variation, the amplitude decrease.
- The amplitude of the oscillation associated with the frequency f_1 at 30°C decreases as the average delivery pressure increases.
  With temperature variation, the amplitude slightly increases.
  Although these magnitude of these variations are of limited significance

- The amplitudes associated with the frequency f_2 become more relevant, and are of the same order of magnitude as the oscillation associated with frequency f_1.
- The amplitudes associated with the remaining frequencies are negligible

From the analysis of the model data, the following observations emerge:

- Increasing the average delivery pressure causes an increase in amplitude at all frequencies.
- Increasing the temperature decreases the oscillation amplitude at all frequencies.

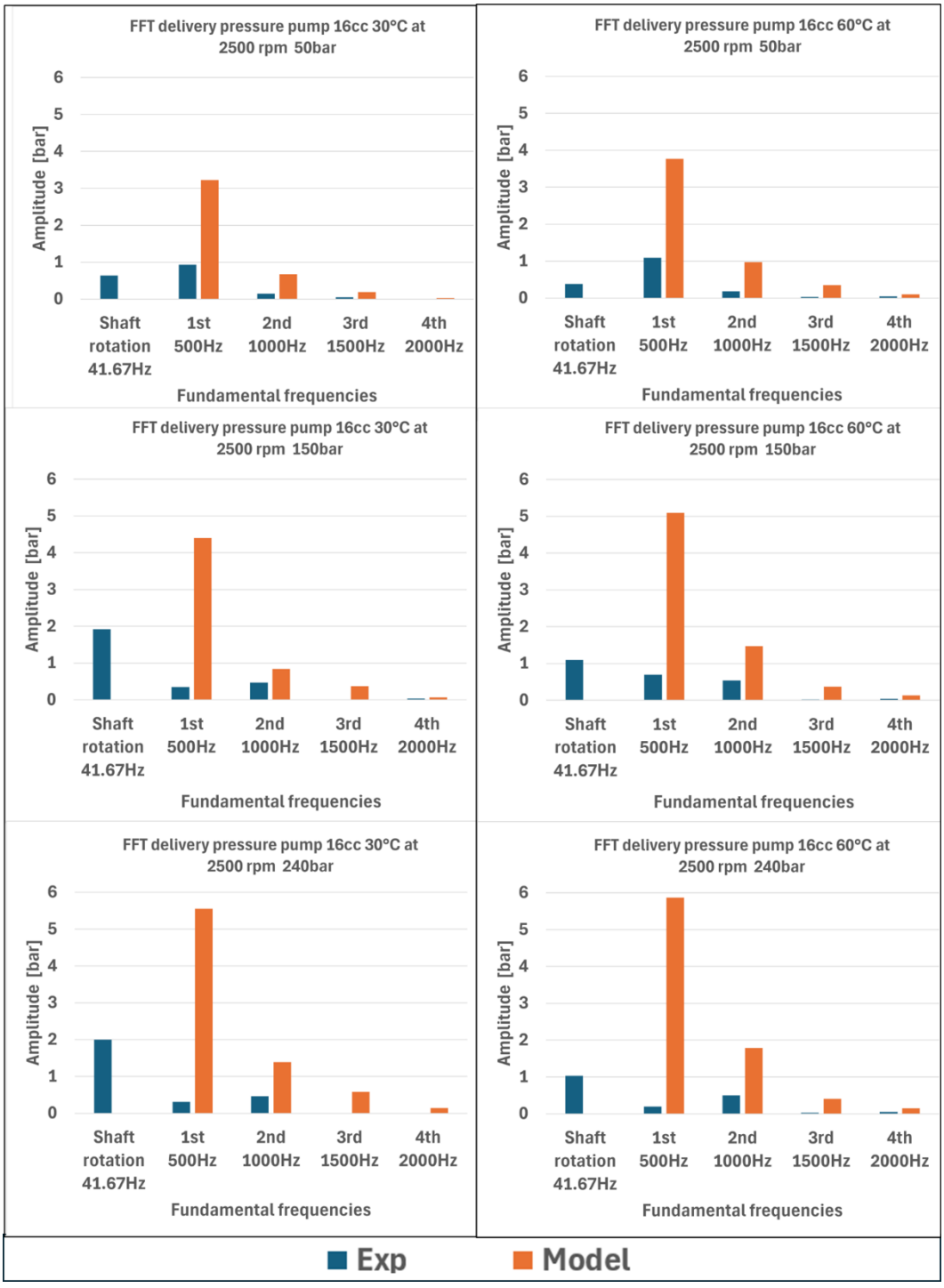

Figure 185 - FFT Pressure Ripple - Pump 16 cc No.3 at 2500rpm

9.4. Conclusion

This chapter investigated the pressure-ripple phenomenon at the delivery line of two spur external-gear pumps (8.2 cc and 16 cc) and assessed the predictive capability of the simulation model against experimental measurements. The analysis focused on the spectral content obtained via FFT.

Summary of experimental findings

- At low delivery pressure, the amplitude at f_{shaft} frequency is small compared with the frequency f_1. With increasing pressure, the amplitude at f_{shaft} frequency grows and can become the dominant spectral component.
- The amplitudes at the second, third, and fourth harmonics are generally negligible, except for the 16 cc pump at 2500 rpm, where the second harmonic becomes comparable to frequency f_1.
- For a fixed rotational speed, the amplitude at frequency f_1 exhibits only a weak dependence on mean delivery pressure and temperature. Conversely, the amplitude at f_{shaft} frequency is strongly condition-dependent, typically increasing with mean delivery pressure and decreasing as temperature rises.

Model–experiment comparison

- The model systematically overestimates spectral amplitudes across most operating conditions; the best agreement is observed at 50 bar and 30 °C.
- In the model, harmonic components other than f_1 tend to be more pronounced than in the measurements.
- The model response is simpler to define than observed experimentally, with amplitudes generally increasing with both mean delivery pressure and temperature.

Interpretation and limitations

- The results indicate that the current model does not fully reproduce the experimentally observed behaviour of the pressure-ripple spectra, and the overestimation of amplitudes can be substantial in specific regimes.
- A plausible hypothesis for the discrepancies is the presence of coupling errors between pump and test rig that are not represented in the simulation. In the campaign, the pump–rig connection was realized using a coupling manufactured by welding two couplings, a configuration that likely introduced misalignment. At low pressure, the f_{shaft} component attributable to such coupling imperfections remains small, the model match better the experimental data, whereas at higher pressure the f_{shaft} amplitude increases and the model data deviation becomes more evident. These coupling effects are also likely to contaminate the amplitudes at neighbouring frequencies.

- Consequently, the measured spectra may include coupling-induced contributions larger than those expected under normal service conditions, while the model, which omits these mechanisms, cannot account for them.

Implications and recommendations for future work

- On the experimental side, a precision pump–rig coupling should be employed to minimise misalignment and isolate the hydraulic sources of pulsation. Where residual imperfections are unavoidable.
- On the modelling side, an extended representation of the mechanical drive should be incorporated. This would allow the model to capture coupling-induced contributions and is expected to reduce the overestimation of spectral amplitudes.

10. Final Conclusion

In this thesis, the PhD activities carried out at the Fluid Power Laboratory of the "Enzo Ferrari" Department of Engineering of the University of Modena and Reggio Emilia are presented, in collaboration with Dana Motion Systems Italia S.r.l., specifically its subsidiary DPC Hydraulics S.r.l. in Reggio Emilia.

The development of a lumped-parameter model of an external spur gear pump in Simcenter Amesim is presented, with the aim of obtaining a digital design-support tool. The mathematical formulation of the model and the underlying assumptions are described.

Under the assumptions of incompressible and isothermal fluid, steady-state conditions, and a fixed lateral gap, the model can:

- estimate the volumetric performance of the pump, including chamber-pressure evolution, pump flow rate, and internal volumetric leakages due to tip clearances, the lateral gap, and tooth-flank gaps.
- estimate the hydro-mechanical performance of the pump, including pump torque, forces acting on the gears, viscous losses due to the lateral gaps, tooth-tip gaps and journal bearings, and mechanical losses due to gear meshing.
- estimate the average gear eccentricities, which are important for a correct estimation of tip- and flank-gap leakage.
- estimate the wear of the pump-housing profile due to the running-in process.
- estimate the pressure ripple on the delivery line.

To validate the model, an experimental campaign was conducted at the DPC Hydraulics S.r.l. laboratories on pumps with 8.2 cc and 16 cc displacement. The experimental activities included component measurements, volumetric and hydro-mechanical performance tests, and pressure-ripple tests.

From the experimental activities it emerged that:

- The model provides a good estimation of pump-housing wear during the running-in process using only a geometrical evaluation, without considering component deformation or thermal effects. In the case of the 8.2 cc pump, the model underestimated the average maximum gear penetration by 0.027 mm, while in the case of the 16 cc pump the average underestimation was 0.05 mm. With regard to the angular extension of the wear zone, the model overestimated the experimental data by an average of 10° for the 8.2 cc pump and 0.75° for the 16 cc pump.
- The model provides good results in the estimation of volumetric flow rate. For the 8.2 cc pump, in the speed range 1500-3500 rpm at 30 °C, the model produced a relative error in the range 0.1-3.8%, with an average of 0.8%, while at 60 °C the relative error was in the range 0.1-11.9%, with an average value of 2.4%. For the 16 cc pump, in the speed range 1000-2500 rpm at 30

°C, the model produced a relative error in the range 0.1-2.2%, with an average of 1.3%, while at 60 °C the relative error was in the range 0.1-6.5%, with an average value of 1.6%.

- For the hydro-mechanical performance, the model underestimated pump torque under all operating conditions, probably due to the lack of consideration of floating journal-bearing tilting and possible mixed-lubrication phenomena. However, the model still provides good results. For the 8.2 cc pump at 30 °C, the model produced a relative error in the range 6-10.2%, with an average of 8.1%, while at 60 °C the relative error was in the range 2.4-15.1%, with an average value of 7.6%. For the 16 cc pump at 30 °C, the model produced a relative error in the range 5.2-9.5%, with an average of 7.8%, while at 60 °C the relative error was in the range 3.1–13.5%, with an average value of 7.9%.
- From the pressure-ripple tests it emerged that the model overestimates the pressure oscillations observed experimentally. The comparison between model results and measured pressure ripple shows that the model does not match the experimental data, as it overpredicts pressure oscillations on the delivery line.

In conclusion, the model shows a good capability in estimating pump performance and the wear induced by the running-in process, thereby demonstrating its usefulness as a digital design-support tool. Some potential industrial applications of the model include:

- studying the effect of variations in tooth geometry on pump performance (e.g. cutting tool parameter variations, number of gear teeth).
- optimising the geometry of the anti-noise recesses on the floating bushing blocks in order to improve volumetric performance or reduce pump noise.
- evaluating the effect of component tolerances on pump performance.
- optimising the running-in process during the manufacturing phase.

However, some critical issues emerged and may be addressed in future work:

- At low speed (1000 rpm for the 8.2 cc pump and 500 rpm for the 16 cc pump), the model shows relevant discrepancies with respect to the experimental data, especially at 60 °C. Investigating this issue by using a more suitable flowmeter for low flow rates could clarify whether the discrepancy is due to measurement uncertainty or whether the model is not adequate for estimating flow rate at low speed.
- Considering floating journal-bearing tilting and a variable lateral gap could improve the estimation of volumetric leakages and viscous losses associated with the lateral gap, as well as by accounting for partial-surface lubrication.
- The model does not reproduce the experimental pressure-ripple results. A plausible explanation for the discrepancies is the presence of coupling errors between the pump and the test rig; therefore, a precision pump–rig coupling

should be used to minimise misalignment and isolate the hydraulic sources of pulsation.

- As shown in Appendix A, volumetric leakage through the flank gaps has an important effect on pressure ripple and also on the estimated chamber pressure in the meshing zone. Further investigation of the correct modelling of this leakage is recommended, through experimental measurements of chamber pressure or CFD simulations.

11. Bibliography

[1] M. Rundo, ‘Models for Flow Rate Simulation in Gear Pumps: A Review’, *Energies*, vol. 10, no. 9, p. 1261, Aug. 2017, doi: 10.3390/en10091261.

[2] S. Manco’ and N. Nervegna, ‘Simulation Of An External Gear Pump And Experimental Verification’, *Proceedings of the JFPS International Symposium on Fluid Power*, vol. 1989, no. 1, pp. 147–160, 1989, doi: 10.5739/isfp.1989.147.

[3] A. Vacca and M. Guidetti, ‘Modelling and experimental validation of external spur gear machines for fluid power applications’, *Simulation Modelling Practice and Theory*, vol. 19, no. 9, pp. 2007–2031, Oct. 2011, doi: 10.1016/j.simpat.2011.05.009.

[4] B. Zardin, E. Natali, and M. Borghi, ‘Evaluation of the Hydro—Mechanical Efficiency of External Gear Pumps’, *Energies*, vol. 12, no. 13, p. 2468, June 2019, doi: 10.3390/en12132468.

[5] R. Rituraj, A. Vacca, and M. Rigosi, ‘Modeling and validation of hydro-mechanical losses in pressure compensated external gear machines’, *Mechanism and Machine Theory*, vol. 161, p. 104310, July 2021, doi: 10.1016/j.mechmachtheory.2021.104310.

[6] M. Borghi, M. Milani, F. Paltrinieri, and B. Zardin, ‘Studying the Axial Balance of External Gear Pumps’, presented at the 2005 SAE Commercial Vehicle Engineering Conference, Rosemont, Illinois, United States, Nov. 2005, pp. 2005-01–3634. doi: 10.4271/2005-01-3634.

[7] M. Borghi e B. Zardin, 'Axial Balance of External Gear Pumps and Motors: Modelling and Discussing the Influence of Elastohydrodynamic Lubrication in the Axial Gap', in *IMECE2015*, Volume 15: Advances in Multidisciplinary Engineering, nov. 2015. doi: 10.1115/IMECE2015-51632.

[8] M. Torrent, P. J. Gamez-Montero, and E. Codina, ‘Motion Modelling of the Floating Bushing in an External Gear Pump Using Dimensional Analysis’, *Actuators*, vol. 12, no. 9, p. 338, Aug. 2023, doi: 10.3390/act12090338.

[9] S. Dhar and A. Vacca, ‘A novel CFD – Axial motion coupled model for the axial balance of lateral bushings in external gear machines’, *Simulation Modelling Practice and Theory*, vol. 26, pp. 60–76, Aug. 2012, doi: 10.1016/j.simpat.2012.03.008.

[10] E. Mucchi, G. D’Elia, and G. Dalpiaz, ‘Simulation of the running in process in external gear pumps and experimental verification’, *Meccanica*, vol. 47, no. 3, pp. 621–637, Mar. 2012, doi: 10.1007/s11012-011-9470-9.

[11] A. Pawar, A. Vacca, and M. Rigosi, ‘Comparative Analysis of External Gear Machine Performance Considering Deformation and Thermal Effects’, *TJFP*, pp. 465–492, Dec. 2024, doi: 10.13052/ijfp1439-9776.2543.

[12] A. Corvaglia, A. Ferrari, M. Rundo, and O. Vento, ‘Three-dimensional model of an external gear pump with an experimental evaluation of the flow ripple’, *Proceedings of the Institution of Mechanical Engineers, Part C: Journal of Mechanical Engineering Science*, vol. 235, no. 6, pp. 1097–1105, Mar. 2021, doi: 10.1177/0954406220937043.

[13] P. Szwemin and W. Fiebig, ‘The Influence of Radial and Axial Gaps on Volumetric Efficiency of External Gear Pumps’, *Energies*, vol. 14, no. 15, p. 4468, July 2021, doi: 10.3390/en14154468.

[14] E. Frosina, A. Senatore, and M. Rigosi, ‘Study of a High-Pressure External Gear Pump with a Computational Fluid Dynamic Modeling Approach’, *Energies*, vol. 10, no. 8, p. 1113, July 2017, doi: 10.3390/en10081113.

[15] F. Orlandi, G. Muzzioli, M. Milani, F. Paltrinieri, and L. Montorsi, ‘Development of a Numerical Approach for the CFD Simulation of a Gear Pump under Actual Operating Conditions’, *Fluids*, vol. 8, no. 9, p. 244, Aug. 2023, doi: 10.3390/fluids8090244.

[16] M. Rundo and N. Nervegna, '*Passi nell’oleodinamica*', 2020.

[17] Siemens Digital Industries Software, ‘Simcenter Amesim™ software User’s Guides - ver.2210’.

[18] *UNI ISO 21771:2024 ,Gears — Cylindrical involute gears and gear pairs — Concepts and geometry*.

[19] M. Callegari, P. Fanghella, and F. Pellicano, '*Meccanica applicata alle macchine'*, 2nd ed. CittàStudiEdizioni.

[20] X. Zhao and A. Vacca, ‘Numerical analysis of theoretical flow in external gear machines’, *Mechanism and Machine Theory*, vol. 108, pp. 41–56, Feb. 2017, doi: 10.1016/j.mechmachtheory.2016.10.010.

[21] Rituraj, T. Ransegnola, and A. Vacca, ‘An Investigation on the Leakage Flow and Instantaneous Tooth Space Pressure in External Gear Machines’, in *2018 Global Fluid Power Society PhD Symposium (GFPS)*, Samara: IEEE, July 2018, pp. 1–8. doi: 10.1109/GFPS.2018.8472358.

[22] B. J. Hamrock, S. R. Schmid, and B. O. Jacobson, '*Fundamentals of Fluid Film Lubrication'*, 2nd ed. CRC Press, 2004. Available: https://doi.org/10.1201/9780203021187

[23] R. Rituraj and A. Vacca, ‘Investigation of flow through curved constrictions for leakage flow modelling in hydraulic gear pumps’, *Mechanical Systems and Signal Processing*, vol. 153, p. 107503, May 2021, doi: 10.1016/j.ymssp.2020.107503.

[24] E. Mucchi, G. Dalpiaz, and A. Fernàndez Del Rincòn, ‘Elastodynamic analysis of a gear pump. Part I: Pressure distribution and gear eccentricity’,

Mechanical Systems and Signal Processing, vol. 24, no. 7, pp. 2160–2179, Oct. 2010, doi: 10.1016/j.ymssp.2010.02.003.

[25] R. Rituraj, A. Vacca, e M. Rigosi, 'Modeling and validation of hydro-mechanical losses in pressure compensated external gear machines', *Mech. Mach. Theory*, vol. 161, p. 104310, lug. 2021, doi: 10.1016/j.mechmachtheory.2021.104310.

[26] Y. Hori, *Hydrodynamic Lubrication*. Springer Tokyo. Available: https://doi.org/10.1007/4-431-27901-6

[27] F. W. Ocvirk, 'Short-bearing approximation for full journal bearings', 1952. [Online]. Available: https://api.semanticscholar.org/CorpusID:118264623

[28] *UNI ISO/TR 14179-1:2024 , Gears—Thermalcapacity Part1: Rating gear drives with thermal equilibrium at 95 °C sump temperature*.

[29] C. Gurd, C. Wink, J. Bair, and C. Fajardo, 'Computing Gear Sliding Losses', 2020.

[30] Y. N. Drozdov e Y. A. Gavrikov, 'Friction and scoring under the conditions of Simultaneous rolling and sliding of bodies', *Wear*, vol. 11, fasc. 4, pp. 291–302, apr. 1968, doi: 10.1016/0043-1648(68)90177-4.

[31] J. E. Shigley, Ed., *Standard handbook of machine design*, 2nd ed. New York: McGraw-Hill, 1996.

[32] J. F. Booker, 'Dynamically Loaded Journal Bearings: Mobility Method of Solution', *Journal of Basic Engineering*, vol. 87, no. 3, pp. 537–546, Sept. 1965, doi: 10.1115/1.3650602.

[33] J. F. Booker, 'Dynamically-Loaded Journal Bearings: Numerical Application of the Mobility Method', *Journal of Lubrication Technology*, vol. 93, no. 1, pp. 168–174, Jan. 1971, doi: 10.1115/1.3451507.

[34] J. F. Booker, 'Mobility/Impedance Methods: A Guide for Application', *Journal of Tribology*, vol. 136, no. 2, p. 024501, Apr. 2014, doi: 10.1115/1.4025760.

[35] P. Flores, J. P. Claro, and J. Ambrósio, 'Journal Bearings Subjected To Dynamic Loads: The Analytical Mobility Method' Mecânica Experimental, 13 (2006) 115-127.

[36] J. F. Booker, 'A Table of the Journal-Bearing Integral', *Journal of Basic Engineering*, vol. 87, pp. 533–535, 1965.

[37] R.B Randall and B. Tech, '*Frequency Analysis'*. Brüel & Kjaer, 1987.

[38] A. Vacca, G. Franzoni, and P. Casoli, 'On the Analysis of Experimental Data for External Gear Machines and Their Comparison With Simulation Results', in *Volume 4: Design, Analysis, Control and Diagnosis of Fluid Power Systems*, Seattle,

Washington, USA: ASMEDC, Jan. 2007, pp. 45–53. doi: 10.1115/IMECE2007-42664.

[39] D. Rabsztyn and K. Klarecki, ‘Experimental Tests of Pressure Pulsation of Gear Pumps’, in *Proceedings of the 13th International Scientific Conference*, E. Rusiński and D. Pietrusiak, Eds, in Lecture Notes in Mechanical Engineering. , Cham: Springer International Publishing, 2017, pp. 461–469. doi: 10.1007/978-3-319-50938-9_48.

[40] P. Casoli, A. Vacca, and G. Franzoni, ‘A Numerical Model For The Simulation Of External Gear Pumps’, *Proceedings of the JFPS International Symposium on Fluid Power*, vol. 2005, no. 6, pp. 705–710, 2005, doi: 10.5739/isfp.2005.705.

Appendix A: Effect of leakage through tooth flank clearances on pressure ripple

As a brief digression, this appendix presents an analysis of the effect of volumetric leakage through the tooth flank clearances on the pressure ripple in the pump delivery line.
Section 1.7.5 introduced the formulations used to model this type of leakage.

The flow rate through the flank clearance is modelled in two ways:

- **Formulation 1** – The flow rate is computed using the formulation proposed by R. Rituraj and A. Vacca [23], which describes laminar flow between two curved surfaces. In this case, the leakage depends on the fluid properties, clearance geometry and pressure difference. No additional tuning parameters are required to use this formulation.
- **Formulation 2** – The flow rate is calculated using the laminar–turbulent orifice equation introduced previously (see Eq. 69). In this case, the leakage depends on the fluid properties, clearance geometry, pressure difference and flow coefficients. The definition of the latter requires specifying the maximum flow coefficient $c_{q,\max}$ and the critical Reynolds number λ_{crit}, which govern the transition between laminar and turbulent flow.The values assigned to $c_{q,\max}$ and λ_{crit} directly affect the volumetric leakage through the tooth flank clearances.

In Section 8, the experimental results of the pressure ripple tests were presented, together with a comparison with the model results obtained using Formulation 1 for the tooth flank leakage.
In this appendix, the same comparison is carried out using Formulation 2 for the tooth flank leakage.

In particular, results are reported only for the external spur gear pump with a displacement of 8.2 cc, operating at 1500 rpm and 3500 rpm, at an oil temperature of 30 °C. Results for other operating conditions and for the pump with 16 cc displacement are omitted, as the purpose of this appendix is solely to illustrate how the modelling of the tooth flank leakage affects the pressure ripple.

Figure 186 shows the Fast Fourier Transform (FFT) of the pressure ripple in the delivery line for the 8.2 cc pump at 30 °C, obtained using Formulation 2 with $\lambda_{\mathrm{crit}} = 1000$ and $c_{q,\max}$ in the range 0.1-0.5.
This analysis shows that decreasing the value of $c_{q,\max}$ reduces the pressure oscillations predicted by the model, leading to a better agreement with the experimental results. Reducing $c_{q,\max}$ implies a reduction in the leakage flow rate estimated by Formulation 2.

The FFT analysis therefore suggests selecting a relatively low value of $c_{q,\max}$ when using Formulation 2. However, the reduced estimation of leakage through the tooth flanks also has other effects:

- an increase in the predicted volumetric efficiency of the pump.
- a higher volumetric efficiency, and therefore a higher delivered flow rate, which in turn leads to a higher average pressure on the delivery line in the simulated pressure ripple tests.
- a reduction in leakage that increases the peak pressure inside the chambers in the meshing zone and, consequently, leads to an increase in the pump torque predicted by the model, with a corresponding reduction in the hydro-mechanical efficiency.

Conclusion

This section has aimed to briefly demonstrate the significant impact of volumetric leakage modelling through the tooth flank clearances on the predicted pressure ripple in the pump delivery line. The results, specifically for the 8.2 cc external spur gear pump at 1500 rpm and 3500 rpm and at 30 °C, highlight that Formulation 2 offers greater flexibility in tuning the model output. This suggests that a careful calibration of the maximum flow coefficient $c_{q,\max}$is crucial for accurately reproducing the dynamic behaviour of the pump pressure.

However, the analysis also revealed a critical trade-off. While reducing $c_{q,\max}$ improves the prediction of the pressure ripple, it simultaneously affects other key performance indicators. In particular, a lower estimated leakage flow rate results in an increased predicted volumetric efficiency and, consequently, a higher average delivery line pressure in the simulations. Furthermore, the reduction in leakage leads to elevated peak pressures within the meshing chambers, which in turn increases the estimated pump torque and reduces the hydro-mechanical efficiency.

These findings underscore the importance of a holistic approach when selecting and calibrating leakage models within 0D pump simulations. While Formulation 2 provides a valuable tool for refining pressure ripple predictions, its parameters must be chosen with an awareness of their broader implications for the overall pump performance characteristics and should be supported by experimental data.

In the specific case of calibrating the model to reproduce the peak pressures inside the chambers, further experimental activities may be required. These may include, for example, direct measurement of the pressure inside the pump chambers or the use of CFD simulations to provide additional insight into the local pressure distribution and leakage phenomena.

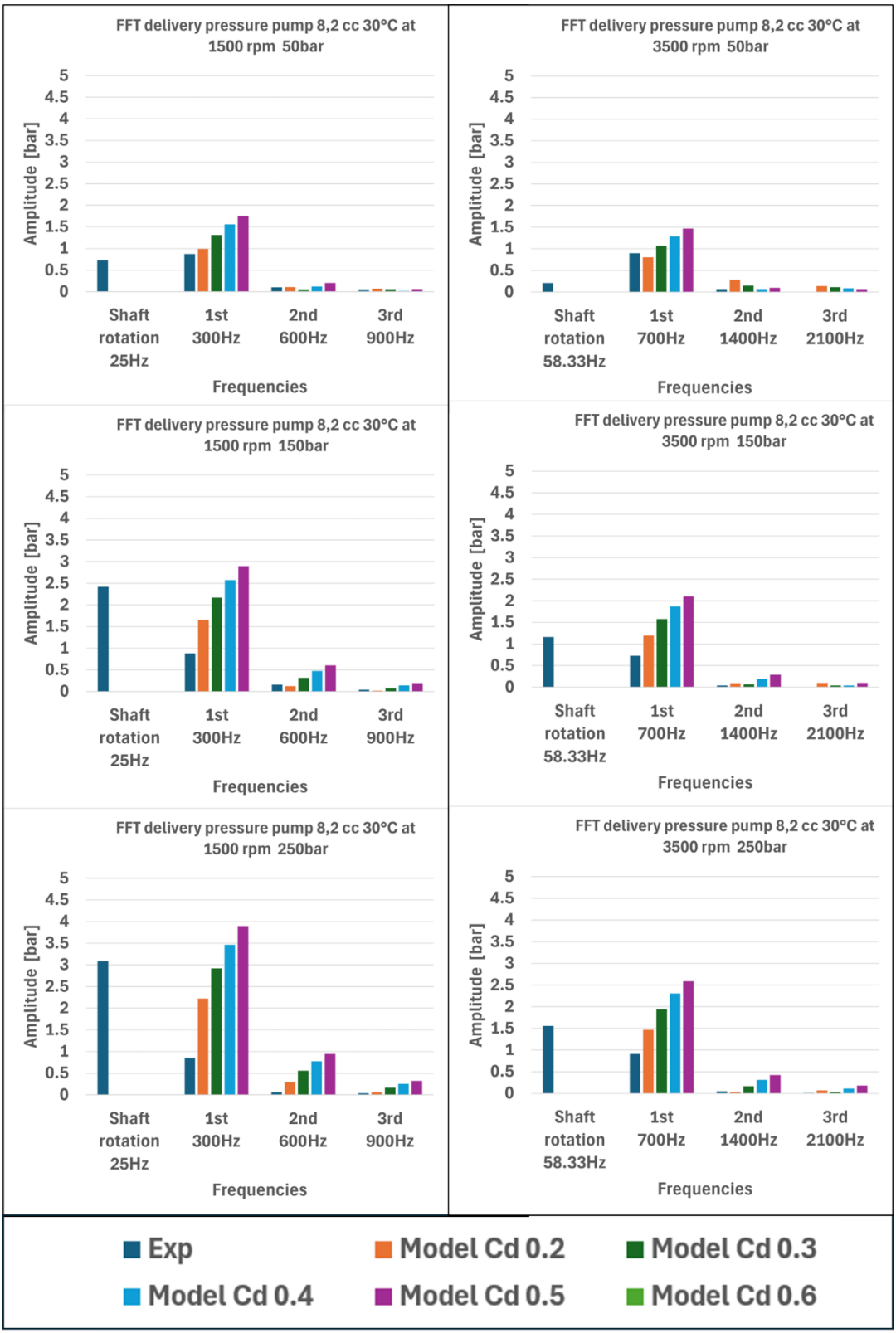

Figure 186 - FFT Pressure Ripple – Pump8.2 cc No.- Formulation 2

Tesi di dottorato finanziata dall'Unione europea- Next Generation EU, Missione 4, componente 2 "Dalla Ricerca all'Impresa" - Investimento 3.3 "Introduzione di dottorati innovativi che rispondono ai fabbisogni di innovazione delle imprese e promuovono l'assunzione dei ricercatori dalle imprese".